UNIVERSITY OF CALGARY

Multimode-Optomechanics, Spin-Optomechanics, and Nonlinear Optics in Photonic Devices

by

David Paul Lake

A THESIS
SUBMITTED TO THE FACULTY OF GRADUATE STUDIES
IN PARTIAL FULFILLMENT OF THE REQUIREMENTS FOR THE
DEGREE OF DOCTOR OF PHILOSOPHY

GRADUATE PROGRAM IN PHYSICS AND ASTRONOMY

CALGARY, ALBERTA
JANUARY, 2020

Abstract

Nanophotonic structures are a technological platform, which enhance processes by confining light to a small physical space. The spatial configuration of the light is known as a mode. In this thesis nanophotonic structures were used to enhance nonlinear optical processes, support optomechanics and multimode optomechanics, and finally to interface with colour centres.

In nonlinear optics experiments, we used Gallium Phosphide (GaP) microdisks to generate second and third harmonic light. The small mode volume and low loss of these structures allow the buildup of a very large optical power within the microdisk, as well as a high degree of spatial overlap between the fundamental and second harmonic modes. This allowed efficient second harmonic generation rates for GaP structures.

The optomechanics experiments included in this thesis were performed in diamond microdisks, which represented the first optomechanics experiments in diamond. In later work, we modified our fabrication process such that a laser could be placed at particular wavelengths relative to the mode without thermal effects shifting the resonance. This, combined with optimization that reduced the optical loss rate, allowed for operation in the so called "sideband resolved regime". This enabled the demonstration of coherent scattering between photons and phonons in these devices.

Expanding on this work, we used a second optical mode in these diamond devices to demonstrate multimode optomechanical effects. This author assisted in demonstrations of wavelength conversion, and the first demonstration of optomechanical multimode amplification in the optical regime. We then went on to realize novel interference effects between widely separated wavelengths of light, which were used to build an optical switch. This same multimode device was used to demonstrate optomechanical pulse storage where the storage time and the phase of the stored pulse were enhanced and controlled using the auxiliary mode.

Finally, this thesis details our work towards the manipulation of quantum emitters embedded in these diamond devices through coupling to mechanical vibrations in the device. This platform has the potential to realize a compact system, where qubits could be directly controlled by telecom wavelength light.

Preface

This thesis contains works previously published, or currently in submission, as detailed below:

1. **Chapter 3: DP Lake**, M Mitchell, H Jayakumar, LF dos Santos, D Curic, PE Barclay. Efficient telecom to visible wavelength conversion in doubly resonant gallium phosphide microdisks. *Appl Phys Lett* 108(3), 031109 (2016).

2. **Chapter 4: DP Lake**, M Mitchell, Y Kamaliddin, PE Barclay. Optomechanically Induced Transparency and Cooling in Thermally Stable Diamond Microcavities. *ACS Photonics* 5(3), 782-787 (2018).

3. **Chapter 5: DP Lake**, M Mitchell, BC Sanders, PE Barclay. Two-color interferometry and switching through optomechanical dark mode excitation. *arXiv preprint arXiv:1906.10754. In submission, Nat Phot.*

4. **Chapter 6: DP Lake**, M Mitchell, PE Barclay. Optomechanical information storage and processing via dynamical reservoir engineering. *In preparation.*

Over the course of this my degree, I have also contributed to the following works:

1. H Jayakumar, B Khanaliloo, **DP Lake**, PE Barclay. Cooling and amplifying motion of a diamond resonator with a microscope. *arXiv preprint arXiv:1810.04196. In submission, Phys Rev Lett.*

2. M Mitchell, **DP Lake**, PE Barclay. Optomechanically amplified wavelength conversion in diamond microcavities. *Optica* 6(7), 832-838 (2019).

3. M Mitchell, **DP Lake**, PE Barclay. Realizing $Q > 300\,000$ in diamond microdisks for optomechanics via etch optimization. *APL Photonics* 4(1), 016101 (2019).

4. PK Shandilya, JE Fröch, M Mitchell, **DP Lake**, S Kim, M Toth, B Behera, C Healey, I Aharonovich, PE Barclay. Hexagonal Boron Nitride Cavity Optomechanics. *Nano Letters* 19(2), 1343-1350 (2019).

5. M Mitchell, B Khanaliloo, **DP Lake**, T Masuda, JP Hadden, PE Barclay. Single-crystal diamond low-dissipation cavity optomechanics. *Optica* 3(9), 963-970 (2016).

6. B Khanaliloo, H Jayakumar, AC Hryciw, **DP Lake**, H Kaviani, PE Barclay. Single-Crystal Diamond Nanobeam Waveguide Optomechanics. *Phys Rev X* 5(4), 041051 (2015).

7. M Wu, AC Hryciw, C Healey, **DP Lake**, H Jayakumar, MR Freeman, JP Davis, PE Barclay. Dissipative and Dispersive Optomechanics in a Nanocavity Torque Sensor. *Phys Rev X* 4(2), 021052 (2014).

Acknowledgements

Writing a thesis has been an interesting experience. While the past several years in the moment often felt like a series of disconnected conundrums (interleaved with occasional moments of clarity), in writing a thesis you are tasked with repurposing this timeline into a coherent story. It also has the effect of encapsulating the past several years as a sort of singular unit, and forced me to reflect on them. One thing however, which only becomes more clear on reflection is just how fortunate I have been to have had amazing mentors, collaborators, friends, and family. I hope that you all know how grateful I am.

Firstly I would like to thank my supervisors over the years. In my undergraduate days Ted Monchesky supervised my undergraduate research project and gave me my first opportunity to do research. I cannot thank Ted enough for this. Without his patience, encouragement, and good references, I seriously doubt I would have ever made it into grad school. I would also like to thank Paul Barclay, my supervisor during my graduate studies. There were countless times where Paul helped me reason through a problem, teaching me how to think like a scientist (or sometimes even like an engineer!). I truly appreciate the style of research environment that Paul fostered, where students are given nearly complete freedom to pursue whatever research interests them.

In the early days of the lab, I learned the ropes by shadowing Hari, our postdoc at the time. I will always strive to try and emulate Hari's cheerful demeanour, whether pulling fibers at 2 am, or standing watch over a cryostat cool down. Later on I started working with Matt Mitchell, both in the lab and in the cleanroom. I will always be impressed by Matt's

calm demeanour, and immense talent. Matt also has the invaluable skill of being able to "just get down to work", while other people are busy endlessly discussing how they would do something. Although we only worked together in the lab for about two weeks, Thomas Lutz taught me just about everything I know about colour centres, for which I am very grateful. In the past year of my Ph.D. I also had the opportunity to work with Prasoon on the stress coupling project. I'd like to thank him for his patience and hard work on this, and I really hope it pays off some day!

Outside of the lab, some of my happiest memories were formed in Calgary on adventures with Elizabeth, Matt, Behzad, and Tamiko. Thanks guys, for all of the memories! I would also like to thank my family, for being so patient with my studies over the years. Finally I would like to thank my partner Elizabeth, for all of her love and support over the years.

To my parents, for patiently answering my questions, and supporting my interests.

Table of Contents

List of Figures and Illustrations

List of Tables

Lists of Symbols and Abbreviations

Symbol	Definition
a	Optical mode amplitude
b	Mechanical mode amplitude
ω_{o}	Optical mode frequency
κ	Optical mode energy loss rate
ω_{m}	Mechanical mode frequency
γ	Mechanical mode energy loss rate

Abbreviation	Definition
CVD	Chemical Vapour Deposition
DOMIT	Double Optomechanically Induced Transparency
EBL	Electron Beam Lithography
GaP	Gallium Phosphide
ICPRIE	Inductively Coupled Plasma Reactive Ion Etch
NV	Nitrogen Vacancy Centre
ODMR	Optically Detected Magnetic Resonance
OMIA	Optomechanically Induced Amplification
OMIT	Optomechanically Induced Transparency
PECVD	Plasma Enhanced Chemical Vapour Deposition
RF	Radiofrequency
SCD	Single Crystal Diamond
SEM	Scanning Electron Microscope
SFG	Sum Frequency Generation
SHG	Second Harmonic Generation
SiV	Silicon Vacancy Centre
SOI	Silicon On Insulator
THG	Third Harmonic Generation

Epigraph

I am a part of all that I have met;

Yet all experience is an arch wherethro'

Gleams that untravell'd world whose margin fades

For ever and forever when I move.

- Lord Alfred Tennyson, *Ulysses*

Chapter 1

Optical Microcavities and Waveguides

1.1 Introduction: Bigger is Not Always Better

Building a photonic device is incontrovertibly a lot of work. Starting with an ultra-pure material and employing a combination of patience, electron beam writes, plasma etches, chemical cleans, and no inconsiderable amount of luck, a device is painstakingly carved out. This is only the beginning of the process; after this the device must be kept in a pristine environment, as slight amounts of dust and humidity can be detrimental to the properties of the device. Interfacing with the device involves the placement of a probe mere tens of nanometers from the surface and throughout its lifetime it must be delicately handled, as any direct contact with fingers or tweezers could result in an untimely demise. So why do researchers go through the trouble of making and testing such devices? In principle, similar devices can be constructed on a tabletop by more conventional means. The answer, which is the essential message of this thesis, is that "bigger is not always better". The construction of these tiny devices allows us access to a rich, interesting, and useful body of physics which is simply not accessible at a larger scale. Over the course of this thesis I will strive to convince the reader of this point.

1.2 Optical Modes

Throughout this thesis, we will frequently encounter modes and study the interactions between them. With this in mind, it is helpful to detail exactly what we mean by "modes" from the outset. A mode is an eigenfunction of an appropriate master equation given a specific set of boundary conditions. Quite often, the motion of everyday objects such as a clamped steel beam or a drumhead can be described as a linear combination of modes. For us, the intimate dependence of modes on the boundary conditions will be of special interest. This enables us to design systems supporting modes with specific features by careful design of the boundaries, or to manipulate them in situ by perturbation of these boundary conditions.

To model the propagation of light in a material, we can make use of the appropriate Maxwell's equations [1, 2],

$$\nabla \cdot \mathbf{D}(\mathbf{r}, t) = \rho, \tag{1.1a}$$

$$\nabla \times \mathbf{E} + \frac{\partial \mathbf{B}}{\partial t} = 0, \tag{1.1b}$$

$$\nabla \cdot \mathbf{B}(\mathbf{r}, t) = 0, \tag{1.1c}$$

$$\nabla \times \mathbf{H} - \frac{\partial \mathbf{D}}{\partial t} = \mathbf{J}, \tag{1.1d}$$

which are written in terms of electric field $\mathbf{E}$ and magnetic field $\mathbf{H}$, as well as the displacement field $\mathbf{D}$ and magnetic induction field $\mathbf{B}$. In the above equations ρ is the charge density, and $\mathbf{J}$ is the current, and each act as sources for the field terms. These source terms are essential to the operation of many optical devices. Two such examples are mirrors, which can be constructed from glass with a thin layer of conductive metal or metasurfaces, which make use of small conductive components situated on a surface to demonstrate exotic optical phenomena [3]. However, in our case we will construct devices from dielectric materials, where there are no electric charges or currents. This permits us to set $\rho = 0$ and $\mathbf{J} = 0$ in Maxwell's equations.

While it may appear that we have four independent fields to deal with, we can simplify matters using constitutive relations. We may write the components of the displacement field in terms of the components of the electric field in a completely general form as [4, 5],

$$D_i = \sum_j \epsilon_{ij} E_j + \sum_{jk} \epsilon_0 \chi^{(2)}_{ijk} E_j E_k + \sum_{jkl} \epsilon_0 \chi^{(3)}_{ijkl} E_j E_k E_l + \mathcal{O}(E^4). \tag{1.2}$$

In the above expression, ϵ_0 is the vacuum permittivity, ϵ is the relative permittivity, and $\chi^{(n)}$ is the n^{th} order nonlinear susceptibility. The higher order terms in the above expansion are relevant in circumstances where the response of the material is no longer linear, which often occurs in situations of very intense electric field. We will revisit this in Chapter 3, but for now we restrict ourselves to linear materials. Furthermore all materials considered in this thesis are optically isotropic, meaning that the relation between the electric field and displacement field is independent of direction. Under these assumptions, Eq. 1.2 simplifies to $\mathbf{D}(\mathbf{r}, t) = \epsilon(\mathbf{r})\mathbf{E}(\mathbf{r}, t)$. Note that the relative permittivity is a scalar value, and since we are dealing with idealized, lossless materials for now it may be taken to be real-valued. Also note that the relative permittivity has explicit dependence on spatial coordinates; this will allow us to describe all sorts of real world constructions, such as waveguides and optical resonators.

In similar fashion, we may relate the $\mathbf{H}$ and $\mathbf{B}$ fields. All materials considered in this work have an extremely weak magnetic response, and the constitutive relations in material turn out to be very close to those in vacuum. To good approximation we may simply write $\mathbf{H}(\mathbf{r}, t) = \frac{1}{\mu_0}\mathbf{B}(\mathbf{r}, t)$, where μ_0 is the vacuum permeability.

Armed with Maxwell's equations and the constitutive relations, we are in a position to derive some useful expressions. First we substitute the constitutive relations in the Maxwell's equations to eliminate the D-field and the B-field. This allows us to write the four coupled first order differential equations as two decoupled second order differential equations by taking the curl of Eqs. 1.1b and 1.1d and then substituting in Eqs. 1.1d and 1.1b, respectively.

Denoting the speed of light as $c = 1/\sqrt{\epsilon_0 \mu_0}$, we find,

$$\nabla \times (\nabla \times \mathbf{E}(\mathbf{r}, t)) = \frac{\epsilon(\mathbf{r})}{c^2} \frac{\partial^2 \mathbf{E}(\mathbf{r}, t)}{\partial t^2}, \tag{1.3}$$

$$\nabla \times \left(\frac{1}{\epsilon(\mathbf{r})} \nabla \times \mathbf{H}(\mathbf{r}, t) \right) = \frac{1}{c^2} \frac{\partial^2 \mathbf{H}(\mathbf{r}, t)}{\partial t^2}. \tag{1.4}$$

While the above equations may not be particularly useful by themselves, there are two different sets of equations that can be easily derived from it which will be quite useful in different circumstances. The first of these is found by taking the Fourier transform of Eqs. 1.3 and 1.4 with respect to time to derive,

$$\boxed{\begin{aligned} \nabla \times (\nabla \times \mathbf{E}(\mathbf{r}, \omega)) &= \epsilon(\mathbf{r}) \left(\frac{\omega}{c} \right)^2 \mathbf{E}(\mathbf{r}, \omega), \qquad (1.5) \\ \nabla \times \left(\frac{1}{\epsilon(\mathbf{r})} \nabla \times \mathbf{H}(\mathbf{r}, \omega) \right) &= \left(\frac{\omega}{c} \right)^2 \mathbf{H}(\mathbf{r}, \omega). \qquad (1.6) \end{aligned}}$$

These are the master equations [5] for the propagation of electromagnetic waves in a linear, dielectric material. Together with the transversality requirements $\nabla \cdot (\epsilon(\mathbf{r}, t)\mathbf{E}(\mathbf{r}, t)) = 0$ and $\nabla \cdot \mathbf{H}(\mathbf{r}, t) = 0$, they can be used to find the allowable configurations of the electromagnetic field within a given dielectric structure which oscillate at a given frequency, ω. They are often used as the starting point for numerical simulations [5, 6].

We can derive the second set of equations for the special case of a homogenous dielectric material (i.e., where ϵ is independent of $\mathbf{r}$). Once again, we begin with Eqs. 1.3 and 1.4, except this time we can move ϵ to the r.h.s. of both expressions. Making use of the vector identity [1] $\boldsymbol{\nabla} \times (\boldsymbol{\nabla} \times \mathbf{V}) = \boldsymbol{\nabla} (\boldsymbol{\nabla} \cdot \mathbf{V}) - \nabla^2 \mathbf{V}$, for some vector $\mathbf{V}$, and the transversality requirements derived from Eqs. 1.1a and 1.1c, we can write the following wave equations for electric and magnetic fields,

$$\boxed{\begin{aligned} \nabla^2 \mathbf{E}(\mathbf{r}, t) &= \frac{n^2}{c^2} \frac{\partial^2 \mathbf{E}(\mathbf{r}, t)}{\partial t^2}, \qquad (1.7) \\ \nabla^2 \mathbf{H}(\mathbf{r}, t) &= \frac{n^2}{c^2} \frac{\partial^2 \mathbf{H}(\mathbf{r}, t)}{\partial t^2}, \qquad (1.8) \end{aligned}}$$

where we have defined the refractive index $n = \sqrt{\epsilon}$ for $\epsilon \in \mathbb{R}$.

In deriving the wave equations, we made the assumption that the dielectric is *homogenous*. Initially this might appear to restrict us to a rather boring geometry where a single refractive index describes all space. However, the situation is not as dire as it appears. Suppose we have two regions of dielectric material, one with refractive index n_1, and the other with refractive index n_2, which share a boundary. We may solve for the wave equation in each region separately, and simply match the boundary conditions to create an overall solution. These conditions may be stated in terms of field components perpendicular and parallel to the boundary as [1, 2],

$$\begin{aligned} E_{\parallel,1} &= E_{\parallel,2}, & \epsilon_1 E_{\perp,1} &= \epsilon_2 E_{\perp,2}, \\ H_{\parallel,1} &= H_{\parallel,2}, & H_{\perp,1} &= H_{\perp,2}. \end{aligned} \tag{1.9}$$

In the next few sections we will focus on Eq. 1.7 and Eq. 1.8 in various different configurations of dielectric material. We will see that the geometry of the dielectrics can cause solutions to be localized, and that the boundary conditions can induce confinement of the modes.

1.2.1 No Confinement: Plane Waves

To begin, we examine the "boring" situation alluded to in the previous section, where a dielectric material with refractive index n_{w} extends through all space. A cross section of this is shown on Fig. 1.1(a). Our aim is to satisfy Eq. 1.7 in all space given some initial condition. One possible ansatz is the plane wave solution $\mathbf{E}(\mathbf{r}, t) = \mathbf{A}\cos(\omega t - \mathbf{k}\cdot\mathbf{r} - \phi)$, where $\mathbf{A}$ is a real constant and ϕ is the phase. Here we have introduced the frequency ω and the wavevector $\mathbf{k} = \{k_{\mathrm{x}}, k_{\mathrm{y}}, k_{\mathrm{z}}\}$. Substituting this ansatz into Eq. 1.7 we find,

$$\left(|\mathbf{k}|^2 - \frac{n^2\omega^2}{c^2}\right)\mathbf{E}(\mathbf{r}, t) = 0. \tag{1.10}$$

In order for this equation to hold, we require that $\omega(\mathbf{k}) = \pm c|\mathbf{k}|/n$ as shown on Fig. 1.1(c). This type of equation, relating the frequency and the wave vector, is called a dispersion relation, for reasons that will become apparent in a moment [7]. While the dispersion is linear as written here, it becomes nonlinear if we allow n to be a function of the wave vector, or in more complicated dielectric geometries. The essential point is that ω and $\mathbf{k}$ are not independent variables. For a given frequency, the wave vector must take on a definite magnitude, and is free to propagate in a straight line in any direction. Geometrically,k will form the surface of a sphere of radius $\omega n/c$ in k-space, as on Fig. 1.1(b).

We can further restrict our solutions by substituting our ansatz into the transversality requirement derived from Eq. 1.1a,

$$0 = \nabla \cdot \mathbf{E}(\mathbf{r}, t) = (\mathbf{k} \cdot \mathbf{A}) \cos(\omega t - \mathbf{k} \cdot \mathbf{r} - \phi). \tag{1.11}$$

If this equation is to hold, the wave vector and electric field must be orthogonal. In fact, following similar arguments we can prove to ourselves that $\mathbf{E}$, $\mathbf{B}$, and $\mathbf{k}$ must all be mutually orthogonal, namely $\mathbf{E} \cdot \mathbf{k} = 0$, $\mathbf{B} \cdot \mathbf{E} = 0$, and $\mathbf{k} \cdot \mathbf{B} = 0$.

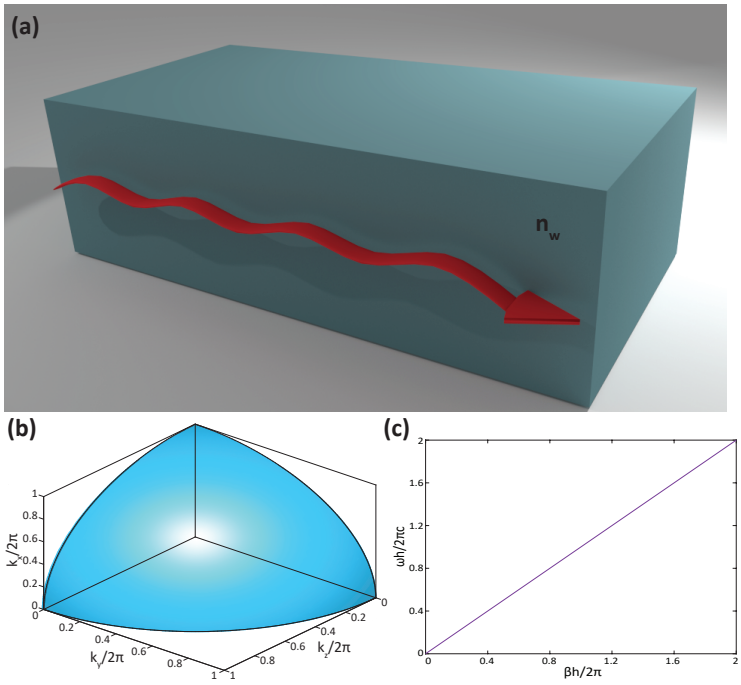

Figure 1.1: (a) Cross section of an isotropic dielectric material with refractive index n_{w}, with a plane wave propagating in the z-direction. (b) Possible values of the wave vector for a fixed energy of a monochromatic wave. (c) Dispersion relations for a plane wave travelling in a linear, isotropic dielectric.

Our solution as written can be cast into a more convenient form by noting that,

$$\Re\{\mathcal{E}^{i(\omega t-\mathbf{k}\cdot\mathbf{r})}\} = \mathbf{A}\cos\left(\omega t - \mathbf{k}\cdot\mathbf{r} - \phi\right), \tag{1.12}$$

where $\mathcal{E} = A^{-i\phi}$ is a complex number. In fact, by allowing the electric field to be complex in our calculations, many operations will become more mathematically convenient. We just need to keep in mind that in the complex representation only the real part of the field physically exists. Furthermore, we must exercise caution when taking products of two or more fields in this complex representation. When in doubt, we can always first take the real parts of the constituent fields, and then perform whatever mathematical operations are required, and change back to a complex representation if desired [8].

We are now in a position to construct a full solution to the wave equation in a homogeneous, isotropic medium. We already have a solution that is valid for a particular $\mathbf{k}$, so it is a natural extension to look for a general solution that is a superposition of these various solutions. Such a solution is called a wave packet, and is given by,

$$\mathbf{E}(\mathbf{r},t) = \int_{-\infty}^{\infty} c(\mathbf{k})\mathcal{E}e^{i(\omega(\mathbf{k})t-\mathbf{k}\cdot\mathbf{r})}d\mathbf{k}, \tag{1.13}$$

where $c(\mathbf{k})$ is a Fourier coefficient. Interestingly Eq. 1.13 has the form of a Fourier transform over k-space. It will allow us to conveniently and explicitly find the evolution of a particular spatial configuration of an electromagnetic wave given some initial condition. To see this, consider the wave packet at $t = 0$,

$$\mathbf{E}(\mathbf{r},0) = \int_{-\infty}^{\infty} c(\mathbf{k})\mathcal{E}e^{-i\mathbf{k}\cdot\mathbf{r}}d\mathbf{k} \rightarrow \mathcal{E}(\mathbf{k}) = \int_{-\infty}^{\infty} \mathbf{E}(\mathbf{r},0)e^{i\mathbf{k}\cdot\mathbf{r}}d\mathbf{r}, \tag{1.14}$$

where we have used the inverse Fourier transform in the second equality to write the solution for all time terms of the solution at $t = 0$. Together with Eq. 1.13, this gives us a general method to construct solutions for electromagnetic waves, even in the presence of dispersion. Each wave packet is constructed from a combination of individual plane waves that propagate independently in the absence of nonlinear effects.

While our approach of solving in inverse space might seem heavy-handed for this particular problem, it will be useful in scenarios for which the spatial distribution of the dielectric medium is more complicated.

1.2.2 1-d Confinement: Slab Modes

Consider a linear, lossless, isotropic, dielectric medium formed into a thin layer in the x-direction, with refractive index n_{w}. This is situated between another dielectric material with refractive index n_{s} as shown on Fig. 1.2. Unlike the previous example, if we set an electromagnetic wave propagating from the origin in a certain direction, it will not in general

continue in the same direction. In fact, provided that $n_{\mathrm{w}} > n_{\mathrm{s}}$, for a number of initial conditions, the propagation will be largely confined to the $x-y$ plane. This is our first example of guided modes.

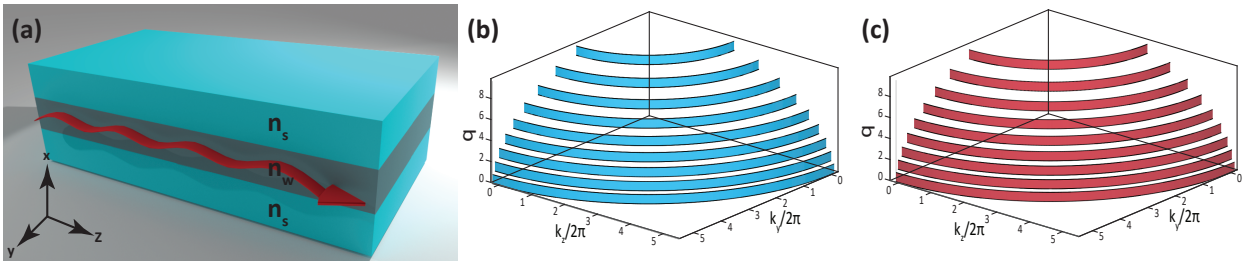

Figure 1.2: (a) Geometry of a slab waveguide, consisting of a slab with height h and refractive index n_{w} and substrate regions with refractive index n_{s}. (b) Allowed values of the k-vector for TE modes with fixed ω. (c) Allowed values of the k-vector for TM modes with fixed ω.

To understand why this is the case, we use Snell's law at the interface. If a ray is incident on the slab-substrate interface from the direction of the slab at an angle less than $\theta_{\mathrm{crit}} = \sin^{-1}\left(\frac{n_{\mathrm{s}}}{n_{\mathrm{w}}}\right)$ it will exit the slab and enter the substrate. However, if it enters at an angle greater than the critical angle $\theta > \theta_{\mathrm{crit}}$, it will be reflected back into the substrate.

Following nearly the same procedure as the previous section, we can solve for the mode in a slab waveguide. Once again we seek solutions to Eq. 1.7, however this time due to the fact that the refractive index changes in the x-direction, we modify our ansatz to make the solution more clear. Since waves may propagate freely in the $y-z$ plane, we will assume plane wave solutions in these directions. Our ansatz then reads, $\mathbf{E}(\mathbf{r},t) = \mathcal{E}(x)e^{i(\omega t - k_{\mathrm{y}}y - k_{\mathrm{z}}z)}$. Placing this into Eq. 1.7, we find,

$$\left(\frac{\partial^2}{\partial x^2} + \frac{n_{\mathrm{w}}^2\omega^2}{c^2} - k_{\mathrm{y}}^2 - k_{\mathrm{z}}^2\right)\mathcal{E}(x) = 0, \quad \text{(Waveguide)} \tag{1.15}$$

$$\left(\frac{\partial^2}{\partial x^2} + \frac{n_{\mathrm{s}}^2\omega^2}{c^2} - k_{\mathrm{y}}^2 - k_{\mathrm{z}}^2\right)\mathcal{E}(x) = 0. \quad \text{(Substrate)} \tag{1.16}$$

To clean up the notation, we define the effective refractive index $n_{\text{eff}} = \frac{c}{n}\sqrt{k_{\text{y}}^2 + k_{\text{z}}^2}$, the mode wavelength $\kappa = \frac{\omega}{c}\sqrt{n_{\text{w}}^2 - n_{\text{eff}}^2}$, and the mode decay rate $\gamma = \frac{\omega}{c}\sqrt{n_{\text{eff}}^2 - n_{\text{s}}^2}$ [8, 9]. While there are many possible solutions to Eqs. 1.15 and 1.16, we are only interested in the subset that are guided modes. Similar to the finite well potential problem from quantum physics, this restricts us to standing waves within the slab, and an evanescently decaying field outside of it. For guided modes κ and γ will be real, and our equations simplify to,

$$\left(\frac{\partial^2}{\partial x^2} + \kappa^2\right)\mathcal{E}(x) = 0, \quad \text{Waveguide,} \tag{1.17}$$

$$\left(\frac{\partial^2}{\partial x^2} - \gamma^2\right)\mathcal{E}(x) = 0, \quad \text{Substrate.} \tag{1.18}$$

Because the H-field obeys the same initial wave equation as the E-field, the solutions to Eqs. 1.17 and 1.18 will be of the same form. Solving for each region of dielectric we find,

$$\mathcal{E}(\mathbf{x}), \mathcal{H}(x) = \begin{cases} C_0 e^{-\gamma x} & \text{for } x \geq d/2 \\ C_1 \cos(\kappa x) + C_2 \sin(\kappa x) & \text{for } -d/2 \geq x \geq d/2 \\ C_3 e^{\gamma x} & \text{for } x \leq -d/2 \end{cases} \tag{1.19}$$

The presence of boundaries between the slab and waveguide dictates that we should take precautions to ensure that boundary conditions consequent from Maxwell's equations are satisfied. This divides our solutions into two broad classes, transverse electric (TE) and transverse magnetic (TM). Matching the $E_{\parallel}$ and $H_{\perp}$ components across the boundaries means that we must match both the amplitude and the derivative of the E-field. This leads to the condition,

$$\tan(\kappa\gamma) = \frac{2\kappa\gamma}{\kappa^2 - \gamma^2}. \tag{1.20}$$

In similar fashion for TM modes, by demanding that $H_{\parallel}$ is continuous across the boundary and matching the $E_{\perp}$ component according to Eq. 1.9 we arrive at the condition,

$$\tan(\kappa\gamma) = \frac{2\kappa\gamma}{\kappa^2(\frac{n^{\mathrm{w}}}{n^{\mathrm{s}}})^2 - \gamma^2}. \tag{1.21}$$

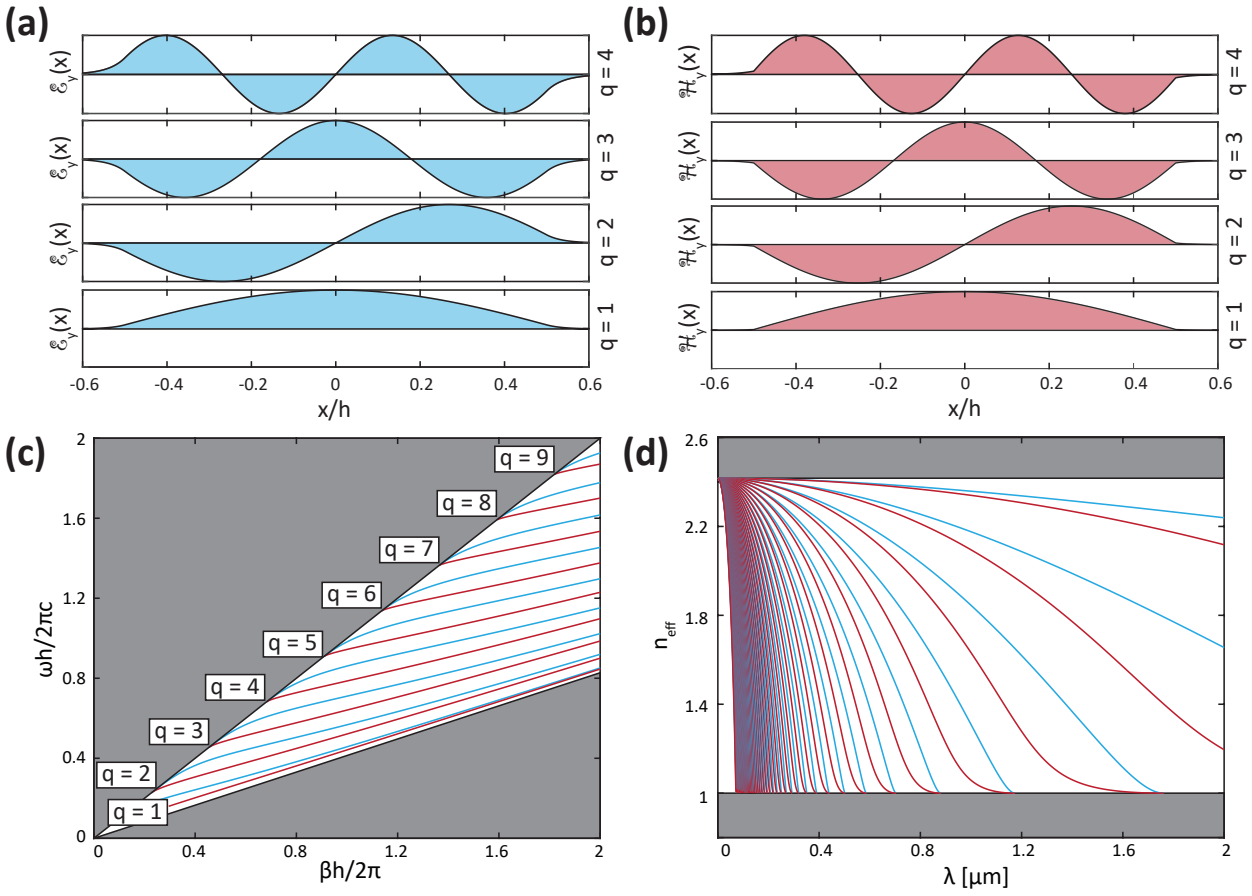

Figure 1.3: Spatial distribution of the y-component of the electric or magnetic field for the first four TE-mode (a) and TM-mode (b) solutions. (c) Dispersion diagram and light cone for TE modes (blue) and TM modes (red). (d) Effective index versus wavelength for TE modes (blue) and TM modes (red).

Solution of Eqs. 1.20-1.21 will give discrete values of κ and γ that are valid for a given value of ω as shown on Fig. 1.3. These solutions may be indexed by an integer, q, which denotes the number of antinodes in each solution. By summing over all these modes, and including a Fourier coefficient, we may construct a general solution to guided modes in the spirit of Eq. 1.13. This is given by,

$$\mathbf{E}(\mathbf{r},t) = \sum_q \int_{-\infty}^{\infty}\int_{-\infty}^{\infty} c_q(k_\mathrm{y},k_\mathrm{z})\mathcal{E}_q(x)e^{i(\omega_q(k_\mathrm{y},k_\mathrm{z})t-k_\mathrm{y}y-k_\mathrm{z}z)}dk_\mathrm{y}dk_\mathrm{z}. \tag{1.22}$$

We see that in this case, the integral over the x-direction has been replaced by a sum.

1.2.3 2-d Confinement: Fiber Modes

Next we will investigate 2-d confinement of an optical mode. The next logical step would be a waveguide with a rectangular cross section, where our ansatz would take the form of $\mathbf{E}(\mathbf{r},t) = \mathcal{E}(x,y)e^{i(\omega t-k_\mathrm{z}z)}$. Such a geometry is solved in [9–11], however because most of the systems studied in this thesis have azimuthal symmetry we will instead study a waveguide with a circular cross section. Working in cylindrical coordinates, we use the ansatz $\mathbf{E}(\mathbf{r},t) = \mathcal{E}(\rho,\phi)e^{i(\omega t-k_\mathrm{z}z)}$, and place this into the wave equation (Eq. 1.7). Note that in cylindrical coordinates, the Laplacian operator becomes $\nabla^2 = \frac{\partial^2}{\partial\rho^2} + \frac{1}{\rho}\frac{\partial}{\partial\rho} + \frac{1}{\rho^2}\frac{\partial^2}{\partial\phi^2} + \frac{\partial^2}{\partial z^2}$. Unlike previous cases, where the

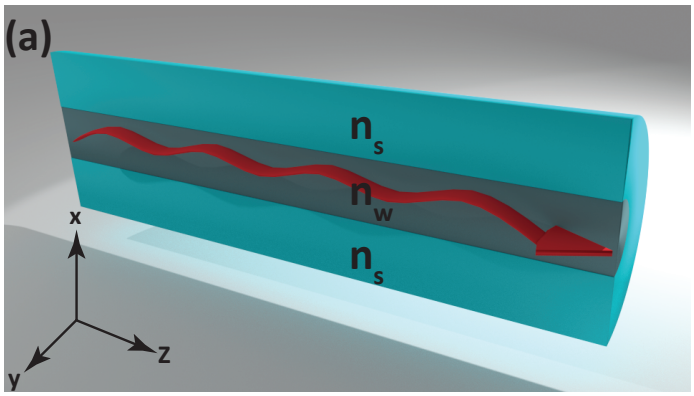

Figure 1.4: Geometry for fiber modes, consisting of a cylindrical waveguiding region with diameter d and refractive index n_w. The surrounding region has refractive index n_s.

various components of our vector field are decoupled from each other, in cylindrical coordinates this will not be the case for E_ρ and E_ϕ components. We may however solve for the E_z component by substituting into the wave equation to find,

$$\left(\frac{\partial^2}{\partial\rho^2}+\frac{1}{\rho}\frac{\partial}{\partial\rho}+\frac{1}{\rho^2}\frac{\partial^2}{\partial\phi^2}-k_{\mathrm{z}}^2+\frac{n_{\mathrm{w}}^2\omega^2}{c^2}\right)\mathcal{E}(\rho,\phi)=0, \quad \text{(Waveguide)} \tag{1.23}$$

$$\left(\frac{\partial^2}{\partial\rho^2}+\frac{1}{\rho}\frac{\partial}{\partial\rho}+\frac{1}{\rho^2}\frac{\partial^2}{\partial\phi^2}-k_{\mathrm{z}}^2+\frac{n_{\mathrm{s}}^2\omega^2}{c^2}\right)\mathcal{E}(\rho,\phi)=0. \quad \text{(Substrate)} \tag{1.24}$$

Next, we search for seperable solutions of the form, $E(\rho,\phi)=P(\rho)\Phi(\phi)$. Using separation of variables, this yields two equations,

$$\frac{\partial^2\Phi}{\partial\Phi^2}+m^2\Phi=0, \tag{1.25}$$

$$\frac{\partial^2 P}{\partial\rho^2}+\frac{1}{\rho}\frac{\partial P}{\partial\rho}+\left(\frac{n_{\mathrm{w,s}}^2\omega^2}{c^2}-k_z^2-\frac{m^2}{\rho^2}\right)P=0. \tag{1.26}$$

where $n_{\mathrm{w,s}}$ takes on the appropriate value as a function of r. The solution for Eq. 1.25 may be written as $\Phi=C_0e^{im\phi}+C_1e^{-im\phi}$. Enforcing that $\Phi(\phi)=\Phi(\phi\pm2\pi)$ requires m to take on an integer value.

As with the previous section, we will define κ and γ terms to simplify the mathematics. Defining $\kappa=\sqrt{\frac{n_{\mathrm{w}}^2\omega^2}{c^2}-k_z^2}$ and $\gamma=\sqrt{k_z^2-\frac{n_c^2\omega^2}{c^2}}$, Eq. 1.26 becomes,

$$\left(\frac{\partial^2}{\partial\rho^2}+\frac{1}{\rho}\frac{\partial}{\partial\rho}+\kappa^2-\frac{m^2}{\rho^2}\right)P=0, \quad \text{(Waveguide)} \tag{1.27}$$

$$\left(\frac{\partial^2}{\partial\rho^2}+\frac{1}{\rho}\frac{\partial}{\partial\rho}-\gamma^2-\frac{m^2}{\rho^2}\right)P=0, \quad \text{(Substrate)} \tag{1.28}$$

The solution to Eq. 1.27 are Bessel functions of the first kind, $J_m(\kappa\rho)$, and second kind $Y_m(\kappa\rho)$. Because Bessel functions of the second kind have a singularity at $r=0$, we can eliminate these solutions as unphysical. Similarly, the solution to Eq. 1.28 are modified Bessel functions of the first kind, $I_m(\gamma\rho)$, and second kind $K_m(\gamma\rho)$. In this case, we can eliminate $I_m(\gamma\rho)$ as unphysical because they grow exponentially for large values of r.

Following identical steps for the z-component of the H-field we can derive equivalent expressions. The spatial part of our modes may now be written as,

$$\mathcal{E}(\rho,\phi),\mathcal{H}(\rho,\phi) = \begin{cases} \left(C_0 e^{im\phi} + C_1 e^{-im\phi}\right) J_m\left(\kappa\rho\right) & \text{for } \rho \leq d/2, \\ \left(C_2 e^{im\phi} + C_3 e^{-im\phi}\right) K_m\left(\gamma\rho\right) & \text{for } \rho > d/2, \end{cases} \tag{1.29}$$

where $C_0 - C_3$ are coefficients. These may be determined by demanding continuity of the tangental components of the E-field and H-field [9]. This leads to the rather formidable expression,

$$\frac{4c^2k_{\mathrm{z}}^2m^2}{\omega^2d^2}\left(\frac{1}{\gamma^2}+\frac{1}{\kappa^2}\right)^2 = \left(\frac{J_m'(\kappa d/2)}{\kappa J_m(\kappa d/2)}+\frac{K_m'(\gamma d/2)}{\gamma K_m(\gamma d/2)}\right)\left(\frac{n_{\mathrm{w}}^2 J_m'(\kappa d/2)}{\kappa J_m(\kappa d/2)}+\frac{n_{\mathrm{c}}^2 K_m'(\gamma d/2)}{\gamma K_m(\gamma d/2)}\right), \tag{1.30}$$

where the primes denote derivatives with respect to ρ. Numerical solution of this equation will lead to a number of discrete modes, which we index by the integer p. The full solution for guided modes in a fiber may then be written as,

$$\mathbf{E}(\mathbf{r},t) = \sum_{m,p}\int_{-\infty}^{\infty} c_{mp}(k_{\mathrm{z}})\mathcal{E}_{mp}(\rho,\phi)e^{i(\omega_{mp}(\mathbf{k_z})t-k_{\mathrm{z}}z)}dk_{\mathrm{z}}. \tag{1.31}$$

where once again we have replaced an integral by an index due to an additional dimension of confinement. Due to the discretization, we only have one direction in which the mode may propagate. This leaves us in an interesting situation, where we could equally well write the total mode solution as an integral over frequency,

$$\mathbf{E}(\mathbf{r},t) = \sum_{m,p}\int_{-\infty}^{\infty} c_{mp}(\omega)\mathcal{E}_{mp}(\rho,\phi)e^{i(\omega t-k_{mp}(\omega)z)}d\omega. \tag{1.32}$$

In the last section of this chapter we will use such a solution to describe propagation of light through a waveguide.

1.2.4 3-d Confinement: Microdisk Modes

As a final example we investigate confinement of electromagnetic waves in three dimensions, working with the particular example of a microdisk, as this structure will recur throughout this thesis. Unlike previous cases we are no longer able to assign a propagating plane wave as the solution for a particular direction. As a consequence our solutions will become entirely discrete, with solutions indexed by integers, p, q, and m, each corresponding to a different dimension of confinement. All regions inside microdisk are defined to have refractive index n_{i}, and all areas external to the microdisk are assigned the refractive index n_{e}. The microdisk has diameter d, height h, and is centred on the origin of our coordinate system, as shown on Fig 1.5(a).

In this geometry once again, only the z-component of the electric and magnetic fields are separable. However, one can rely upon the confinement provided in the vertical direction to define TE and TM modes, where all other field components are related the z-component by [12],

$$\begin{aligned} \mathrm{TM} &= \{E_z, H_r, H_\phi\} & \mathrm{TE} &= \{H_z, E_r, E_\phi\} \\ H_r &= \frac{m}{r\mu_0\omega} E_z & E_r &= -\frac{m}{r\epsilon_{\mathrm{o}} n^2 \omega} H_z \\ H_\phi &= \frac{-i}{\mu_0\omega}\frac{\partial E_z}{\partial r} & E_\phi &= \frac{i}{\epsilon_{\mathrm{o}} n^2\omega}\frac{\partial H_z}{\partial r} \end{aligned} \tag{1.33}$$

With these considerations, we define $F = \{E_z, H_z\}$ depending on if we wish to solve for TM or TE modes. To solve this, we employ separation of variables, and let $F(r, z, \phi, t) = R(r)Z(z)\Phi(\phi)e^{i\omega t}$. Placing this assumption into the wave equation (Eq. 1.7) we find,

$$\frac{r^2 R''}{R} + \frac{rR'}{R} + \frac{r^2 Z''}{Z} + \frac{\Phi''}{\Phi} + r^2\kappa_{\mathrm{o}}^2 n^2 = 0, \tag{1.34}$$

where in this case primes denote partial differentiation with respect to the relevant coordinate, and $\kappa_o = \omega/c$. Slightly rearranging this equation, we can isolate for dependence on the azimuthal degree of freedom. This must be equal to a constant, which we label $-m^2$ for convenience. Explicitly we have,

$$-\frac{\Phi''}{\Phi} = m^2 = \frac{r^2 R''}{R} + \frac{rR'}{R} + \frac{r^2 Z''}{Z} + r^2\kappa_o^2 n^2. \tag{1.35}$$

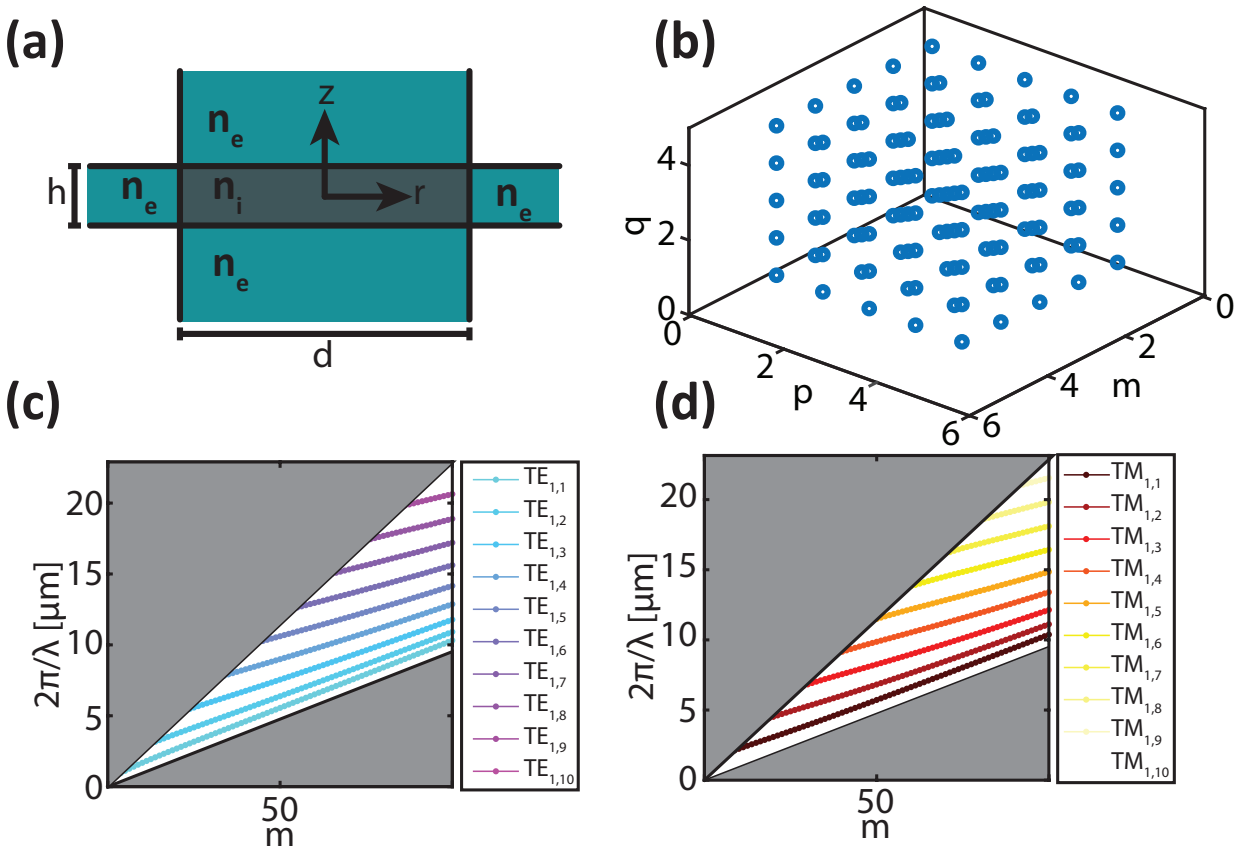

Figure 1.5: (a) Geometry for the microdisk mode calculations. The microdisk (gray) of width d and height h has index of refraction n_i, and the surrounding medium (turquoise) has index n_e. (b) "k-space" diagram for the discretized mode solutions. (c) Dispersion diagram and light cone for TE modes. (d) Dispersion diagram and light cone for TM modes.

Using the rotational symmetry of the problem, we find the m must be an integer, and the unnormalized solutions for Φ may be written as $\Phi = e^{\pm im\phi}$. Placing this back into Eq. 1.34, we have the two-dimensional problem,

$$\frac{R''}{r^2 R} + \frac{R'}{rR} + \frac{Z''}{Z} - \frac{m^2}{r^2} + \kappa_{\mathrm{o}}^2 n^2 = 0. \tag{1.36}$$

At this point, we begin to solve for the regions shown on Fig 1.5(a) separately. Within each of these regions, the refractive index is constant, which allows us to separate variables in each region, and then match boundary conditions. Isolating for variables with z-dependence on the left hand side we find,

$$\frac{Z''}{Z} + \kappa_{\mathrm{o}}^2 n_q^2 = \overline{n}^2 \kappa_{\mathrm{o}}^2 = -\frac{R''}{r^2 R} - \frac{R'}{rR} + \frac{m^2}{r^2}, \tag{1.37}$$

where we have chosen our constraints to match our results for a slab waveguide,

$$Z'' + \kappa_{\mathrm{o}}^2 \left(n^2 - \overline{n}_q^2 \right) Z = 0. \tag{1.38}$$

Because there are multiple solutions to the effective refractive index for a given value of k_{o}, we index these solutions by an integer, q, which gives the number of vertical antinodes. Placing our solutions back into Eq. 1.37, we finally arrive at an expression for the radial equation,

$$r^2 R'' + rR' + r^2 \left(k_{\mathrm{o}}^2 \left(\overline{n}^2 - n_{\mathrm{i}}^2 + n_{\mathrm{e}}^2 \right) - \frac{m^2}{r^2} \right) R = 0. \tag{1.39}$$

This is similar in form to the expressions we encountered in solving for the fiber modes. The solutions to this equations are Bessel functions for the case that $k_{\mathrm{o}}^2 \left(\overline{n}^2 - n_{\mathrm{i}}^2 + n_{\mathrm{e}}^2 \right) > 0$, and Hankel functions for the case $k_{\mathrm{o}}^2 \left(\overline{n}^2 - n_{\mathrm{i}}^2 + n_{\mathrm{e}}^2 \right) < 0$. Accordingly, we find that solutions may

be written as,

$$R(r) = \begin{cases} AJ_m(\kappa r) + BY_m(\kappa r) & \text{for } r \leq d/2 \\ CI_m(\gamma r) + DK_m(\gamma r) & \text{for } r > d/2 \end{cases} \tag{1.40}$$

where $\kappa = k_o\overline{n}$, $\gamma = k_o\sqrt{n_{\text{int}}^2 - n_{\text{ext}}^2 - \overline{n}^2}$, J_m and Y_m are Bessel functions of the first and second kind, and I_m and K_m are modified Bessel functions of the first and second kind. These can be further simplified by enforcing that the solution must be finite within the disk ($B = 0$), and must decay to zero at infinity ($C = 0$).

For large radius, we may approximate the Bessel functions in our expressions as,

$$R(r) = \begin{cases} A\sqrt{\frac{2}{\pi\kappa r}}\cos\left(\kappa r - \frac{m\pi}{2} - \pi/4\right) & \text{for } r \leq d/2 \\ D\sqrt{\frac{1}{2\pi\gamma r}}\exp(-\gamma r) & \text{for } r > d/2 \end{cases} \tag{1.41}$$

In keeping with typical approximations for microdisks, we will replace radial dependence of the modes using the exponential decay from the above expressions for regions outside the microdisk. As most of the mode will live inside of the dielectric for the modes studied here this is a reasonable approximation to make. To further simplify matters we will also neglect the factor of $1/\sqrt{r}$ in front of these expressions. Using these assumptions, we can match boundary conditions, to find the relations for TE and TM modes as [12],

$$\left(\frac{\alpha\overline{n}^2}{n_e^2} + \frac{2m}{d}\right) J_m(\kappa r) = k_o\overline{n}J_{m+1}(\kappa r)\,(\text{TE}) \tag{1.42}$$

$$\left(\alpha + \frac{2m}{d}\right) J_m(\kappa r) = k_o\overline{n}J_{m+1}(\kappa r)\,(\text{TM}) \tag{1.43}$$

The resulting dispersion curves for this expression are shown for TE and TM mode on Fig 1.5(c,d).

Finally we arrive to the general solution for the field,

$$\mathbf{E}(\mathbf{r}, t) = \sum_{m,p,q} c_{mpq}\mathcal{E}_{mpq}(\rho, \phi, z)e^{i\omega_{mpq}t}. \tag{1.44}$$

As expected we have lost our final integral: due to the three dimensional confinement, the electromagnetic field will exist as a superposition of modes.

1.2.5 Summary

In this section we have seen that modes can arise as solutions to the wave equations, (Eq. 1.7 and Eq. 1.8) in a given dielectric geometry. For the simple examples we considered here, dimensions that were invariant under translation were described by plane wave solutions, and dimensions where the electromagnetic field was localized to a certain region gave rise to discrete mode solutions. These ideas are summarized on Table 1.1, and will be useful to us in coming chapters.

Confinement	**Structure**	**E-Field Mode**	**Momentum or Index**
None	Homogeneous	$\mathcal{E}e^{i(\omega t-k_x x-k_y y-k_z z)}$	k_x, k_y, k_z
1-d	Slab	$\mathcal{E}_q(x)e^{i(\omega t-k_y y-k_z z)}$	q, k_y, k_z
2-d	Fiber	$\mathcal{E}_{pq}(x,y)e^{i(\omega t-k_z z)}$	q, p, k_z
3-d	Microdisk	$\mathcal{E}_{mpq}(x,y,z)e^{i\omega t}$	q, p, m

Table 1.1: Summary of the modes present in the geometries presented in the previous sections.

Another important type of geometry, which we have neglected to mention, is periodic structures. A simple example of this is a dielectric Bragg stack, which consists of several dielectric slabs stacked atop of each other with alternating refractive indices. Because this system only possess translational symmetry for integer multiples of the slab thickness, the possible plane wave solutions in this direction will be restricted according to Bloch's theorem. This can be used, for example, to create waveguides optimized to support only a certain wavelength. Furthermore, by sandwiching a section with one periodicity between layers with a different periodicity, one can confine a mode to a certain region. Such ideas are used

to create a category of device known as photonic crystals. They are a rich area of research, with significant technological applications. An excellent text on this topic may be found in [5].

1.3 Putting it together: Light in Waveguides and Resonators

1.3.1 Why Do Modes Couple?

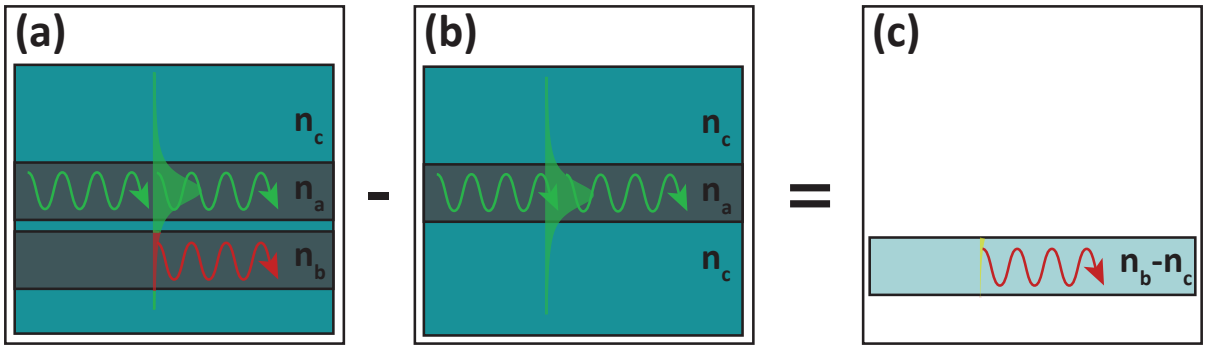

Figure 1.6: (a) Coupled mode dielectric geometry for two waveguides with refractive indices n_{a} and n_{b} respectively embedded in a material with refractive index n_{c}. Light is initially launched into waveguide a, and some portion is coupled into waveguide b. (b) By subtracting the solution for waveguide a in isolation, we can isolate the perturbation induced by the presence of waveguide b. (c) Driving term generated in waveguide b due the the local change in the refractive index.

Consider some waveguide a with 2-d confinement, which is brought into close proximity with some other waveguide b. If we propagate light through a mode in a we will find that some portion of it will leave through a mode in waveguide b. In such scenarios, we say the modes of the waveguides are coupled. From a naive ray optics picture, this might seem to

be an unexpected result. After all, any electromagnetic waves impinging on the interface are supposed to undergo total internal reflection. In fact, this coupling mechanism has been known to some extent for quite some time. In early optics experiments, Newton brought a slightly curved piece of glass into contact with a prism. To his surprise, he found that when light impinged on this system, considerably more light travelled through the interface than could possibly be explained by propagation only at the vanishingly small point of contact [13]. This situation is alleviated in the ray optics picture by accounting for the Goos-Hänchen shift [9], but as we shall see, can be naturally explained by viewing the electromagnetic field in terms of modes.

Let us consider waveguide a in the absence of coupling as shown on Fig. 1.6 (b). We know from our mode solutions from the previous section that the electromagnetic field will not be entirely confined to the waveguiding region, but will have a rapidly decaying evanescent field extending out from the waveguide. The displacement field for an area outside the device is simply $D_{\mathrm{a}} = \epsilon_{\mathrm{c}} E_{\mathrm{a}}$. Suppose that we place waveguide b in this region as indicated by the red part of the mode on Fig. 1.6 (a). For the sake of simplicity, we can assume that this perturbation is weak enough that it does not cause a change in the propagation of the mode within the waveguide. We may now write the displacement field within waveguide b as a sum of the former value, plus the change due to bringing waveguide b into this region, $D_{\mathrm{ab}} = \epsilon_{\mathrm{c}} E_{\mathrm{a}} + (\epsilon_{\mathrm{b}} - \epsilon_{\mathrm{c}})\, E_{\mathrm{a}}$. As shown on Fig. 1.6 (c), we can see that the effect of placing a waveguide in the vicinity is the creation of a polarization field $D_{\mathrm{a}} - D_{\mathrm{ab}} = (\epsilon_{\mathrm{b}} - \epsilon_{\mathrm{c}})\, E_{\mathrm{a}} = P_{\mathrm{source}}$. This polarization acts a generating term, injecting light into a mode in waveguide b.

Spatial Perturbation

To make our ideas from the previous section more concrete, consider the case of two parallel waveguides, aligned to the z-direction [7]. We have an instinct from the previous arguments, that P_{source} arises from the shift in the dielectric constant due to the waveguides. To help us

isolate this in our calculations and to simplify the algebra we define the functions,

$$\Delta n_{\mathrm{a}}^2 = \begin{cases} \epsilon_{\mathrm{a}} - \epsilon_{\mathrm{e}} = n_{\mathrm{a}}^2 - n_{\mathrm{e}}^2 & \text{Inside waveguide } a, \\ 0 & \text{Outside waveguide } a, \end{cases} \tag{1.45}$$

and,

$$\Delta n_{\mathrm{b}}^2 = \begin{cases} \epsilon_{\mathrm{b}} - \epsilon_{\mathrm{e}} = n_{\mathrm{a}}^2 - n_{\mathrm{e}}^2 & \text{Inside waveguide } b, \\ 0 & \text{Outside waveguide } b. \end{cases} \tag{1.46}$$

Using the notation defined above, Eq. 1.7 (the wave equation) becomes,

$$\left(\nabla^2 - \frac{n_{\mathrm{e}}^2 + \Delta n_{\mathrm{a}}^2 + \Delta n_{\mathrm{b}}^2}{c^2}\frac{\partial^2}{\partial t^2}\right)\mathbf{E}(x,y,z,t) = 0. \tag{1.47}$$

In general it may not be possible – or very often we do not want – to solve this expression exactly. However if we have access to the mode solutions for each waveguide individually and if they are only weakly coupled, we can use them to construct a solution. These modes will be solutions to the following wave equations, respectively,

$$\left(\nabla^2 - \frac{n_{\mathrm{e}}^2 + \Delta n_{\mathrm{a}}^2}{c^2}\frac{\partial^2}{\partial t^2}\right)\mathbf{E}_{\mathrm{a}}(x,y,z,t) = 0, \tag{1.48}$$

$$\left(\nabla^2 - \frac{n_{\mathrm{e}}^2 + \Delta n_{\mathrm{b}}^2}{c^2}\frac{\partial^2}{\partial t^2}\right)\mathbf{E}_{\mathrm{b}}(x,y,z,t) = 0. \tag{1.49}$$

Following the arguments of previous sections, we write our solutions in terms of the modes of the waveguide. For the sake of simplicity we will consider only one mode in each waveguide. We can then construct the overall solution as a superposition, explicitly,

$$\mathbf{E}_{\mathrm{a}}(x,y,z,t) = \boldsymbol{\mathcal{E}}_{\mathrm{a}}(x,y)e^{-i(\beta_{\mathrm{a}}z-\omega t)}, \tag{1.50}$$

$$\mathbf{E}_{\mathrm{b}}(x,y,z,t) = \boldsymbol{\mathcal{E}}_{\mathrm{b}}(x,y)e^{-i(\beta_{\mathrm{b}}z-\omega t)}, \tag{1.51}$$

$$\mathbf{E}(x,y,z,t) = A(z)\mathbf{E}_{\mathrm{a}}(x,y,z,t) + B(z)\mathbf{E}_{\mathrm{a}}(x,y,z,t). \tag{1.52}$$

Note that if we were to strictly adhere to the notation of the previous section we would probably use k_z instead of β_a and β_b. In literature the β notation is often used for waveguides, and is called a "propagation constant".

Our final task is to find an equation that governs the z-dependence of the spatial envelopes $A(z)$ and $B(z)$. To do this we substitute Eq. 1.52 into Eq. 1.47, and use Eqs. 1.48 and 1.49 to simplify. Collecting leftover terms into the expression yields,

$$\left(\frac{d^2A}{dz^2} - 2i\beta_\mathrm{a}\frac{dA}{dz}\right)\boldsymbol{\mathcal{E}}_\mathrm{a}(x,y)e^{-i(\beta_\mathrm{a}z-\omega t)} + \left(\frac{d^2B}{dz^2} - 2i\beta_\mathrm{b}\frac{dB}{dz}\right)\boldsymbol{\mathcal{E}}_\mathrm{a}(x,y)e^{-i(\beta_\mathrm{b}z-\omega t)} \tag{1.53}$$
$$= -k_\mathrm{o}^2\Delta n_\mathrm{b}^2 A\boldsymbol{\mathcal{E}}_\mathrm{a}(x,y)e^{-i(\beta_\mathrm{a}z-\omega t)} - k_\mathrm{o}^2\Delta n_\mathrm{a}^2 B\boldsymbol{\mathcal{E}}_\mathrm{b}(x,y)e^{-i(\beta_\mathrm{b}z-\omega t)}.$$

To simplify this, we make a series of related assumptions, which forms the basis of what is known as coupled mode theory [7]. Our major assumption is that coupling between these waveguides is weak, which will have a few repercussions. Firstly we can assume a slow exchange of energy between the waveguides, allowing us to set the second order spatial derivatives equal to zero. Next, we assume orthogonality between the modes. This is certainly true for modes that exist in the same dielectric structure, where it can be shown that the following orthogonality conditions hold [7, 11],

$$\frac{\beta_\mathrm{m}}{2\omega\mu}\int\int E_m \cdot E_n^* dxdy = \delta_{mn}, \tag{1.54}$$
$$\frac{\beta_\mathrm{m}}{2\mu}\int\int H_m \cdot \frac{E_n^*}{\epsilon} dxdy = \delta_{mn}, \tag{1.55}$$

with the integrals taken over all space. Note that this condition is written for the electric field itself and not for $\mathcal{E}(x,y)$. Because the electric field is written in terms of a mode profile and slowly varying envelopes $A(z)$ and $B(z)$ we may choose normalization conditions on the modes or envelopes individually as convenient, provided that the value of the electric field is preserved.

In the present case however, the mode solutions we are using are solutions to two different sets of boundary conditions, and may not be strictly orthogonal. While techniques exist to overcome this, we can assume that the overlap between the modes in different waveguides is small enough that Eq. 1.54 is a valid approximation [14]. Using this assumption, we multiply by the complex conjugate of each mode, and integrate over all space, arriving at the coupled mode equations,

$$\frac{dA}{dz} = -i\gamma_{\mathrm{ab}} B e^{i(\beta_{\mathrm{a}}-\beta_{\mathrm{b}})z} - i\gamma_{\mathrm{aa}} A, \tag{1.56}$$

$$\frac{dB}{dz} = -i\gamma_{\mathrm{ab}} A e^{i(\beta_{\mathrm{b}}-\beta_{\mathrm{a}})z} - i\gamma_{\mathrm{aa}} B, \tag{1.57}$$

where,

$$\gamma_{\mathrm{aa}} = \frac{\epsilon_{\mathrm{o}}\omega}{4} \int\int \boldsymbol{\mathcal{E}}_{\mathrm{a}}^{*} \Delta n_{\mathrm{b}} \boldsymbol{\mathcal{E}}_{\mathrm{a}} dA, \tag{1.58}$$

$$\gamma_{\mathrm{bb}} = \frac{\epsilon_{\mathrm{o}}\omega}{4} \int\int \boldsymbol{\mathcal{E}}_{\mathrm{b}}^{*} \Delta n_{\mathrm{a}} \boldsymbol{\mathcal{E}}_{\mathrm{b}} dA, \tag{1.59}$$

$$\gamma_{\mathrm{ab}} = \frac{\epsilon_{\mathrm{o}}\omega}{4} \int\int \boldsymbol{\mathcal{E}}_{\mathrm{a}}^{*} \Delta n_{\mathrm{a}} \boldsymbol{\mathcal{E}}_{\mathrm{b}} dA, \tag{1.60}$$

$$\gamma_{\mathrm{ba}} = \frac{\epsilon_{\mathrm{o}}\omega}{4} \int\int \boldsymbol{\mathcal{E}}_{\mathrm{b}}^{*} \Delta n_{\mathrm{b}} \boldsymbol{\mathcal{E}}_{\mathrm{a}} dA. \tag{1.61}$$

The coupled mode equations above contain momentum shifts due to the presence of the waveguide, as well as coupling terms. With the benefit of hindsight, we can apply these shifts directly into Eq. 1.50 by setting $\beta_{\mathrm{a}} \rightarrow \beta_{\mathrm{a}} + \gamma_{\mathrm{aa}}$ and into Eq. 1.50 by setting $\beta_{\mathrm{b}} \rightarrow \beta_{\mathrm{b}} + \gamma_{\mathrm{bb}}$. Our final coupled mode equations now read,

$$\frac{dA}{dz} = -i\gamma_{\mathrm{ab}} B e^{i(\beta_{\mathrm{a}}-\beta_{\mathrm{b}})z}, \tag{1.62}$$

$$\frac{dB}{dz} = -i\gamma_{\mathrm{ab}} A e^{i(\beta_{\mathrm{b}}-\beta_{\mathrm{a}})z}. \tag{1.63}$$

These expressions indicate an exchange between the waveguides as a function of z, which is dependent not only on the strength of the coupling coefficients, γ_{ab} and γ_{ba}, but also on phase matching terms $\beta_{\mathrm{a}} - \beta_{\mathrm{b}}$ and $\beta_{\mathrm{b}} - \beta_{\mathrm{a}}$. This points to two general requirements to achieve good coupling: we must have good overlap between modes to enhance the coupling strength, and we must phase match the waveguides to be able to transfer all of the energy from one waveguide to another. Good spatial overlap can be achieved by, for example, placing waveguides in close proximity, and ensuring that the device geometry is small enough to ensure a large evanescent field. Phasematching can be ensured by designing the geometry of the waveguides to ensure that phasematching conditions are met. For example, one could attempt have have similar effective indices in both waveguides at the desired optical wavelength.

Temporal Perturbation

In the previous section, we found that perturbation with respect to spatial coordinates allowed us to describe coupling between two waveguides as a differential equation with respect to the spatial coordinates. In this section we will describe the coupling of a waveguide and a resonator. Because the resonator is very localized in comparison to the waveguide, differential equations with respect to z would not be particularly useful. Instead we will use temporal perturbation to derive differential equations with respect to time.

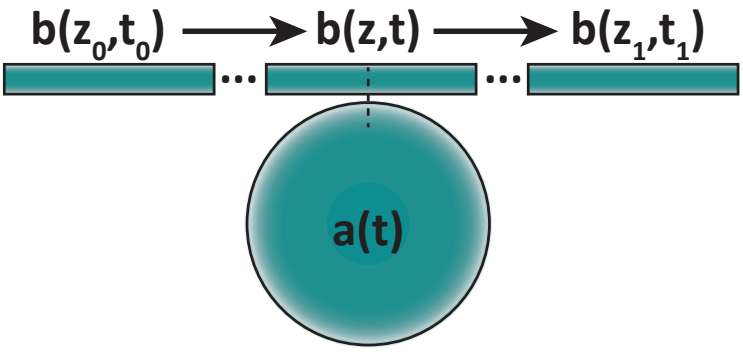

Figure 1.7: Waveguide-cavity coupling geometry. The resonator is shown as a circle, and has refractive index n_{a}. The waveguide is the rectangular regions, and has refractive index n_{b}. The dotted lines represent long lengths of the waveguide, and the dashed line indicates the mirror symmetry of the system.

Consider the geometry shown on Fig. 1.7. To make matters easier, we assume the resonator couples only to the waveguide, and does not experience significant loss to other channels such as material absorption. As before, we use the solutions for each waveguide individually, and demand that they fulfill Eq. 1.47. The essential difference here is that we construct solutions as a linear combination of modes using coefficients that are functions of time instead of space. In this case we will focus on the coupling of a single resonator mode to a continuum of waveguide modes. With these considerations in mind, we arrive at the ansatz,

$$\mathbf{E}_{\mathrm{a}}(x,y,z,t) = \boldsymbol{\mathcal{E}}_{\mathrm{a}}(x,y,z)e^{-i\omega_{\mathrm{a}}t}, \tag{1.64}$$

$$\mathbf{E}_{\mathrm{b}}(x,y,z,t,\omega) = \boldsymbol{\mathcal{E}}_{\mathrm{b}}(x,y)e^{-i(\omega t-\beta(\omega)z)}, \tag{1.65}$$

$$\mathbf{E}(x,y,z,t) = a(t)\mathbf{E}_{\mathrm{a}}(x,y,z,t) + b(t)\int \mathbf{E}_{\mathrm{b}}(x,y,z,t,\omega)d\omega. \tag{1.66}$$

where $a(t)$ and $b(t)$ encode the slow time evolution of the electric field in the resonator and the waveguide, respectively. Placing our ansatz into Eq. 1.47, and using the fact that E_{a} and E_{b} are each solutions in the absence of the opposite dielectric structure, we find the

expression,

$$(\ddot{a} - 2i\omega_{\mathrm{a}}\dot{a})\,\boldsymbol{\mathcal{E}}_{\mathrm{a}}(x,y,z)e^{-i\omega_{\mathrm{a}}t} + \int \left(\ddot{b} - 2i\omega_{\mathrm{a}}\dot{b}\right)\boldsymbol{\mathcal{E}}_{\mathrm{b}}(x,y,\omega)e^{-i(\omega t-\beta(\omega)z)}d\omega$$
$$= \frac{\Delta n_{\mathrm{b}}^2\omega_{\mathrm{a}}^2 a\boldsymbol{\mathcal{E}}_{\mathrm{a}}(x,y,z)e^{-i\omega_{\mathrm{a}}t}}{n_{\mathrm{e}}^2 + \Delta n_{\mathrm{b}}^2} + \int \frac{\Delta n_{\mathrm{a}}^2\omega_{\mathrm{b}}^2 b\boldsymbol{\mathcal{E}}_{\mathrm{b}}(x,y,\omega)e^{-i(\omega t-\beta(\omega)z)}}{n_{\mathrm{e}}^2 + \Delta n_{\mathrm{a}}^2}d\omega. \tag{1.67}$$

Note that in the above expressions all exponentials have an opposite sign to what we might expect. Physically this convention make no difference because we are only taking the real part of the field, it is only the relative sign between the propagation constant and time that determine the direction a wave will travel in a waveguide.

Once again we will have to make a few approximations. Assuming that the coupling is weak, we can discard second derivatives in time. We can then use the orthogonality of the modes to derive the following expressions,

$$\dot{a} = \int \gamma_{\mathrm{ab}}(\omega)b(\omega)e^{-i(\omega-\omega_{\mathrm{a}})t}d\omega + \gamma_{\mathrm{aa}}a, \tag{1.68}$$

$$\dot{b}(\omega) = \gamma_{\mathrm{ba}}(\omega)be^{-i(\omega_{\mathrm{a}}-\omega)t} + \gamma_{\mathrm{bb}}b(\omega). \tag{1.69}$$

Each of these equations includes a self term due to coupling, which shifts the frequency of the modes. While this might be important if one wants to take into account frequency shifts in the resonator due to coupling, we are are not interested in such cases here. As before, we absorb the self terms by redefining the frequency of the resonator and waveguide, and move into a rotating frame with the definitions,

$$a_{\mathrm{new}}(t) = a_{\mathrm{old}}(t)e^{-i(\omega_{\mathrm{a}}+\gamma_{\mathrm{aa}})t} \tag{1.70}$$

$$b_{\mathrm{new}}(t,\omega) = b_{\mathrm{old}}(t,\omega)e^{-i(\omega+\gamma_{\mathrm{bb}})t} \tag{1.71}$$

This yields the following equations of motion for the mode amplitudes,

$$\dot{a} = -i\omega_{\mathrm{a}} t + \int \gamma_{\mathrm{ab}}(\omega) b(\omega) d\omega \tag{1.72}$$

$$\dot{b}(\omega) = -i\omega b(\omega) + \gamma^{*}_{\mathrm{ab}}(\omega) a. \tag{1.73}$$

To solve these expressions, we will require either initial or final conditions. Both sets of conditions will be useful to us, as we often want to inject a known signal into the waveguide and predict the dynamics, or in the second case to predict the dynamics from a signal at the output. We will consider the initial conditions to be time t_0 and location z_0, and final conditions to be time t_1 and location z_1, as shown on Fig. 1.7. The formal solution for Eq. 1.73 in terms of the initial conditions is,

$$b(\omega) = e^{-i\omega(t-t_0)} b_0(\omega) + \gamma_{\mathrm{ab}}(\omega) \int_{t_0}^{t} e^{-i\omega(t-\tau)} a(\tau) d\tau. \tag{1.74}$$

Notice that the two terms in Eq.1.74 come from two different sources. The first term represents the unperturbed evolution of photons launched into the waveguide at z_0, t_0 up until they arrive at z, t. The second term describes interactions with the cavity mode at z, t. Placing Eq.1.74 into Eq. 1.72 we find,

$$\dot{a} = -i\omega_{\mathrm{a}} a + \int |\gamma_{\mathrm{ab}}(\omega)|^2 \int_{t_0}^{t} e^{-i\omega(t-\tau)} a(\tau) d\tau d\omega + \int \gamma_{\mathrm{ab}}(\omega) e^{-i\omega(t-t_0)} a_0(\omega) d\omega. \tag{1.75}$$

The coupling term at this point has an explicit frequency dependence. However, if the dispersion of the waveguide is small compared to the eventual bandwidth of the cavity, we can make the Markov approximation: $\gamma_{\mathrm{ab}}(\omega) = \sqrt{\frac{\kappa}{2\pi}}$. Note that if this were not the case, we could expand the coupling term in a Taylor series, which would lead to a Fano lineshape as

opposed to the Lorentzian lineshapes we will derive here. We now have,

$$\begin{aligned}\dot{a} &= -i\omega_{\mathrm{a}}a + \frac{\kappa}{2\pi}\int_{t_0}^{t}\left(\int e^{-i\omega(t-\tau)}d\omega\right)a(\tau)d\tau + \sqrt{\frac{\kappa}{2\pi}}\int e^{-i\omega(t-t_0)}b_0(\omega)d\omega \\ &= -i\omega_{\mathrm{a}}a + \frac{\kappa}{2\pi}\int_{t_0}^{t}2\pi\delta(t-\tau)a(\tau)d\tau + \sqrt{\kappa}a_{\mathrm{in}},\end{aligned} \tag{1.76}$$

where we have defined an input operator, a_{in}. Note that as defined a convenient and conventional normalization condition is to take a to have units of energy, which means that a_{in} will have units of power. Taking the integral over the δ-function to give a factor of $1/2$, we arrive at an expression for the cavity in terms of the optical input,

$$\boxed{\dot{a} = -\left(i\omega_{\mathrm{a}} + \frac{\kappa}{2}\right)a + \sqrt{\kappa}a_{\mathrm{in}}.} \tag{1.77}$$

Similar expressions can be derived in terms of the optical output, and then boundary conditions can be applied depending on the specific configuration of the waveguide and resonator. These are covered in more detail in Appendix A.1.

Identical expressions to Eq. 1.77 can be derived by assuming linear coupling, and applying energy conservation and time reversal symmetry arguments [14, 15]. While such arguments are certainly much cleaner, we have chosen the current approach to mode descriptions and couplings in as close analogy to the quantum treatment as possible.

1.3.2 Quantum Light in Dielectrics

This section is not intended to be a detailed review of quantization procedures, but is included to point out some of the similarities and differences between the classical and quantum treatment of modes in a dielectric. In many ways, it is less of a logical leap to quantize under these conditions than in free space. The arguments here will nearly identically follow the classic text by Walls and Milburn [16].

We begin with the Hamiltonian for a dielectric [2],

$$\mathcal{H} = \int (\mathbf{E} \cdot \mathbf{D} + \mathbf{H} \cdot \mathbf{B})\, d\mathbf{r}. \tag{1.78}$$

Our intention is to quantize the E and B fields. As has been pointed out in [17, 18] errors will arise in this approach if nonlinear effects are included, and one ought to quantize the D field. In our case, we will restrict ourselves to the linear situation. Using the constitutive relations (Eq. 1.2) the Hamiltonian becomes,

$$\mathcal{H} = \frac{1}{2} \int \left(\epsilon \mathbf{E}^2 + \mu_0 \mathbf{H}^2 \right) d\mathbf{r} \tag{1.79}$$

We will work with the vector potential in the Coulomb gauge ($\nabla \cdot A = 0$) where $\mathbf{E} = -\frac{\partial \mathbf{A}}{\partial t}$ and $\mathbf{B} = \nabla \times \mathbf{A}$. This can be inserted into Maxwell's equations (Eqs.1.1a-1.1d) to find,

$$\nabla^2 \mathbf{A} = \frac{1}{\mu\epsilon} \frac{\partial^2}{\partial t^2} \mathbf{A} \tag{1.80}$$

This has the form of a wave equation, which we have seen several examples of how to solve. Taking a hint from Section 1.3.1, we write an ansatz consisting of the mode solutions and slowly evolving time-dependent coefficients. This time around instead of working with a complex solution and leaving the fact that only the real part is physical implicit, we will include a complex conjugate to ensure that our solutions are explicitly real and physical,

$$\mathbf{A}_i(x, y, z, t) = \sum_i \left(c_i(t) \boldsymbol{\mathcal{E}}(x, y, z) e^{-i\omega_i t} + c_i^*(t) \boldsymbol{\mathcal{E}}^*(x, y, z) e^{i\omega_i t} \right). \tag{1.81}$$

As mentioned before, modes within the same structure can be shown to be orthogonal. We are also free to choose a normalization factor for the modes, or for the time dependent coefficients, $c_i(t)$. Choosing one will immediately determine the other. In this case we choose,

$$\int_v \boldsymbol{\mathcal{E}} P_i^*(x, y, z) \boldsymbol{\mathcal{E}}_j(x, y, z) dv = \delta_{ij}. \tag{1.82}$$

This condition can be combined with the transversality condition to find a normalization constraint on $c_i(t)$. For reasons that will become apparent later, we also make the change of variables $c_i(t) = a_i(t)\sqrt{\frac{\hbar}{2\omega_i\epsilon}}$. This gives expressions for the vector potential and electric field as,

$$\mathbf{A}_i(x,y,z,t) = \sum_i \sqrt{\frac{\hbar}{2\omega_i\epsilon}} \left(a_i(t)\boldsymbol{\mathcal{E}}_i(x,y,z)e^{-i\omega_i t} + a_i^*(t)\boldsymbol{\mathcal{E}}_i^*(x,y,z)e^{i\omega_i t} \right), \tag{1.83}$$

$$\mathbf{E}_i(x,y,z,t) = i\sum_i \sqrt{\frac{\hbar\omega_i}{2\epsilon}} \left(a_i(t)\boldsymbol{\mathcal{E}}_i(x,y,z)e^{-i\omega_i t} - a_i^*(t)\boldsymbol{\mathcal{E}}_i^*(x,y,z)e^{i\omega_i t} \right). \tag{1.84}$$

Finally we identify the time dependent coefficient with the raising and lowering operators of the quantum harmonic oscillator ($a_i(t) \to \hat{a}_i(t), a_i^*(t) \to a^\dagger(t)$). These obey the canonical relations $\left[\hat{a}_i, \hat{a}_j^\dagger\right] = \delta_{ij}$, and $[\hat{a}_i, \hat{a}_j] = \left[\hat{a}_i^\dagger, \hat{a}_j\dagger\right] = 0$. Substituting these results into the Hamiltonian given by Eq. 1.79, we recover the Hamiltonian of the quantum harmonic oscillator,

$$\hat{H} = \sum_i \hbar\omega_i \left(\hat{a}_i^\dagger \hat{a}_i + \frac{1}{2} \right). \tag{1.85}$$

Just as calculating equations of motion for the slowly varying envelopes in Section 1.3.1 gave us information about how the electromagnetic field will act as a function of time, calculating the time evolution of the raising and lowering operators will give us insight into the evolution of our quantum fields. To make this explicit, we will derive the quantum analogue to temporal coupled mode theory, known as input-output theory.

1.3.3 Input-Output Theory

Input-output theory [19, 20] arose from the need to describe a damped quantum system where one explicitly keeps the evolution of the larger system inducing the damping. This situation may be described by the Hamiltonian $\hat{H} = \hat{H}_\mathrm{a} + \hat{H}_\mathrm{b} + \hat{H}_\mathrm{ab}$ where $\hat{H}_\mathrm{a}$ describes the dynamics of the system we care about, $\hat{H}_\mathrm{b}$ describes the dynamics of the large system, and

$\hat{H}_{\rm ab}$ describes the coupling between the two. They are given by [20],

$$\hat{H}_{\rm b} = \int_{-\infty}^{\infty} \hbar\omega \hat{b}^\dagger(\omega)\hat{b}(\omega)d\omega, \tag{1.86}$$

$$\hat{H}_{\rm ab} = i\hbar \int_{-\infty}^{\infty} \gamma(\omega)\left(\hat{b}^\dagger(\omega)\hat{a} - \hat{a}^\dagger\hat{b}(\omega)\right)d\omega. \tag{1.87}$$

This gives the equations of motion,

$$\dot{\hat{a}} = -\frac{i}{\hbar}\left[\hat{a}, \hat{H}_{\rm a}\right] - \int_{-\infty}^{\infty} \gamma(\omega)\hat{b}(\omega)d\omega, \tag{1.88}$$

$$\dot{\hat{b}}(\omega) = -i\omega\hat{b}(\omega) + \gamma(\omega)\hat{a}. \tag{1.89}$$

These are quantum analogues to Eq. 1.72 and Eq. 1.73 so we will use the same strategy for solution. Solving for $\hat{b}(\omega)$ in terms of the initial conditions gives,

$$\hat{b}(\omega) = e^{-i\omega(t-t_0)}\hat{b}_0(\omega) + \gamma(\omega)\int_{t_0}^{t} e^{-i\omega(t-\tau)}\hat{a}(\tau)d\tau \tag{1.90}$$

Placing this into Eq. 1.88, we find

$$\dot{\hat{a}} = -\frac{i}{\hbar}\left[\hat{a}, \hat{H}_{\rm a}\right] + \int_{-\infty}^{\infty} |\gamma_{\rm ab}(\omega)|^2 \int_{t_0}^{t} e^{-i\omega(t-\tau)}\hat{a}(\tau)d\tau d\omega + \int_{-\infty}^{\infty} \gamma(\omega)e^{-i\omega(t-t_0)}\hat{b}_0(\omega)d\omega \tag{1.91}$$

We then make the Markov approximation $\gamma(\omega) = \sqrt{\frac{\kappa}{2\pi}}$, to find,

$$\begin{aligned}
\dot{\hat{a}} &= -\frac{i}{\hbar}\left[\hat{a}, \hat{H}_{\rm a}\right] + \frac{\kappa}{2\pi}\int_{t_0}^{t}\left(\int_{-\infty}^{\infty} e^{-i\omega(t-\tau)}d\omega\right)\hat{a}(\tau)d\tau + \sqrt{\frac{\kappa}{2\pi}}\int_{-\infty}^{\infty} e^{-i\omega(t-t_0)}\hat{b}_0(\omega)d\omega \\
&= -\frac{i}{\hbar}\left[\hat{a}, \hat{H}_{\rm a}\right] + \frac{\kappa}{2\pi}\int_{t_0}^{t} 2\pi\delta(t-\tau)\hat{a}(\tau)d\tau + \sqrt{\kappa}\hat{a}_{\rm in} \\
&= -\frac{i}{\hbar}\left[\hat{a}, \hat{H}_{\rm a}\right] - \frac{\kappa}{2}\hat{a} + \sqrt{\kappa}\hat{a}_{\rm in}
\end{aligned} \tag{1.92}$$

where we have defined $\hat{a}_{\rm in} = \frac{1}{\sqrt{2\pi}}\int_{-\infty}^{\infty} e^{-i\omega(t-t_0)}\hat{b}_0(\omega)d\omega$. This expression will be very useful later in this thesis, where it will describe the evolution of the system driven by an optical waveguide.

Similar arguments can be used to derive the evolution of the cavity in terms of the outputs. Relating this to the inputs given above we find the input-output relations, [19, 20]

$$\hat{a}_{\rm in} - \hat{a}_{\rm out} = \sqrt{\kappa}\hat{a}. \tag{1.93}$$

Suppose that our system is a single optical mode with $\hat{H}_{\rm a} = \hbar\omega_{\rm a}\hat{a}^\dagger\hat{a}$. The equation of motion will read,

$$\boxed{\dot{\hat{a}} = -\left(i\omega_{\rm a} + \frac{\kappa}{2}\right)\hat{a} + \sqrt{\kappa}\hat{a}_{\rm in}.} \tag{1.94}$$

Chapter 2

Nanofabrication

2.1 Introduction

The creation of nanophotonic devices benefits tremendously from the tools, techniques, and materials developed for use in the semiconductor industry. For example Silicon-On-Insulator (SOI) wafers, which typically consist of an ≈ 250 nm layer of silicon atop a layer of Silicon Dioxide (SiO_2), were originally produced to reduce parasitic capacitance between proximal circuit components and offer insulation between components. This has since been borrowed for photonic applications, where the SiO_2 layer may be easily removed from underneath silicon components by a wet acid etch. In the next section we will briefly introduce the main tools we used in our fabrication process, and then detail the process itself in the final section.

2.2 Fabrication Tools and Techniques

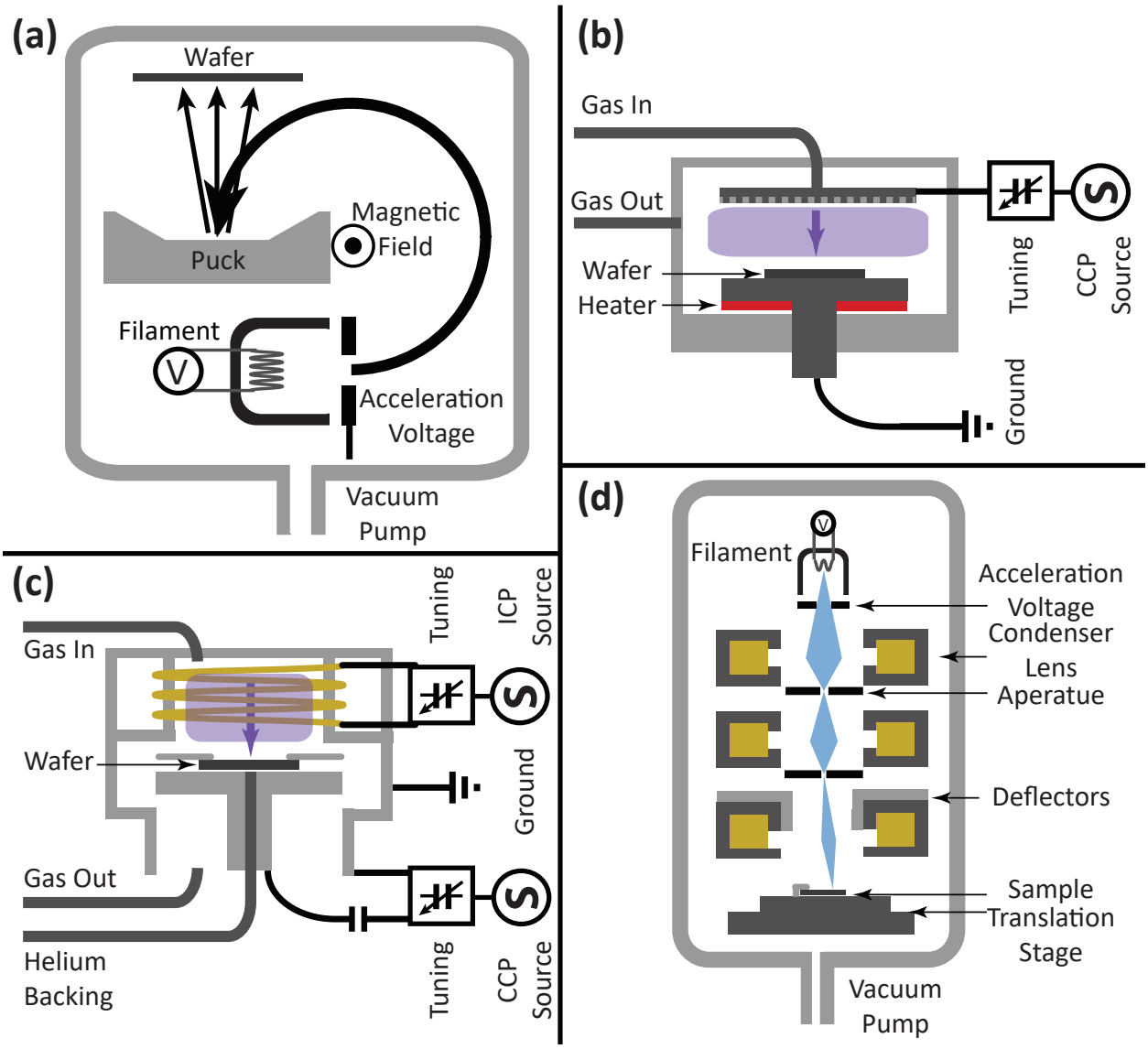

Figure 2.1: (a) Working principle of an E-beam evaporation tool. (b) Main components of a PECVD tool. (c) Cross section of an ICP-RIE tool. (d) Main components of an E-beam lithography tool.

2.2.1 Electron-Beam Evaporation

Electron beam evaporation is a method to deposit a material onto a substrate in a thin layer. In our fabrication procedure it is used to deposit titanium onto the substrate to make the surface conductive. A cartoon of the working principle of a typical E-beam evaporator is shown on Fig. 2.1(a). Initially, an electron gun ejects electrons from the cathode in the direction of the anode. The electrons are then steered using an adjustable magnetic field such that they strike a target, in our case a titanium puck. The kinetic energy of the electrons are converted to heat on striking the target, which causes sublimation of the target material. Once a critical buildup of vapour in the target chamber is achieved, a valve is opened to the deposition chamber, and the vapour coats the substrate. The entire system is kept under vacuum, which prevents arcing of the electron gun, provides a collision free path for the electrons, and prevents cooling of the puck from contact with room temperature gas.

Note that this process is similar to, but slightly different from, sputtering. In the case of sputtering, the material is expelled from the target due to the kinetic energy of the incident beam, as opposed to sublimation due to heating.

2.2.2 Plasma Enhanced Chemical Vapour Deposition

Plasma Enhanced Chemical Vapour Deposition (PECVD) is another method of depositing thin films onto a substrate. PECVD takes places inside of a chamber such as the one depicted in the cartoon on Fig. 2.1(b). Precursor gases enter the chamber through a shower head situated at the top of the chamber and byproducts are removed via pumping near the bottom edges. The sample is placed on a plate at the bottom of the chamber, oftentimes using physical clamping. On entering the chamber, the precursor gases are subject to an intense AC electromagnetic field. Because electrons have much lower mass than the nuclei, they are able to track the motion of the alternating field, whereas the nuclei are comparatively unaffected. Eventually, this imparted energy, in conjunction with collisions with mobile

electrons, will cause the precursor gases to ionize. When these ionization processes exceed the loss mechanisms, a runaway chain reaction occurs and forms a plasma. This process is known as Townsend discharge [21].

While other chemical vapour deposition (CVD) techniques exist, PECVD differs in the use of a plasma to enhance the CVD process. This allows the desired chemical reactions to occur at a faster rate compared to CVD, or can enable chemical reactions to take place which would not have been possible in the absence of the plasma. This has significant advantages. For example, the self bias mechanism has the benefit of attracting positively charged ions to the surface of the sample, where the requisite chemical processes for film deposition may take place. Furthermore, the dissociation of electrons and ions creates extreme electron mobility, and extremely high effective temperatures for these electrons. This can enable chemical processes that would be extremely unlikely to occur at lower temperatures. Oftentimes CVD techniques rely upon heating substrates to high temperatures to achieve similar goals.

In our diamond fabrication process PECVD is used to deposit Silicon Nitride (Si_3N_4). This process uses the precursor gases Silane (SiH_3) and Ammonia (NH_3), which if appropriately balanced can deposit Si_3N_4 with H_2 gas as a byproduct. In practice, the deposited film is not perfectly stoichiometric, and will contain additional hydrogen within the film. This can in principle be removed through annealing [22].

2.2.3 Inductively Coupled Plasma – Reactive Ion Etch

In addition to enabling chemical reactions on the surface of samples, which can lead to the conformal deposition of material, plasma may also be used to etch away material. Indeed plasma etching is an integral part of modern semiconductor processes, as it allows directional etching, as opposed to chemical etches, which are often (but not always) isotropic. Plasmas are able to etch material via three principle processes. Firstly, physical etching may take place, where the kinetic energy of fast moving ions mills and dislodges material. Secondly, chemical etching may occur, where free radicals, precursor gases, and any other electrically

neutral substances diffuse towards the sample and chemically react with the sample surface to create volatile or unstable byproducts, which are then pumped out of the chamber. Thirdly ion assisted etching may occur, where ions are accelerated towards the sample, accelerating the chemical etch on impact. Note that unlike chemical etching, which can be isotropic, ion assisted etching is inherently directional.

ICP-RIE stands for Inductively Coupled Plasma-Reactive Ion Etch. Just as in the PECVD system described above, this tool has a capacitively coupled component where an alternating electromagnetic field is created inside a capacitor formed between the chamber walls, and the bottom plate as shown on Fig. 2.1(c). However, unlike the particular PECVD described above, the chamber walls are grounded and the bottom plate is coupled to the RF source via a capacitor. This capacitor allows the AC drive to pass, while also decoupling the bottom plate from ground [1]. Electrons will strike the chamber walls, as well as the sample and the bottom plate. Because the bottom plate is not grounded, the absorption of electrons will cause a large accumulation of charge. This will create a bias across the chamber known as the 'self bias', or 'DC bias', and will cause ions to be accelerated towards the sample. This process is self limiting; if the bias becomes very large, more ions will strike the sample, thus reducing the bias, however if the bias is quite small, then fewer ions will be attracted towards the plate.

In addition to the capacitive coupling ICP-RIE also uses inductive coupling. This secondary coupling is generated by a set of coils wound about the chamber, as depicted on Fig. 2.1(c). These secondary coils induce electric field lines that run in concentric circles in a plane parallel to the sample. This configuration allows excellent control over the properties of the plasma etch. Because the motion of ions and electrons from inductive coupling is parallel to the sample, it does not directly control the acceleration of ions towards the substrate. It does however permit control over the degree of ionization inside of the chamber. On the other hand the capacitive coupling may be used to control both the acceleration and the

[1] We say the system is capacitively coupled because the plasma is inside a capacitor, not because the RF source is connected to the bottom plate through a capacitor.

ionization rate. Using these two controls in tandem, a user can set the forward acceleration of ions via the capacitive coupling, and then adjust the degree of ionization with the inductive controls. The coupling mechanisms above are highly dependent on the etch conditions, and the inductive and capacitive loads in the circuits driving the plasma may vary quite significantly from etch to etch. To overcome this the capacitive and inductive coupling are each incorporated into separate tuning circuits, which ensures good power transfer and low reflected power.

Control over the temperature of the sample is also important, as it can determine which chemical reaction take place, and well as the speed of these reactions. Most ICP-RIE tools permit control over this with a combination of electric resistance heating and cryogenic cooling. The base plate and sample are kept in good thermal contact by use of a backing flow of helium as depicted in Fig. 2.1(c).

2.2.4 Electron Beam Lithography and Scanning Electron Microscopy

Electron Beam Lithography (EBL), is used to define the geometry of the devices we want to create. The main advantage of EBL over more commonly used optical lithography is the small feature sizes enabled by use of electrons. The operation and design principle of an EBL system is very similar to an SEM (Scanning Electron Microscopy). Electrons are initially ejected from a tungsten cathode within an electron gun, as depicted on Fig. 2.1(d). These are then focused through one or more condenser lenses and apertures. The condenser lenses are formed from coils of wire encased in a yoke, as depicted on Fig. 2.1(d). The user varies the current through the coils to adjust the strength of the lens, and the yoke increases the gradient of the magnetic field in the small area though which the electron beams passes. The purpose of the condenser lens is ensure that a large portion of the electron beam passes through the aperture. The purpose of the aperture is to ensure that the diameter of the electron beam is well-defined. A smaller aperture will permit smaller features to be resolved, at the expense of overall beam current. After passing through this initial stage, the beam

enters an objective lens which focusses the beam on the sample. This objective also includes deflector plates, such that the beam may be scanned over the sample. It is worth mentioning that the lenses used in an EBL or SEM do not act in an exactly analogous manner to their optical counterparts. An optical lens is constructed in such a way that a point source located in the focal plane will form parallel rays on the other side of the lens. In an EBL or SEM, the lens does not magnify the image, but serves to ensure that electrons are incident on only a very small, circular area of the substrate.

In an SEM system electrons are scattered from the sample, and are subsequently recorded by a camera. By simultaneously scanning the electron beam over the surface and recording counts on a camera an image of the sample may be constructed. In an EBL, the sample is coated with electron beam resist. This electron beam resist may either be positive tone, where the exposed areas harden and define a mask after development, or negative tone, where the exposed areas weaken and will form open areas after development. An EBL tool will also be constructed with extremely sensitive stage positioners, utilizing laser interferometers, to allow the definition of a masks over large areas with minimal stitching artifacts between write fields.Finally, an EBL will also be equipped with an electrostatic beam blanker, which prevents unwanted exposure of unpatterned parts of the sample.

2.2.5 Wet Etching

Wet etching is the submersion of a sample in an etchant for the purposes of cleaning it or etching a sacrificial layer. For example, Hydrofluoric Acid (HF) will etch SiO_2 over Si with an extremely large selectivity, providing an efficient way to undercut SOI structures.

Piranha is a colloquial name for a mixture of sulphuric acid (H_2SO_4) and peroxide H_2O_2, which is used to clean organics from substrates in preparation for further processing steps. It is typically mixed in a 3:1 ratio, to prevent explosive results. When mixed, this solution will undergo a highly exothermic reaction, and will bubble vigorously.

2.3 Diamond Surface Preparation

One of the principle motivations for creating photonic devices from diamond is the presence of colour centres, which can act as quantum qubits [23–25]. Embedding these devices within a photonic structure would allow efficient optical access to these colour centres. While this is certainly an attractive platform in principle, perhaps the greatest technical hurdle facing networked colour centres is their tendency to have large linewidths when adjacent to surfaces. This is only made worse when the colour centres are created by means of ion implantation. In order to mitigate the issue, we use a surface cleaning and annealing process based on the work of Chu et al. [26], as will be described in this section.

Due to differing requirements, and the necessity to involve many people and geographic locations, this process has had a tendency to get somewhat disorganized within the group. As a consequence, many samples have undergone various variations of this process. Furthermore, in the literature itself, there is variation in the process utilized by various groups, or even the same groups over a period of time. With this in mind, here we detail an 'idealized' process, based off the work of Sangtawesin et al. [27]. To the best of our knowledge, this represents the state of the art in diamond implantation.

Our samples are CVD (Chemical Vapour Deposition) grown diamonds, purchased from element 6. These are SCD samples, with a {100} top face. These may be acquired in either optical grade, with nitrogen concentrations below 1 ppm and quantum (formerly electronic) grade with nitrogen concentrations below 5 ppb. As purchased, these samples are either single- or double-sided polished to < 30 nm Ra, where Ra is the mean deviation of the surface profile.

1. Mechanical Polishing

   Samples are initially cleaned in a piranha solution in order to remove any contaminants from initial packaging. Note that if samples have progressed beyond the diamond etch stage of fabrication, they must be sent out for polishing before further fabrication.

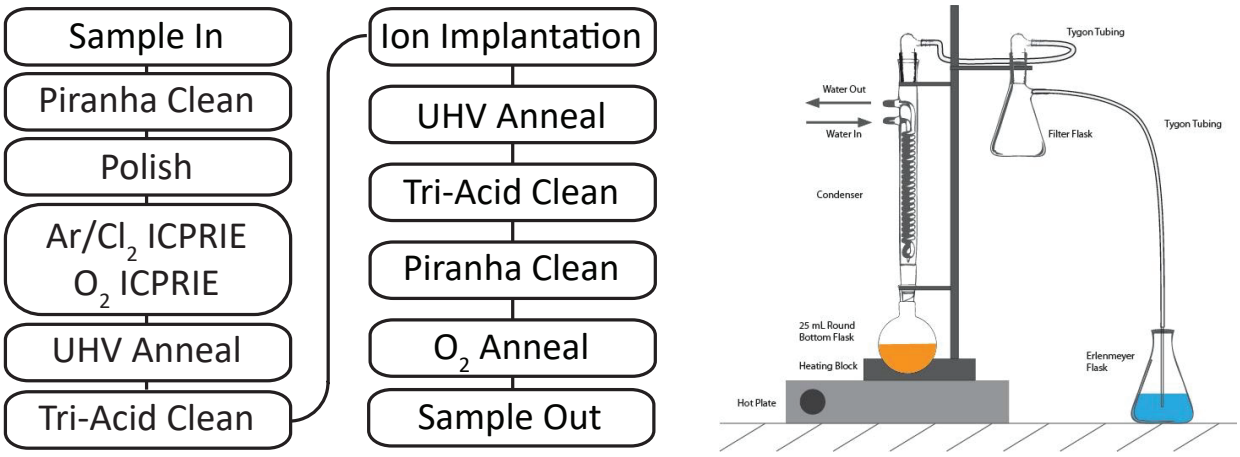

Figure 2.2: Diamond surface preparation workflow and equipment used for tri-acid cleaning.

While there may be areas of the chip that appear to be clean, we have observed anecdotally that these areas will not etch properly if fabrication were to proceed without first polishing the substrate. The samples are polished by Delaware Diamond Knives, which can achieve up to 5 nm Ra. It is interesting to note that due to the hardness of diamond the samples can only be polished by other diamonds.

2. Plasma Treatment

At this point the surface of the samples cannot be further polished by mechanical means. However, the surface of the diamond will posses areas of high stress due to the mechanical polishing. This stress can cause inhomogeneous broadening of colour centres within the diamond [26–28], as well as issues with fabrication. To relieve this stress, the diamond surface is etched using a ICP-RIE etch with Ar/Cl chemistry. This will also further smooth the surface [29]. For this we use the PlasmaLab etcher at NINT, beginning with a chamber clean (Table 2.1) followed by a condition step, and then the etch (Table 2.2). Note that the sample is only placed in the chamber during the etch step, but the carrier wafer will be used in all steps. In these tables 't' is the duration of the etching step, 'T' is the temperature, 'He' gives the rate of flow for the helium backing, 'P_{ch}' is the pressure of the chamber, 'RF' is the set power, actual

power, and reflected power of the RIE component, 'DC Bias' gives the range of bias achieved between the substrate and ground, and 'ICP' is the set power, actual power, and reflected power of the ICP component. The last two columns give the flow rates of the plasma precursors. Some parameters, such as the helium backing, will vary from etch to etch, but the data given in these charts come from a time when these etches were working well.

Purpose	**t** [**h:m:s**]	**T** [**°C**]	**He** [**sccm**]	**Pch** [**mTorr**]	**RF** [**W**]	**DC Bias** [**V**]	**ICP** [**W**]	**O_2** [**sccm**]	**SF_6** [**sccm**]
Clean	01:00:00	20	12.8	50.1	100/102/3	448-452	2000/2003/3	100	10.1

Table 2.1: PlasmaLab cleaning recipe. Recipe name: "OPT-Chamber Clean 20 °C"

Purpose	**t** [**h:m:s**]	**T** [**°C**]	**He** [**sccm**]	**Pch** [**mTorr**]	**RF** [**W**]	**DC Bias** [**V**]	**ICP** [**W**]	**Ar** [**sccm**]	**Cl_2** [**sccm**]
Condition	00:15:00	17	13.0	2.9	250/254/3.5	492-470	1500/1506/3.5	25.0	40.1
Etch	00:30:00	17	14.8	3.1	250/254/8.5	457-473	1500/1506/2.5	25.1	40.0

Table 2.2: PlasmaLab Ar/Cl_2 etch recipe. Recipe name: "Diamond Ar/Cl2".

The Ar/Cl_2 etch will proceed quite quickly through the diamond. This etch is followed by an oxygen etch, which for convenience is also performed on the PlasmaLab at NINT. We begin with a 30 minute version of the clean on Table 2.1 without the sample, followed by the recipe on Table 2.3 with the sample.

Purpose	**t** [**h:m:s**]	**T** [**°C**]	**He** [**sccm**]	**Pch** [**mTorr**]	**RF** [**W**]	**DC Bias** [**V**]	**ICP** [**W**]	**O_2** [**sccm**]
Condition	00:15:00	15	18.2	10.1	80/82/2.5	324-328	850/857/1.5	30.1
Etch	00:30:00	15	18.6	10.0	80/81.5/3	329-331	850/857/2	30.1

Table 2.3: PlasmaLab anisotropic O_2 etch recipe. Recipe name: "Birgit etch - RF 80/ICP 850".

3. Anneal

At this point the sample is ready for annealing. This step is performed in Calgary, where we have a vacuum furnace capable of reaching 1200 °C, and a turbo pump connected to the vacuum tube. At the time of writing this thesis all of our annealing

has taken place in a glass vacuum tube, but on the advice of Professor Nathalie de Leon we have purchased alumina tubes. While this has the disadvantage that the sample may no longer be optically measured, it should prevent the formation of SiC (Silicon Carbide) on the surface of the diamond. The suggested ramp sequence in [27] is as follows,

(a) T1 = 100 °C, Ramp = 1 hour, Hold = 11 hours

(b) T2 = 400 °C, Ramp = 4 hours, Hold = 8 hours

(c) T3 = 800 °C, Ramp = 6-12 hours, Hold = 8 hours

(d) T4 = 1200 °C, Ramp = 6-12 hours, Hold = 2 hours

Temperatures at 400 °C aim to move interstitial defects, 800 °C aids in the formation of colour centres, and 1200 °C eliminates divacancies and multivacancies [28]. While ramping temperatures, careful attention should be paid to the pressure, as quick changes in temperature may cause pressure spikes. It is also a good idea to pre-bake the vacuum tube equipment at low pressure before this process is undertaken.

4. Tri-Acid

Following the anneal procedure, there will be a layer of graphite on the surface of the sample. Graphite is notoriously difficult to remove from surfaces. In the case of diamond a 1:1:1 mixture by volume of Sulphuric (H_2SO_4, 95.0-98.0% concentration), Perchloric ($HClO_4$, 70% concentration), and Nitric acid (HNO_3, 68-70% concentration) is used to remove this layer. Beyond the usual acid handling procedures, special care must be taken when handling perchloric acid, as it can form highly explosive crystals. To prevent this, the apparatus in Fig. 2.3 is used to minimize and neutralize vapours, and the entire apparatus is placed in a wash-down fume hood. Samples are to be left in the tri-acid mixture for at least an hour.

5. Implantation

After tri-acid cleaning the samples are sent out for ion implantation. Charged ions of a desired species are accelerated towards the sample. These ions will embed in the sample, creating damage tracks which will result in the creation of vacancies. Implantation depths, straddles, and the spatial distribution of created vacancies may be calculated using SRIM (Stopping Range of Ions in Matter), a free Monte Carlo software package [30]. Nitrogen and silicon naturally predominantly occur in ^{14}N and ^{28}Si isotopes, respectively. With this in mind, it is sometimes useful to implant ^{15}N or ^{29}Si isotopes if one wishes to approximately identify which colour centres were implanted. This will be evident through differences in the hyperfine structure.

In the past we have used either Materials Diagnostics or Innovion for implantation. In either case, samples must first be mounted on a wafer before being sent for implantation. If one requires a step-like distribution of colour centres, multiple fluences and acceleration voltages may be used [28]. Another useful trick is to request that the sample be angled during implantation. We have usually used an angle of 5° in the past. This is to prevent "channeling", which is the tendency for ions to travel along certain crystal axes preferentially, leading to unintentionally deep implantation depths.

6. Anneal

   This proceeds as the previous anneal step.

7. Tri-Acid

   This proceeds as the previous tri-acid step.

8. O_2 Anneal and Piranha

   After tri-acid cleaning the sample is annealed under a mixture of O_2 and Ar. This should take place in a range between 445 - 450 °C. Following this step, the sample is cleaned in a piranha mixture, as detailed in the next section.

2.4 Diamond Nanofabrication Process

2.4.1 Overview of Diamond Fabrication Techniques

The fabrication process we use for diamond was originally developed in our group by Aaron Hrcyiw and Behzad Khanililoo for the fabrication of diamond nanobeam devices [31]. The principal difficulty in creating these structures was in developing a robust and repeatable method to undercut devices such that they were released from the substrate. This was a difficult problem; the goal was to create devices from SCD in order to benefit from the long coherence times of quantum emitters embedded within the diamond. Unfortunately, SCD is only available in very small dimensions (typically 3 mm $\times$ 3 mm $\times$ 0.5 mm), and unlike SOI, does not contain a sacrificial layer that may be removed by wet etching. Ideally this procedure would involve "standard" cleanroom procedures and equipment such as those listed in the preceding section, so that it could in principal be reproducible, and scalable.

Prior to the work of Khanaliloo et al. [31], a number of different approaches had been applied to the problem. Initially ion beam milling techniques where used on thinned diamond layers. Here a beam of ions (Ga^+) [32] were accelerated towards the diamond to physically mill the material. Unfortunately thinning diamond material is a difficult process. To circumvent this problem, the group of Marko Lončar pioneered the use of a Faraday cage in ICP-RIE etching [33,34]. In this process, a metal cage, formed into the shape of a triangular prism, was placed over the sample in the etching chamber. As ions were accelerated downwards during the fabrication process, they were deflected by the cage. This enabled undercut structures with a triangular cross section to be etched using ICP-RIE. By comparison, the process of Khanililoo et al. did not require thinning of the diamond samples, or specialized equipment such as Faraday cages, but only ICP-RIE etching.

The process of Khanililoo et al. [31] was later applied by Mitchell et al. [35] in the Barclay group to construct microdisks, which were used for the first demonstration of cavity optomechanics in diamond. In 2017 Mouradian et al., from the group of Dirk Englund used

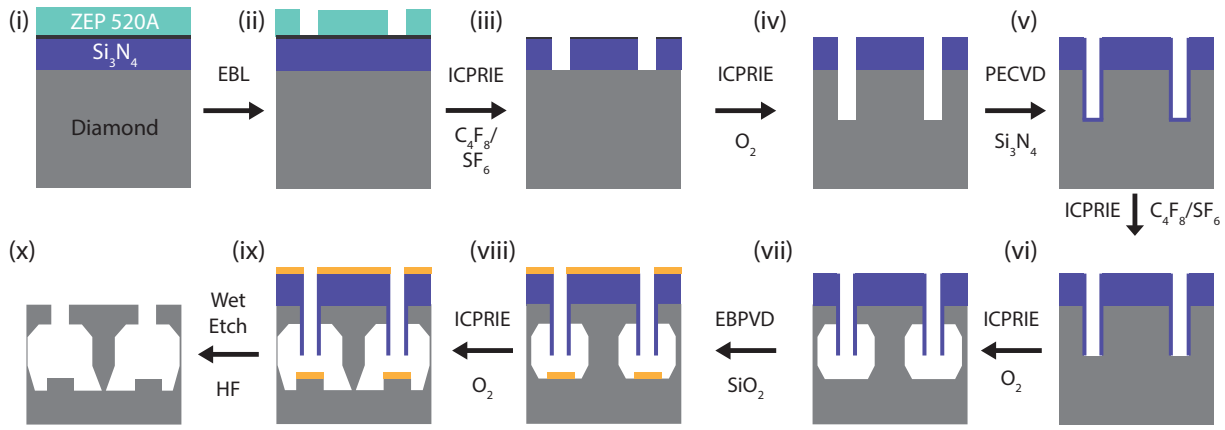

Figure 2.3: (i) Substrate preparation, (ii) E-beam lithography (iii) First silicon nitride etch (iv) First diamond etch (v) Second silicon nitride deposition (vi) Second silicon nitride etch (vii) Second diamond etch (viii) Pedestal Shaping (ix) Second diamond etch (continued) (x) Hard mask removal.

this process to create photonics crystals [36]. Due to changes in the various tool conditions, the entire process used by our group needed to be ported over to new etchers, and the steps re-optimized. Additional steps were also inserted to help improve the thermal properties of the microdisks as detailed in [37]. This work was completed as a collaboration between Matthew Mitchell and myself, with the steps detailed in the remainder of this chapter.

2.4.2 Equipment Used and Purpose of Each Step

Fabrication of diamond samples within our group occurs in Edmonton, and is completed with a combination of tools available at nanoFAB and NINT (National INstitute of Technology). This process flow is detailed in the cartoon on Fig. 2.3.

i Substrate preparation

- Piranha Clean: Wet Process Piranha Wet Deck 2B, (nanoFab)
- Nitride Deposition: PECVD (Trion), (nanoFab)
- Titanium Deposition: JUV E-Beam Evaporator, (NRC)

- Photoresist Deposition: Brewer Spinner and Hotplate, (nanoFab)

In order for the following steps to succeed, it is important that we start with a clean surface from the outset. If the surface is not clean at this stage, there is no way to fix it later and the following steps will fail. If one is concerned with the coherence times of quantum emitters inside of the diamond, then further surface preparation must be undertaken, as detailed in the previous section. Every fabrication run begins with piranha cleaning the diamond piece and any silicon test pieces we will be using. We make sure to use our own glassware for this step to prevent contamination.

Following this clean, we deposit approximately 300 nm of SiN_x as a hard mask to protect certain parts of the diamond later on in the process. If one wants to make nanobeams or photonic crystals, it is a good idea to use a thinner layer to aid in the faithful transfer of small features. To ensure the most reproducible conditions possible, we have been performing a physical clean and cool before every deposition. We have also been mounting both the diamond sample and some silicon test pieces to the carrier wafer before deposition to prevent the sample from being blown around and flipping during chamber venting. The test pieces allow us to infer the thickness of the nitride using filmetrics, as the spot size of the filmetrics tool is too large for direct use with a diamond sample.

Because diamond and silicon nitride are excellent insulators, we need to deposit titanium before the EBL step. This is done using an EBL evaporator at NINT, with the sample mounted on a silicon carrier wafer using vacuum grease. Finally, we mount the sample in a spinner, and pipette ZEP as the electron beam resist layer for the upcoming EBL step.

ii E-beam lithography

- E-beam lithography: RAITH150 Two EBL System, (nanoFab)
- Cold Development: Cold plate (Stir-Kool SK-12D), (nanoFab)

We follow standard EBL steps. Cold development is used to develop the pattern because it slows down the development process. This gives us more control over the development endpoint, and decreases our chances of over or under developing the resist. We use IPA [2] to quench the development.

iii First silicon nitride etch

- Silicon Nitride etch: ICP-RIE (Oxford Estrelas), (nanoFab) OR
- Silicon Nitride etch: ICP-RIE (Oxford Plasmalab), (NRC)

This first plasma etch transfers the pattern from the electron beam resist into the silicon nitride hard mask. Because it uses C_4F_8 / SF_6 chemistry, this etch will only attack exposed SiN_x, and will stop at the diamond layer. If using Estrelas, we first clean the chamber with the following recipe:

Purpose	**t** [**h:m:s**]	**T** [**C**]	**He** [**sccm**]	**Pch** [**mTorr**]	**RF** [**W**]	**DC Bias** [**V**]	**ICP** [**W**]	**O2** [**sccm**]
Clean	01:30:00	0	25.9	20	150	231	2000	100

Table 2.4: Recipe: Extended Chamber Clean with Wafer.

Prior to etching the diamond sample, we etch the silicon test pieces with the SiN_x film we deposited earlier. From this we can extract an etch rate for the SiN_x. Because the patterns we wish to transfer into the SiN_x mask on the diamond piece contain small features, they will etch more slowly than the fully exposed SiN_x on the test pieces. To compensate for this, we have been etching the SiN_x on diamond for 20% longer than required time calculated from the etch rate measurements. The recipe for Estrelas follows:

[2] Isopropyl Alcohol, not India Pale Ale.

Purpose	**t** [**h:m:s**]	**T** [**C**]	**He** [**sccm**]	**Pch** [**mTorr**]	**RF** [**W**]	**DC Bias** [**V**]	**ICP** [**W**]	**C4F8** [**sccm**]	**SF6** [**sccm**]
Condition	0:10:00	15	12	10	20	55.5	1200	14	14
Etch	0:02:30	15	12	10	20	55.5	1200	14	14

Table 2.5: Recipe: Si Mixed Etch.

iv First diamond etch

- Resist strip: UV / Ozone Bonder, (nanoFab)
- (Optional) Piranha Clean: Wet Process – Piranha – Wet Deck 2B, (nanoFab)
- Diamond etch: ICP-RIE (Cobra Metal Etch) OR
- Diamond etch: ICP-RIE (Oxford Plasmalab), (NRC)

To minimize the amount of debris during the next steps of the process, we remove the electron beam resist by first exposing it to UV, and then washing it in remover PG. If this does not remove all the electron beam resist, we can use a piranha clean. With this complete, we do an anisotropic diamond etch with O_2 chemistry to define the sides of our devices. On Cobra, this begins with the following cleaning step:

Purpose	**t** [**h:m:s**]	**T** [**C**]	**He** [**sccm**]	**Pch** [**mTorr**]	**RF** [**W**]	**DC Bias** [**V**]	**ICP** [**W**]	**O2** [**sccm**]	**SF6** [**sccm**]
Clean	1:00:00	15	3	10	100	210	2000	50	5

Table 2.6: Recipe: Clean + SF6.

And is followed by a condition and etch:

Purpose	t [h:m:s]	T [C]	He [sccm]	Pch [mTorr]	RF [W]	DC Bias [V]	ICP [W]	O2 [sccm]
Condition	0:15:00	15	3	10	110	311	1000	28.8
Etch	0:12:00	15	3	10	110	316	1000	28.6

Table 2.7: Recipe: Diamond O2 Etch.

v Second silicon nitride deposition

- Nitride Deposition: PECVD (Trion), (nanoFab)

This second SiN_x deposition will be used to protect the sidewalls of our devices. It is thinner than our first deposition (we typically aim for 150 nm), which will allow us to expose the diamond only in the patterned areas in the next step.

vi Second silicon nitride etch

- Silicon Nitride etch: ICP-RIE (Oxford Estrelas), (nanoFab) OR
- Silicon Nitride etch: ICP-RIE (Oxford Plasmalab), (NRC)

This etch removes the silicon nitride protective layer from the bottom of the trenches of our sample. The duration of this etch is of critical importance. It most be long enough to expose the diamond layer in the trenches of the sample, but short enough to leave enough SiN_x protecting the device. Quite often samples are prone to 'breakthrough' where the nitride along the upper edges of the sample fails, resulting in etching of the diamond below. This likely indicates that the seam where the two layers of nitride meet are the weakest point in the mask. Ensuring that the maximum amount of material possible is positioned in this area significantly helps with preventing breakthrough.

vii Second diamond etch

- Diamond isotropic etch: ICP-RIE (Oxford Plasmalab), (NRC)

Undercutting of structures starts with this quasi-isotropic plasma etch. Because there is no bias applied to this etch it is quite slow, to counteract this to some degree, the base temperature of the etch has been increased to the maximum the tool can handle. To get up to temperature, and to clean the chamber, we start with the following cleaning step,

Purpose	**t** [**h:m:s**]	**T** [**C**]	**He** [**sccm**]	**Pch** [**mTorr**]	**RF** [**W**]	**DC Bias** [**V**]	**ICP** [**W**]	**O2** [**sccm**]	**SF6** [**sccm**]
Clean	2:00:00	15	13.7	50	100	452	2000	100	10

Table 2.8: Recipe: Pre-SCD Iso Clean.

This is followed by a clean, and the first part of the quasi-isotropic etch:

Purpose	**t** [**h:m:s**]	**T** [**C**]	**He** [**sccm**]	**Pch** [**mTorr**]	**RF** [**W**]	**DC Bias** [**V**]	**ICP** [**W**]	**O2** [**sccm**]
Condition	0:15:00	250	7.8	15	0	0	3000	90.2
Etch	5:00:00	250	6.8	15	0	0	3000	90.0

Table 2.9: Recipe: Diamond Isotropic - ICP 3000.

viii Pedestal Shaping (Only for microdisks)

- Silicon Oxide deposition: JUV E-Beam Evaporator, (NRC)

Using e-beam evaporation we deposit amorphous SiO_2 into the trenches of our devices. This is used for the microdisk samples to help control their shape.

ix Second diamond etch (continued)

- Diamond isotropic etch: ICP-RIE (Oxford Plasmalab), (NRC)

This is the same as step (vii)

x Hard mask removal

- HF clean: Wet Process – HF/BOE – Wet Deck 1A/1B (nanoFab)
- Piranha clean: Wet Process – Piranha – Wet Deck 2B, (nanoFab)

At this point the devices are fully defined, and we just need to clean things up. The HF step seems to remove the silicon nitride after $\approx 1/2$ hour, but in theory HF should not etch silicon nitride much at all. If newer silicon nitride recipes at nanoFab are more resistant to HF, we might need to consider another method for this. As a final step, we do a piranha clean to remove organics, and to improve surface termination for colour centres.

2.4.3 Etch Optimization

Troubleshooting

Over the course of the diamond fabrication process, the PECVD etches will require some special attention. Even a recipe that has been working very well for one fabrication run, may not work well on the next fabrication run. Chamber conditions will change over time and it is important to be able to deal with and to compensate for this. In order to keep track of the health of the etch, a few important things to watch for are:

- Reflected Power

  If the instrument has high reflected power after the strike step (anything larger than a few Watts as a rule of thumb), the etch should be stopped immediately as high reflected powers can damage the instrument. The cause of this is often that the tuning circuits have fallen into a local minimum that is far from the global minimum. Try running the etch again after adjusting the tuning capacitors. Note that the ideal capacitor values for the strike step, and the etch step may differ.

- DC bias

This is a good indication of the overall health of your etch. Changes in the bias might be due to change in conductivity of the sample due to contamination, backing, or changes in the tool itself. If the DC bias drifts excessively far, try cleaning the back of the wafer with a nitrogen gun, or using a fresh carrier wafer. Note that for consistency with past etches, test grade wafers must be used, as higher grade wafers will have a different conductivity and will change the etch.

- Backing

  An excessively high helium flow rate indicates (i) that your wafer warped, (ii) that your wafer is dusty on the back, (iii) a potential misalignment in mounting, or (iv) buildup of debris / misalignment in the chamber clamps. If the problem still persists after trying cleaning and a new wafer, you may have to manually clean the chamber and adjust the wafer clamping.

Pseudo Bosch Silicon Etching

Plasma etches typically remove material from a substrate via chemical etching and mechanical etching. In chemical etching, ions impinge on the substrate, and combine with the substrate to form chemically volatile compounds, which may be pumped out of the chamber. Mechanical etching on the other hand, occurs when ions impact the substrate, and dislodge material. Often in an etch one of these mechanisms will dominate, so we will say the etch is a 'chemical etch' or a 'mechanical etch'. In addition to this, etches may also use passivation. Passivated etches deposit material during the etch to protect the sidewalls, ideally creating a smooth profile.

The SiN etches we used are based on the Bosch etch, which was originally formulated for deep etching of silicon [21]. In the Bosch etch, SF_6 and C_4F_8 precursors are alternately pumped into the chamber. The SF_6 etches the SiN chemically, by combining with silicon to form volatile SiF_4, and mechanically through bombardment of F ions [21]. In contrast, C_4F_8 acts to passivate the etch by forming a fluorocarbon film on the substrate. This alternation

between etching and passivation permits fast etching, while maintaining a vertical sidewall profile. However, due to the alternation between etching and passivation, the sidewall profiles will be scalloped.

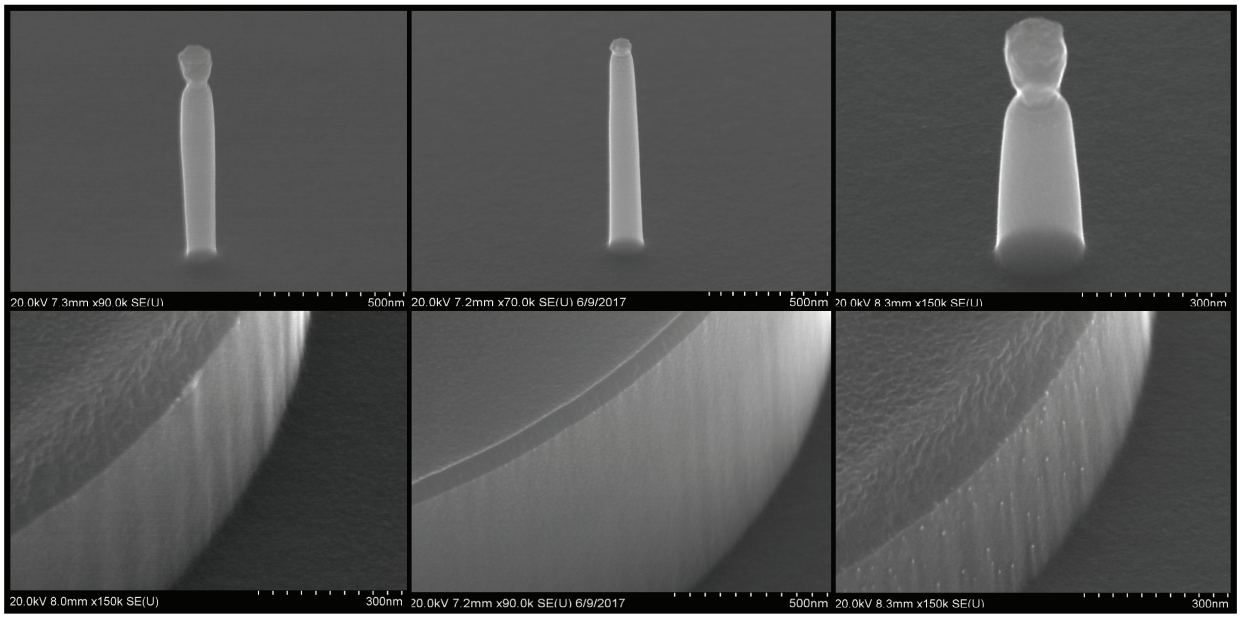

Figure 2.4: Comparison of passivation in a Pseudo Bosch etch. The columns are for etches with $C_4F_8/SF_6 = \{12/16, 14/14, 20/12\}$.

In the pseudo Bosch etch [21, 38], the etching and passivation gases are injected at the same time. This will slow down the progress of the etch, as the downwards etch rate must exceed the deposition rate of the passivation layer, however it can create very smooth, near-vertical sidewalls, which are ideal for photonic structures. An example of the results of changing gas ration are shown on Fig. 2.4. Here the columns contain data with $C_4F_8/SF_6 = \{12/16, 14/14, 20/12\}$. In the first column, we see the effects of under passivation, resulting in scalloped edges and etch overhang. In the second column, the etch has been well passivated, resulting in smooth edges and a vertical sidewall profile. In the last column, the etch has been over passivated, resulting in sloped sidewalls, and debris on the sidewalls.

Oxygen Diamond Etching

All final surfaces on the device will have been formed using the O_2 etch. Unlike the pseudo Bosch etch, this etch is not passivated, and relies on the injection of only a single species. This limits the available control parameters to temperature, gas flow, chamber pressure, RF power, and ICP power. In Fig. 2.5 we show the effect of increasing RF power. In general a higher RF power will cause the sidewalls to become more vertical, and the etch rate will increase.

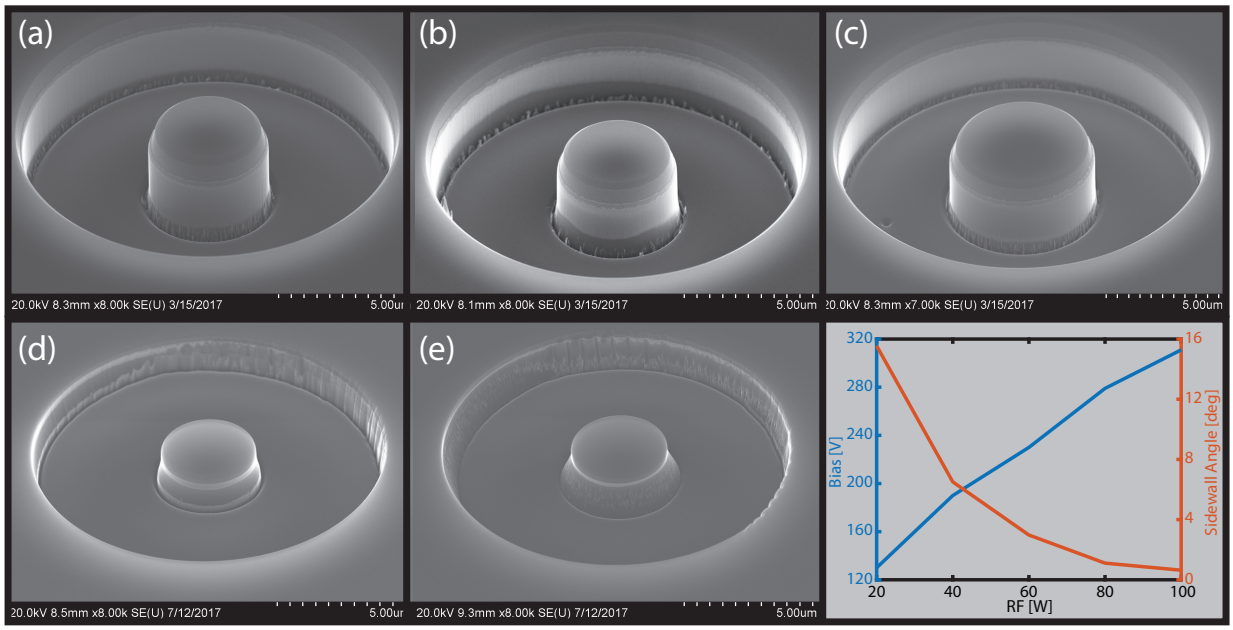

Figure 2.5: (a-e) Oxygen etch RF sweep, etched with the parameters on Table 2.10.

Plot	ICP [W]	RF [W]	DV Bias [V]
a	850	20	130
b	850	40	190
c	850	60	230
d	850	80	279
e	850	100	311

Table 2.10: RF parameter sweep for the diamond oxygen etch.

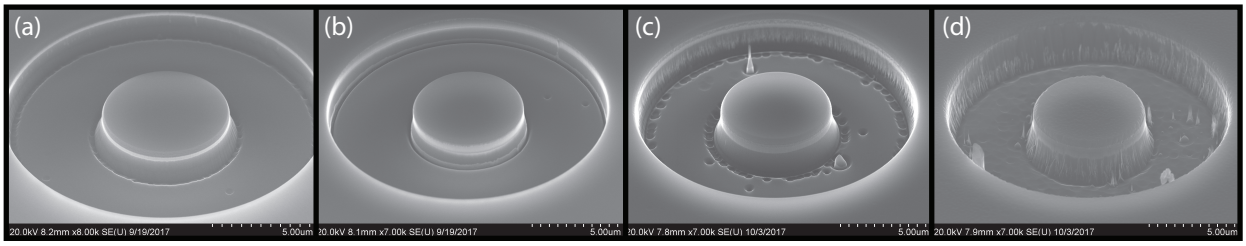

Figure 2.6: (a-d) Oxygen etch ICP sweep, etched with the parameters on Table 2.11

An example of sweeping ICP power while adjusting RF to maintain constant bias is shown on Fig. 2.6, with parameters as shown on Table 2.11.

Plot	ICP [W]	RF [W]	DV Bias [V]
a	850	80	281
b	1000	90	280
c	1150	100	291
d	1300	110	293

Table 2.11: RF parameter sweep for the diamond oxygen etch.

Chapter 3

Nonlinear Optics

3.1 Introduction: Efficient Telecom to Visible Wavelength Conversion in Doubly Resonant GaP Microdisks

This chapter presents this author's work "Efficient telecom to visible wavelength conversion in doubly resonant GaP microdisks", *Appl. Phys. Lett.* 108(3), 031109 (2016), with the slight modification of the insertion of two more panels into Fig. 3.1. In this work, we demonstrated that efficient second harmonic generation (SHG) could be achieved in Gallium Phosphide (GaP) devices.GaP possess $\overline{4}$ symmetry, such that rotation by $\pm 90^{o}$ is equivalent to inverting the domain [49]. This is leveraged here to achieve quasi-phasematching by choosing a geometry where light is forced to propagate along a curved path.

Finally, a thermal shifting technique was developed to tune the fundamental and second harmonic mode into resonance. In addition to the data presented here, we also observed third harmonic generation (THG). Because the collection of THG light was not particularly

efficient, this was not included in this work, but is subject to ongoing investigation in the lab. Note that since this time, a much more elegant approach to the calculations detailed here has been published [39].

D.P. Lake, H. Jayakumar, L.F. dos Santos, and D. Curic acquired the data. M. Mitchell fabricated the devices. D.P. Lake designed the experiment, and wrote the manuscript with P.E. Barclay.

3.2 Second Harmonic Generation

Since the first observation of second harmonic generation (SHG) in 1961 [40], it has become a ubiquitous demonstration of nonlinear optics. In recent years there has been mounting interest in SHG within micron-scale optical structures such as waveguides and cavities [41–51]. These experiments seek to take advantage of devices whose combination of large optical quality factor, Q, and small mode volume, V, provide enhancements to electromagnetic per-photon field intensities at both fundamental and second harmonic wavelengths. Furthermore, the compact nature of these optical devices lends itself to convenient integration into complex on-chip photonic circuits. To date SHG has been demonstrated in a number of microresonator geometries including microdisks [46, 50–52], microrings [53], microspheres [54], photonic crystal nanocavities [44,45,47,48] and waveguides [55,56]. An impressive $9 \times 10^{-2}\text{mW}^{-1}$ conversion efficiency was achieved by Fuŕst et. al. in macroscopic (mm) sized whispering gallery mode resonators [57]. Conversion between 1985 nm and 993 nm light with normalized outside and circulating efficiencies of 10^{-5}mW^{-1} and 10^{-3}mW^{-1}, respectively, have been demonstrated in μm-scale gallium arsenide microdisks with low optical absorption at IR wavelengths [51]. Microcavities have also been utilized in nonlinear optical processes including sum-frequency generation [58], and third harmonic generation [59].

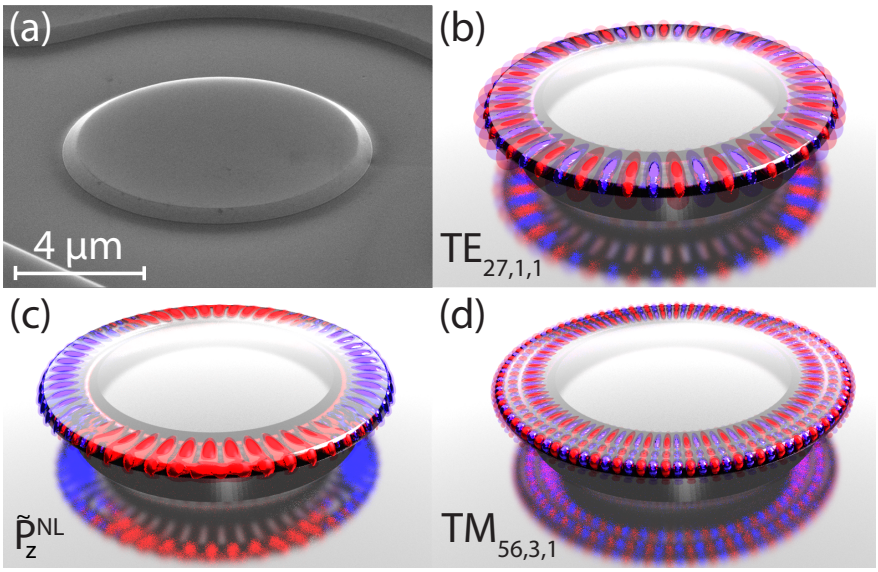

Figure 3.1: (a) SEM of a GaP microdisk before being undercut. (b) $m = 27$ fundamental TE mode. (c) $\tilde{\mathrm{P}}_z^{\mathrm{NL}}$. generated by the mode shown in (b). (d) $m = 56$ third order TM mode

In this work we study microdisk cavities such as the device shown in Fig. 3.1(a), fabricated from gallium phosphide (GaP). The optical transparency window of GaP spans wavelengths from 550 nm to IR, making it a promising material for nonlinear wavelength conversion between C-band (1550 nm) and visible wavelengths [47]. Second harmonic conversion efficiency can be enhanced by fabricating microcavities supporting high-Q optical resonances at λ_c and $\widetilde{\lambda}_c$ that are resonant with the pump (λ_o) and second harmonic wavelengths ($\widetilde{\lambda}_o = \lambda_o/2$), respectively. The high sensitivity of small-V devices to fabrication imperfections and variations in material optical properties, combined with their large free-spectral range, makes it challenging in practice to realize high-Q/V doubly-resonant microcavities. Approaches for addressing this problem include near-field perturbative tuning [60], and bulk temperature tuning [52]. Here we demonstrate a method for tuning optical resonance wavelengths in-situ using dispersive intracavity thermo-optic effects, and utilize this tuning to enable highly-efficient conversion between $\lambda_o = 1545\,\mathrm{nm}$ and $\widetilde{\lambda}_o = 772\,\mathrm{nm}$, with normalized outside efficiency in excess of $3.8 \times 10^{-4}\ \mathrm{mW}^{-1}$.

Efficient SHG in microcavities requires, in addition to resonances at λ_o and $\widetilde{\lambda}_o$, a phase-matching mechanism to overcome dispersion intrinsic to the microcavity. A common approach to achieve this, known as quasi-phasematching, relies upon periodic domains with alternating nonlinear susceptibility [4]. The zincblende structure of GaP possess $\overline{4}$ symmetry [4], which can be used to realize quasi-phasematching of microdisk whispering gallery modes without explicit creation of periodic domains [49, 51, 61]. The microdisks studied here support radially polarized (TE) modes near λ_o, and both TE and vertically ($\hat{z}$) polarized (TM) modes near $\widetilde{\lambda}_o$, that are coupled by the second order nonlinear susceptibility of GaP. The amplitude of the radial and $\hat{z}$ field components these modes varies with $e^{im\theta}$, where m is the azimuthal mode number and θ is the cylindrical angular coordinate. The corresponding cartesian in-plane components E_x and E_y of the TE modes experiences a sign change with period $|\Delta\theta| = \pi$. As a result, the second order nonlinear polarization along z, $\widetilde{\mathsf{P}}_z^{\mathsf{NL}} = 2\epsilon_0 d_{14} E_x E_y$ where d_{14} is the relevant nonlinear susceptibility tensor element of GaP, experiences a sign change with period $|\Delta\theta| = \pi/2$. This is visualized in Fig. 3.1(b), and can be interpreted as momentum imparted by the periodic effective inversion of crystal orientation, creating azimuthal momentum components at $2m \pm 2$. As a result, the time-averaged coupling between $\widetilde{\mathsf{P}}_z^{\mathsf{NL}}$ and the TM microdisk mode with azimuthal index $\widetilde{m}$ is maximized when $\widetilde{m} = 2m \pm 2$. This ± 2 offset can compensate for microdisk dispersion [49], so that satisfying $\lambda_c|_m = 2\widetilde{\lambda}_c|_{2m\pm2}$ becomes possible.

The impact of these effects on SHG is captured by [49]:

$$\widetilde{P} = |K|^2 \frac{\widetilde{\lambda}_c/2\widetilde{Q}_e}{\widetilde{\Delta}(\lambda_o, P_d)^2 + (\widetilde{\lambda}_c/2\widetilde{Q}_t)^2} \left[\frac{\lambda_c/2Q_e}{\Delta(\lambda_o, P_d)^2 + \lambda_c^2/4Q_t^2}\right]^2 P^2, \tag{3.1}$$

which describes the second harmonic power $\widetilde{P}$ output into a waveguide coupled to the microdisk for IR pump power P input to the waveguide. $Q_{e,t}$ and $\widetilde{Q}_{e,t}$ are the external waveguide coupling (e) and the total (t) quality factors of the pump and IR microdisk modes,

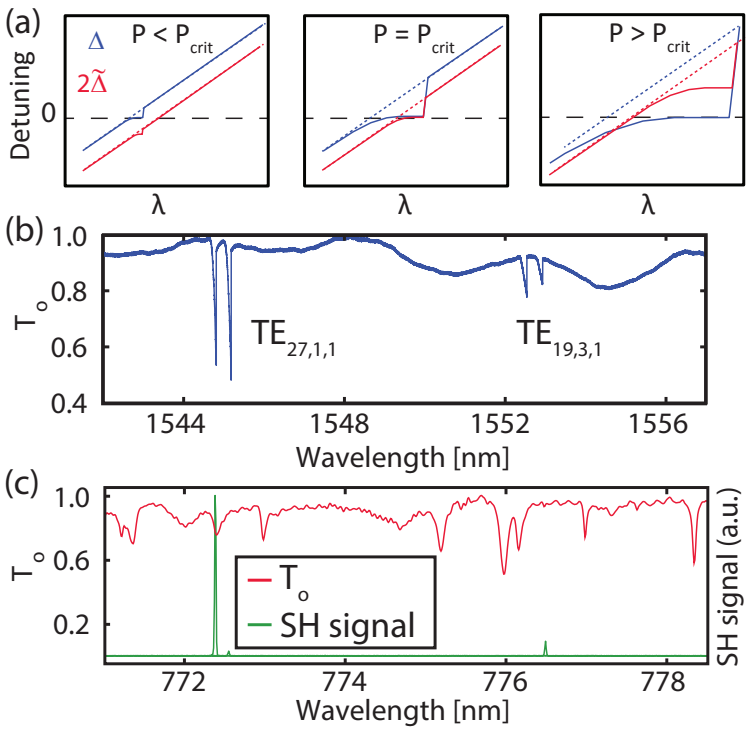

Figure 3.2: (a) Cartoon of influence of P on detunings $\Delta(\lambda_o; P)$ (blue) and $2\widetilde{\Delta}(\lambda_o; P)$ (red) for $\eta > 0$. The dashed lines show the expected behavior in absence of thermo-optic effects. (b) IR transmission spectrum of a fiber taper coupled to a 6.52 µm diameter microdisk. (c) Red line: Visible transmission spectrum of the fiber taper. Green line: SHG signal generated by the IR input light from (b) and collected by the fiber taper. Note that for the P used in (b) and (c), the shortest wavelength IR mode nearly satisfies the double resonance condition.

respectively. The quasi-phasematching is captured by the second harmonic coefficient, K, given in the Supplementary Material. The remaining terms describe the cavity enhancement, and are maximized at "double resonance" where both the pump and second harmonic fields are resonant with a cavity mode, i.e. $\Delta = \widetilde{\Delta} = 0$. Here, $\Delta(\lambda_o, P_d) = \lambda_o - \lambda_c(P_d)$ and $\widetilde{\Delta}(\lambda_o, P_d) = \widetilde{\lambda}_o - \widetilde{\lambda}_c(P_d) = \lambda_o/2 - \widetilde{\lambda}_c(P_d)$ are the detunings between the pump and second harmonic fields, respectively, and the microdisk modes. Due to photothermal effects discussed below, λ_c and $\widetilde{\lambda}_c$ depend on the pump power dropped into the cavity, P_d.

In microdisks, double resonance is generally not satisfied intrinsically. However, adjusting the microdisk temperature, T, can compensate for an initially non-zero relative detuning $|\lambda_c - 2\widetilde{\lambda}_c|$. Changes in T modify λ_c and $\widetilde{\lambda}_c$ via thermal expansion and the thermo-optic effect [62], and tuning rates $d\lambda_c/dT$ and $d\widetilde{\lambda}_c/dT$ can differ due to dispersion of the modal confinement,

refractive index (n_{GaP}), and thermo-optic coefficient. In the experiment described below, the wavelength dependence of the normalized thermo-optic coefficient $(1/n_{\mathrm{GaP}})dn_{\mathrm{GaP}}/dT$ is the dominant mechanism for tuning rate dispersion. For GaP we calculate this coefficient at λ_c and $\widetilde{\lambda}_c$ to be 3.4×10^{-5} [K^{-1}] and 2.9×10^{-5} [K^{-1}] respectively [63], which leads to a differential tuning coefficient $\eta = 1 - (2d\widetilde{\lambda}_c/dT)/(d\lambda_c/dT) = 0.176$.

In our experiment we do not have independent control of T. However, because of linear optical absorption and accompanying heating, T is proportional to $P_d(\Delta)$. For a given η and initial $|\lambda_c - 2\widetilde{\lambda}_c|$, it is possible to find a critical power $P = P_{\mathrm{crit}}$ where double resonance is achieved. The principle of this scheme is illustrated in Fig. 3.2(a), where we sketch Δ and $2\widetilde{\Delta}$ versus λ_o for three values of P, assuming $\eta > 0$. As λ_o is tuned towards λ_c from blue to red, the increase in $P_d(\Delta)$ heats the cavity, causing both λ_c and $\widetilde{\lambda}_c$ to shift to longer wavelengths. For $P < P_{\mathrm{crit}}$ (left panel in Fig. 3.2(a)) the deviation is relatively small and double resonance is never realized. When $P = P_{\mathrm{crit}}$ (center panel in Fig. 3.2(a)), the double resonance condition is satisfied. For $P > P_{\mathrm{crit}}$ (right panel in Fig. 3.2(a)), λ_c is shifted past $2\widetilde{\lambda}_c$ before λ_o reaches λ_c, and double resonance is never achieved. A sharp change in Δ and $\widetilde{\Delta}$ occurs in all three scenarios when λ_o "catches up" to the thermally shifted λ_c [62].

We now show that this tuning scheme can be used to demonstrate SHG at double resonance in GaP microdisks fabricated following Mitchell et al. [64]. To identify promising microdisks for efficient SHG, devices were characterized using fiber taper mode spectroscopy at IR wavelengths, while the spectrum of SHG produced by the microdisk and collected by the fiber taper was simultaneously measured. Figure 3.2(b) shows the transmission through the fiber taper when it is positioned in the near field of a 6.52 µm diameter microdisk, measured with $P \sim 0.5\,\mathrm{mW}$ from a tunable IR wavelength laser (New Focus TLB-6700). Evanescent coupling from the fiber taper to high-Q microdisk doublet modes [12] results in sharp transmission dips and corresponding large P_d. Through comparison with finite difference time domain (MEEP) simulations of the microdisk mode spectrum measured from $1470-1570\,\mathrm{nm}$, we identify doublets near 1545 nm and 1554 nm as corresponding to TE-polarized modes

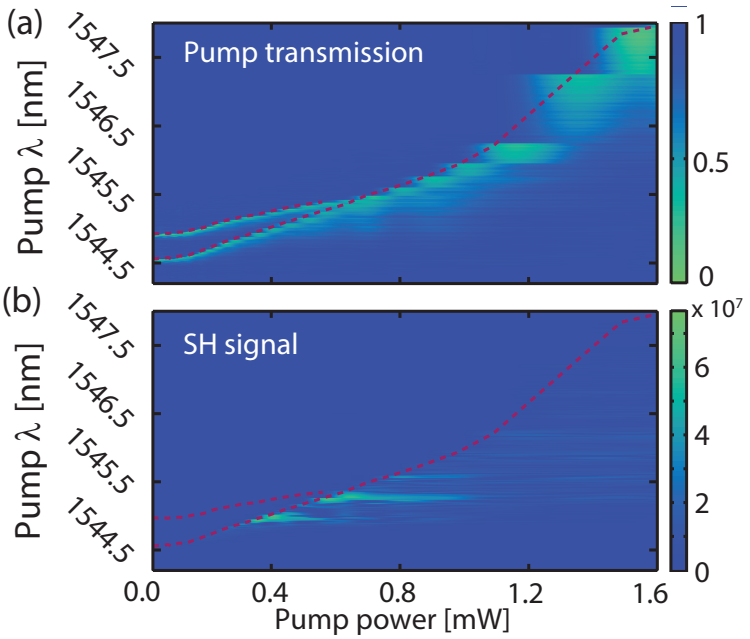

Figure 3.3: (a) Normalized transmission of the pump through the fiber taper when λ_o is scanned from 1544 nm to 1548 nm (in the direction of increasing λ_o) for various fixed values of P. A thermally induced cavity resonance shift is evident with increased P. The red dashed line traces over points of minimum transmission where $\lambda_o = \lambda_c$. (b) SHG signal corresponding to the operating conditions in (a). The dashed line traces λ_c from (a), and serves as a guide to the eye.

with m, radial (p), and axial (q) numbers $\{27, 1, 1\}$ and $\{19, 3, 1\}$, respectively. From fits to the doublet lineshape, we measured unloaded Q of 1.1×10^5 and 2.8×10^4 for the $p = 1$ and $p = 3$ doublets, respectively. Figure 3.2(c) shows that SHG is observed when pumping both modes, and is strongest for the $p = 1$ mode.

To study the initial alignment between modes near $\widetilde{\lambda}_c$ and the SHG signal, we measured the fiber taper transmission using a visible supercontinuum source and spectrometer detection. Comparing the transmission and SHG spectra in Fig. 3.2(c) reveals that the strongest SHG occurs when exciting a doublet mode with SHG emission at $\widetilde{\lambda}_o = \lambda_o/2$ that is close to a resonance at $\widetilde{\lambda}_c \sim 772.2\,\text{nm}$ ($\{m, p, q\} = \{56, 3, 1\}$, $\widetilde{Q} \sim 9600$). In contrast, SHG from the other mode in the doublet is weak, as it is off resonance from $\widetilde{\lambda}_c$.

Further insight into the role played by double resonance was provided using the tuning scheme described above. We scanned λ_o from blue to red across λ_c for a range of fixed values of P and measured the pump transmission (Fig 3.3(a)), and the corresponding SHG (Fig. 3.3(b)) as a function of P and λ_o. Each point in Figs. 3.3(a) and 3.3(b) is the integrated intensity of the narrowband signal detected by the IR and visible spectrometers at λ_o and $\widetilde{\lambda}_o$ respectively, for a given $\{\lambda_o, P\}$. The redshift of λ_c in the pump transmission spectrum in Fig. 3.3(a) with increasing P results from thermo-optic effects in the microdisk. These effects are also responsible for the asymmetric "shark fin" lineshape evident in Fig. 3.2(b) [62]. Note that the jagged edges in Fig. 3.3(a) for high P are due to the discrete stepping of P. Figure 3.3(b) shows that SHG is most intense when exciting the shorter wavelength mode of the doublet, consistent with the observation in Fig. 3.2(c). Additionally, SHG is maximized at an intermediate value of P. As described below, this can be explained by the P_d dependence of $\widetilde{\Delta}(\lambda_o = \lambda_c)$ illustrated in Fig. 3.2(a).

The SHG behaviour can be investigated more quantitatively by analyzing the subset of data in Fig. 3.3 where the pump is on-resonance ($\Delta = 0$). In this case the SHG signal is described by a simplified form of Eq. (3.1) [49]:

$$\widetilde{P}(\Delta = 0) \propto \frac{(\widetilde{\lambda}_c/2\widetilde{Q}_t)^2}{\widetilde{\Delta}(\lambda_o, P)^2 + (\widetilde{\lambda}_c/2\widetilde{Q}_t)^2} \times |K|^2 P^2 \tag{3.2}$$

This expression is a product of two functions: the first captures the impact of the P dependence of the detuning $\widetilde{\Delta}$ between the SHG signal ($\widetilde{\lambda}_o = \lambda_c/2$) and the nearest cavity mode ($\widetilde{\lambda}_c$), and the second describes the usual P^2 dependence of SHG, and scales with the effective nonlinear susceptibility of the microdisk modes of interest. Conveniently, $\widetilde{\Delta}$ is a linear function of P and λ_o for $\Delta = 0$ (see Supplementary Information), allowing Eq. (3.2) to be easily fit to experimental data.

In Fig. 3.4 we analyze the $\Delta = 0$ data from Fig. 3.3 using Eq. (3.2). We only consider the shorter λ_c doublet mode, and find $\lambda_c(P; \Delta = 0)$ from the data in Fig. 3.3(a). In Fig. 3.4(a), we plot SHG absolute efficiency vs. P for $\Delta = 0$. Here absolute efficiency is defined as $\widetilde{P}/P$, where powers are measured in the fiber taper immediately before (P) and after ($\widetilde{P}$) the microdisk, taking into account asymmetric fiber taper insertion loss. We emphasize that because of the P dependence of λ_c shown in Fig. 3.3(b), for every value of P, the selected λ_o corresponding to $\Delta = 0$ varies. For low $P < 0.18$ mW, the absolute efficiency is observed to increase approximately linearly with P, as thermo-optic effects are small compared to the intrinsic "cold cavity" $\widetilde{\Delta}|_{P=0}$. In this region we estimate $\widetilde{\Delta}$ to range from $-34\,\mathrm{pm}$ to $-28\,\mathrm{pm}$. As P approaches $P = P_{\mathrm{crit}} = 0.35\,\mathrm{mW}$, thermo-optic effects become significant, $\widetilde{\Delta} \to 0$ satisfying double resonance, and the absolute efficiency increases superlinearly with P to a maximum value of 1.5×10^{-4} . For $P > P_{\mathrm{crit}}$, absolute efficiency is observed to decrease.

The observed P dependence of $\widetilde{P}(\Delta = 0)$ is consistent with $\widetilde{\Delta}(P; \Delta = 0)$ increasing monotonically with P from $\widetilde{\Delta} < 0$ to $\widetilde{\Delta} > 0$. We test this quantitatively by comparing the predictions from Eq. (3.2) with the measured data in Fig. 3.4(a). Here the required fitting parameters are an overall scaling factor, and the differential thermo-optic tuning coefficient η that determines the linear dependence of $\widetilde{\Delta}$ on P for $\Delta = 0$. We find a best fit for $\eta = 0.181$, which is within 3% of the theoretical value presented above. In applying this model, we included a λ_o dependence in the scaling factor that follows an Airy function and accounts for etaloning in the non-wedged neutral density filters used in this experiment, resulting in oscillations evident in the data.

Further analysis of the SHG signal at $\Delta = 0$ is given in Fig. 3.4(b), which shows the SHG signal for varying λ_o. Here we are plotting $\widetilde{P}$ normalized by P^2 in order to isolate the cavity contribution described in Eq. (3.2). The resulting fit of Eq. (3.2) to the data, shown in Fig. 3.4(b), has good agreement. For this fit, we use the value for η found above, and treat Q_t as a fitting parameter; the fit predicts $\widetilde{Q}_t \sim 1.0 \times 10^4$, in close agreement with the spectrometer

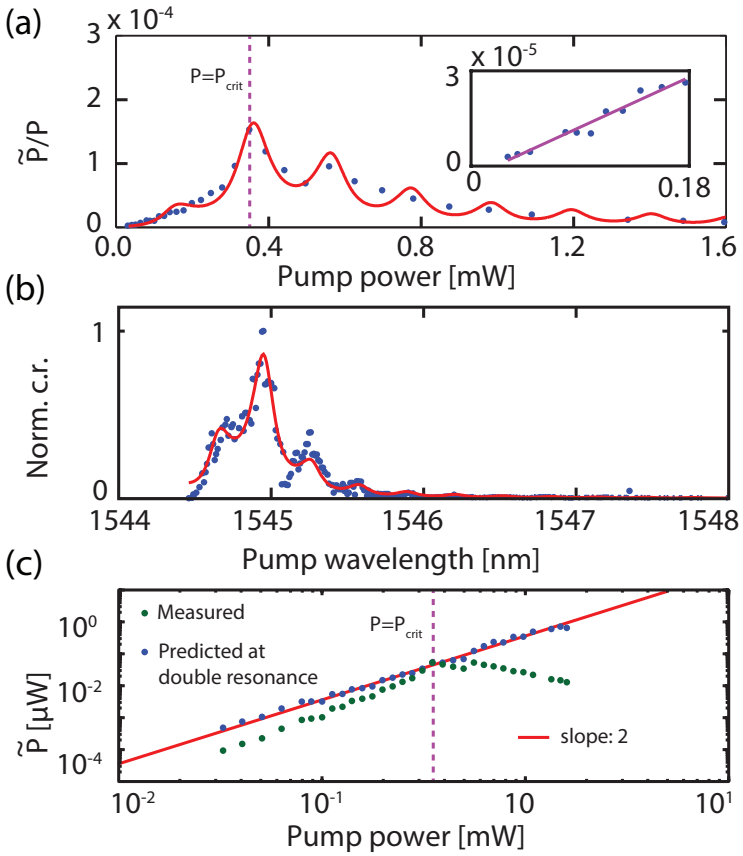

Figure 3.4: (a) SHG absolute efficiency $\widetilde{P}/P$ versus P for $\Delta = 0$. The red line is a fit to the data using Eq. (3.2). The inset highlights low P data and includes a linear fit. (b) Normalized SHG count rate ($\propto \widetilde{P}/P^2$) plotted versus pump wavelength λ_o for $\Delta = 0$, where the red line is a fit to the data adapted from Eq. (3.2). (c) SH power vs. P for $\Delta = 0$. The green points show the unprocessed measured data. The blue points show the predicted SH power if $\widetilde{\Delta} = 0$ for the entire range of P. The red line is a weighted least squares fit to the data of a function proportional to P^2, and indicates a normalized SHG efficiency $\widetilde{P}/P^2 = 3.8 \pm 0.2 \times 10^{-4}\,\mathrm{mW}^{-1}$.

measured value in Fig. 3.2(c). As in the P-dependent fit in Fig. 3.4(a), we included a λ_o dependent scaling factor to account for etaloning from the neutral density filters that creates the observed oscillations.

Finally, in Fig. 3.4(c) we analyze the SHG signal power vs. P at $\Delta = 0$. In this analysis, we plot $\widetilde{P}$ in absolute measured units, as well as scaled by the P dependent microdisk resonance response described by the first term in Eq. (3.2) and predicted from the fit to $\widetilde{\Delta}(P; \Delta = 0)$ obtained for Fig. 3.4(a). This latter scaling isolates the term in Eq. (3.2) that describes the microdisk nonlinear susceptibility, and is ideally proportional to $|K|^2 P^2$. As shown in Fig. 3.4(c), when scaled in this manner, the data is well described by a P^2 dependence. This plot represents the predicted SHG signal if the enhancement provided by the microdisk density of states is fixed to its maximum value at $\widetilde{\Delta} = \Delta = 0$. Note that in our experiment, this efficiency is only realized when $P = P_{\text{crit}}$, as evident by comparing the unscaled and predicted data in Fig. 3.4(c).

The maximum normalized outside efficiency, defined as $\widetilde{P}/P^2$, was found from the point of highest efficiency in Fig. 3.4(a) to be 4.4×10^{-4} mW^{-1} for the case $P = P_{\text{crit}}$. The weighted least squares fit to the scaled data shown in Fig. 3.4(c) can be used as a consistency check, and gives the predicted normalized outside efficiency if the double resonance condition $\Delta = \widetilde{\Delta} = 0$ is satisfied over the entire range of P. We find a normalized efficiency of $(3.8 \pm 0.2) \times 10^{-4}$ mW^{-1}, in good agreement with the measured maximum normalized outside efficiency at P_{crit} in Fig. 3.4(b) where the double resonance condition is satisfied. In comparison, the SHG signal at low P shown in the inset Fig. 3.4(b), where $\widetilde{\Delta}$ is approximately constant (i.e. independent of P), has a normalized outside efficiency of 1.78×10^{-4} mW^{-1}. This illustrates that the SHG normalized outside efficiency $\widetilde{P}/P^2$, in addition to the total efficiency $\widetilde{P}/P$ shown in Fig. 3.4(b), is enhanced through satisfaction of the double resonance condition at $P = P_{\text{crit}}$.

In conclusion, we have demonstrated resonant second harmonic generation from 1550 nm to 775 nm in a GaP microdisk with maximum normalized outside efficiency of 3.8×10^{-4} mW^{-1} for $P = P_{\mathrm{crit}} = 0.35\,\mathrm{mW}$, which is larger than previously reported values in similarly sized structures used for 2000 nm to 1000 nm wavelength conversion [51]. We have shown that this efficiency is achieved via double resonance between high-Q modes of the GaP microdisk at both IR ($Q \sim 1.1 \times 10^5$) and visible ($\widetilde{Q} \sim 1.0 \times 10^4$) wavelengths. Further improvements to the efficiency could be made by spectrally aligning higher-$\widetilde{Q}$ modes, and optimizing fiber taper coupling at visible wavelengths. Control of the differential tuning independent of pump power could be realized by thermally heating using light from an additional optical mode not involved in the nonlinear conversion process. As GaP is a piezoelectric material, it may be possible to tune the modes through electronic means [65]. The geometry presented in this letter can also be adapted for use in other nonlinear optics scenarios such as four wave mixing and downconversion [66–69]. With the present system we have already observed third harmonic generation, although efficient collection of the resultant 515 nm light via fiber taper requires additional optimization.

We would like to thank Aaron C. Hryciw, and J.P. Hadden for their assistance with this project. This work was supported by NRC, CFI, iCORE/AITF, NSERC, and CNPq.

3.3 Supporting Information

3.3.1 Thermal Tuning

The thermal dependance of the laser cavity detuning can be approximated by the expression [62]:

$$\Delta(\delta T) \approx \lambda_o - \lambda_c \left[1 + a\delta T\right], \tag{3.3}$$

with $a = \epsilon + \frac{1}{n}\frac{dn}{dT}$. Here δT is the deviance from the equilibrium temperature, ϵ is the thermal expansion coefficient, and n is the refractive index.

Furthermore, we can write an expression for the change in cavity temperature due to optical absorption when the cavity is pumped at resonance and is in thermal equilibrium:

$$\Delta T = \frac{2Q^2}{Q_\kappa Q_{abs}} \frac{P_f}{K_{th}} = c_{th} P_f, \tag{3.4}$$

where Q_{abs} is the quality factor associated with optical absorption in the cavity, and K_{th} is the inverse of the thermal time constant of the cavity. This expression is derived by considering the rate at which power is absorbed into the cavity when optically pumped on resonance, and equating it to $K_{th}\delta T$, the rate at which power is dissipated. For simplicity we have grouped together terms into the constant c_{th}

Making use of equations (3.4) and (3.3) we can write expressions for $\widetilde{\Delta}$ for the case when $\Delta = 0$:

$$\widetilde{\Delta} = \begin{cases} a_1 \lambda_o + a_0 \\ \\ b_1 P_f + b_0, \end{cases} \tag{3.5}$$

where:

$$a_0 = -\left[1 - \frac{\widetilde{a}}{a}\right] \widetilde{\lambda}_o, \tag{3.6}$$

$$a_1 = \frac{1}{2} - \frac{\widetilde{a}\widetilde{\lambda}_o}{a\lambda_o}, \tag{3.7}$$

$$b_0 = c_{th}\left[\frac{a\lambda_0}{2} - \widetilde{a}\widetilde{\lambda}_o\right], \tag{3.8}$$

$$b_1 = \frac{\lambda_o}{2} - \widetilde{\lambda}_o. \tag{3.9}$$

3.3.2 SHG in Doublets

The optical resonance used in the current experiment was a doublet mode. Such modes occur in whispering-gallery type resonators when surface roughness causes the coupling rate between clockwise and counter clockwise propagating mode to exceed the combined loss rate to all other channels [12]. The transmission spectra of the doublet contains two distinct

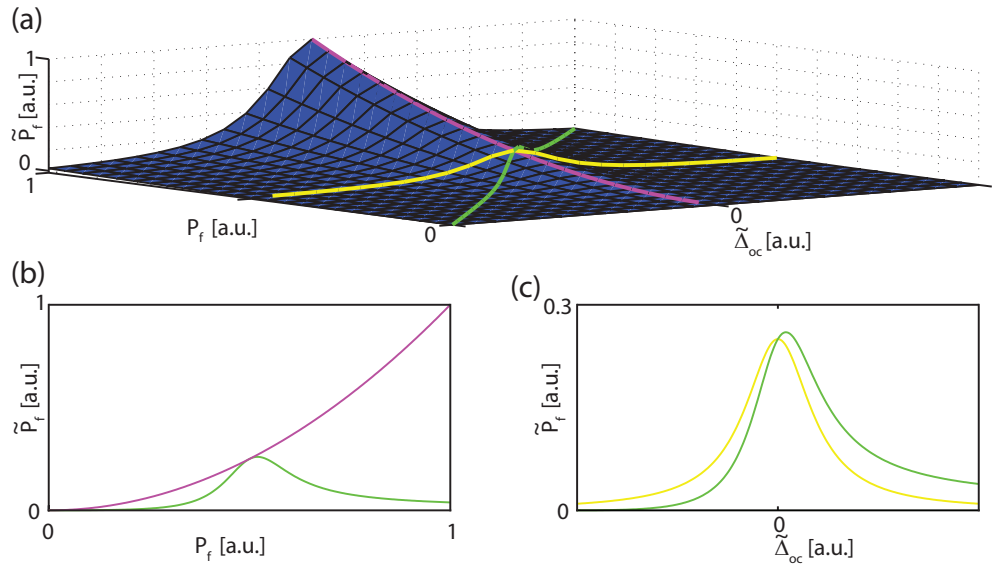

Figure 3.5: (a) Second harmonic signal for the special case $\Delta = 0$, as a function of P_f and $\tilde{\Delta}$. The coloured curves represent possible trajectories of an experiment. (b) Power dependence of second harmonic generation for the case of constant detuning (magenta curve) and for variable detuning (green curve). (c) Detuning dependence of second harmonic generation of constant power (yellow curve), and for varied power (green curve).

resonances, each of which is a standing wave created from linear combinations of clockwise and counter clockwise propagating modes. In the case of the doublet considered in the current experiment, these standing waves are spectrally well separated, which permits the individual excitation of each of these modes. We write the amplitude of the standing wave at the fundamental frequency ω_0, as [12]:

$$A = \frac{-\kappa/\sqrt{2}S_f}{\imath(\Delta_\omega) - \gamma_t/2}, \tag{3.10}$$

where A is the amplitude of the standing wave mode, S_f is the amplitude of the forward propagating mode in the fiber taper, κ is the waveguide-cavity coupling, Δ_ω is the laser-cavity detuning in terms of frequency, and γ_t is the energy decay rate of the cavity into all channels. Here $|A|^2$ is normalized to energy, and $|S_f|^2$ is normalized to power.

In contrast to the travelling wave fundamental modes considered elsewhere [49], a standing wave fundamental mode will excite both clockwise and counter clockwise modes at the second harmonic frequency $\widetilde{\omega}_o = 2\omega_o$. The coupled mode equations describing this process may be written as:

$$\frac{d\,\widetilde{a}^{cw}}{dt} = (\imath\widetilde{\omega}_c - \widetilde{\gamma}_t/2)\widetilde{a}^{cw} + \widetilde{\zeta}, \tag{3.11}$$

$$\frac{d\,\widetilde{a}^{ccw}}{dt} = (\imath\widetilde{\omega}_c - \widetilde{\gamma}_t/2)\widetilde{a}^{ccw} + \widetilde{\zeta}, \tag{3.12}$$

where ζ is the second harmonic source term, $\widetilde{\gamma}_t$ is the energy decay rate of the loaded cavity around the cavity frequency $\widetilde{\omega}_c$, and $\widetilde{a}^{cw,ccw} = \widetilde{A}^{cw,ccw}e^{\imath\omega_o t}$ with ω_o representing the laser frequency and $\widetilde{A}^{cw,ccw}$ as the amplitude of the clockwise or counterclockwise propagating modes. Note that in our experiment, the second harmonic mode was found to be a singlet mode, so surface roughness did not appreciably couple the clockwise and counter clockwise propagating modes at $\widetilde{\omega}_c$.

The explicit form of the nonlinear source term may be written as:

$$\widetilde{\zeta} = 2\pi\frac{\widetilde{v}_g}{2\pi R}\left|\left\langle\frac{d\widetilde{A}^{cw,ccw}}{d\theta}\right\rangle\right| \tag{3.13}$$

where $\widetilde{v}_g$ is the group velocity of the SH mode, and R is the radius of the disk. The first term of this expression gives the frequency at which the SH mode circulates the disk in units of rad/s, and the second term describes the average gain per cycle.

The nonlinear source term can be calculated from the spatial profile of the optical modes as:

$$\widetilde{\zeta} = \frac{A^2\delta\omega_{FSR}}{4\pi}\int_0^{2\pi}\left[K_+e^{\imath(\Delta m+2)\theta} + K_-e^{-\imath(\Delta m+2)\theta}\right]d\theta \tag{3.14}$$

where $\widetilde{\zeta}$ is the source term, $\delta\omega_{FSR}$ is the free spectral range of the microdisk at ω_0, and K_+, K_- are the second harmonic coefficients, and Δm is the mismatch in the azimuthal numbers of the microdisk at ω_0 and $\widetilde{\omega}_0$, defined as $\Delta m \equiv \widetilde{m} - 2m$. The explicit form of the second

harmonic coefficients, as derived in [49], may be written as:

$$K_+ = -\frac{d_{14}}{2\epsilon_0\widetilde{\omega}_0 n^4}\int_0^\infty\int_{-h/2}^{h/2}\rho\widetilde{\psi}\left(\frac{m\psi}{r}+\frac{\partial\psi}{\partial\rho}\right)^2 dzd\rho, \tag{3.15}$$

$$K_- = \frac{d_{14}}{2\epsilon_0\widetilde{\omega}_0 n^4}\int_0^\infty\int_{-h/2}^{h/2}\rho\widetilde{\psi}\left(\frac{m\psi}{r}-\frac{\partial\psi}{\partial\rho}\right)^2 dzd\rho, \tag{3.16}$$

where n is the refractive index of GaP at ω_0, and ψ, $\widetilde{\psi}$ give the radial and vertical dependence of the $\hat{z}$-component of the modes at ω_0 and $\widetilde{\omega}_0$. Here we have assumed the normalization conditions $\int|\psi|^2dA = \delta\omega_{fsr}/2\pi$ and $\int|\widetilde{\psi}|^2dA = \delta\widetilde{\omega}_{fsr}/2\pi$ where the integrals are taken over the infinite half-plane [49].

Finally we use 3.11, 3.12 to solve for the steady state amplitudes of the second harmonic modes propagating in the clockwise and counter clockwise directions:

$$\widetilde{A}^{cw} = \frac{\widetilde{\zeta}}{\imath\widetilde{\Delta}_\omega - \widetilde{\gamma}_t/2}, \tag{3.17}$$

$$\widetilde{A}^{ccw} = \frac{\widetilde{\zeta}}{\imath\widetilde{\Delta}_\omega - \widetilde{\gamma}_t/2}, \tag{3.18}$$

where $\widetilde{\Delta}_\omega$ is the laser-cavity detuning $\omega_o/2 - \widetilde{\omega}_c$.

Making use of the amplitude normalizations, and waveguide-cavity coupling parameters, we can relate $\widetilde{P}_{f,b}$, the power in the taper at $\widetilde{\lambda}_o$ in either the forward or backward direction and P_f, the power in the taper at λ_o to the amplitudes:

$$P_f = |S_f|^2, \tag{3.19}$$

$$\widetilde{P}_{f,b} = |\widetilde{S}_{f,b}|^2 = \frac{|\widetilde{\kappa}|^2|\widetilde{A}_{f,b}|^2}{2} \tag{3.20}$$

Combining equations (3.10), (3.14), (3.17), (3.19), (3.20) and writing the decay rates in terms of their respective quality factors we arrive at a final expression in terms of $\widetilde{P}_{f,b}$ and P_f:

$$\widetilde{P}_{f,b} = |K|^2\frac{\widetilde{\lambda}_c/2\widetilde{Q}_\kappa}{\widetilde{\Delta}^2 + (\widetilde{\lambda}_c/2\widetilde{Q}_t)^2}\left[\frac{1}{2}\frac{\lambda_c/2Q_\kappa}{\Delta^2 + (\lambda_c/2Q_t)^2}\right]^2 P_f^2. \tag{3.21}$$

with:

$$|K|^2 = \frac{\lambda_c}{2\pi c}\delta\lambda_{FSR}^2\Big[K_+ e^{\imath\pi(\Delta m+2)}\mathrm{sinc}[\pi(\Delta m+2)] + K_- e^{\imath\pi(\Delta m-2)}\mathrm{sinc}[\pi(\Delta m-2)]\Big]^2. \quad (3.22)$$

In order to better visualize the physics behind the data analysis of the main text, we have plotted Eq. (3.21) in Fig. 3.5 for the case $\Delta = 0$. In this instance, the expression for $\widetilde{P}_f$ is separable into a function of P_f and a function of $\widetilde{\Delta}$. We display this on Fig. 3.5 along with three curves representing various paths in $P_f - \widetilde{\Delta}$ space which an experiment might take. The magenta curve represents the case of fixed detuning $\widetilde{\Delta} = 0$, which demonstrates the typical quadratic dependence on P_f expected from a second harmonic experiment. The yellow curve is the case of fixed power, with a variable detuning, which displays the Lorentzian line shape contributed by the cavity resonance lineshape. Lastly, the green curve represents the case where both detuning and pump power are varied.

Chapter 4

Optomechanics

4.1 Canonical Optomechanical System

In this chapter we introduce optomechanics, which is a topic at the centre of the bulk of this thesis. Optomechanics is a field of study which investigates the interaction of optical and mechanical degrees of freedom [70]. It is a relatively young and growing field of research, with far ranging applications. Among these applications are practical sensors, such as magnetometers [71], accelerometers and torque sensors [72, 73] and even the Laser Interferometer Gravitational-Wave Observatory (LIGO) [74, 75]. Beyond sensing, optomechanics also permits the study of fundamental physics, such as ground state cooling of a mechanical resonator [76, 77], storage of classical and quantum signals [78–81], squeezing [82, 83], quantum correlations [84], and entanglement of mechanical oscillators [85].

4.1.1 Equations of Motion

One can model the canonical optomechanical system as a cavity constructed from two opposing mirrors. One of these mirrors is partially reflective and fixed in space, and the other attached to the end of spring, as shown on Fig. 4.1. Photons enter through the partially reflective mirror and reflect back and forth repeatedly prior to exiting the cavity. Every time

a photon is incident on the far cavity mirror, it will impart a momentum $\Delta p = 2p = 2h/\lambda$, where p is the momentum of a single photon, and λ is the wavelength. This interaction, known as the radiation pressure force, will cause the mirror to recoil and the spring to compress. The motion of the mirror will in turn influence the photons in the cavity through the Doppler shift. If the mirror is moving away from an incident photon, then the reflected photon will be red shifted. Conversely, if the mirror is moving towards an incident photon, it will be blue shifted. Furthermore, the motion of the mirror will cause the resonance frequency of the optical cavity to shift. If the cavity is elongated, the cavity frequency decreases, whereas is the cavity is shortened, the cavity frequency will increase.

Now that we have a qualitative understanding of how the canonical optomechanical system should act, let us try and model this system quantitatively. To simplify the problem, we will focus on a single mode of the optical cavity and a single mode of the mechanics. From our work in Section 1.3.2 we know that optical and mechanical modes may be described as harmonic oscillators, so here we define the creation and annihilation operators for the optical mode and mechanical mode as $\hat{\alpha}^\dagger$, $\hat{\alpha}$ and $\hat{b}^\dagger$, $\hat{b}$ respectively. In this way we can write the operator for the mechanical displacement as $\hat{x} = x_0\left(\hat{b} + \hat{b}^\dagger\right)$, where $x_0 = \sqrt{\frac{\hbar}{2m\omega_\mathrm{m}}}$ is the zero point fluctuations, m is the effective mass of the mechanical oscillator, and ω_m is the frequency of the mechanical mode. From Section 1.3.3, we know that one can model the interaction of a mode with the environment through use of input-output

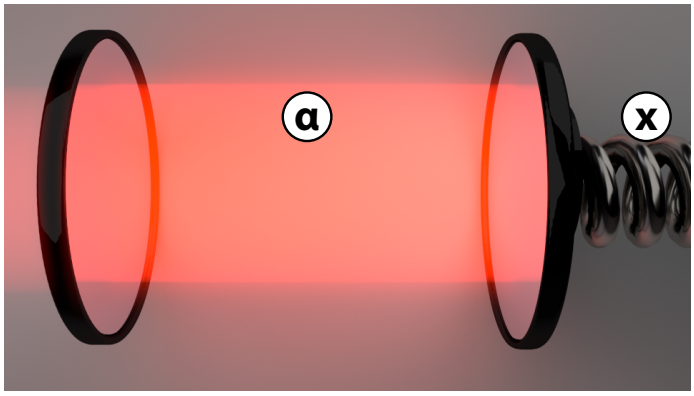

Figure 4.1: Cartoon of the canonical optomechanical system. Here α is the amplitude of the optical mode, and x is the position of the spring affixed to the mirror.

equations [19, 20]. We will assume that the optical mode has losses associated with external coupling to an input-output port (the partially reflective mirror), as well as intrinsic losses, such as scattering out of the mode, radiative losses, and material absorption. The mechanical mode is assumed to only possess intrinsic losses, but it is no major obstacle to generalize this to include other loss terms. With these assumptions, and using Eq. 1.94 we arrive at,

$$\dot{\hat{\alpha}} = -\frac{i}{\hbar}\left[\hat{\alpha}, \hat{H}\right] - \frac{\kappa}{2}\hat{\alpha} + \sqrt{\kappa_{\mathrm{ex}}}\hat{a}_{\mathrm{in}} + \sqrt{\kappa_{\mathrm{i}}}\hat{f}_{\mathrm{in}}, \tag{4.1}$$

$$\dot{\hat{b}} = -\frac{i}{\hbar}\left[\hat{b}, \hat{H}\right] - \frac{\gamma}{2}\hat{b} + \sqrt{\gamma}\hat{b}_{\mathrm{in}}, \tag{4.2}$$

where κ_{ex}, κ_{i}, $\kappa = \kappa_{\mathrm{i}} + \kappa_{\mathrm{ex}}$ are the external, intrinsic, and total energy decay rates, and γ is the total mechanical decay rate. In the above $\hat{a}_{\mathrm{in}}$, $\hat{f}_{\mathrm{in}}$ and $\hat{b}_{\mathrm{in}}$ are inputs from the external optical coupling, internal optical coupling, and mechanical coupling. The Hamiltonian, which governs the dynamics of the optical and mechanical mode is denoted by $\hat{H}$.

To simplify matters, suppose for the moment that there is no interaction between the optical and mechanical modes. In this case the Hamiltonian is the sum of two independent harmonic oscillators representing the optical mode and the mechanical mode respectively,

$$\hat{H} = \hbar\omega_{\mathrm{o}}\hat{\alpha}^{\dagger}\hat{\alpha} + \hbar\omega_{\mathrm{m}}\hat{b}^{\dagger}\hat{b}, \tag{4.3}$$

where ω_{o} is the frequency of the optical mode, and ω_{m} is the frequency of the mechanical mode [1]. At this point we can include optomechanical coupling based on the discussion above by expanding the cavity frequency in a Taylor series [86],

$$\omega_{\mathrm{o}}(x) = \omega_{\mathrm{o}}(x)|_{x=0} + x\frac{\partial\omega_{\mathrm{o}}(x)}{\partial x}|_{x=0} + ... \tag{4.4}$$

[1] We have excluded terms $\hbar\omega_{\mathrm{o}}/2$ and $\hbar\omega_{\mathrm{m}}/2$ as they will not contribute to the effects we consider here.

This expression is typically abbreviated by defining $G = -\frac{\partial\omega_{\rm o}(\partial x)}{x}$ [70]. The optomechanical coupling rate is generally stronger for systems with smaller dimensions. This can be inferred by considering a simple Fabry-Perot cavity of length L. Such a cavity will contain several different modes, with resonant frequencies of the form $\omega_{\rm o} = \frac{\pi mc}{L}$ where m is an integer, and c is the speed of light. Allowing the cavity length to change as a function of x, we find for small displacements $\omega_{\rm o}(x) = \frac{\pi mc}{L+x} \approx \omega_{\rm o}(0) - \frac{x\omega_{\rm o}(0)}{L}$. This implies $G = \omega_{\rm o}/L$, indicating that the optomechanical coupling will be stronger for devices with smaller dimensions.

Inserting Eq. 4.4 into Eq. 4.3 we find,

$$\begin{aligned}\hat{H} &= \hbar(\omega_{\rm o} - G\hat{x})\hat{\alpha}^\dagger\hat{\alpha} + \hbar\omega_{\rm m}\hat{b}^\dagger\hat{b} \\ &= \hbar\omega_{\rm o}\hat{\alpha}^\dagger\hat{\alpha} + \hbar\omega_{\rm m}\hat{b}^\dagger\hat{b} - Gx_0\left(\hat{b}+\hat{b}^\dagger\right)\hat{\alpha}^\dagger\hat{\alpha} \\ &= \hbar\omega_{\rm o}\hat{\alpha}^\dagger\hat{\alpha} + \hbar\omega_{\rm m}\hat{b}^\dagger\hat{b} - g_0\left(\hat{b}+\hat{b}^\dagger\right)\hat{\alpha}^\dagger\hat{\alpha},\end{aligned} \tag{4.5}$$

where we have defined the single phonon optomechanical coupling rate, $g_0 = x_0 G$, for convenience.

We are now in a position to derive equations of motion. Placing Eq. 4.5 into Eqs. 4.1-4.2, we find,

$$\dot{\hat{\alpha}} = -\left(i\omega_{\rm o} + \frac{\kappa}{2}\right)\hat{\alpha} + ig_0\hat{\alpha}\left(\hat{b}+\hat{b}^\dagger\right) + \sqrt{\kappa_{\rm ex}}\hat{a}_{\rm in} + \sqrt{\kappa_{\rm i}}\hat{f}_{\rm in}, \tag{4.6}$$

$$\dot{\hat{b}} = -\left(i\omega_{\rm m} + \frac{\gamma}{2}\right)\hat{b} + ig_0\hat{\alpha}^\dagger\hat{\alpha} + \sqrt{\gamma}\hat{b}_{\rm in}. \tag{4.7}$$

Examination of the above expressions reveals that the frequency of the optical mode shifts proportional to the mechanical displacement, x, and the mechanical mode contains a term $\hat{\alpha}^\dagger\hat{\alpha}$, implying that the mechanical degree of freedom will undergo displacement proportional to the number of photons in the cavity. Note that these couplings are nonlinear, as they contain products of two operators. Note that we could have equivalently defined equations of motion in terms of $\dot{\hat{\alpha}}$ and $\dot{\hat{x}}$ [70].

Unfortunately, the single photon coupling rates are much smaller than the decay rate of the optical cavity in nearly all physically realizable systems. This would seem to imply that small inputs to the system, such as single photons, cannot have any appreciable effect. By this token optomechanical systems would not appear to be very useful for quantum applications! Fortunately we can make use of the weak nonlinearity of the optomechanical interaction to construct a linear system with massively enhanced coupling rates. All the optomechanical experiments detailed in this thesis will make use of this linearized system.

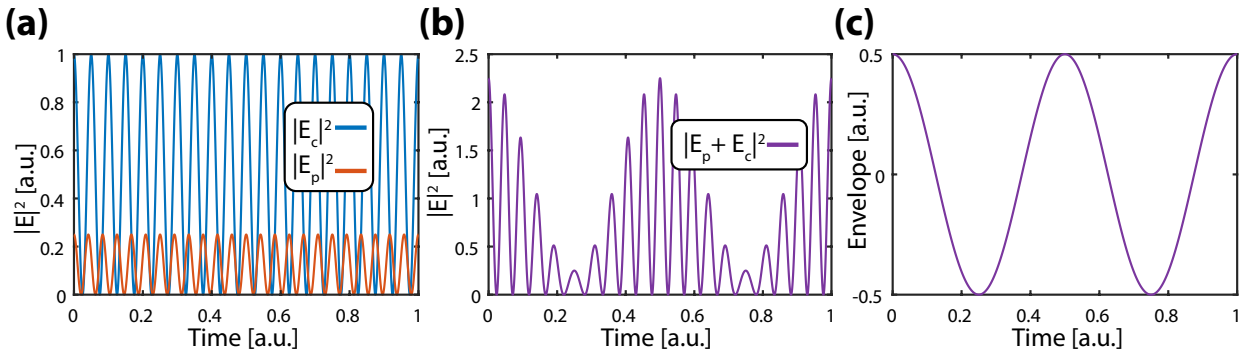

Figure 4.2: (a) Electric field squared for two electromagnetic waves oscillating at slightly different frequencies. Here we take $|E_\mathrm{c}| \gg |E_\mathrm{p}|$ (b) Temporal interference pattern formed by the interference of E_c and E_p. (c) Slowly varying envelope formed by the interference of E_c and E_p.

Suppose we drive the system with a strong, monochromatic laser drive with amplitude α at frequency ω_c. We can gain an understanding of our system by investigating how this strong control interferes with a weak, monochromatic probe laser with amplitude a and frequency ω_p. In a classical setting, the electric fields of these two beams would have a time dependence of the form $E_\mathrm{c}(t) = \mathcal{E}_\mathrm{c}\cos(\omega_\mathrm{c}t + \phi_\mathrm{c})$ and $E_\mathrm{p}(t) = \mathcal{E}_\mathrm{p}\cos(\omega_\mathrm{p}t)$. If we ignore interference effects, the energy in the electric field of the control will be proportional to $|E_\mathrm{c}|^2 = |\mathcal{E}_\mathrm{c}|^2(1-\cos(2\omega_\mathrm{c}t + 2\phi_\mathrm{c})/2$, and the energy in the electric field of the probe will be proportional to $|E_\mathrm{p}|^2 = |\mathcal{E}_\mathrm{p}|^2(1-\cos(2\omega_\mathrm{p}t)/2$, as plotted in Fig. 4.2(a). In this case, when we

average over the fast oscillations, the energy of each laser is constant, and creates a constant radiation pressure force in the cavity. Furthermore, because the probe amplitude is very small, the radiation pressure force generated by this beam will be negligibly small.

This situation changes if we permit the control and probe laser to interfere, and we accrue an additional term $|E_{\mathrm{p}}||E_{\mathrm{c}}|\left(\cos((\omega_{\mathrm{c}}-\omega_{\mathrm{p}})t+\phi_{\mathrm{c}})+\cos((\omega_{\mathrm{c}}+\omega_{\mathrm{p}})t+\phi_{\mathrm{c}})\right)$, as shown in Fig. 4.2(b). In this case, the radiation pressure force has a term which is linearly proportional to the amplitude of the probe. Because this is multiplied by the amplitude of the control laser, the strength of this interaction can be greatly enhanced. This interaction term contains a quickly oscillating part, which will average to a constant at optical frequencies, and a slowly oscillating part which cannot be averaged to a constant. This slow term, plotted in Fig. 4.2(c), will oscillate at a frequency determined by the difference between the control and probe. Interestingly, by adjusting the frequency of the control laser, this frequency may be adjusted, or even change sign. This allows one to tune the beats so that they may be near the frequency of the mechanical oscillator. In a similar fashion, the phase of these oscillations can be seen to change depending on the phase of the control, ϕ_{c}. As we shall see, this will allow us to 'customize' the interactions between optics and mechanics in our system, and is the essential feature of linearized optomechanics.

Now that we have a qualitative sense of how a control laser affects an optomechanical system, we are ready to construct a quantitative model. Revisiting Fig. 4.2(c) for a moment, we notice the oscillations present in the plot may become negative, as we have isolated for *fluctuations* in the field about a steady-state value. Interestingly, this also implies that the AC part of the radiation pressure force for may be negative. These are clearly sinusoidal, and may be represented by a harmonic oscillator. Because this harmonic oscillator couples more strongly to the mechanics than the probe, and because it can be made to have similar frequency to the mechanics, this is the term which is important for optomechanical interactions. We isolate for the fluctuations by subtracting the mean amplitude from $\hat{\alpha}(t)$, and

moving into a frame rotating with the control laser using the definitions,

$$\hat{a}(t) = \Big(\hat{\alpha}(t) - \alpha\Big)e^{i\omega_c t}, \tag{4.8}$$

$$\alpha = \langle\hat{\alpha}(t)\rangle, \tag{4.9}$$

where $\hat{a}(t)$ is the operator for the cavity fluctuations, and α is the amplitude of the control laser. Notice that because we are in the rotating frame $\hat{a}(t)$ does not represent the probe laser, but rather the slowly varying fluctuation amplitude. We will also apply the same recipe to the optical inputs with the substitutions,

$$\hat{a}_{\rm in}(t) = \Big(\hat{\alpha}_{\rm in}(t) - \alpha_{\rm in}\Big)e^{i\omega_c t}, \tag{4.10}$$

$$\alpha_{\rm in} = \langle\hat{\alpha}_{\rm in}(t)\rangle. \tag{4.11}$$

Note that these substitutions explicitly preserve the canonical commutation relations for the cavity operators because $\left[\hat{\alpha}_{\rm in}(t), \hat{\alpha}^\dagger_{\rm in}(t)\right] = \left[\hat{a}(t), \hat{a}^\dagger(t)\right] = 1$, and for the input operators because $\left[\hat{\alpha}(t), \hat{\alpha}^\dagger(t)\right] = \left[\hat{a}(t), \hat{a}^\dagger(t)\right] = 1$.

Placing these assumptions into Eqs. 4.6-4.7, and dropping the explicit dependence on time in our notation for the operators, we find,

$$\dot{\hat{a}} = \left(i\Delta - \frac{\kappa}{2}\right)(\alpha + \hat{a}) + ig_0(\alpha + \hat{a})\left(\hat{b} + \hat{b}^\dagger\right) + \sqrt{\kappa_{\rm ex}}(\alpha_{\rm in} + \hat{a}_{\rm in}) + \sqrt{\kappa_0}\hat{f}_{\rm in}, \tag{4.12}$$

$$\dot{\hat{b}} = -\left(i\omega_{\rm m} + \frac{\gamma}{2}\right)\hat{b} + ig_0\left(|\alpha|^2 + \alpha^*\hat{a} + \alpha\hat{a}^\dagger + \hat{a}^\dagger\hat{a}\right) + \sqrt{\gamma}\hat{b}_{\rm in}, \tag{4.13}$$

where $\Delta = \omega_c - \omega_o$ is the control-cavity detuning. For weak coupling, $g < \kappa/2$, we can assume that the control is undepleted by optomechanical interactions, and solve for the case $g_0 \to 0$. This gives the solution,

$$\alpha = \frac{\sqrt{\kappa_{\rm ex}}\alpha_{\rm in}}{-i\Delta + \kappa/2}. \tag{4.14}$$

The solution for the control can then be inserted back into Eqs. 4.12-4.13. We use the fact that $|\alpha| \gg \langle \hat{a} \rangle$ to neglect the coupling term $ig_{\rm o}\hat{a}\left(\hat{b}+\hat{b}^\dagger\right)$ in Eq. 4.12, and make a similar assumption in Eq. 4.13 to neglect the weak term $ig_{\rm o}\hat{a}^\dagger\hat{a}$. Lastly, we eliminate $ig_{\rm o}|\alpha|^2$ by redefining the zero-point of our mechanics. Under these assumptions, we can now write the linearized equations of motion for a canonical cavity optomechanical system,

$$\boxed{\begin{aligned}\dot{\hat{a}} &= \left(i\Delta - \frac{\kappa}{2}\right)\hat{a} + i\left(g^*\hat{b} + g\hat{b}^\dagger\right) + \sqrt{\kappa_{\rm ex}}\hat{a}_{\rm in} + \sqrt{\kappa_0}\hat{f}_{\rm in}, \qquad (4.15)\\ \dot{\hat{b}} &= -\left(i\omega_{\rm m} + \frac{\gamma}{2}\right)\hat{b} + i\alpha\left(g^*\hat{a} + g\hat{a}^\dagger\right) + \sqrt{\gamma}\hat{b}_{\rm in}, \qquad (4.16)\end{aligned}}$$

where we have introduced the enhanced optomechanical coupling rate $g = g_0\alpha$.

The linearized equations can be used to derive a number of physical effects. To prepare for this, we take the Fourier transform of Eqs. 4.15-4.16 to find the equations of motion in frequency space,

$$\hat{a}(\omega) = \frac{ig\left(\hat{b}(\omega) + \hat{b}^\dagger(\omega)\right) + \sqrt{\kappa_{\rm ex}}\hat{a}_{\rm in}(\omega) + \sqrt{\kappa_0}\hat{f}_{\rm in}(\omega)}{-i(\Delta+\omega) + \frac{\kappa}{2}}, \qquad (4.17)$$

$$\hat{b}(\omega) = \frac{ig\left(\hat{a}(\omega) + \hat{a}^\dagger(\omega)\right) + \sqrt{\gamma}\hat{b}_{\rm in}(\omega)}{-i(-\omega_{\rm m}+\omega) + \frac{\gamma}{2}}. \qquad (4.18)$$

It can be clearly seen from these two expressions that the optics and mechanics are linearly coupled, but at the moment the consequences of this coupling are probably not apparent. Depending on the sort of physical effects we are interested in, we may wish to solve for the optics or for the mechanics. In the next two sections we shall do each in turn, and see what emerges. Note that in what follows we will not explicitly write out the frequency dependence of various operators in order to keep the notation uncluttered.

4.1.2 Mechanical Effects: Spring Effect and Damping

First, we solve for the mechanics by substituting Eq. 4.15 into Eq. 4.16,

$$\left(i\left(\omega_{\rm m}-\omega\right)+\frac{\gamma}{2}\right)\hat{b} = -\frac{|g|^2(\hat{b}+\hat{b}^\dagger)-ig\sqrt{\kappa_{\rm ex}}\hat{a}_{\rm in}-ig\sqrt{\kappa_0}\hat{f}_{\rm in}}{-i(\Delta+\omega)+\frac{\kappa}{2}} + \frac{|g|^2(\hat{b}+\hat{b}^\dagger)-ig\sqrt{\kappa_{\rm ex}}\hat{a}^\dagger_{\rm in}-g\sqrt{\kappa_0}\hat{f}^\dagger_{\rm in}}{i(\Delta-\omega)+\frac{\kappa}{2}}+\sqrt{\gamma}\hat{b}_{\rm in}. \tag{4.19}$$

Note that in the above we have been careful to apply the correct sign to all terms involving a factor of "$i\omega$", keeping in mind that they were generated by Fourier transforming a time derivative. Under the rotating wave approximation, we can discard all $\hat{b}^\dagger$ terms, as they will oscillate at $2\omega_{\rm m}$ in a frame rotating with $\hat{b}$. Next, we assume weak coupling ($g<\kappa/2$), and that $\gamma \ll \kappa$. This assures us that the mechanical system only samples a very small section of the optical response, centred about the mechanical frequency. In this case we can take $\omega \to \omega_{\rm m}$ in the terms on the right hand side of Eq. 4.19 [2].

After applying the above assumptions, we inverse Fourier transform to recover the equation of motion for the mechanics in the time domain,

$$\dot{\hat{b}} = -\left(i\omega_{\rm m}-\frac{\gamma}{2}\right)\hat{b}+\sqrt{\gamma}\hat{b}_{\rm in}-\frac{i(\Delta+\omega_{\rm m})+\kappa/2}{(\Delta+\omega_{\rm m})^2+\kappa^2/4}\left(|g|^2\hat{b}-ig\sqrt{\kappa_{\rm ex}}\hat{a}_{\rm in}-ig\sqrt{\kappa_0}\hat{f}_{\rm in}\right) - \frac{i(\Delta-\omega_{\rm m})-\kappa/2}{(\Delta-\omega_{\rm m})^2+\kappa^2/4}\left(|g|^2\hat{b}-ig\sqrt{\kappa_{\rm ex}}\hat{a}^\dagger_{\rm in}-ig\sqrt{\kappa_0}\hat{f}^\dagger_{\rm in}\right). \tag{4.20}$$

In this expression, we see that in addition to the usual terms for a damped harmonic oscillator in the first line, there are also complex terms proportional to $\hat{b}$ and the optical inputs. The self terms, proportional to $\hat{b}$, are of particular interest. The real parts of the self terms will either work with or against the motion of the mechanics contingent on if they are in-phase or out of phase with the oscillation of $\hat{b}$. This will contribute to damping or anti-damping. On the other hand, purely imaginary terms that are $\pm\pi/2$ out of phase with the mechanics, will contribute to positive or negative frequency shifts. The terms associated with the optical

[2] As an alternative, we could assume that $\hat{a}_{\rm in}$ is strictly monochomatic.

inputs can act as a noisy drive to the mechanics, particularly at microwave frequencies where the thermal occupation of the mechanics can be large. At optical frequencies however, these inputs can be taken to be vacuum. Even so, as we will see in some of the following sections, they can cause additional noise in the mechanics. For large classical signals however, these will not be significant.

Grouping real and imaginary terms together, and taking the expectation value of the operators $b = \langle \hat{b} \rangle$, $b_{\rm in} = \langle \hat{b}_{\rm in} \rangle$, we find equations describing the optomechanical spring effect ($\delta\omega_{\rm m}$) and optomechanical damping ($\gamma_{\rm opt}$) [87],

$$\boxed{\begin{aligned} \dot{b} =& -\left(i\omega_{\rm m} + i\delta\omega_{\rm m} + \frac{\gamma}{2} + \frac{\gamma_{\rm opt}}{2}\right) b + \sqrt{\gamma} b_{\rm in}, && (4.21) \\ \delta\omega_{\rm m} =& |g|^2 \left(\frac{\Delta + \omega_{\rm m}}{(\Delta + \omega_{\rm m})^2 + \kappa^2/4} + \frac{\Delta - \omega_{\rm m}}{(\Delta - \omega_{\rm m})^2 + \kappa^2/4}\right), && (4.22) \\ \gamma_{\rm opt} =& |g|^2 \left(\frac{\kappa/2}{(\Delta + \omega_{\rm m})^2 + \kappa^2/4} - \frac{\kappa/2}{(\Delta - \omega_{\rm m})^2 + \kappa^2/4}\right). && (4.23) \end{aligned}}$$

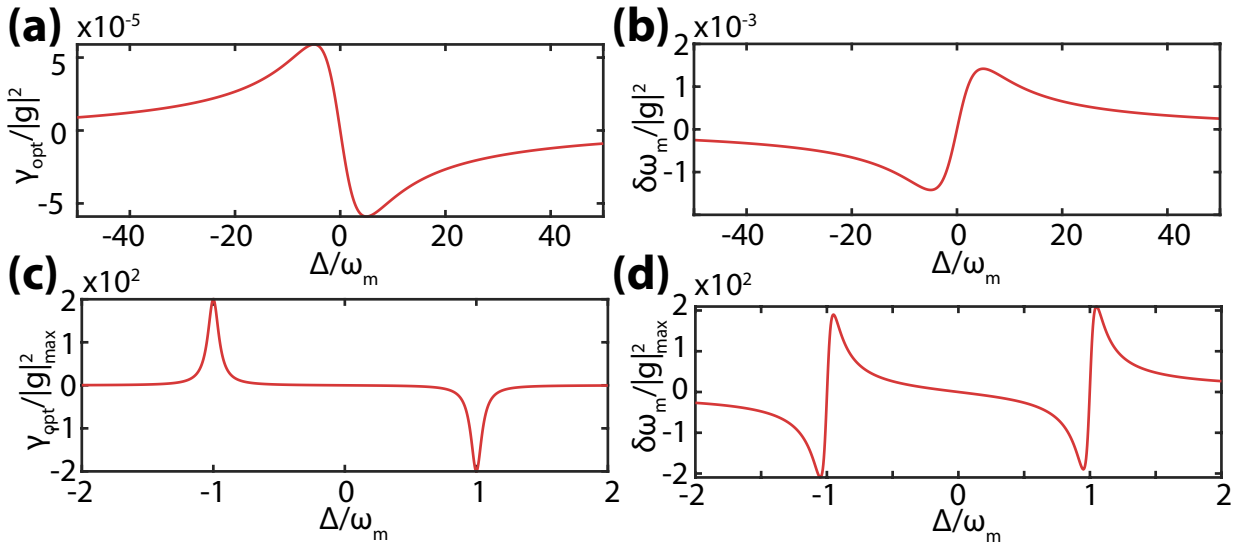

Figure 4.3: Optomechanical damping (a) and spring effect (b) as a function of laser detuning, for the case of a sideband unresolved system. Here we have set $\kappa/\omega_{\rm m} = 10$. Optomechanical damping (c) and spring effect (d) as a function of laser detuning, for the case of a sideband resolved system. Here we have chosen $\omega_{\rm m}/\kappa = 10$.

Both the optical spring effect and damping are plotted on Fig. 4.3, for cases when the system is sideband unresolved ($\omega_{\rm m} < \kappa/2$), and sideband resolved ($\omega_{\rm m} > \kappa/2$). Interestingly we see that the behaviour in each of these two operating regimes is quite different. In the case of sideband unresolved systems, the point of maximum damping and antidamping occur at $\Delta = -\kappa/2$ and $\Delta = \kappa/2$, respectively, and essentially follows the derivative of the cavity lineshape with respect to detuning. In contrast to this, for sideband resolved systems maximum damping and antidamping occur at $\Delta = -\omega_{\rm m}$ and $\Delta = \omega_{\rm m}$. In this case the two terms in the brackets of Eq. 4.23 have almost no overlap as a function of Δ.

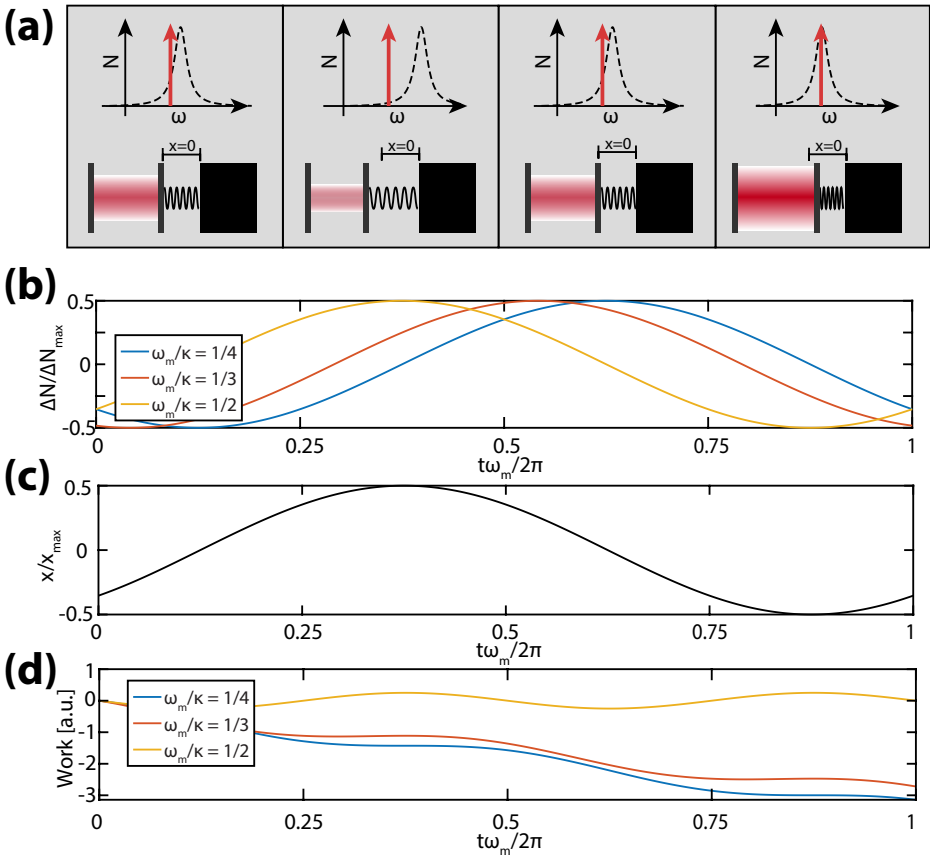

Figure 4.4: Toy model of optomechanical cooling in the sideband unresolved regime. (a) Snapshots of the cavity-control laser detuning and the mechanical displacement. (b) Change in the photon number in the cavity from equilibrium, corresponding to the snapshots in (a). This is plotted for three different degrees of sideband resolvedness. (c) Mechanical displacement, corresponding to the snapshots in (a). (d) Work done on the system, which becomes negative after one cycle, indicating cooling. This is plotted for three different degrees of sideband resolvedness.

The fact that the optimal detuning for optomechanical damping is contingent upon the detuning of the control laser hints that there are different mechanisms underlying each process. In the case of unresolved systems, the cooling mechanism may be understood by the toy model on Fig. 4.4. Here the cooling process is understood as a feedback mechanism in the time domain, which may be broken up into four steps. Displacement of the mechanical

oscillator will induce a change in the cavity frequency, which causes a change in the number of photons in the cavity, and consequently the backaction force. Crucially, this change does noise happen instantaneously, but has a phase lag associated with it which is set by the detuning and the cavity linewidth. At the end of one mechanical oscillation the total work done by the radiation pressure force on the mechanics is negative, indicating cooling of the mechanical mode.

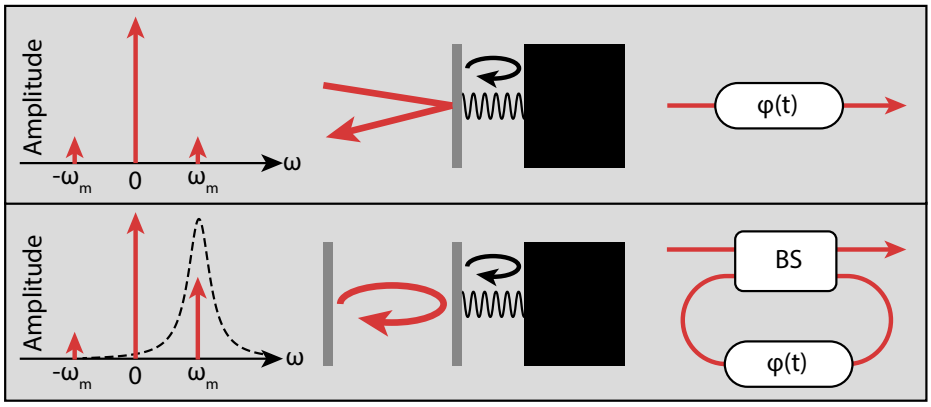

Figure 4.5: Toy model of optomechanical cooling in a scattering picture. In the upper panels, a simple optomechanical system is shown. The upper-left panel shows a control laser and two sidebands generated by mechanical modulation as illustrated in the upper-middle panel. Altogether this system acts like a phase modulator, as illustrated on the upper-right panel. The lower panels illustrate a similar system, but with the inclusion of an optical cavity. This leads to an asymmetry in the scattering of the control laser, an ultimately optomechanical cooling of the mechanical mode.

Eventually, as the system becomes more sideband resolved the population in the cavity will not be able to keep up with mechanical oscillations. In this case, the picture shown on Fig. 4.5 is more appropriate. Initially we consider a simple system consisting of a single mirror affixed to a spring. As this spring oscillates at ω_{m}, it will phase modulate the reflected beam. In the frequency domain, the phase modulation will generate two sidebands at $\pm\omega_{\mathrm{m}}$ in a frame rotating with the laser. These are called the Stokes and anti-Stokes scattering

terms. If a second mirror is added to this system, we recover the dynamics of a cavity optomechanical system. Depending on the location of the cavity, either the Stokes or the anti-Stokes terms will be enhanced. This induces a picture quite similar to that shown on Fig. 4.2, where a time-modulated backaction force will be created which either opposes, or supports the motion of the mechanical element. One can also arrive to the same conclusion through energy conservation arguments. If photons are primarily scattered to a higher frequency, then they will necessarily carry away energy from the mechanics as the exit the cavity. Conversely if they are primarily scatted to a lower frequency, then they will donate energy to the mechanics.

4.1.3 Optical Effects: OMIT and OMIA

Having described the effect of the optics on the mechanics, we are now ready to calculate in the effect of mechanics on the optics. This time, we substitute Eq. 4.16 into Eq. 4.15 to find,

$$\left(-i(\Delta+\omega)+\frac{\kappa}{2}\right)\hat{a} = -\frac{|g|^2\left(\hat{a}+\hat{a}^\dagger-ig\sqrt{\gamma}\hat{b}_{\rm in}\right)}{i(\omega_{\rm m}-\omega)+\frac{\gamma}{2}}+\frac{|g|^2\left(\hat{a}+\hat{a}^\dagger-ig\sqrt{\gamma}\hat{b}^\dagger_{\rm in}\right)}{-i(\omega_{\rm m}+\omega)+\frac{\gamma}{2}} + \sqrt{\kappa_{\rm ex}}\hat{a}_{\rm in}+\sqrt{\kappa_0}\hat{f}_{\rm in}. \tag{4.24}$$

Echoing our strategy in the previous section we will discard $\hat{a}^\dagger$ terms under the rotating wave approximation. This allows us to isolate a rather complicated expression for the optics,

$$\hat{a} = \left(-i(\Delta+\omega)+\frac{\kappa}{2}+\frac{|g|^2}{i(\omega_{\rm m}-\omega)+\frac{\gamma}{2}}-\frac{|g|^2}{-i(\omega_{\rm m}+\omega)+\frac{\gamma}{2}}\right)^{-1} \times\left(\sqrt{\kappa_{\rm ex}}\hat{a}_{\rm in}+\sqrt{\kappa_0}\hat{f}_{\rm in}+\frac{ig\sqrt{\gamma}\hat{b}_{\rm in}}{i(\omega_{\rm m}-\omega)+\frac{\gamma}{2}}-\frac{ig\sqrt{\gamma}\hat{b}^\dagger_{\rm in}}{-i(\omega_{\rm m}+\omega)+\frac{\gamma}{2}}\right). \tag{4.25}$$

This expression in undeniably unwieldy, but contains a number of interesting and important physical effects. To help understand this expression, we will examine it in parts. After building an intuition, we will be in a better position to understand the entire expression. As a sanity check, notice that if we set $g \to 0$, we recover the expression for the bare optical cavity.

OMIT

Optomechanically induced transparency (OMIT) [88–90], is a phenomena where a transparency window is opened in an optical cavity through optomechanical means. A well coupled cavity will not permit the transmission of light when driven on resonance, but rather reflect the incident light. Therefore, if a window is opened at the cavity resonance, the cavity may be considered to be "transparent" in this region. This transparency is achieved through the application of a strong control laser red detuned from the cavity by the mechanical frequency ($\Delta = -\omega_{\mathrm{m}}$). OMIT is important, as it demonstrates that the interaction between optics and mechanics is coherent.

Starting with Eq. 4.25, we insert this detuning. Assuming the system is sideband resolved ($\omega_{\mathrm{m}} > \kappa$), we can neglect the $|g|^2/(-i(\omega_{\mathrm{m}}+\omega)+\gamma/2)$ term. For the sake of simplicity, we will work with classical amplitudes, and also neglect the thermal occupation of the mechanics by setting the mechanical input terms to zero. With all of these assumptions in place, we uncover the expression,

$$\boxed{a = \frac{\sqrt{\kappa_{\mathrm{ex}}} a_{\mathrm{in}}}{i(\omega_{\mathrm{m}} - \omega) + \frac{\kappa}{2} + \frac{|g|^2}{i(\omega_{\mathrm{m}} - \omega) + \frac{\gamma}{2}}}.} \tag{4.26}$$

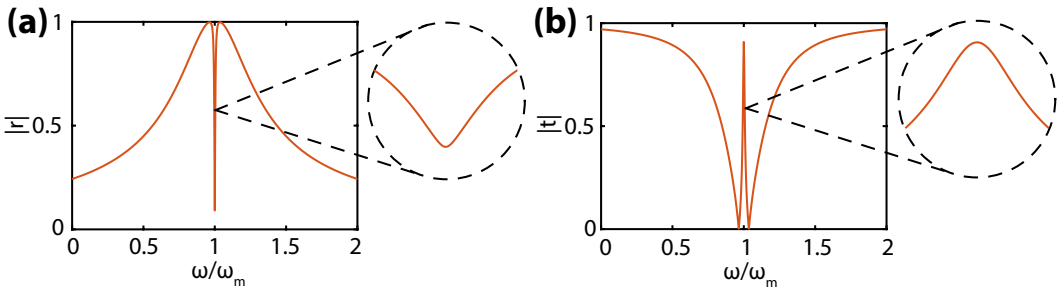

Figure 4.6: (a) Reflection amplitude for OMIT with $\omega/\kappa = 2$ and $C = 10$. (b) Transmission amplitude for the same parameters as (a).

The degree of transparency is parametrized by the ratio of optomechanical scattering over the mechanical damping rate, known as the cooperativity $C = \frac{4|g|^2}{\kappa\gamma}$, and is plotted in Fig. 4.6. In practice, one measures OMIT by measuring the transmission or reflection of a probe laser as it is scanned across the optical cavity.

OMIA

One can attain the opposite effect, known as optomechanically induced absorption (OMIA) and optomechanically induced amplification by instead using a blue-detuned control laser $\Delta = \omega_{\mathrm{m}}$ [89, 90]. In this case we can neglect the $|g|^2/(i(\omega_{\mathrm{m}} - \omega) + \gamma/2)$ term in Eq. 4.25, to find,

$$\boxed{a = \frac{\sqrt{\kappa_{\mathrm{ex}}}a_{\mathrm{in}}}{-i(\omega_{\mathrm{m}} + \omega) + \frac{\kappa}{2} - \frac{|g|^2}{-i(\omega_{\mathrm{m}}+\omega)+\frac{\gamma}{2}}}.} \tag{4.27}$$

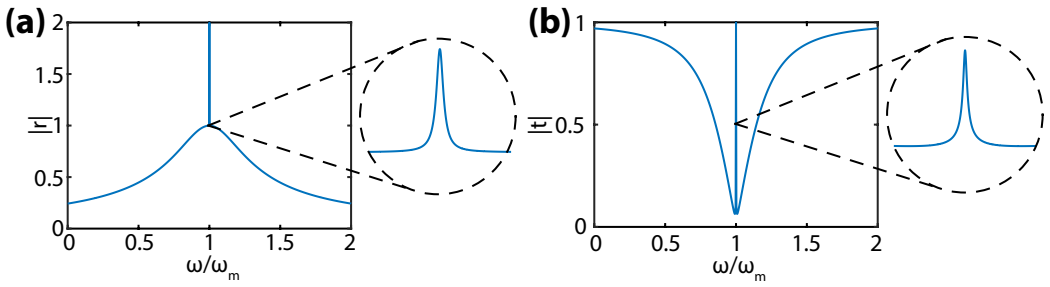

Figure 4.7: (a) Reflection amplitude for OMIA with $\omega/\kappa = 2$ and $C = 10$. Note that the reflection coefficient is greater than unity, indicating an optical gain. (b) Transmission amplitude for the same parameters as (a).

The response in this situation is plotted on Fig. 4.6 for the case of amplification. Note that in the case of amplification $C > 1$, both the transmission and reflection will be positive spikes at $\omega = \omega_{\mathrm{m}}$. However in the absorption regime, $C < 1$, the transmission will have a dip at $\omega = 0$. Note that is is possible to have a transmission or reflection exceeding unity, indicating an optical gain, where energy is extracted from the control laser.

Mechanical Transduction

Perhaps the most obvious, practical, and useful application of cavity optomechanics is the fact that it can act as a very sensitive tool to measure mechanical displacement. Motion of the mechanics will induce a change in the properties of the outgoing cavity light, which can then be measured by an external source. This is particularly useful because mechanical systems can be very easily engineered to couple to other degrees of freedom. For example mechanical motion can drive a capacitor in an electric circuit, or if magnetic material is deposited on the mechanical element, it can act as a magnetometer. Mechanical motion can even be used to couple several different optomechanical systems together.

To describe the cavity field, we once again use Eq. 4.25. This time we will initially look only at cases where the mechanics is not strongly affected by the optics. To do this we note that the optical spring and damping terms were $\mathcal{O}(g^2)$, whereas transduction of the

mechanics to the optics is only $\mathcal{O}(g)$. This gives us the solution,

$$\begin{aligned}\hat{a} &= \frac{1}{-i(\Delta+\omega)+\frac{\kappa}{2}}\left(\frac{ig\sqrt{\gamma}\hat{b}_{\mathrm{in}}}{i(\omega_{\mathrm{m}}-\omega)+\frac{\gamma}{2}}-\frac{ig\sqrt{\gamma}\hat{b}_{\mathrm{in}}^{\dagger}}{-i(\omega_{\mathrm{m}}+\omega)+\frac{\gamma}{2}}\right),\\ &= \frac{ig}{-i(\Delta+\omega)+\frac{\kappa}{2}}\left(\hat{b}+\hat{b}^{\dagger}\right),\\ &= \frac{ig}{-i(\Delta+\omega)+\frac{\kappa}{2}}\left(\frac{\hat{x}}{x_0}\right).\end{aligned} \tag{4.28}$$

From the last line of the equation, we can see that the output is related to the operator for the mechanical displacement. From the first term, however, we can see that terms associated with $\hat{b}$ or $\hat{b}^{\dagger}$ are preferentially selected depending on the detuning between the control laser and the cavity. We will explore more about this topic in Section 4.2.2, where is is discussed in the context of how one actually goes about measuring the output of the mechanical cavity.

Noise Squashing, and Limitations on Measurement

Now that we have a sense of what sort of optical output we expect for $\mathcal{O}(g)$ interactions, where the mechanics is not strongly perturbed by the optics, we are ready to include $\mathcal{O}(g^2)$ terms. Once again we will initially neglect probe terms, finding,

$$\begin{aligned}\hat{a} =& \left(-i(\Delta+\omega)+\frac{\kappa}{2}+\frac{|g|^2}{i(\omega_{\mathrm{m}}-\omega)+\frac{\gamma}{2}}-\frac{|g|^2}{-i(\omega_{\mathrm{m}}+\omega)+\frac{\gamma}{2}}\right)^{-1}\\ &\times\left(\frac{\hat{a}+ig\sqrt{\gamma}\hat{b}_{\mathrm{in}}}{i(\omega_{\mathrm{m}}-\omega)+\frac{\gamma}{2}}-\frac{\hat{a}^{\dagger}+ig\sqrt{\gamma}\hat{b}_{\mathrm{in}}^{\dagger}}{-i(\omega_{\mathrm{m}}+\omega)+\frac{\gamma}{2}}\right),\\ \approx&\frac{1}{-i(\Delta+\omega)+\frac{\kappa}{2}}\left(\frac{ig\sqrt{\gamma}\hat{b}_{\mathrm{in}}}{i(\omega_{\mathrm{m}}+\delta\omega_{\mathrm{m}}-\omega)+\frac{\gamma+\gamma_{\mathrm{opt}}}{2}}-\frac{ig\sqrt{\gamma}\hat{b}_{\mathrm{in}}^{\dagger}}{-i(\omega_{\mathrm{m}}+\delta\omega_{\mathrm{m}}+\omega)+\frac{\gamma+\gamma_{\mathrm{opt}}}{2}}\right).\end{aligned} \tag{4.29}$$

In the first line, we have what *looks* like an equation for the unperturbed mechanics, filtered by either an OMIT line shape for the case $\Delta=-\omega_{\mathrm{m}}$ or an OMIA line shape for the case $\Delta=\omega_{\mathrm{m}}$. However, by solving for the mechanics more directly one can see that in fact the mechanics itself is actually being damped or anti-damped at these detunings.

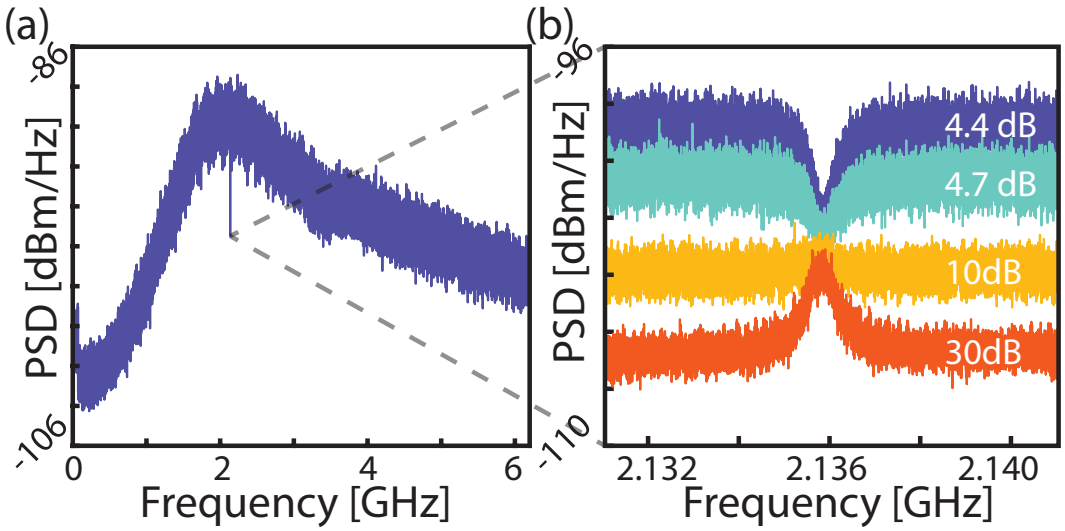

Figure 4.8: (a) Broadband reflection measurement for OMIT with a noisy probe input. (b) Zoom-in of the transparency window for various powers of the broadband probe laser. Broadband reflection measurement for OMIT with a noisy probe input. (b) Zoom-in of the transparency window for various powers of the broadband probe laser. For low probe powers, incoherent scattering from the control laser dominates the signal, resulting narrow peak. For higher probe powers coherent scattering processes will dominate, resulting in the usual OMIT dip.

A natural question to ask at this point is what happens when we retain all of the terms in Eq. 4.25. In this case we see that the optical output will be a combination of and OMIT or OMIA process, along with a transduction term which will leave a signature of the perturbed mechanics on the optics. One can directly measure this by injecting a broadband probe signal into an optical cavity with control laser strong enough that $\mathcal{O}(g^2)$ terms are relevant. Data acquired with detuning $\Delta = -\omega_{\mathrm{m}}$ is shown on Fig. 4.8. In Fig. 4.8(a), we show a broadband probe reflection signal, where the broad peak is the cavity reflection, and the dip at 2.136 GHz is the OMIT transparency window. In Fig. 4.8(b) we explore in competition between

the mechanical signal, and the OMIT signal by increasing probe power. From this we can see that at low probe powers one attains something similar to the damped mechanical signal, whereas for high probe powers we have OMIT.

While this competition might seem unimportant, it becomes an issue if the control laser used in the experiment has significant phase noise. In this case, we also have probe photons. This can lead to a skew in the Stokes and anti-Stokes scattering as measured by the optical output. This effect is known as noise squashing, and is a significant issue in thermometry experiments [91, 92]. Note that even with a perfect laser, there will always be fluctuations present due to the vacuum input.

4.2 Spectrums and Retrospection

In the previous two sections we were able to make significant progress by making assumptions about how optomechanical coupling would perturb the equations of motion for the optics and the mechanics. This eventually enabled us to derive Eqs. 4.15-4.16, from which we were able to predict a number of useful effects that one can achieve with the canonical optomechanical system. However, as was evident by the end of this section, taking the obvious approach resulted in expressions which we sometimes very unwieldy. In this section we will address these shortcomings by approaching the problem from a different perspective. We will use the intuition we built in our previous approach to help us approach certain problems in a more direct manner.

4.2.1 The Interaction Hamiltonian

Starting with the Hamiltonian given in Eq. 4.3, we would like to include additional terms which directly give us the linearized equations of motion, Eqs. 4.15-4.16. This is achieved by the expansion given in Eq. 4.4, and the subsequent linearization of the equations through the substitutions $\hat{\alpha} \rightarrow \alpha + \hat{a}$ and $\hat{\alpha}_{\text{in}} \rightarrow \alpha_{\text{in}} + \hat{a}_{\text{in}}$ [70]. Note this can be seen as a transformation by

the unitary displacement operator $\hat{D}(\alpha) = e^{(\alpha\hat{a} - \alpha^*\hat{a}^\dagger)}$. We also move into a frame rotating with the control laser using the unitary $\hat{U}_{\hat{\alpha}} = e^{i\omega_c \hat{a}^\dagger \hat{a} t}$, and the usual interaction picture transformation of the Hamiltonian $\hat{H}_{\rm new} = \hat{U}\left(\hat{H}_{\rm old} - i\hbar\frac{\partial}{\partial t}\right)\hat{U}^\dagger$. These transformations serve the same purpose as before, allowing us to clearly isolate for the fluctuation terms in the cavity.

In the interest of cleaning up notation, we reorganize the total Hamiltonian as the sum of a steady state and an interaction Hamiltonian $\hat{H} = \hat{H}_0 + \hat{H}_{\rm int}$, where,

$$\boxed{\begin{aligned} \hat{H}_0 &= -\hbar\Delta\hat{a}^\dagger\hat{a} + \omega_{\rm m}\hat{b}^\dagger\hat{b}, \qquad (4.30)\\ \hat{H}_{\rm int} &= -\hbar g\left(\hat{a} + \hat{a}^\dagger\right)\left(\hat{b} + \hat{b}^\dagger\right). \qquad (4.31)\end{aligned}}$$

The linearized optomechanical Hamiltonian given in Eq. 4.31 may be used directly to to derive all of the expressions found in the previous sections. However, for sideband resolved systems ($\omega_{\rm m} > \kappa$), additional assumptions are often made at this point to build intuition. For this, we move into an interaction picture using $\hat{U} = e^{i\hat{H}_0 t/\hbar} = e^{-i(\Delta\hat{a}^\dagger\hat{a} - \omega_{\rm m}\hat{b}^\dagger\hat{b})t}$. The interaction Hamiltonian now reads,

$$\hat{H}_{\rm int} = -g\left(\hat{a}e^{i\Delta t} + \hat{a}^\dagger e^{-i\Delta t}\right)\left(\hat{b}e^{-i\omega_{\rm m} t} + \hat{b}^\dagger e^{i\omega_{\rm m} t}\right). \qquad (4.32)$$

This expression will be simplified for red detunings ($\Delta \approx -\omega_{\rm m}$), where we will have two slowly rotating terms which contribute and two which can be set to zero under the rotating wave approximation. Moving out of the interaction picture, we are left with a beamsplitter-type Hamiltonian,

$$\boxed{\hat{H}_{\rm int}^{\rm red} = -\hbar g\left(\hat{a}\hat{b}^\dagger + \hat{a}^\dagger\hat{b}\right).} \qquad (4.33)$$

This indicates that for a red-detuned control laser, we may exchange photons and phonons through an optomechanical interaction. It is important to recall there that $\hat{a}$ represents optical fluctuations. So when we say that a photon is 'annihilated' we mean that it has

been frequency down-shifted into the control laser, and when we say a photon has been 'created', we mean that a photon from the control laser has been up-shifted into the cavity. This Hamiltonian is indispensable whenever we wish to coherently exchange energy, for such applications as memories, wavelength conversion [78–80, 93, 94], OMIT [88–90], and ground state cooling of the mechanical mode [76, 77].

The interaction will take on a different flavour for blue detunings ($\Delta \approx \omega_{\mathrm{m}}$). In this case the surviving terms will form a two mode squeezing Hamiltonian,

$$\boxed{\hat{H}_{\mathrm{int}}^{\mathrm{blue}} = -\hbar g \left(\hat{a}\hat{b} + \hat{a}^{\dagger}\hat{b}^{\dagger}\right).} \tag{4.34}$$

This Hamiltonian will either create or annihilate photons and phonons together, which generates correlation between the optics and the mechanics. This Hamiltonian is useful for such applications such as squeezing [82, 83], entanglement [85, 95], heralded single phonon generation [96], and amplification [94, 97].

4.2.2 Measuring Mechanical Motion, and the Standard Quantum Limit

In this section we will take a step aside, and review our previous results from a slightly different perspective. While all of these results *can* be derived by continuation of our previous arguments, they will have a particularly nice interpretation in terms of the spectrums introduced here.

Our ultimate goal in this section is to explain how one would go about measuring the motion of a mechanical oscillator in the most sensitive way possible, and to discover what the ultimate limits of such a measurement would be. The basic idea is that fluctuation of the position of the mechanical oscillator will modulate the frequency of the optical cavity, which induces phase shifts in the light output from the cavity. These phase fluctuations can be converted into amplitude fluctuations through interference with a local oscillator in

a homodyne measurement. These oscillations are then measured on a photodetector, whose electrical output signal is sent to an RSA (real time spectrum analyzer). The RSA is set to measure a quantity called the power spectral density, which gives a signal containing information about the mechanical oscillator.

Classical Noise (and Sensing)

In order to understand this measurement, it helps to quickly review the operation of spectrum analyzers. For concreteness, suppose that the RSA measures a time varying voltage signal $v(t)$ for some length of time, T. We would like to define a corresponding operator in frequency space for this time interval, but must take into account that the finite duration of the measurement limits the range of frequencies that we can measure. Accordingly, we window the Fourier transform $v(\omega) = \frac{1}{\sqrt{T}} \int_0^T e^{i\omega t} v(t) dt$. This allows us to define the spectral density as $S(\omega) = \lim_{T\to\infty} \langle |v(\omega)|^2 \rangle$, where we have averaged over several independent acquisition events. Note that our spectral density needs to be divided by the impedance of the RSA, (nominally $50\,\Omega$ for most high speed electronics) in order to represent power per unit frequency. In literature [98] this factor is not normally included in order to keep the notation clean, so we will also neglect it here.

Another, seemingly unrelated way to characterize our signal is the correlation function $G_{vv}(t, t') = \langle v(t) v(t') \rangle$. For a stationary process, we can write this with the shorthand notation $G_{vv}(t) = \langle v(t) v(0) \rangle$. Suprisingly, it can be shown that is related to the spectral density by the Wiener-Khinchin theorem (see Appendix C.2.1),

$$S_{vv}(\omega) = \frac{1}{\sqrt{2\pi}} \int_{-\infty}^{\infty} e^{i\omega t} G_{vv}(t) dt, \tag{4.35}$$

$$G_{vv}(t) = \frac{1}{\sqrt{2\pi}} \int_{-\infty}^{\infty} e^{-i\omega t} S_{vv}(\omega) dt. \tag{4.36}$$

Interestingly, this indicates that the spectral density not only gives us a measure of the average power at a given frequency, but also gives an indication of correlations present in the noise. This is an invaluable tool for making sense of noisy signals. If the correlation time of signal is short, the spectral density will be very broad; and if the correlations are long, then the spectral density will be quite localized.

Now that we have an idea of how the RSA acquires a signal, let us try and relate this signal to the mechanical motion in the simplest possible case. The voltage we measure on the photodetector will be linearly proportional to the mechanical motion and the power of the control laser. We denote the constant of proportionality as the transduction coefficient K. In addition to this there will be other random sources of noise such as the detector electronics, which we denote as v^{tech} for "technical noise". Altogether this gives us the simple relation: $v(t) = K|\alpha|^2 x(t) + v^{\text{tech}}(t)$. Using the Wiener-Khinchin theorem in Eq. 4.35 to relate this to correlations, we find,

$$\begin{aligned} S_{vv}(\omega) &= \int_{-\infty}^{\infty} e^{i\omega t} \langle v(t) v(0) \rangle d\omega \\ &= \int_{-\infty}^{\infty} e^{i\omega t} \langle \Big(K|\alpha|^2 x(t) + \eta(t) \Big) \Big(K|\alpha|^2 x(0) + \eta(0) \Big) \rangle d\omega, \\ &\approx K^2 \left|\alpha\right|^4 S_{xx}(\omega) + S_{vv}^{\text{tech}}(\omega). \end{aligned} \tag{4.37}$$

In the last line we have made the key assumption that the signal from the mechanics and the technical noise are uncorrelated, such that the cross correlation terms will average out for sufficiently long acquisition time. The signal we see on the RSA then has two distinct contributions, one from the mechanics, and one from the technical noise. If the technical noise has a very small correlation time, then it will form a very wide floor in frequency space. This allows us to subtract away the noise floor, and isolate the signal from the mechanics.

Suppose that we integrate the area under of the curve of the mechanical signal. This gives,

$$\begin{aligned}
\int_{-\infty}^{\infty} S_{vv}(\omega)d\omega &= K^2 \left|\alpha\right|^4 \int_{-\infty}^{\infty} S_{xx}(\omega)d\omega, \\
&= K^2 \left|\alpha\right|^4 \int_{-\infty}^{\infty}\int_{-\infty}^{\infty} e^{i\omega t}\langle x(t)x(0)\rangle dt d\omega, \\
&= K^2 \left|\alpha\right|^4 \int_{-\infty}^{\infty}\left(\int_{-\infty}^{\infty} e^{i\omega t}\right) d\omega \langle x(t)x(0)\rangle dt, \\
&= K^2 \left|\alpha\right|^4 \int_{-\infty}^{\infty} \delta(t)\langle x(t)x(0)\rangle dt, \\
&= \frac{K^2 \left|\alpha\right|^4}{2\pi}\langle x^2\rangle, \qquad (4.38)
\end{aligned}$$

where we have once again made use of the Wiener-Khinchin theorem. This gives the intriguing result that the area under the curve of the spectral density is proportional to $\langle x^2\rangle$. If the measurements are performed with a sufficiently weak control laser such that optomechanical damping is negligible, then we may safely assume that the mechanics is in thermal equilibrium with the environment. In this case we apply the equipartition theorem, $\frac{1}{2}K_{\mathrm{B}}T = \frac{1}{2}m\langle x^2\rangle$, where K_{B} is Boltzmann's constant and T is the temperature. This means that the area under the curve is proportional to the temperature of the mechanical oscillator.

In the above discussion we neglected to mention how the correlations in the mechanical motion came about. After all, the mechanical oscillator is taken to be driven by contact with a thermal environment, which will have very small correlation times. To model this, we suppose that the environment acts as a random fluctuating force $F(t)$. Working once again in a classical picture, this yields,

$$m\ddot{x} + m\gamma_{\mathrm{m}}\dot{x} + m\omega_{\mathrm{m}}^2 x = F(t), \qquad (4.39)$$

where m is the mass of the oscillator.

Fourier transforming this expression we find,

$$\hat{x}(\omega) = \chi(\omega)F(\omega), \tag{4.40}$$

$$\chi_{xx}(\omega) = \frac{1}{m}\frac{1}{\omega_{\rm m}^2 - \omega^2 - i\gamma\omega}, \tag{4.41}$$

where $\chi_{xx}(\omega)$ is the mechanical susceptibility. Because $F(t)$ is random then any particular run of the experiment, even under identical starting conditions, will produce a different $x(t)$.

To make progress we average over several realizations of the experiment, and write the solutions in terms of the spectrums of the previous sections,

$$S_{xx}(\omega) = |\chi_{xx}(\omega)|^2 S_{FF}(\omega), \tag{4.42}$$

where $S_{FF}(\omega)$ is the spectrum of the random force. Casting the problem in terms of spectrums allows us to use statistical information about the dynamics of the bath to gain statistical information about the response of the mechanical system. Referring to Eq. 4.42 however, we see that correlations in the output will be added by the filtering provided by the mechanical mode, which has a memory $\tau_{\rm m} = 1/\gamma_{\rm m}$. In this way, measurement of the correlations give direct information about the mechanical system.

It is also worth noting that the damping term, and the fluctuation term are linked. This can be seen by using Eq. 4.39 and assuming $\gamma \ll \omega_{\rm m}$ to find [98],

$$\frac{d}{dt}\langle E\rangle = -\gamma\langle E\rangle + \frac{S_{FF}(\omega_{\rm m})}{2m} \tag{4.43}$$

In equilibrium, we can set the time derivative to zero, and derive the classical fluctuation-dissipation theorem $S_{FF}(\omega_{\rm m}) = 2m\gamma\,\langle E\rangle = 2m\gamma K_{\rm B}T$.

Quantum Noise (and Cooling)

In this section, we develop a quantum version of the machinery we developed in the previous section to deal with classical noise. As it turns out, if we take a naive approach, and simply replace the classical operators in the previous section with quantum operators, we will run into issues. The main issue is that the order of the quantum operators matters in the evaluation correlators.

This may not seems obvious at first, because we are used to thinking that a quantum operator always commutes with itself. The more accurate statement is that a quantum operator always commutes with itself at the same point in time. This means that for some operator, $\hat{x}(t)$, we have $[\hat{x}(t), \hat{x}(t)] = 0$, but cannot in general state that $[\hat{x}(t), \hat{x}(t')] = 0$. In order to evaluate this commutator, we need access to the time evolution of $\hat{x}(t')$. For example, if $\hat{x}(t)$ represents an undamped quantum harmonic oscillator $\hat{x}(t) = \hat{x}(0)\sin(\omega_{\mathrm{m}} t) + \frac{\hat{p}(0)}{m\omega_{\mathrm{m}}}\cos(\omega_{\mathrm{m}} t)$, and we can use the commutation relations $[\hat{x}, \hat{p}] = i\hbar$ to find that $[\hat{x}(t), \hat{x}(t)] \neq 0$. Carrying over these ideas to the evaluation of correlation functions, we see that while it is always true that $\langle x(t)x(t')\rangle = \langle x(t')x(t)\rangle$ we *cannot* in general state $\langle \hat{x}(t)\hat{x}(t')\rangle \neq \langle \hat{x}(t')\hat{x}(t)\rangle$.

This should cause problems when we attempt to define a spectrum. Depending on the order of operators in the correlation function we would have two different definitions for quantum spectrums! It is not clear which definition is "correct". To gain insight, suppose we calculate the spectrum for the quantum version of the force operator we encountered in the previous section, assuming a stationary process. If we assume a correlator with the ordering $\langle \hat{F}(t)\hat{F}(t')\rangle = \langle \hat{F}(\tau)\hat{F}(0)\rangle$ we have the definition for the quantum spectrum,

$$S_{\hat{F}\hat{F}}(\omega) = \int_{-\infty}^{\infty} e^{i\omega\tau} \langle \hat{F}(\tau)\hat{F}(0)\rangle \, d\tau. \tag{4.44}$$

For comparison, let us assume the opposite ordering $\langle \hat{F}(t)\hat{F}(t')\rangle = \langle \hat{F}(0)\hat{F}(\tau)\rangle$ and evaluate once more,

$$\begin{aligned}\int_{-\infty}^{\infty} e^{i\omega\tau}\,\langle \hat{F}(0)\hat{F}(\tau)\rangle\,d\tau, &= \int_{-\infty}^{\infty} e^{-i\omega\tau}\,\langle \hat{F}(0)\hat{F}(-\tau')\rangle\,d\tau,' \\ &= \int_{-\infty}^{\infty} e^{-i\omega\tau}\,\langle \hat{F}(\tau')\hat{F}(0)\rangle\,d\tau', \\ &= S_{\hat{F}\hat{F}}(-\omega), \end{aligned} \tag{4.45}$$

where we have explicitly assumed a stationary process, which allows us to time shift both operators in the correlation function. Comparing these two, seemingly different definitions for quantum spectrums reveals that they are related in frequency space. With this in mind, we choose Eq. 4.44 as the definition of the quantum spectrum, and will insert a negative frequency argument as required. We note that unlike the classical spectrum, the quantum spectrum need not be symmetric in frequency. The asymmetry in this spectrum is directly related to the fact that $\hat{F}(t)$ does not have to commute with itself at different points in time.

As it turns out, the asymmetry has further implications. One can attain the driving term for the quantum version of Eq. 4.39 through the use of an interaction Hamiltonian of the form $\hat{H} = \hat{F}(t)\hat{x}$. This type of coupling will be able to drive transitions between different energy states of the harmonic oscillator representing our mechanical system. An explicit calculation of these transition rates based on [98, 99] is given in Appendix A.3, where we find,

$$\Gamma_{n\to n+1} = (n+1)\Gamma_{\uparrow} = \frac{x_0^2(n+1)}{\hbar^2} S_{\hat{F}\hat{F}}(-\omega_{\mathrm{m}}), \tag{4.46}$$

$$\Gamma_{n\to n-1} = n\Gamma_{\downarrow} = \frac{x_0^2 n}{\hbar^2} S_{\hat{F}\hat{F}}(\omega_{\mathrm{m}}), \tag{4.47}$$

where n is the Fock state number. This allows us to write down a simple rate equation based on the Fig. 4.9(a) for the probability of the system being in Fock state $|n\rangle$,

$$\dot{P}_n = (n\Gamma_\uparrow P_{n-1} + (n+1)\Gamma_\downarrow P_{n+1}) - (n\Gamma_\downarrow + (n+1)\Gamma_\uparrow)\, P_n. \tag{4.48}$$

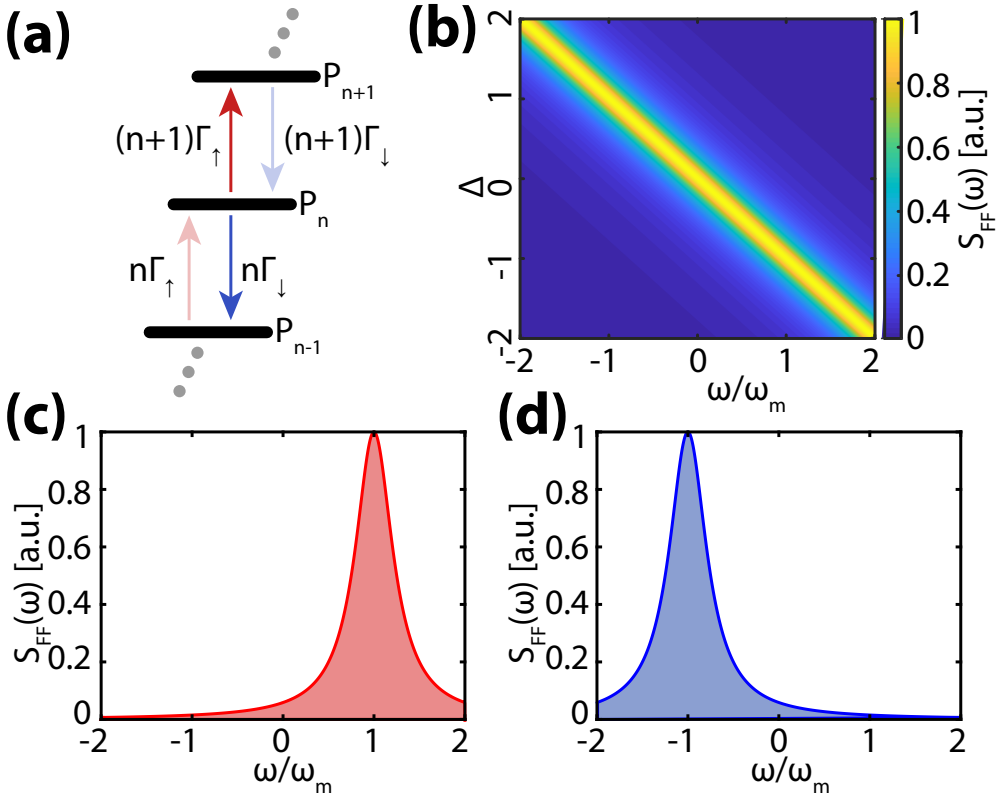

Figure 4.9: (a) Rate equation for the mechanical system subject to an external, noisy source. (b) Backaction force spectrum as a function of laser detuning and frequency. (c) Backaction force spectrum for the case of optimal cooling ($\Delta = -\omega_{\rm m}$) in the sideband resolved regime. (d) Backaction force spectrum for the case of optimal heating ($\Delta = \omega_{\rm m}$) in the sideband resolved regime.

This immediately allows us to calculate the expectation value for the energy. Defining $\langle E\rangle = \sum_{n=0}^{\infty} \hbar\omega_{\rm m}(n+1/2)P_n$, we calculate,

$$\begin{aligned}
\frac{\langle \dot{E}\rangle}{\hbar\omega_{\rm m}} =& \sum_{l=0}^{\infty}\left(l+\frac{1}{2}\right) l\Gamma_{\uparrow}P_{l-1} + \sum_{m=0}^{\infty}\left(m+\frac{1}{2}\right)(m+1)\,\Gamma_{\downarrow}P_{m+1} \\
&- \sum_{n=0}^{\infty}\left(n+\frac{1}{2}\right)\left(n\Gamma_{\downarrow}+(n+1)\Gamma_{\uparrow}\right)P_m \\
=& \sum_{l'=-1}^{\infty}\left(l'+\frac{3}{2}\right)(l'+1)\,\Gamma_{\uparrow}P_{l'} + \sum_{m'=1}^{\infty}\left(m'-\frac{1}{2}\right)m'\Gamma_{\downarrow}P_{m'} \\
&- \sum_{n=0}^{\infty}\left(n+\frac{1}{2}\right)\left(n\Gamma_{\downarrow}+(n+1)\Gamma_{\uparrow}\right)P_m \\
=& \sum_{l'=0}^{\infty}\left(l'+\frac{3}{2}\right)(l'+1)\,\Gamma_{\uparrow}P_{l'} + \sum_{m'=0}^{\infty}\left(m'-\frac{1}{2}\right)m'\Gamma_{\downarrow}P_{m'} \\
&- \sum_{n=0}^{\infty}\left(n+\frac{1}{2}\right)\left(n\Gamma_{\downarrow}+(n+1)\Gamma_{\uparrow}\right)P_m \\
=& \frac{\langle E\rangle}{\hbar\omega_{\rm m}}(\Gamma_{\uparrow}-\Gamma_{\downarrow}) + (\Gamma_{\uparrow}+\Gamma_{\downarrow})/2
\end{aligned} \tag{4.49}$$

Plugging in the explicit rate definitions from Eqs. 4.46-4.47 we arrive at the quantum analogy to Eq. 4.43,

$$\frac{d}{dt}\langle E\rangle = -\gamma\langle E\rangle + \frac{\overline{S}_{\hat{F}\hat{F}}(\omega_{\rm m})}{2m}, \tag{4.50}$$

where,

$$\gamma = \frac{x_0^2}{\hbar^2}\left(S_{\hat{F}\hat{F}}(\omega_{\rm m}) - S_{\hat{F}\hat{F}}(-\omega_{\rm m})\right), \tag{4.51}$$

$$\overline{S}_{\hat{F}\hat{F}}(\omega_{\rm m}) = \frac{S_{\hat{F}\hat{F}}(\omega_{\rm m}) + S_{\hat{F}\hat{F}}(-\omega_{\rm m})}{2}. \tag{4.52}$$

We see that just as in the classical case, the damping and noise terms are related, with the key difference that the noise term is played by the symmetrized spectrum defined in Eq. 4.52. On the other hand, the damping is just the difference between energy leaving and entering

the system, and is once again related to the noise term. In equilibrium, we can once again write down the fluctuation-dissipation theorem as, $\overline{S}_{\hat{F}\hat{F}}(\omega_{\rm m}) = 2m\gamma \langle E \rangle = 2m\gamma(N_{\rm bath}+1/2)$, where $N_{\rm bath}$ is the occupation of the bath the mechanical system is in contact with.

Now that we know how to calculate transition rates using quantum spectrums, we can use this to derive expressions for optomechanical cooling. While this can be derived by directly solving the equations of motion, the use of quantum spectrums will allow us to clearly see the contribution of various factors. Looking back to the un-linearized version of the optomechanical interaction Hamiltonian, we see that we can write $\hat{H}_{\rm int} = -G\hat{\alpha}^\dagger\hat{\alpha}\hat{x}$, which implies $\hat{F} = -G\hat{\alpha}^\dagger\hat{\alpha}$. This means that we need to consider the effect of two random forces: the usual thermal coupling to the environment, and the optomechanical backaction force [100, 101]. Placing these two rates into an equation analogous to Eq. 4.48 we find,

$$\begin{aligned}\dot{P}_n =& n(\Gamma_\uparrow + \Gamma_\uparrow^{\rm th})P_{n-1} + (n+1)(\Gamma_\downarrow + \Gamma_\downarrow^{\rm th})P_{n+1} \\ &- n(\Gamma_\downarrow + \Gamma_\downarrow^{\rm th})P_n - (n+1)(\Gamma_\uparrow + \Gamma_\uparrow^{\rm th})P_n. \end{aligned} \tag{4.53}$$

This time we are interested in the average phonon number instead of the energy. Defining $\langle n \rangle = \sum_{n=0}^{\infty} nP_n$, we find,

$$\dot{\langle n \rangle} = (\langle n \rangle + 1)\left(\Gamma_\uparrow + \Gamma_\uparrow^{\rm th}\right) - \langle n \rangle \left(\Gamma_\downarrow + \Gamma_\downarrow^{\rm th}\right). \tag{4.54}$$

This can be simplified by recalling that damping is the difference between scattering rates out of and into the system, giving the definitions, $\gamma_{\rm opt} = \Gamma_\downarrow - \Gamma_\uparrow$, $\gamma_{\rm m} = \Gamma_\downarrow^{\rm th} - \Gamma_\uparrow^{\rm th}$. With this simplification, we find a final expression for the average phonon number in steady-state,

$$\langle n \rangle = \frac{\Gamma_\uparrow + \Gamma_\uparrow^{\rm th}}{\gamma_{\rm m} + \gamma_{\rm opt}}. \tag{4.55}$$

where,

$$\Gamma_{\uparrow} = \frac{x_0^2}{\hbar^2} S_{\hat{F}\hat{F}}(-\omega_{\rm m}) = g_0^2 S_{\hat{N}\hat{N}}(-\omega_{\rm m}), \tag{4.56}$$

$$\Gamma_{\downarrow} = \frac{x_0^2}{\hbar^2} S_{\hat{F}\hat{F}}(+\omega_{\rm m}) = g_0^2 S_{\hat{N}\hat{N}}(\omega_{\rm m}), \tag{4.57}$$

$$\Gamma_{\uparrow}^{\rm th} = N_{\rm th}\gamma_{\rm m}, \tag{4.58}$$

$$\Gamma_{\downarrow}^{\rm th} = (N_{\rm th}+1)\,\gamma_{\rm th}. \tag{4.59}$$

Depending on the choice of detuning, one can adjust center frequency of $S_{\hat{N}\hat{N}}(\omega_{\rm m})$ as shown on Fig. 4.9 (b). In fact, by adjusting the detuning, the scattering rates can be made highly asymmetric as shown on Fig. 4.9(c) for the case of cooling, and Fig. 4.9(d) for the case of heating.

From the expression above, it can be shown that ground state cooling is not possible in the sideband unresolved regime, but is possible in the sideband resolved regime. Interestingly, the above expressions point to an ultimate limit on the achievable phonon population. Even if the mechanical system receives no thermal phonons, there will be a persistent contribution $S_{\hat{N}\hat{N}}(-\omega_{\rm m})$ from the optomechanical backaction. This term is explored in the next section.

The Standard Quantum Limit

Armed with a practical knowledge of spectrums, we can now address the question of the ultimate limits of our detection scheme. With a purely classical signal we expect to measure something of the form shown in Eq. 4.37. Suppose that we are working in the rather dreamy picture, where we have no sources of technical noise ($v^{\rm tech}(t) = 0$). If we assume that the mechanics is in thermal equilibrium with some other system at zero temperature, then one would expect the signal on the spectrometer to disappear. In a classical picture there is no ultimate limit to the size of signal that we might measure, with the "small" caveat that the equipment itself must not have any classical noise.

The above picture is of course, not accurate when one takes quantum effects into account. Firstly, there will be zero point fluctuations present even at zero temperature, so we would expect to measure a signal proportional to the zero point fluctuations. Recalling from the discussion above that a classical system always measures the double-sided spectrum, we might assume that we in fact will measure $\overline{S}_{\hat{v}\hat{v}}(\omega) = |K(\omega)|^2 \overline{S}_{\hat{x}\hat{x}}(\omega)$. As it happens, we will also need to consider two sources of noise that arise due to quantum constraints.

1. Shot noise: Light arrives at a detector with Poissonian statistics. One cannot build a signal based on the arrival one photon, so we must time-average over several photons. Eventually the integrated signal will emerge.

2. Backaction noise: We are detecting the motion of our mechanical system through its effect on an optical field. Conversely this optical field will also couple to the mechanics. Even if the light is in a coherent state, it will contain vacuum fluctuations. These will exert a random force on the mechanics.

This suggests that we include two random terms associated with each of these factors into our expression for the measured voltage at the RSA,

$$v(t) = K\left(x + \delta x^{\mathrm{ba}}\right) + \delta v^{\mathrm{sn}}. \tag{4.60}$$

Just as before, we will use this relation to calculate the spectrum the RSA measures. However, this time around we must be careful to include the fact that the RSA measures the symmetrized spectrum. This gives,

$$\begin{aligned}
\overline{S}_{\hat{v}\hat{v}}(\omega) &= |K(\omega)|^2 \left(\overline{S}_{\hat{x}\hat{x}}(\omega) + \overline{S}^{\mathrm{ba}}_{\hat{x}\hat{x}}(\omega)\right) + \overline{S}^{\mathrm{sn}}_{\hat{v}\hat{v}}(\omega) \\
&= |K(\omega)|^2 \left(\overline{S}_{\hat{x}\hat{x}}(\omega) + \overline{S}^{\mathrm{ba}}_{\hat{x}\hat{x}}(\omega) + \overline{S}^{\mathrm{imp}}_{\hat{x}\hat{x}}(\omega)\right), \\
&= |K(\omega)|^2 \left(\overline{S}_{\hat{x}\hat{x}}(\omega) + \overline{S}^{\mathrm{add}}_{\hat{x}\hat{x}}(\omega)\right),
\end{aligned} \tag{4.61}$$

where we have assumed that the backaction and shot noise are uncorrelated. We have also defined the imprecision spectrum, $\overline{S}^{\rm imp}_{\hat{x}\hat{x}}(\omega)$ and added noise spectrum $\overline{S}^{\rm add}_{\hat{x}\hat{x}}(\omega)$ in keeping with literature conventions [98]. This allows use to map the shot noise onto an equivalent noise in the oscillator. It can be shown (see Appendix A.3.1) that $\overline{S}^{\rm ba}_{\hat{x}\hat{x}}(\omega) = |\chi_{xx}(\omega)|^2\overline{S}_{\hat{F}\hat{F}}(\omega)$ and $\overline{S}^{\rm imp}_{\hat{x}\hat{x}}(\omega)\overline{S}_{\hat{F}\hat{F}}(\omega) = \frac{\hbar^2}{4}$. This allows us to write that added noise as,

$$\boxed{\overline{S}^{\rm add}_{\hat{x}\hat{x}}(\omega) = |\chi_{xx}(\omega)|^2\overline{S}_{\hat{F}\hat{F}}(\omega) + \frac{\hbar^2}{4}\frac{1}{\overline{S}_{\hat{F}\hat{F}}(\omega)}.} \tag{4.62}$$

Unfortunately, this presents an ultimate limit on the sensitivity of direct position measurement. If the control laser power is decreased, we have less backaction but more shot noise. If the control laser power is increased we have more backaction and less shot noise. The best we can hope to do is find a compromise between these cases by optimizing laser power.

4.3 Introduction: Optomechanically Induced Transparency and Cooling in Thermally Stable Diamond Microcavities

The remainder of this chapter consists of the previous published work "Optomechanically induced transparency and cooling in thermally stable diamond microcavities". The advancements in this paper were made possible by modifications and optimization of the fabrication procedure which made it possible to place a laser red detuned from the cavity. There is also an original criterion, calculated in the supplementary materials, which give the power at with the red-detuned side of the cavity is no longer accessible.

DP Lake, M Mitchell, Y Kamaliddin set up the experiment and acquired the data. DP Lake, M Mitchell, Y Kamaliddin analyzed the data, and DP Lake, M Mitchell, PE Barclay wrote the manuscript.

4.4 Optomechanically Induced Transparency and Cooling and Cooling in Thermally Stable Diamond Microcavities

Nanophotonic cavity optomechanical devices localize light within nanostructures supporting both optical and mechanical resonances, creating large optical forces that can coherently couple light to phonons of a mechanical mode. These devices provide a testbed for fundamental studies of quantum science [70, 102], with hallmark experiments demonstrating phenomena such as optomechanically induced transparency [88, 89, 103], optomechanical cooling [76], observation of a mechanical resonator's zero point motion [104], quantum optical–mechanical correlations [84, 105–108], and entanglement between mechanical resonators [109]. Within the realm of quantum technology, the ability of these systems to coherently interface GHz frequency phonons with optical photons has sparked efforts to create transducers [110] that optomechanically convert quantum information between photonic channels and solid state [111] or superconducting microwave [112–115] qubits via a shared mechanical coupling.

Diamond cavity optomechanical devices [35, 116] are poised to advance experiments in quantum optomechanics, in part thanks to device performance improvements from diamond's best-in-class Young's modulus, low intrinsic mechanical dissipation, high thermal conductivity, and large optical transparency window from $\sim$ 230 nm to far–IR [117]. In addition, these devices offer an interface between highly coherent diamond colour centre spins and optically controlled phonons via strain coupling [111], which could enable quantum transducers between spins and quantum phononic and photonic states [118–120], as well as platforms for entangling remote spins via nanomechanical coupling [121, 122]. To date, nanomechanical devices used for spin manipulation have relied on piezo actuated phonon-strain coupling [123–128]. Incorporating coherent cavity optomechanics would enable optical control of phonon-spin interactions with sensitivity necessary for operation at the single phonon level and enable new photon-spin interfaces that are independent of the spin optical properties.

A requirement for realizing the large-amplitude mechanical oscillations required to couple to colour centres is the phonon lasing criterion, $C > 1 - \frac{\kappa_{ex}}{\kappa_o + \kappa_{ex}}$, where $C \equiv 4Ng_0^2/\kappa_o\Gamma_m > 1$, is the optomechanical cooperativity, N is the intracavity photon number, g_0 is the single–photon optomechanical coupling rate, and κ_o and Γ_m are the optical cavity and mechanical resonator energy decay rates, and κ_{ex} is the cavity external coupling rate [70, 89]. Additionally, large C is important in other coherent optomechanical processes such as light pulse storage [78] and wavelength conversion [103, 129], where the spectral response and conversion efficiency are dependent on C, respectively. This should not be confused with the much more stringent case of quantum–coherent interactions which requires that $2g_0\sqrt{N} > (\kappa_o, \gamma)$, where $\gamma = \Gamma_m(n_{th} + 1)$ is the mechanical decoherence rate and n_{th} is the thermal equilibrium phonon occupation of the mechanical mode [70, 130]. We have developed single–crystal diamond microdisks that achieve $C > 1 - \frac{\kappa_{ex}}{\kappa_o + \kappa_{ex}}$ by coupling optical whispering gallery modes to GHz frequency (ω_m) mechanical radial breathing mode resonances [35]. The microdisk mechanical resonances have a large mechanical quality factor $Q_m \equiv \omega_m/\Gamma_m$ that is enhanced by restriction of phonon leakage into the substrate by a nanoscale pedestal, while the optical modes have optical quality factor $Q_o \equiv \omega_o/\kappa_o \sim 10^5$, where $\omega_o/2\pi \sim 200$ THz is the optical mode frequency, and can support $N > 10^6$ photons without suffering from nonlinear absorption that degrades device performance in other less transparent materials such as silicon [131].

However, in previous work, at high N the device performance becomes limited by linear optical absorption and accompanying heating. The resulting change in microdisk temperature is exacerbated by the $\sim$ 100 nm waist of the microdisk pedestal, in which thermal conductivity is reduced at room temperature due to size effects by approximately an order of magnitude compared to in bulk diamond [35], resulting in thermo-optic instability [62] for red laser–cavity detunings needed for applications such as coherent phonon–photon coupling and optomechanical cooling. Here we overcome this limitation through modification of the microdisk pedestal shape to improve its thermal conductivity without affecting Q_m,

enabling demonstration of optomechanically induced transparency, a hallmark of coherent phonon-photon coupling, as well as stable optomechanical cooling in diamond microdisks for the first time.

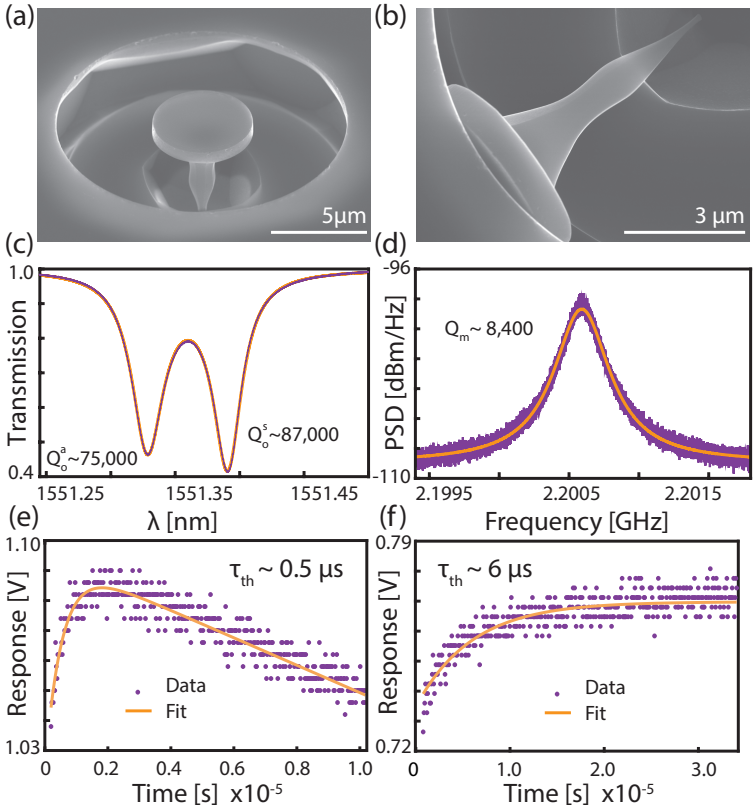

Figure 4.10: Characterization of single–crystal diamond microdisk structures fabricated using modified plasma undercutting method. (a) Scanning electron micrograph (SEM) of a "flared" microdisk structure. (b) Top down SEM view of the modified pedestal shape using the modified undercutting method described above. (c) Typical high–Q_o doublet optical mode for the device studied here. (d) RBM of microdisk measured at low input power exhibiting a $Q_m \sim 8,400$. (e,f) Response of the optical transmission for an input step function for microdisks with similar sized flared and hourglass shaped pedestals, respectively. The exponential rise is fit to extract the thermal time constant. The negatively sloped feature in (e) is an EDFA artifact, resultant from the large input powers required to achieve thermal bistability.

4.4.1 Device Characterization: Optical, Mechanical and Thermal Properties

An example of the diamond microdisk devices studied here is shown in the scanning electron micrograph image in Fig. 4.10(a). These devices were fabricated by modifying the diamond undercutting process demonstrated in Ref. [35], as described in the Supporting Information, to shape the pedestal supporting the microdisk into the flared profile shown in Fig. 4.10(b). Note that the device in Fig. 4.10(b) was broken as result of being over–undercut, and its minimum pedestal dimension is smaller than that of the devices studies here, which are ~ 350 nm. The optical and mechanical modes of the microdisks were characterized by monitoring the transmission of a tuneable diode laser (Newport TLB 6700B) through a dimpled optical fiber taper evanescently coupled to the microdisk. Scans of transmission for varying laser wavelength ($\lambda_{\rm p}$) when coupled to the 5 μm diameter microdisk considered in the remainder of this work revealed resonances such as those shown in Fig. 4.10(c). The doublet resonance structure indicates the presence of backscattering induced standing wave optical modes, which are either a symmetric or anti-symmetric combination of the degenerate travelling wave modes in the microdisk (see Supporting Information). The modes studied here have a central wavelength of $\lambda_{\rm o} \equiv 2\pi {\rm c}/\omega_{\rm o} \sim 1550$ nm, splitting of $\frac{\lambda_{\rm o}^2}{2\pi c}\kappa_{\rm bs} \sim 70$ pm, where $\kappa_{\rm bs}$ is the backscattering rate, and intrinsic (unloaded) $Q_{\rm o}^{\rm (s,a)} = \omega_{\rm o}/\kappa_{\rm o}^{\rm (s,a)} = 8.7 \times 10^4$ and 7.4×10^4, where $\kappa_{\rm o}^{\rm (s,a)}$ are the optical energy decay rates of the symmetric and antisymmetric (red and blue shifted) modes of the doublet, respectively. This places the system near the resolved sideband regime, with $\omega_{\rm m}/\kappa_{\rm o}^{\rm (s,a)} \sim 1.0$ and 0.84. Typically these devices are operated in the under–coupled regime with $\kappa_{\rm ex}/\kappa_{\rm o} \sim 0.58$, where $\kappa_{\rm ex}$ is the external energy coupling loss rate.

The microdisk's mechanical resonances were probed by fixing $\lambda_{\rm p}$ slightly off-resonance from the cavity modes and monitoring fluctuations in optical transmission due to mechanical motion using a high-speed photodetector (Newport 1554-B). Initial measurements were performed at low optical input power $P_{\rm in}$ to avoid modifying the mechanical mode dynam-

ics via optomechanical back action [70]. The power spectral density (PSD) of this signal, as analyzed on a real time spectrum analyzer (Tektronix RSA5106A) and shown in Fig. 4.10(d), reveals the thermal motion of a mechanical resonance at $\omega_{\rm m}/2\pi \sim 2.2$ GHz, with a mechanical quality factor $\rm Q_m = \omega_m/\Gamma_m \sim 8,400$. Comparison to COMSOL finite element simulations of the microdisk suggest that this mechanical mode is the fundamental radial breathing mode (RBM) of the microdisk, as the measured $\omega_{\rm m}$ is within 5% of the simulated value. The RBM studied here has an effective mass predicted from simulation of $m_{\rm eff} \sim$ 45 pg, corresponding to a quantum zero point motion amplitude, $x_{\rm zpm} \sim 0.30$ fm, where $x_{\rm zpm} = \sqrt{\hbar/2m_{\rm eff}\omega_{\rm m}}$.

Reaching the regime of coherent optomechanical coupling can in principle always be achieved by operating with high enough $P_{\rm in}$ to increase N so that $C > 1$. In practice, even in absence of nonlinear absorption, N is limited by linear absorption and thermo-optic dispersion, particularly in small optical mode volume devices such as microdisks. The microdisk pedestal shape plays a critical role in determining whether $C > 1$ can be reached, as it influences $Q_{\rm m}$ ($\propto C$) [35] as well as the device's ability to conduct thermal energy away from the microdisk and mitigate optical heating. The importance of the pedestal's thermal conductance can be seen by considering the threshold for N above which the microdisk becomes bistable due to the thermo-optic effect [132, 133], for $\lambda_{\rm p}$ red-detuned from $\lambda_{\rm o}$ as required for optomechanically induced transparency [88, 89, 103] and cooling [76]:

$$\left(\frac{\eta P_{\rm in} Q_{\rm o}}{\hbar\omega_{\rm o}^2}\right) \equiv N < \frac{C_p}{|\beta|\tau_{\rm th}\hbar\omega_{\rm o}^2}\left(\frac{Q_{\rm abs}}{Q_{\rm o}}\right) \tag{4.63}$$

(see Supporting Information). Here $\tau_{\rm th}$ and C_p are the microdisk thermal time constant and the heat capacity, respectively, and $\beta = d\lambda_{\rm o}/dT$ is the microdisk thermo-optic coefficient that accounts for thermal expansion and refractive index temperature dependence [62]. The on-resonance fiber taper waveguide-microdisk power coupling efficiency is defined as η, and

$1/Q_{\mathrm{abs}}$ is the contribution to $1/Q_{\mathrm{o}}$ from linear absorption. Equation (4.63) illustrates the inverse relationship between τ_{th} and maximum N. Note that in the anomalous case of $\beta < 0$, the cavity becomes bistable for blue instead of red detuning.

To determine the impact of the pedestal shape on the properties of the microdisks, we compare the flared pedestal devices from this work with hourglass pedestal devices studied previously [35]. In Ref. [35] it was found that increasing pedestal width degraded Q_{m}. However, the Q_{m} of the flared pedestal device measured here is similar to the best valued reported for the hourglass microdisks, despite the larger width of the flared pedestals. However, as shown by measurements of τ_{th} in Fig. 4.10(e-f), the highest Q_{m} flared and hourglass pedestal microdisks have $\tau_{\mathrm{th}} \sim 0.5$ μs and 6 μs, respectively, indicating that the flared pedestal devices studied here can support over an order of magnitude larger N in the red-detuned regime compared to previous hourglass pedestal devices. Here τ_{th} was measured by monitoring the response of the microdisk to an optical pulse that causes λ_{o} to shift via the photothermal effect, as described in the Supporting Information.

4.4.2 Optomechanical Spring Effect

The optomechanical parameters of the system were further probed by means of the optical spring effect [70, 134, 135]. For this measurement, P_{in} was increased via an erbium doped fiber amplifier (EDFA: Pritel LNHPFA-30) connected to the tunable laser output. The laser wavelength was then discretely stepped across the optical cavity resonances, and the PSD of the transmitted signal was acquired at each step. By fitting a Lorentzian lineshape to the PSD, both $\omega_{\mathrm{m}}(\Delta; P_{\mathrm{in}}) = \omega_m^0 + \delta\omega_{\mathrm{m}}(\Delta; P_{\mathrm{in}})$ and $\Gamma_{\mathrm{m}}(\Delta; P_{\mathrm{in}}) = \Gamma_{\mathrm{m}}^0 + \Gamma_{\mathrm{opt}}(\Delta; P_{\mathrm{in}})$ as a function of pump-cavity detuning, $\Delta = \omega_{\mathrm{p}} - \omega_{\mathrm{o}}$, were extracted. The results of this measurement for intermediate input power ($P_{\mathrm{in}} \sim 4.7$ mW) are shown in Figs. 4.11(a) and 4.11(b). Here the data is fit to analytic expressions for the predicted values of the optomechanical spring effect $\delta\omega_{\mathrm{m}}$ and optomechanical damping Γ_{opt}, taking into account the doublet nature of the optical mode (see Supporting Information). Using measurements of $N(\Delta) = N^{\mathrm{s}}(\Delta) + N^{\mathrm{a}}(\Delta)$ shown

in Fig. 4.11(c) determined from the power dropped into the microdisk and $\kappa^{s,a}$ we are able to extract the sole fitting parameter, $g_0/2\pi \sim 17$ kHz. The optomechanical coupling rate is not expected to vary for each mode of the doublet, which was confirmed in our analysis by allowing g_0 to vary for the symmetric and antisymmetric modes, which gave the same result as a single g_0 value. In general, as the coupling rates to each of the modes will depend on the phase of fields compared to the point of fiber taper coupling, κ_{ext} can differ for each mode [12]. However, for the modes considered in this work κ_{ext} was approximately equal for each mode, and a single value was used. Unlike previous measurements of the optical spring effect in diamond microdisks [35], $\delta\omega_m$ here was dominated by optomechanical back-action owing to the device's reduced τ_{th} and low optical heating.

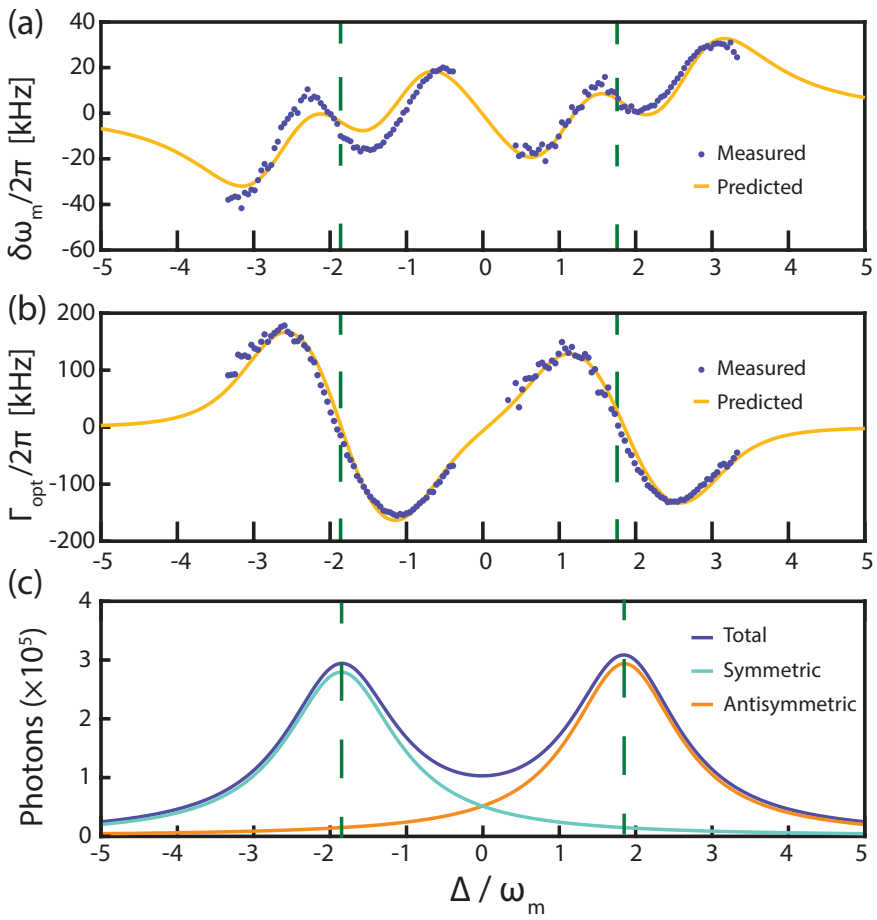

Figure 4.11: Characterization of optomechanical coupling via the spring effect for the device shown in Fig. 4.10, for $P_{\rm in} \sim 4.7$ mW. Shift in (a) mechanical resonance frequency $\delta\omega_{\rm m}$ and (b) optomechanical damping $\Gamma_{\rm opt}$ as a function of laser detuning. The fits are from the optomechanical spring effect calculation with a single–photon optomechanical coupling rate of $g_0/2\pi \sim 17$ kHz as the sole free parameter, and the measured N shown in (c). Dashed lines indicate $\Delta \pm \kappa_{\rm bs}/2 = 0$ (corresponding to the resonance frequency of each doublet mode), and illustrate that $\delta\omega_{\rm m}$ and $\Gamma_{\rm opt} = 0$ when the laser is on-resonance with the cavity mode.

The cavity optomechanical damping, $\Gamma_{\rm opt}$, modifies the mechanical normal-mode temperature, $T_{\rm eff}$, as in experiments of ground state cooling [76], or generation of self–oscillations that drive stress fields for coupling to diamond colour center spins [35]. The normal-mode temperature can be measured as a function of Δ from the area under the PSD normalized by

the wavelength dependent optomechanical transduction (see Supporting Information) and assuming that for large $|\Delta|$ the cavity is in thermal equilibrium with the room-temperature environment (see Supporting Information). Figure 4.12(a) shows the normal mode temperature $T_{\rm eff}$ and corresponding phonon occupation $n_{\rm m}$ measured using this technique. Also shown is a prediction of $T_{\rm eff}$ obtained by inputting the fit of $\Gamma_{\rm opt}(\Delta)$ from Fig. 4.11(b) to the optomechanical back-action cooling expression,

$$n_{\rm m} = n_{\rm th} \times \frac{\Gamma_{\rm m}^0}{\Gamma_{\rm m}^0 + \Gamma_{\rm opt}(\Delta)}, \tag{4.64}$$

where $n_{\rm m}$ is the final phonon number, $n_{\rm th} = k_B T/\hbar\omega_{\rm m}$ is the equilibrium thermal phonon occupation [70]. This expression is valid in the high–T limit $n_{\rm th} \gg n_{\rm min}$ applicable here, where $n_{\rm min} = 0.088$ is the minimum backaction limited phonon number achievable through optomechanical damping, which in the resolved sideband regime is given by $n_{\rm min} = (\kappa/4\omega_{\rm m})^2$, which holds for the device studied here [70]. The good agreement indicates that the Δ dependent normalization of the PSD is accurate, and that optical absorption and heating is small compared with changes to $n_{\rm m}$ from optomechanical backaction.

At higher $P_{\rm in}$, microdisk heating and modal thermo-optic dispersion become significant, and the transduction calibration could not be readily applied to measurements of PSD area for varying Δ. However, measurement of optomechanical cooling using Eq. (4.64) with Δ optimized to maximize $\Gamma_{\rm opt}$ was possible: for $N \sim 1 \times 10^6$ ($P_{\rm in} \sim 20$ mW), $T_{\rm eff} = 60$ K ($n_{\rm m} = 588$ phonons) was measured for the symmetric mode, as shown in Fig. 4.12(b). Here $T_{\rm eff}$ includes an increase in bath temperature (i.e. $n_{\rm th}$) of 4 K due to optical heating, inferred from the shift in $\lambda_{\rm o}$ calibrated by its independently measured temperature dependence (see Supporting Information). This optimized cooling was obtained when red-detuned by $\omega_{\rm m}$ from the higher-$Q_{\rm o}$ doublet mode, as expected for a sideband-resolved cavity optomechanical

device. This detuning was not achievable in previous work with hourglass pedestal microdisks due to an inability to operate at red-detuning with P_{in} large enough to significantly reduce n_{m} because of thermal instability [35].

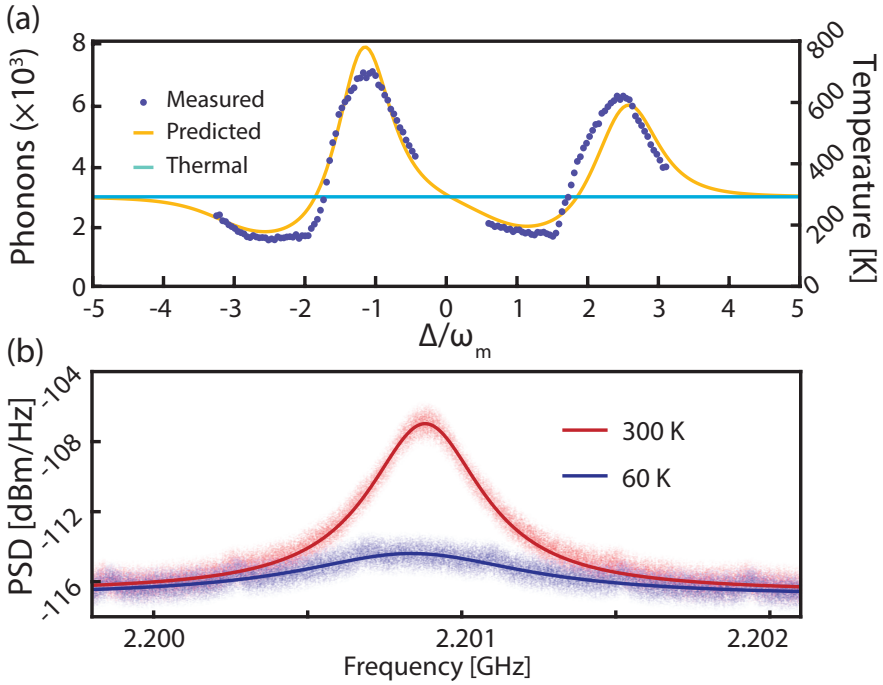

Figure 4.12: Optomechanical heating and cooling. (a) Measured phonon occupation and temperature of the RBM, and the corresponding values predicted from the fit to Γ_{opt} in Fig. 4.11(b). (b) PSD at the operating point $\Delta \sim -\kappa_{\mathrm{bs}}/2 - \omega_{\mathrm{m}}$ of maxiumum cooling (blue), and at Δ tuned to the point of zero damping (red). Small peaks at intervals of 500 kHz are from technical noise.

4.4.3 Optomechanically Induced Transparency

Optomechanically induced transparency (OMIT) is a signature of coherent coupling between optical and mechanical resonances, and has been demonstrated in cavity optomechanical systems such as microtoroids [88], optomechanical crystals (OMC's) [89], and microdisks [103]. OMIT occurs when a strong control field (ω_{c}) is red–detuned from the microdisk such that $\Delta_{\mathrm{oc}} = \omega_{\mathrm{o}} - \omega_{\mathrm{c}} = \omega_{\mathrm{m}}$, resulting in destructive interference between anti-Stokes photons

scattered from the control field and a weak probe field ($\omega_{\rm p}$). This creates a transparency window (dip) in the probe transmission (reflection) spectrum when $\Delta_{\rm pc} = \omega_{\rm p} - \omega_{\rm c} = \omega_{\rm m}$ (corresponding to $\omega_{\rm p} = \omega_{\rm o}$ if the control field detuning condition is ideally satisfied) whose amplitude and width depends on the cooperativity [70, 88, 89].

To characterize OMIT in the diamond microdisks, the laser output was amplified to $P_{\rm in} \sim 40$ mW, and its wavelength was slowly stepped across the cavity resonance, creating a control field with varying $\Delta_{\rm oc}$. At each $\Delta_{\rm oc}$, a phase electro–optic modulator (EOM) driven by a vector network analyzer (VNA:Keysight E5036A) was used to create a sideband on the control field that serves as the probe, and whose frequency can be swept across the cavity resonance, varying $\Delta_{\rm pc}$. The probe field reflected by the microdisk back into the fiber taper was measured using a high–bandwidth photoreceiver connected to an optical circulator, and analyzed by the VNA. The symmetric mode of the microdisk doublet ($\omega_{\rm o} - \frac{\kappa_{\rm bs}}{2}$) was used for all of the measurements described below. Figure 4.13(a) shows the results of these measurements for several $\Delta_{\rm oc}$, with each exhibiting a sharp OMIT feature when $\Delta_{\rm pc} = \omega_{\rm m}$. Here $\overline{R}$ is the reflectivity normalized by its maximum value in absence of OMIT. When $\Delta_{\rm oc}$ is tuned away from $\omega_{\rm m}$ the OMIT feature exhibits a Fano shape due to the phase difference between the scattered control field and the probe field. At the OMIT condition $\Delta_{\rm oc} = \omega_{\rm m}$ the dip amplitude reaches a maximum, as shown in detail in Fig. 4.13(b). From the dip amplitude $\sim 0.8 = 1 - 1/(1 + C)^2$ [103], cooperativity $C \sim 1.2$ was extracted. This C was achieved with an intracavity photon number of $N \sim 2.7 \times 10^6$, and corresponds to $g_0/2\pi = 18$ kHz, in excellent agreement with the value predicted from the optomechanical spring effect fits in Figs. 4.12(a) and (b).

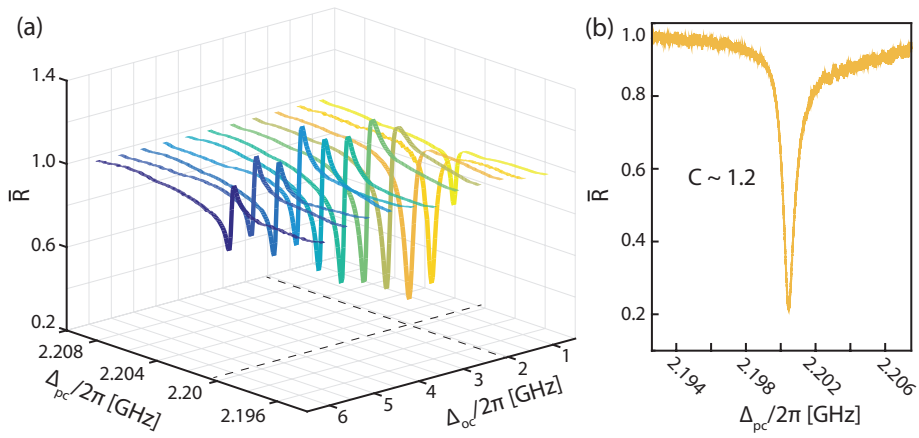

Figure 4.13: Optomechanically induced transparency. (a) Probe reflection,$\bar{R}$, as a function of Δ_{oc} and Δ_{pc} shown for OMIT using the symmetric mode of the doublet. (b) OMIT response corresponding to $C \sim 1.2$ for $N \sim 2.7 \times 10^6$, with $\Delta_{\mathrm{pc}} = \Delta_{\mathrm{oc}} = \omega_{\mathrm{m}}$.

Compared with previous demonstrations of OMIT in microdisks [103], the diamond devices demonstrated here support nearly two orders of magnitude higher N and 2.6 times higher C, despite their lower Q_{o}. Furthermore, this performance is realized without thermal stabilization or cryogenic cooling. This enables optomechanical cooling with large N in the red-detuned regime not accessible in previous studies [35]. Additionally, the microdisk geometry combined with the broadband transparency of diamond allows these devices to simultaneously support high-Q_{o} optical modes spanning a broad wavelength range, for example at both the 637 nm range of diamond NV centre emission and in the 1550 nm telecommunications wavelength band [35]. The $C > 1$ OMIT shown here will allows these multiwavelength cavities to be used for optomechanical wavelength conversion [103, 129], and the broad microdisk mode spectrum will allow conversion over a larger range than diamond OMC [116]. Finally, any improvement to Q_{m}, either through low-temperature operation [31] or engineering of the microdisk connection to the pedestal [136] would greatly increase the maximum achievable cooperativity.

4.4.4 Conclusion

In summary we have demonstrated optomechanically induced transparency, cooling, and full characterization of the optical spring effect in single-crystal diamond microdisks. Access to the red–detuned sideband, and the associated aforementioned phenomena was enabled by improving the thermal stability of the microdisk by modify the pedestal geometry. Future work will seek to further enhance Q_{o} and Q_{m} by improving the fabrication process and investigating post-fabrication surface treatments. Furthermore, recent work has demonstrated that the diamond undercutting fabrication technique utilized here may be applied to other geometries such as photonic crystals [36], which holds promise for the fabrication of future optomechanical devices. Finally, implantation of NV's or SiV's in these devices will allow the study of the interaction of solid state qubits with coherently driven cavity–optomechanics, as spin-photon coupling rates between the RBM and NV ground state are predicted to reach 0.6 MHz [35].

4.5 Supporting Information

4.5.1 Modified Fabrication Process

Compared to previous work fabricating microdisks from bulk single–crystal diamond a modified undercutting approach was utilized in this work, as described in Fig. 4.14. This modification entails the deposition of a $\sim$ 100 nm thick layer of electron beam evaporated SiO_2, partway through the quasi-isotropic undercutting step shown in Fig. 4.14(v-vi). This partial masking layer results in a faster horizontal undercut rate at the bottom of the pedestal compared to the top, as shown in Fig. 4.14(vii), which alters the final pedestal shape. In this work (100) single–crystal diamond chips purchased from element 6 are used, which to the best of our knowledge are the only crystallographic orientation used with this fabrication method to date [31, 35, 36, 137]. As it is believed that the quasi-isotropic etch is ultimately

limited by various speeds of etching along the crystal planes [137], a sample with different crystal orientation could also potentially be used to alter the device geometry: in this case, the support pedestal of the microdisk.

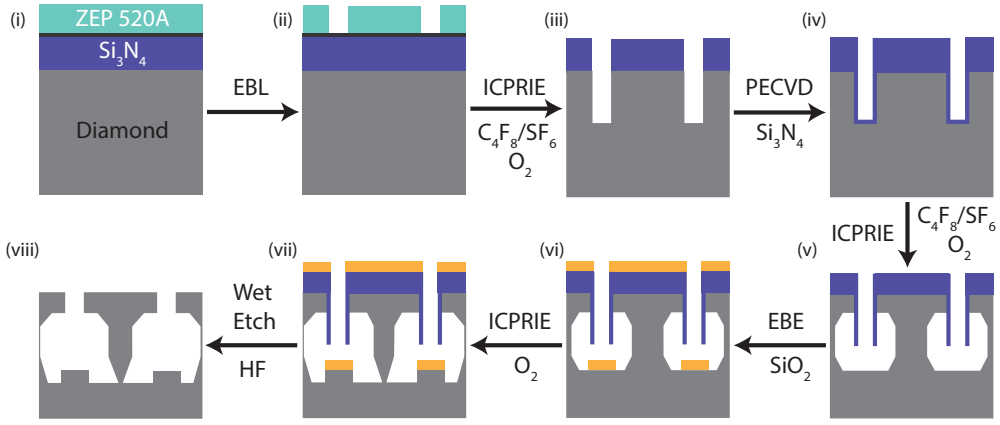

Figure 4.14: Modified plasma undercutting method. (i) Polished single–crystal diamond chips are cleaned in boiling piranha and coated with a 300 nm thick PECVD Si_3N_4 layer, coated with $\sim$ 5 nm of Ti as an anti-charging layer, and EBL resist (ZEP 520A). (ii) The microdisks are patterned in ZEP using EBL and developed in ZED N50. (iii) Patterns are transferred to the Si_3N_4 hard mask using an ICPRIE etch. ZEP is removed using a deep-UV exposure and Remover PG. (iv) Patterns are transferred to the diamond using an anisotropic O2 plasma ICPRIE etch, followed by sidewall protection via a conformal coating of PECVD Si_3N_4. (v) A short ICPRIE etch removes Si_3N_4 from the bottom of the etch windows, followed by an initial zero bias O_2 ICPRIE plasma which partially undercuts the microdisks. (vi) A $\sim$ 100 nm layer of SiO_2 is deposited via electron beam evaporation (EBE). (vii) A second zero bias O_2 plasma etch is performed, finishing the plasma undercutting process. (viii) The sample is soaked in HF to remove the remaining Si_3N_4 layer, followed by a piranha clean.

4.5.2 Thermal Response

Following the analysis of Carmon et al [62], we can write an equation governing the time evolution of the cavity temperature in response to an input field with power $P_{\text{in}}(t)$,

$$\frac{d}{dt}\Delta T = P_{\text{in}}(t) f\left(\lambda_p, \Delta T\right) - \frac{\Delta T}{\tau_{\text{th}}}, \tag{4.65}$$

where for a singlet mode,

$$f\left(\lambda, \Delta T\right) = \frac{\eta Q_{\mathrm{o}}}{C_p Q_{\mathrm{abs}}} \frac{\left[\Delta\lambda/2\right]^2}{\left[\lambda_p - \lambda_o(1+\beta\Delta T)\right]^2 + \left[\Delta\lambda/2\right]^2}. \tag{4.66}$$

In the above ΔT is the difference between the cavity temperature and environment temperature, τ_{th} is the thermal time constant, C_p is the heat capacity of the cavity, and β is defined as a temperature coefficient of resonance–wavelength accounting for thermal expansion and refractive index perturbations, $\beta = \epsilon + \frac{dn}{dT}/n_0$. The fraction of light coupled into the cavity is defined as η, λ_p is the input field wavelength, $\lambda_o(\Delta T)$ is the cavity resonance wavelength, Q_{o} is the cavity intrinsic quality factor, and Q_{abs} is the quality factor due to absorption only.

For a constant input signal, the equilibrium temperature ΔT_{eq} of the cavity can be found by setting $\frac{d}{dt}\Delta T = 0$, and solving the cubic equation $a(\Delta T_{\mathrm{eq}})^3 + b(\Delta T_{\mathrm{eq}})^2 + c(\Delta T_{\mathrm{eq}}) + d = 0$. As only real solutions to this equation are physical, we can deduce the number of valid solutions at equilibrium by determining the number of real roots associated with the cubic equation. To do so one can evaluate the discriminant, Δ, as,

$$\Delta = \frac{q^2}{4} + \frac{p^3}{27}, \tag{4.67}$$

$$p = \frac{3ac - b^2}{3a^2}, \tag{4.68}$$

$$q = \frac{2b^3 - 9abc + 27a^2 d}{27a^3}. \tag{4.69}$$

This can be divided into three distinct cases,

$$\Delta < 0 : \text{Three real, distinct roots.} \tag{4.70}$$

$$\Delta = 0 : \text{Three real, degenerate roots.}$$

$$\Delta > 0 : \text{One real root, and two complex roots.}$$

The case where $\Delta < 0$ is shown in Fig. 4.15, where 3 real distinct roots exist resulting in a thermal bistability.

To determine if the red-detuned side of the cavity is accessible for a given input pump power, we evaluate Δ at zero detuning, e.g. $\lambda_p = \lambda_o(1+\beta\Delta T)$. This leads to the requirement for access to red detunings,

$$\frac{1}{\tau_{\mathrm{th}} Q_{\mathrm{o}}} > |\beta| \left(\frac{\eta Q_{\mathrm{o}}}{Q_{abs}}\right) \left(\frac{P_{\mathrm{in}}}{C_p}\right). \tag{4.71}$$

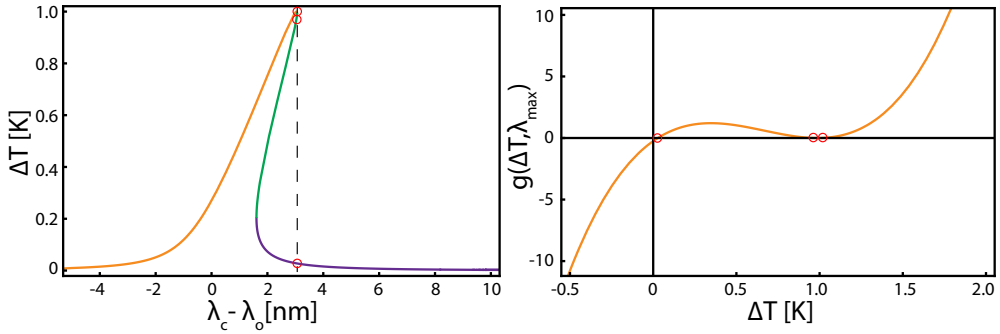

Figure 4.15: (a) Cavity temperature at equilibrium as a function of laser–cavity detuning found by numerically solving Eqn. 4.65, with $\frac{d}{dt}\Delta T = 0$. (b) Equilibrium temperature solutions at maximum shift in resonance wavelength, λ_{max}.

To measure the thermal time constant, the input field is modulated between two distinct powers, as shown in Fig. 4.16(a). For relatively small modulations, the time evolution of the cavity temperature will resemble the input field, low pass filtered by the finite response time of the thermal cavity shift. This can then be read out by choosing a laser drive wavelength where changes in the cavity resonance frequency result in a change in optical transmission, namely,

$$P_{\mathrm{out}}(t) \approx T\left[1 + \frac{\partial T}{\partial \lambda_o}\frac{\partial \lambda_o}{\partial \Delta T}\Delta T\right] P_{\mathrm{in}}(t), \tag{4.72}$$

where P_{out} is the power output into the taper and T is the transmission through the cavity. Together Eqs. 4.65-4.72 were used to fit experimental data to derive τ_{th}.

In the cooling experiments described in the main text, the application of a strong pump laser caused the device to heat. The degree of this temperature shift was derived by measuring the shift in λ_o as a function of temperature in a separate experiment, as shown in Fig. 4.16(b).

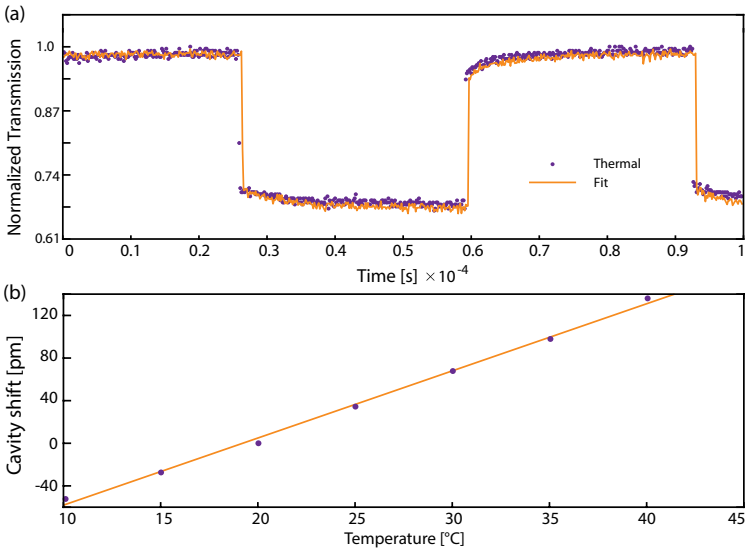

Figure 4.16: (a) Transmission of an optical cavity in response to a square wave driving function. (b) Cavity shift, relative to ambient conditions, as a function of temperature for the device and mode used in the main text. The cavity temperature was varied using a thermoelectric heater. The linear line of best fit shown was used to calculate the laser absorption induced heating present in the cooling experiment described in the main text.

4.5.3 Optical Spring Effect

Microdisk resonators typically support degenerate clockwise and counter clockwise propagating modes, with amplitudes $\alpha_{\mathrm{cw}}, \alpha_{ccw}$ respectively. In the case that the coupling between these modes due to backscattering exceeds loss to all other channels, standing wave modes are supported, which are either a symmetric $\alpha_{\mathrm{s}} = 1/\sqrt{2}\,(\alpha_{\mathrm{cw}} + \alpha_{\mathrm{ccw}})$ or anti-symmetric $\alpha_{\mathrm{a}} = 1/\sqrt{2}\,(\alpha_{\mathrm{cw}} - \alpha_{\mathrm{ccw}})$ combinations of the travelling wave modes [12].f

Using the fact that $\langle\alpha_{\rm a}|\alpha_{\rm s}\rangle = 0$, we can write the optomechanical spring effect as [70],

$$\begin{aligned}\delta\omega_{\rm m} =& g^2\left[\frac{\Delta-\omega_{\rm m}}{\kappa_{\rm s}^2/4+(\Delta-\kappa_{\rm bs}/2-\omega_{\rm m})^2}\right]\\ &+g^2\left[\frac{\Delta+\omega_{\rm m}}{\kappa_{\rm s}^2/4+(\Delta-\kappa_{\rm bs}/2-\omega_{\rm m})^2}\right]\\ &+g^2\left[\frac{\Delta-\omega_{\rm m}}{\kappa_{\rm a}^2/4+(\Delta+\kappa_{\rm bs}/2-\omega_{\rm m})^2}\right]\\ &+g^2\left[\frac{\Delta+\omega_{\rm m}}{\kappa_{\rm a}^2/4+(\Delta+\kappa_{\rm bs}/2-\omega_{\rm m})^2}\right]\end{aligned} \tag{4.73}$$

where $g = g_0 N$ is the optomechanical coupling parameter to the doublet mode, $\kappa_{\rm s,a}$ are the cavity decay rates, $\kappa_{\rm bs}$ is the backscattering coupling rate, $\omega_{\rm m}$ is the mechanical frequency rate and Δ is the laser-cavity detuning.

Using similar arguments, it can be shown that the optomechanical damping rate for doublets is,

$$\begin{aligned}\Gamma_{\rm opt} =& g^2\left[\frac{\kappa_{\rm s}}{\kappa_{\rm s}^2/4+(\Delta-\kappa_{\rm bs}/2-\omega_{\rm m})^2}\right]\\ &-g^2\left[\frac{\kappa_{\rm s}}{\kappa_{\rm s}^2/4+(\Delta-\kappa_{\rm bs}/2-\omega_{\rm m})^2}\right]\\ &+g^2\left[\frac{\kappa_{\rm a}}{\kappa_{\rm a}^2/4+(\Delta+\kappa_{\rm bs}/2-\omega_{\rm m})^2}\right]\\ &-g^2\left[\frac{\kappa_{\rm a}}{\kappa_{\rm a}^2/4+(\Delta+\kappa_{\rm bs}/2-\omega_{\rm m})^2}\right].\end{aligned} \tag{4.74}$$

4.5.4 Transduction

Modelling the mechanical mode amplitude as $x(t) = x_0 \cos(\omega_{\mathrm{m}} t)$, where x_0 is the zero point fluctuation of the mechanical mode, the amplitudes of the field in the symmetric optical mode α_{s} and anti-symmetric optical mode α_{a} are modulated by the mechanics as:

$$\begin{aligned}\alpha_{\mathrm{s,a}}(t) =& \alpha_{\mathrm{in}} \sqrt{\frac{\kappa_{\mathrm{ex}}}{2}} \mathcal{L}_{\mathrm{s,a}}(0) \times \\ & \left[1 - \frac{\mathrm{i} x_0 G \mathcal{L}_{\mathrm{s,a}}(\omega_{\mathrm{m}})}{2} e^{-\mathrm{i}\omega_{\mathrm{m}} t} - \frac{\mathrm{i} x_0 G \mathcal{L}_{\mathrm{s,a}}(-\omega_{\mathrm{m}})}{2} e^{\mathrm{i}\omega_{\mathrm{m}} t}\right]\end{aligned} \tag{4.75}$$

where $G = g_0/x_0$, κ_{ex} is the external coupling rate to the fiber, $|\alpha_{\mathrm{in}}|^2 = P_{\mathrm{in}}$, and

$$\mathcal{L}_{\mathrm{s,a}}(\omega) = \frac{1}{-\mathrm{i}\left(\omega \pm \kappa_{\mathrm{bs}}/2 + \Delta\right) + \kappa_{\mathrm{s,a}}/2}. \tag{4.76}$$

In the experiment we measure the reflected signal, R, which may be written in terms of the optical mode amplitudes as,

$$R = \sqrt{\frac{\kappa_{\mathrm{ex}}}{2}} \left|\alpha_{\mathrm{s}} - \alpha_{\mathrm{a}}\right|^2 P_{\mathrm{in}}. \tag{4.77}$$

Solving for the power spectral density of the reflected signal, S_{RR} in terms of the power spectral density of the driven harmonic mechanics signal, S_{xx} and ignoring small terms, we can find the transduction coefficients $K(\Delta)$ which satisfies the expression:

$$\frac{S_{\mathrm{RR}}(\omega)}{P_{\mathrm{in}}^2} = \left|K(\Delta)\right|^2 S_{xx}. \tag{4.78}$$

where,

$$S_{xx} = 2\pi x_0^2 \left[\delta(\omega - \omega_{\mathrm{m}}) + \delta(\omega + \omega_{\mathrm{m}})\right] \tag{4.79}$$

Chapter 5

Multimode Optomechanics: I

5.1 Introduction: Two-Colour Interferometry and Switching Through Optomechanical Dark Mode Excitation

The work contained in the this chapter extends our optomechanical experiments from single mode systems, where a single optical mode is coupled to a single mechanical mode, to multimode systems with two optical modes. We used this same system to demonstrate wavelength conversion and amplification between the two optical modes [94]. Building on this experiment, here we demonstrate that this multimode optomechanical system can also be used to realize interference between widely separated optical modes, enabling the creation of an optical switch.

D.P. Lake and M. Mitchell fabricated the device, performed the experiments, and analyzed the data. D.P. Lake developed the theory, and all authors contributed to writing the manuscript.

5.2 Two-Colour Interferometry and Switching Through Optomechanical Dark Mode Excitation

5.2.1 Introduction

Interference is a ubiquitous physical phenomenon central to applications ranging from detection of gravitational waves [138] to the implementation of modulators and other integrated photonics technology [7, 139, 140]. Each of these examples interfere light at or near the same wavelength to convert differences in phase to changes in intensity. The emergence of frequency bin qubits [141–143] and a desire to interface quantum networking components based on different photonic technologies [144] has created the need for devices that interfere light with widely separated frequencies. Typically, this challenge has been addressed using nonlinear atomic [145, 146] or solid-state [147–150] materials, whose nonlinear optical susceptibility combined with precise photonic dispersion engineering can mediate interactions between different wavelengths of light. Here we demonstrate that cavity optomechanics [70] provides a realization of multi-colour optical interference that can be implemented in transparent linear materials through light's interaction with a nanofabricated mechanical resonator.

By coherently coupling light confined in an optical cavity to the motion of a mechanical resonance of the same cavity, light can be slowed and stored [78, 88, 89]. The signature of this coherent optomechanical coupling between phonons and photons is a narrow transmission window in the otherwise opaque optical cavity resonance spectrum, referred to as optomechanically induced transparency (OMIT) [88, 89], whose highly dispersive optical response is independent of the phase of its input field. In contrast, we demonstrate that phase is critically important to the optical properties of multimode optomechanical systems, in which multiple optical fields are injected into an optomechanical device. In the optical domain, multimode cavity optomechanical devices have been used for experimental demonstrations of wavelength conversion [103, 129, 151]. Microwave-frequency multimode devices have enabled low-noise frequency conversion [97] and entanglement between photons [152], whereas

hybrid electro-optomechanical devices have used coherent interference between optomechanically and piezomechanically driven motion to bridge microwave and optical frequencies [115]. Optical-frequency optomechanical devices whose intensity response is sensitive to the relative phase of multiple input optical fields with widely separated wavelengths, i.e., that involve interference between different colours of light, have yet to be reported despite proof-of-principle demonstrations based on atomic media [153–156] and recent advances in cavity optomechanical mediated coupling between multiple mechanical modes [157, 158].

Here we utilize a chip-based cavity optomechanical device with two optical modes coherently coupled to a single mechanical resonance to show that double optomechanically induced transparency (DOMIT), in which two optical modes coherently couple to the same mechanical mode, enables interference between photons separated by over 5 THz in frequency. Exploiting this effect, we demonstrate a novel phase-sensitive two-colour optical XOR gate [159]. This multi-colour interference is mediated by the mechanical bright mode and the mechanical dark mode [151, 160], which are directly excited for the first time here. This is in contrast to the partial dark mode excitation achieved in previous multimode optomechanical systems. In these works, which were focused on wavelength conversion, finite optomechanical cooperativity, C, precluded perfect dark mode excitation [151]. Furthermore, the optical XOR gate demonstrated here will be useful for multicolour classical and quantum optical information processing, e.g., for demonstrating quantum interference [148, 149] between frequency binned qubits [141–143], as well as optical sensing and metrology [150] using interference between widely separated wavelengths.

5.2.2 Double Optomechanically Induced Transparency (DOMIT)

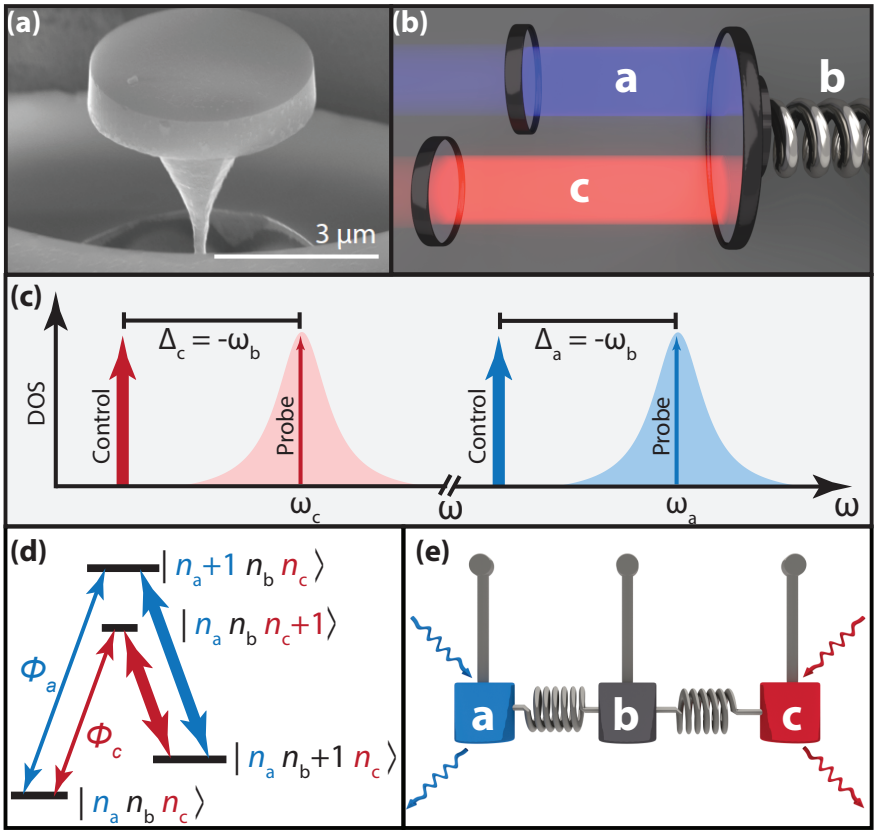

Figure 5.1: (a) Scanning electron micrograph of a diamond microdisk similar to the $\sim$5 μm diameter one studied in this work. (b) Schematic of a multimode optomechanical system where two Fabry Perot optical modes, a and c, are coupled to the same mechanical mode, b. (c) Frequency-domain illustration of the control and probe lasers used throughout this work, and their respective optical cavity modes. (d) The double-Λ level scheme used in this work, where the labels $n_{\rm a}, n_{\rm b}, n_{\rm c}$ represent the energy levels of modes a, b, and c, respectively. The thick lines represent photon-phonon exchange mediated by the control field, and the thin lines represent the probe fields with phase difference $\phi = \phi_{\rm a} - \phi_{\rm c}$. (e) DOMIT can be described by three coupled harmonic oscillators. The optical modes may be driven in-phase-, or out-of-phase, exciting either the mechanically bright or the mechanically dark mode.

Photon-photon interference and mechanical dark mode excitation demonstrated here uses a diamond microdisk cavity optomechanical system (Fig. 5.1(a)) whose essential elements can be analyzed as a generic Fabry Perot cavity shown in Fig. 5.1(b). The cavity supports two optical modes with widely separated frequencies ω_{a} and ω_{c}, each coupled via radiation pressure to a common mechanical resonator with frequency ω_{b} established in the generic system by one of the cavity mirrors. Each optical mode is excited with a weak probe field and a strong control laser that is red-detuned from its cavity mode by the mechanical frequency, $\Delta_{\mathrm{a}} = \Delta_{\mathrm{c}} = -\omega_{\mathrm{b}}$, represented graphically in Fig. 5.1(c). If the mechanical frequency exceeds the dissipation rate of each optical cavity mode, the system is in the resolved sideband regime, and the interaction Hamiltonian simplifies to [70]

$$\hat{H}_{\mathrm{int}} = -\hbar \left[\left(G_{\mathrm{a}} \hat{a}^{\dagger} + G_{\mathrm{c}} \hat{c}^{\dagger} \right) \hat{b} + \left(G_{\mathrm{a}}^{*} \hat{a} + G_{\mathrm{c}}^{*} \hat{c} \right) \hat{b}^{\dagger} \right], \tag{5.1}$$

where $\hat{a}\,(\hat{a}^{\dagger})$ and $\hat{c}\,(\hat{c}^{\dagger})$ are the creation (annihilation) operators of the optical probe field photons, $\hat{b}\,(\hat{b}^{\dagger})$ is the creation (annihilation) operator of the mechanical resonator phonons, and we employ the rotating wave approximation. Here $G_{\mathrm{a}} = g_{\mathrm{a}}\alpha_{\mathrm{a}}$ and $G_{\mathrm{c}} = g_{\mathrm{c}}\alpha_{\mathrm{c}}$ are the control- field assisted optomechanical coupling rates for modes a and c, set by the single photon-phonon coupling rates $g_{\mathrm{a,c}}$, and the control field amplitudes $|\alpha_{\mathrm{a,c}}|^2 = n_{\mathrm{a,c}}$. The specific cavity geometry determines $g_{\mathrm{a,c}}$, which generally increases as the effective cavity length decreases, whereas the control field amplitudes are set by their intracavity photon numbers $n_{\mathrm{a,c}}$, which are typically limited by nonlinear optical effects in the cavity. The system can be described by a double-Λ energy diagram, as illustrated in Fig. 5.1(d), which forms a closed loop under excitation from the two sets of control and probe fields.

In this DOMIT configuration, each of $\hat{a}$, $\hat{b}$, and $\hat{c}$ oscillate in the rotating frame at the same frequency. This allows relative phases between the various fields to be defined, despite their typically vast frequency differences. The key property is that the phases of each of the four fields forming the double-Λ loop affects the optical response [161, 162]. This is in

contrast to a single-Λ system, whose optical response depends only on the intensity of the control field. This behaviour is clearly elucidated by studying symmetric and antisymmetric combinations of the cavity's optical modes. These modes are referred to as the 'mechanically dark' $\left(\hat{\zeta}_{\rm dk} = (G_{\rm c}\hat{a} - G_{\rm a}\hat{c})/(\mathrm{i}\,\overline{G})\right)$ and 'mechanically bright' $\left(\hat{\zeta}_{\rm br} = (G_{\rm a}^{*}\hat{a} + G_{\rm c}^{*}\hat{c})/(\overline{G})\right)$ modes, as the dark mode can be entirely decoupled from the mechanical resonator while the bright mode can be maximally coupled; here $\overline{G} = \sqrt{|G_{\rm a}|^2 + |G_{\rm c}|^2}$.

These three modes are analogous to the modes of three coupled pendula, as shown in Fig. 5.1(e), in which the outer two pendula move in opposite directions while the central pendulum is stationary (dark mode); alternatively the three pendula move in the same direction (bright mode). This basis, with analogies in atomic physics [153, 156], elegantly reveals the importance of optical phase to the system's behaviour. The classical amplitudes of the bright and dark modes when both probe fields are resonant with their respective cavity modes are (see Supplementary Information):

$$\begin{aligned}\zeta_{\rm dk} &= \frac{2\sqrt{\kappa_{\rm ex}}s_{\rm in}}{\kappa}\sin\left(\phi/2\right),\\ \zeta_{\rm br} &= \frac{2\sqrt{\kappa_{\rm ex}}s_{\rm in}}{\kappa\left(1+\overline{C}\right)}\cos\left(\phi/2\right),\end{aligned} \tag{5.2}$$

where $\kappa_{\rm ex}$ and κ are the external coupling and total loss rates of the cavity modes respectively, $s_{\rm in}$ is the input amplitude of the two probe lasers, $\overline{C} = 4\overline{G}^2/\kappa\gamma_{\rm b}$ is the two-mode optomechanical cooperativity, and $\gamma_{\rm b}$ is the damping rate of the mechanical resonance. For simplicity, we assume that κ, $\kappa_{\rm ex}$ and $s_{\rm in}$ are the same for each optical mode. In our experimental setup described below, $\phi_{\rm a}$ is the phase difference between control and probe field belonging to mode a and $\phi_{\rm c}$ is the phase difference between control and probe field belonging to mode c. The total phase difference is then $\phi = \phi_{\rm a} - \phi_{\rm c}$. As each of the probe fields are derived from their respective control field via electro-optic modulation, changes to the

control field phases do not affect the system response because they will also shift the probe phase by the same amount. Note that in principle the system could be operated with any of the four control and probe phases used to determine the nature of the interference.

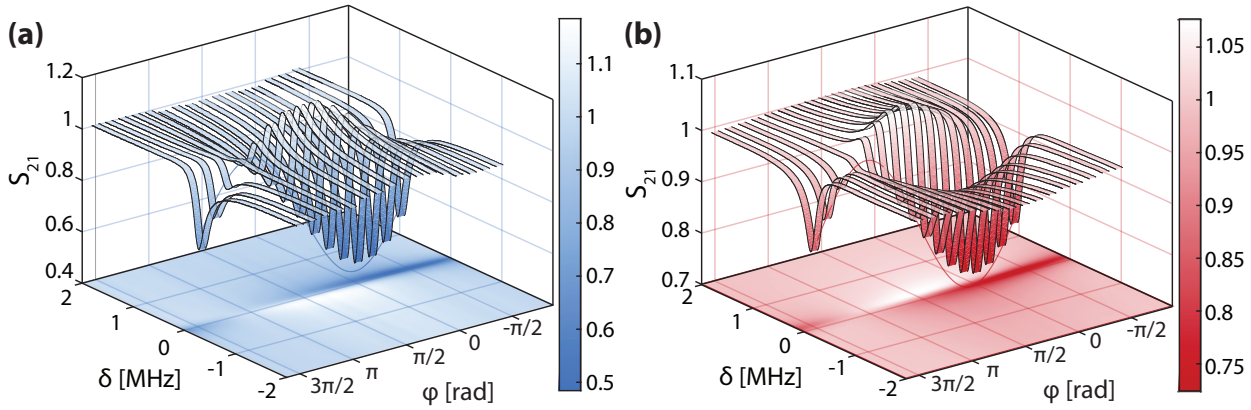

Figure 5.2: (a,b) Cavity optical response to the probe signal for modes a and c respectively, as a function of cavity-probe detuning δ_Δ, and the probe phase difference ϕ, as recorded by the vector network analyzer from the photodetected heterodyne signal. The control fields are at fixed detuning $\Delta_\mathrm{a} = \Delta_\mathrm{c} = -\omega_\mathrm{b}$.

Equation (5.2) shows that adjusting ϕ to $\pm\pi$ e.g., by delaying one of the probes, allows complete selective excitation of ζ_dk. In contrast, previous experimental studies of dark-modes in wavelength conversion [151] only allow complete dark-mode excitation in the limit $\overline{C} \to \infty$. When all DOMIT processes are resonant, this delay corresponds to a half period of the mechanical resonator. Equation (5.2) also shows that full optical power transfer to the dark mode is possible, while the bright mode has a reduced maximum amplitude due to coherent optomechanical transfer of energy to the mechanical resonator. Optically manipulating the system in this basis is central to optomechanical wavelength conversion free from mechanical thermal decoherence effects [160, 163] when the optomechanical coupling exceeds the thermal decoherence rate [79, 129, 151]. However, none of these previous single

OMIT studies have completely isolated or selectively populated the mechanically dark mode. Conceptually related studies demonstrating optomechanical control of interference between two mechanical modes have not yet been used to interfere different colours of light.

To demonstrate DOMIT, we evanescently coupled control and probe fields via an optical fiber taper waveguide into modes of a diamond microdisk device similar to that in Fig. 5.1(a) and previous studies [35, 90]. Our modes have resonant wavelengths $\lambda_{\rm a} \sim 1520$ nm and $\lambda_{\rm c} \sim 1560$ nm and sufficiently low optical loss ($\kappa_{\rm a}/2\pi \sim 0.87$ GHz, $\kappa_{\rm c}/2\pi \sim 1.20$ GHz) to allow resolved sideband optomechanical coupling to the microdisk's $\omega_{\rm b}/2\pi = 2.1$ GHz fundamental mechanical radial breathing mode (dissipation rate $\gamma_{\rm b}/2\pi = 0.285$ MHz). Typical optical and mechanical mode spectroscopy measurements are described in the Supplementary Information. The per-photon optomechanical coupling rates, $g_{\rm a} = g_{\rm c} \sim 2\pi \times 25$ kHz, allow optomechanical cooperativity > 1 and observation of OMIT when approximately $n_{\rm a,b} > 5 \times 10^5$ control photons are coupled into either of the cavity modes [90]. Achieving this large photon number is possible in our microdisks due to diamond's low nonlinear absorption and excellent thermal properties. In all of our measurements presented below, the input control fields are detuned from their respective cavity modes such that OMIT conditions $\Delta_{\rm a} = \Delta_{\rm c} = -\omega_{\rm b}$ for each mode are satisfied. The deviation of the OMIT line shape from a Lorentzian [88,89] can be attributed to the use of an amplitude modulator with nonzero chirp in generating one of the probe lasers, and imperfect detuning of the control fields, as studied in previous work [94]. Note that the microdisks support regularly spaced modes spanning the IR and visible spectrum [35]; our modes are chosen due to the compatibility of their wavelengths with telecommunications equipment needed for the measurements described below.

To excite $\zeta_{\rm dk}$ and $\zeta_{\rm br}$, OMIT spectra [90] for modes a and c were recorded for varying relative phase ϕ between the two probe fields, as shown in Figs. 5.2(a,b). In these measurements, ϕ is controlled by adjusting a delay between two radio frequency (RF) signals split from the same signal generator, which are then used to create the probe fields through optical

modulation of two independently running control lasers (see Methods and Supplementary Information for details). Our setup is robust to phase drifts of either control laser, as discussed above. Each pair of probe and control fields is isolated by optical filtering and then detected on a high-speed photodetector as a function of varying probe-cavity detuning δ_Δ. Each probe amplitude is then measured by downmixing the heterodyne signal that it creates through interference with its corresponding control field using a vector network analyzer. At $\phi = 0$, the deep OMIT window present in each probe output spectrum when $\delta_\Delta = 0$ indicates excitation of $\zeta_{\rm br}$, whereas, when $\phi = \pi$, the response of the bare cavity, which is broad compared to the OMIT window ($\kappa \gg \gamma_{\rm b}(1+C)$), is restored for all probe detunings, indicating excitation of $\zeta_{\rm dk}$. The depth of the OMIT window as a function of the phase delay is fit using solutions to Eq. (5.2) in the a and c basis (see Supplementary Information), and is shown for $\delta_\Delta^{\rm a,c} = 0$ in Figs. 5.2(a,b), where it is seen to agree well with theory.

5.2.3 Optomechanical Bright and Dark Mode Coupling

When OMIT resonance conditions for both modes are satisfied, i.e., $\Delta_{\rm a} = \Delta_{\rm c} = -\omega_{\rm b}$ and $\delta_\Delta^{\rm a} = \delta_\Delta^{\rm c} = 0$, the $\zeta_{\rm br}$ and $\zeta_{\rm dk}$ states are decoupled from each other. However, by incrementing cavity-probe detuning of one mode by $+\delta_\Delta$, and decrementing cavity-probe detuning of the other mode by $-\delta_\Delta$, we induce a bright-dark state coupling. This can also be accomplished by shifting $\Delta_{\rm a}$ and $\Delta_{\rm c}$ in the same manner. Coupling between bright and dark states manifests as a temporal oscillation in the intensity of the probe fields transmitted through the cavity, allowing differences in their interaction with the dissipative mechanical resonator to be observed directly.

Our measurement of both probe colours is plotted in Fig. 5.3(a), for the case that $2\delta_\Delta = 3.37$ MHz and $\phi = 0$, after digitally down-mixing the total (probe and control) photodetected signal from each colour recorded on a high-speed oscilloscope to remove fast oscillations near $\omega_{\rm b}$ due to beating between probe and control fields. Each down-mixed signal is proportional to the amplitude, equivalently, the square root of energy, of the intracavity

field at its respective probe frequency. As the modulation depth is bounded above by the dark-state transmission (bare cavity response), and bounded below by the bright-state transmission (OMIT window depth), the oscillation amplitude follows the δ_Δ dependence of the OMIT features. This dependence is confirmed by measuring the dependence of oscillation amplitude on increasing δ_Δ, as shown in Fig. 5.3(b), which matches well with theoretical predictions (see Supplementary Information for details), giving estimates of $\overline{C} = 3.6$ and $\overline{C} = 4.2$ from fits to ω_a and ω_c photodetected signals, respectively. This discrepancy in the cooperativities is attributed to non-ideal modulation when creating each probe and imbalance of the cooperativities of each mode.

We can also reconstruct the output of ζ_dk and ζ_br by inferring a and c from the measured phase and amplitude of the output probe fields in Fig. 5.3(a). This reconstruction requires the additional step of accounting for a slight phase shift due to differing optical path lengths at ω_a and ω_c caused by dispersion in the experimental setup, whose effect can be seen in the inset of Fig. 5.3(a). This deleterious phase shift was corrected in post-processing while determining ζ_br and ζ_dk. An example of the reconstructed bright and dark mode intensity is shown in Fig. 5.3(c), where flopping between the bright and dark state is evident. Notably, a difference in maximum intensity of ζ_dk and ζ_br is evident from their differing peak values. This difference can be related to the energy dissipated by the bright state due to its interaction with the mechanical resonance, and is found from Eq. (5.2) generalized for non-zero δ_Δ (see Supplementary Information) to scale as $(1+\overline{C}/(1+4(\delta_\Delta/\gamma_\mathrm{b})^2)^{-2}$. Additional measurements of the intensity of a, c, ζ_br, and ζ_{dk} as a function of δ_Δ and time are plotted in Figs. 5.3(d–g), which clearly show how the oscillation period decreases with increasing δ_Δ, as expected theoretically. The effect of mismatch in operating parameters between mode a and c is calculated in the supplementary material, where the main effect of mismatch in optomechanical coupling or probe amplitudes is to decrease the contrast of the interference, whereas mismatch in frequency or optical decay rates leads to dissipative and dispersive coupling between the bright and dark states.

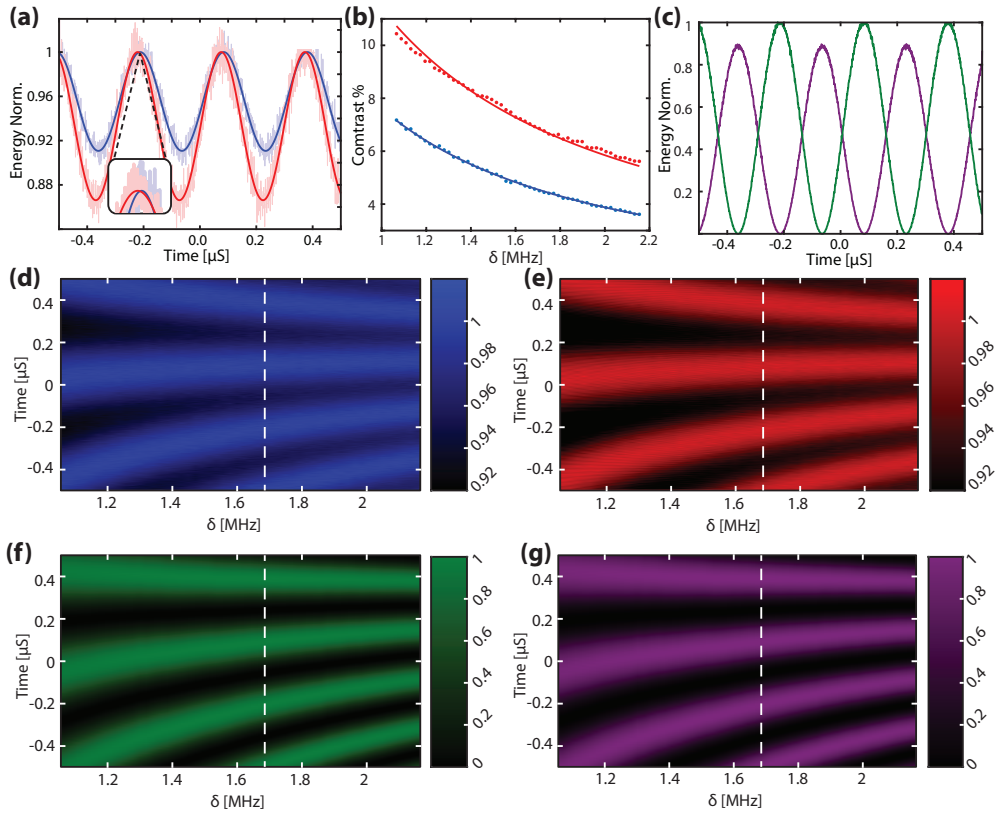

Figure 5.3: (a) Example of the oscillations in stored energy in mode a (blue trace) and mode c (red trace) for $2\delta_\Delta = 3.37$ MHz, measured by downmixing the heterodyne signal at each colour in the time domain to isolate each probe amplitude. Inset: highlight of the slight time delay between the output of modes a and c caused by dispersion in the setup. (b) Amplitude of the oscillations for mode a (blue) and mode c (red) as a function of δ_Δ, and corresponding predictions from the model given in the text. (c) Normalized bright (purple) and dark (green) state energy for $2\delta_\Delta = 3.37$ MHz, as inferred from the optical output of modes a and c shown in (a). (d-g) Oscillations as a function of time and δ_Δ of outputs from modes a, c, ζ_{br}, and ζ_{dk} respectively.

5.2.4 Two-Colour Switching

The phase-dependent response of this multicolour DOMIT system, together with our ability to selectively excite ζ_{dk} or ζ_{br}, can be harnessed to create a novel form of a phase-dependent all-optical switch. In this device the output intensity of one probe is dependent on the phase of the other probe, and follows the truth table of an XOR gate with probe field phases of 0

and π mapping onto Boolean values 0 and 1. The maximum contrast achievable is determined by the maximum OMIT dip depth, and is given by $\overline{C}^2/(1+\overline{C})^2$. This indicates that, in principle, the contrast can be made to approach unity for systems with large cooperativity.

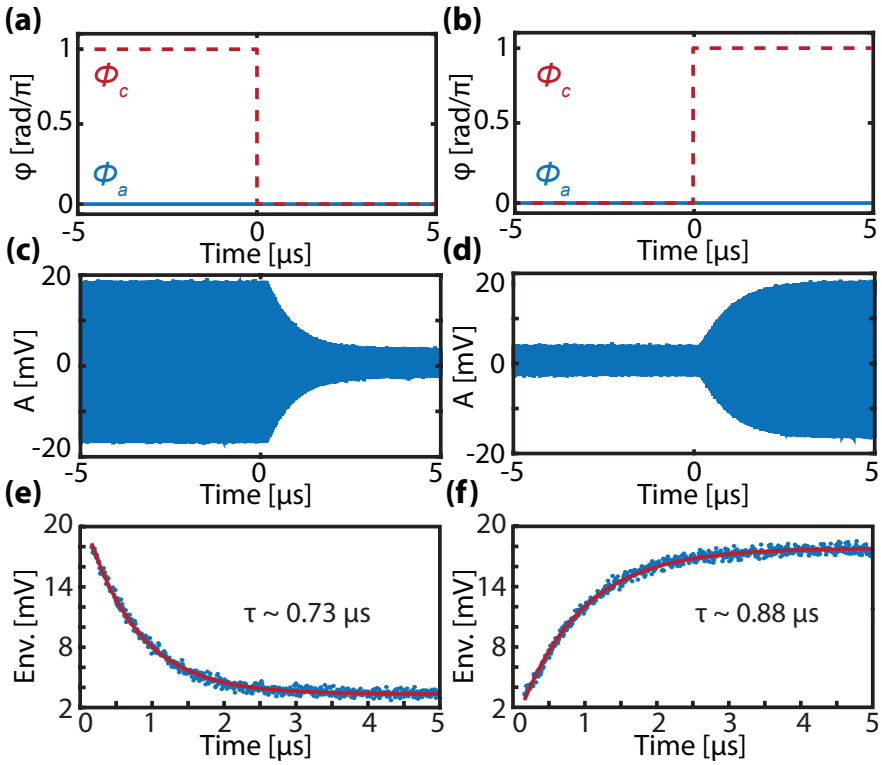

Figure 5.4: (a,b) Phases of the input probe fields vs. time which cause probe c to switch the response of probe a off and on, respectively. (c,d) Photodetected cavity output of probe a when the input phase of probe c is switched temporally as shown in (a) and (b). The rapid oscillations are caused by beating between the control and probe, and the envelope reveals the action of the switch. (e,f) Envelope extracted from the peak values of the data in (c,d) and fit with exponentially falling and rising functions, respectively.

This switching action can be inferred from Figs. 5.2(a,b), and directly observed in the time domain by varying the phase ϕ_c of the mode c probe following a temporal step function, while maintaining constant phase ϕ_a of the mode a probe, as sketched in Fig. 5.4(a) for switching off and Fig. 5.4(b) for switching on. Experimental time domain data showing the resulting change in probe a transmission is shown in Figs. 5.4(c,d). As mentioned above, the relative phase $\phi = \phi_a - \phi_c$ is controlled by introducing an electrical phase delay in the RF signal driving the electro-optic modulator responsible for creating the mode c probe (see Methods

and Supplemental Information for details). The rapid oscillations are due to beating between the probe and control laser, whereas the oscillation envelope is proportional to the amplitude of the transmitted probe. From this upper envelope, shown in Figs. 5.4(e,f), we can measure the switch response speeds: fits with an exponential function yield fall and rise times of 0.73 μs and 0.88 μs respectively. Assuming that $\kappa_{\mathrm{a,c}} \gg \gamma_{\mathrm{b}}$, the switching speed can be shown to be $\tau^{-1} = \gamma_{\mathrm{b}}(1 + \overline{C})$, which approaches zero for sufficiently large $\overline{C}$. This switching speed implies $\overline{C} = 2.96$ and $\overline{C} = 3.89$ respectively, for the fall and rise times illustrated in Figs. 5.4(c,d), consistent with expectations for the control field amplitudes. The observed differences in the fall and rise times are presumed to be due to differences in intracavity control field amplitudes during the respective measurements.

5.2.5 Discussion

In summary, we demonstrate coherent interference between spectrally-separated optical modes mediated by optomechanical coupling. By adjusting the phase between different colour probe fields entering the cavity, we selectively excite either a mechanically bright or a mechanically dark mode, and demonstrate controllable coupling between the two modes. Notably, we exploit difference between bright- and dark-state transmission to demonstrate a novel two-colour, all-optical switch, where the control and target are at different wavelengths.

Our system has great potential for applications to quantum information processing where interference between frequency binned qubits is desirable [142], such as frequency-domain Hong-Ou-Mandel interference [148,149], chromatic and time-domain interferometry [141,150, 164], and microwave-to-optical conversion via the optomechanical dark mode [115]. As the diamond devices studied here have high-quality optical modes in the visible spectrum [35], interference between telecommunication wavelength light and light resonant with quantum emission from diamond nitrogen vacancy (637 nm) and silicon vacancy (736 nm) colour centres will be feasible in future studies, providing a path towards linking quantum networking components. Furthermore, as detailed in the supplementary information, our technique

could be extended to many optical modes whose operating wavelengths are only limited by the transparency of the diamond and the existence of high-Q modes; thus, our technique could lead to many-colour interference processes. Finally, we note that this interference is quite general and could be utilized for non-optical inputs such as magnetic or electric fields, provided they couple to the mechanical degree of freedom. Future experiments operating in the quantum domain will benefit from cryogenic pre-cooling of the device to its mechanical quantum ground state, which is achievable at dilution fridge temperatures for the > 2 GHz frequency mechanical mode measured in this article.

5.3 Methods

The device used for all experiments in this work is a $\sim 5\,\mu$m microdisk resonator fabricated from single crystal diamond using the process outlined in [37, 137]. A full schematic of the experimental apparatus used in the experiments is given in the SI. In all of the measurements light was coupled evanescently into and out of the microdisk using a dimpled optical fiber taper positioned using motorized stages, as discussed in [35, 90].

To measure the optomechanically induced transparency (OMIT) spectra of each microdisk mode, sidebands were created on each respective control laser for use as probe fields, using either phase, $\phi(t)$, or amplitude, $A(t)$, electro-optic modulators. For the data in Fig. 5.2 of the main text, the electrical RF drive for each modulator was derived from the same vector network analyzer (VNA), with one path undergoing a controllable phase shift relative to the other. This controllable phase shift was achieved by placing an electronic phase shifter before one of the electro–optic modulators (EOMs). Because the phase shifter transmission varied as a function of phase, a variable electrical attenuator was calibrated and used to maintain balance between the probe laser powers at every step in phase, by controlling the RF modulation amplitude. An optical variable attenuator (VA) was used on the 1560 nm laser arm to attempt to balance the input power of each laser before they were combined via

a 50/50 waveguide coupler, and amplified with an erbium doped amplifier (EDFA) before being routed to the sample chamber (a nitrogen purged enclosure) and device. The other output of the 50/50 coupler was used to perform slow laser wavelength locking via a photodetector (PD) and optical spectrum analyzer (OSA) connected to the control computer. The signal exiting the sample chamber was then divided on a 90/10 waveguide coupler. The 10% port was routed to a low speed PD for use in measuring the cavity transmission during the initial setup, and the 90% port was sent to the wavelength division multiplexer (WDM). By connecting the WDM to a high-speed photodetector, the output of either mode a or c could be selected.

For the bright–dark mode coupling experiment (Fig. 5.3 in the main text) and the time domain switch (Fig. 5.4 in the main text), a two–channel arbitrary waveform generator (AWG) was used as the RF source, with one channel assigned to each modulator. Acquisition was performed using a digital spectrum analyzer (DSA), which was triggered by the AWG. To isolate the beat note between the probe field of one mode and the converted probe from the other mode the signal acquired on the DSA was digitally downmixed post–acquisition.

5.3.1 Experiment Setup and Calibration

The optomechanical cavity utilized in this work is a single–crystal diamond (SCD) microdisk, fabricated according to the process outlined in Refs. [37, 137], an example of which is shown in Fig. 5.5(a). An advantage of microdisk cavities is that they support multiple optical whispering gallery modes across their transparency window, all of which exhibit dispersive optomechanical coupling to the fundamental radial breathing mode (RBM) of the microdisk [90], as illustrated schematically in Fig. 5.5(b). Diamond's large electronic bandgap, Young's modulus, and best-in-class thermal conductivity make it an ideal material for use in cavity optomechanics as it can support large intracavity photon number N, and high optical and

mechanical quality factors. Additionally, colour center qubits present in diamond, such as silicon and nitrogen vacancies, make it a promising platform for realizing hybrid quantum systems [117].

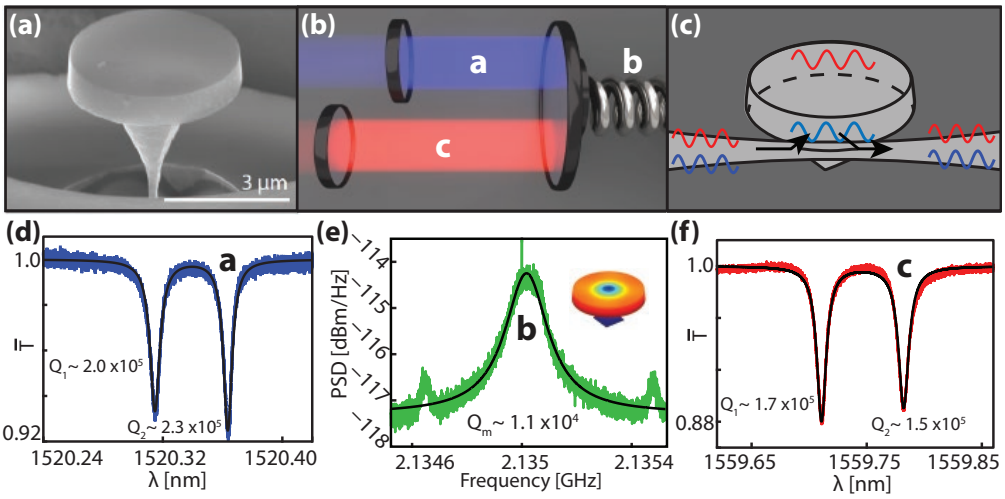

Figure 5.5: (a) Scanning electron micrograph of a diamond microdisk similar to the one used in this work. (b) Cartoon of a canonical multimode optomechanical system. Here mode b, represented as a spring, is dispersively coupled to both optical modes a and c. (c) Cartoon of fiber taper–microdisk coupling. (d) Normalized fiber taper transmission scan of mode a used in this experiment, with fit. (e) Power spectral density of the fiber taper transmission when the input laser is tuned near a cavity mode, revealing fluctuations from thermomechanical motion of the cavity's mechanical radial breathing mode, b. A COMSOL simulated displacement field profile of the radial breathing mode is shown in the inset. (f) Normalized fiber taper transmission scan of optical mode c, with fit.

Light from two tuneable diode lasers was coupled into and out of the microdisk using a dimpled optical fiber taper positioned adjacent to the microdisk as illustrated in the cartoon in Fig. 5.5(c). The spatial overlap of the evanescent field of the fiber and the optical modes of the microdisk permit efficient coupling, allowing measurement of cavity modes in transmission and reflection. Two telecommunications wavelength modes at $\lambda_a = 2\pi c/\omega_a = 1520$ nm and $\lambda_c = 2\pi c/\omega_c = 1560$ nm were selected for this work, as they were in the operat-

ing range of the available lasers (Newport TLB-6700) and optical amplifier (Pritel EDFA). However, this could be extended to visible wavelengths, where these devices have demonstrated high quality optical modes [35]. The optical modes are each dispersively coupled to the microdisk's fundamental mechanical radial breathing mode (RBM) whose frequency is $\omega_{\rm b}/2\pi = 2.1$ GHz, with vacuum optomechanical coupling rates, $g_{0,\rm a}, g_{0,\rm c} \sim 2\pi \times 25$ kHz. Measurements of the fiber taper optical transmission spectrum for wavelengths scanned across modes a and c are shown on Figs. 5.5(d,f), and the power spectral density of the fluctuations imparted on photodetected output due to thermally driven mechanical motion of the RBM when the input laser is tuned close to resonance with an optical mode [165–167] is shown on Fig. 5.5(e). Note that both optical modes are standing wave doublets due to surface roughness induced coupling between the clockwise and counterclockwise propagating whispering gallery modes of the microdisks [168]. For all of the measurements presented here the long wavelength doublet mode was used, and the lower wavelength doublet mode was assumed to not influence the observed phenomena. This device operates in the sideband resolved regime, $\omega_{\rm b} \gg \kappa_{\rm a}, \kappa_{\rm c}$, where $\kappa_{\rm a}/2\pi \sim 0.87$ GHz, and $\kappa_{\rm c}/2\pi \sim 1.20$ GHz are the energy decay rates of the optical modes. A previous study [37] found that the optical quality factor, $Q = \omega/\kappa$, of this device is likely still limited by surface roughness induced by the fabrication procedure.

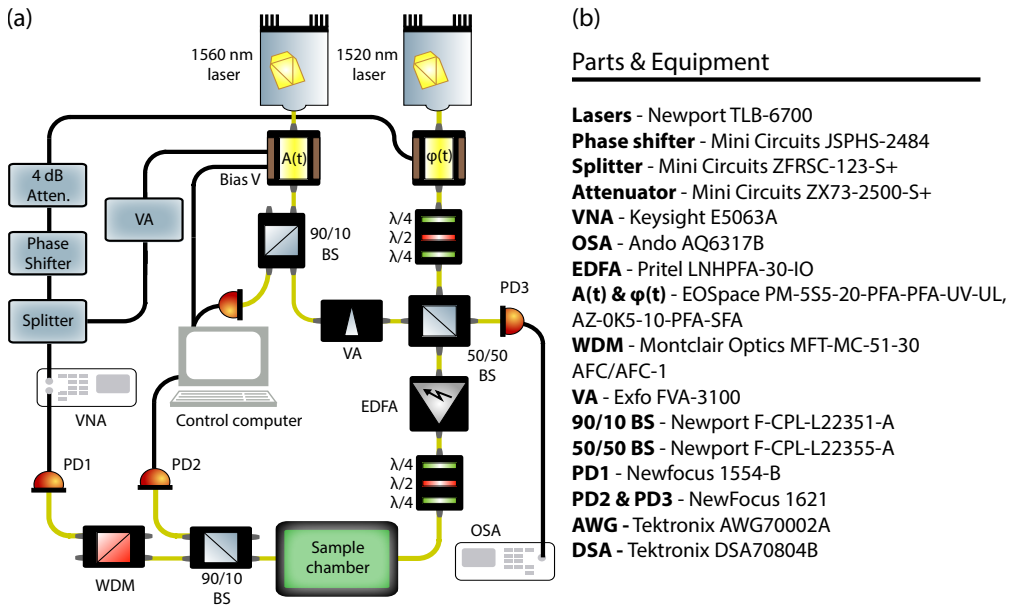

Figure 5.6: (a) Setup used in the experiments. The Vector Analyzer (VNA) acted as the RF source for modulators on each path. The resulting signal was spectrally filtered to isolate for the mode of interest. Key: OSA (Optical spectrum analyzer), BS (Beam splitter), VA (Variable attenuator), BS (Beam splitter), EDFA (Erbium doped fiber amplifier), WDM (Wavelength division multiplexer), PD (Photodetector). (b) Parts and equipment used in the experiment.

Figure 5.6 shows a schematic representation of the experimental setup used for the above measurements and those shown in the main text. Additional information can be found in the methods section of the main text.

5.3.2 Electro–Optic Modulation and Probe Measurement Model

The results demonstrated here require strong control fields and weak probe fields, which were generated through EOM modulation of the control fields. Due to the available equipment, a phase EOM was used for the mode near ω_a and an amplitude EOM for the mode near ω_c. This leads to differences in the probe transduction as measured on the high speed PD.

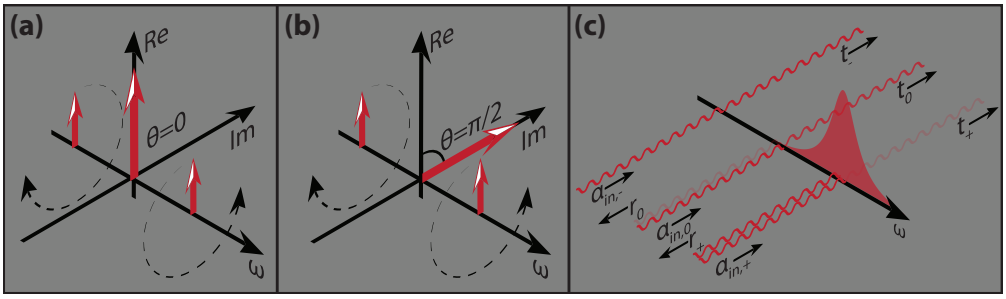

Figure 5.7: (a) Frequency components of pure amplitude modulation in a frame rotating at the carrier frequency. The two sidebands are placed at $\pm\omega_{\mathrm{m}}$, where ω_{m} is the frequency of modulation. Here the modulation is in a direction parallel to the carrier tone. (b) Frequency components of a pure phase modulation. Unlike the case of amplitude modulation, the modulation occurs in a direction perpendicular to the carrier tone. (c) Illustration of the expected reflected and transmitted signals for the case of a red detuned pump laser modulated such that one sideband is near resonance with the cavity.

For weak modulation ($\beta \ll 1$, where β is the index of modulation), we can assume the output of the EOM has three distinct frequency components at ω, $\omega \pm \omega_{\mathrm{m}}$, where ω is the frequency of the carrier tone and ω_{m} is the frequency of modulation. For convenience we will work in a frame rotating with the carrier at ω. The type of modulation can be inferred from the sum of the sideband components in the imaginary plane. For pure amplitude modulation they will oscillate parallel to the carrier with frequency ω_{m}, whereas for pure phase modulation they will oscillate perpendicular to the carrier as illustrated in Fig. 5.7(a,b). We note that since we are working in the rotating frame, we can choose the phase of the carrier out of convenience, as only the relative phase between the sidebands and the carrier tone influences the result.

In practice, the construction of amplitude EOMs is often such that the chirp is non-zero, which results in non-zero phase modulation of the outgoing field. With this in mind, we can write the transmission of the modulated field through the cavity as $|\alpha_{\text{out}}\rangle = t\,|\alpha_{\text{in}}\rangle$, where

$$t = \mathbf{diag}\{t_+, t_0, t_-\},\ |\alpha_{\text{in}}\rangle = \alpha_{\text{in}}^0 \left(\tfrac{\beta}{2}e^{-i\omega_m t}, e^{i\theta}, \tfrac{\beta}{2}e^{i\omega_m t}\right)^{\mathbf{T}}. \tag{5.3}$$

In the previous expression, t_+, t_0, t_- are the transmission coefficients at the upper sideband, carrier frequency, and lower sideband, respectively. The angle between the sidebands and the carrier is θ, where $\theta = n\pi$ for a pure amplitude modulator and $\theta = \pi/2 \pm n\pi$ for a pure phase modulator, where n is an integer.

The frequency components of the field transmitted through the cavity can be projected using the matrices

$$\mathbf{P}_+ = \begin{pmatrix} 0 & 1 & 0 \\ 0 & 0 & 1 \\ 0 & 0 & 0 \end{pmatrix}, \mathbf{P_0} = \begin{pmatrix} 1 & 0 & 0 \\ 0 & 1 & 0 \\ 0 & 0 & 1 \end{pmatrix}, \mathbf{P}_- = \begin{pmatrix} 0 & 0 & 0 \\ 1 & 0 & 0 \\ 0 & 1 & 0 \end{pmatrix}. \tag{5.4}$$

Using the above expressions, we can write the signal measured on the PD up to a constant as $S = S_0 + S_1 + S_2$, where

$$S_0 = \langle\alpha_{\text{out}}|\, P_0\, |\alpha_{\text{out}}\rangle\,, \tag{5.5}$$

$$S_1 \cos(\omega_m t + \phi_1) = \langle\alpha_{\text{out}}|\, P_+\, |\alpha_{\text{out}}\rangle + \langle\alpha_{\text{out}}|\, P_-\, |\alpha_{\text{out}}\rangle\,, \tag{5.6}$$

$$S_2 \cos(2\omega_m t + \phi_2) = \langle\alpha_{\text{out}}|\, P_+^2\, |\alpha_{\text{out}}\rangle + \langle\alpha_{\text{out}}|\, P_-^2\, |\alpha_{\text{out}}\rangle\,. \tag{5.7}$$

By electronic filtering we isolate the $\mathcal{O}(\omega_{\text{m}})$ component of the signal, where

$$S_1 = \beta \left| t_0^* t_+ e^{-i\theta} + t_0 t_-^* e^{i\theta} \right|. \tag{5.8}$$

To find the expected signal we use $\theta = 0.6093$[Rad], as measured directly from the OMIT spectra, and an agreement with the manufacturer's specifications. In this work the control laser is red detuned from a sideband-resolved cavity, as illustrated in Fig. 5.7(c). In this case the lower sideband passes un–attenuated ($t_- = 1$, $r_- = 0$), and the control laser is approximately real $t_0 \approx t_0^*$. In this case, to first order in modulation angle, the expected signal is

$$S_1 \approx \beta t_0 \sqrt{(r_+ - 1 - \cos(2\theta))^2 + \sin^2(2\theta)}, \tag{5.9}$$

where we have used the fact that $t_+ + r_+ = 1$. Using the chirp parameter [169] specified by the manufacturer for the amplitude EOM we calculate $\theta = 0.6093$ [rad]. This value also agrees well to direct fits to the OMIT lineshapes.

In the case of pure phase modulation ($\theta = \pi/2 \pm n\pi$) this simply reduces to

$$S_1 \approx \beta t_0 |r_+|. \tag{5.10}$$

5.3.3 Data Analysis

In order to examine the bright and dark state coupling as shown in Fig. 5.3 in the main text, time-domain data was directly acquired on the DSA. For this dataset we digitally down mixed by the carrier frequency ω_b, which allowed us to extract both the amplitude of the signal, and the phase relative to the carrier signal for modes a and c. Due to chirp in the amplitude modulator, dispersion in the fiber, and difference in the optical path length of the two output arms of the WDM, a delay between the mode outputs was observed. To correct for this we fit the oscillating output of each mode to a sinusoidal function, and subtract the phase difference. Using this we are able to reconstruct the output of the dark and bright states.

5.3.4 Double Optomechanically Induced Transparency

In this work, two optical modes a and c exhibit dispersive optomechanical coupling to the mechanical mode b. We denote the frequencies of these modes as ω_{a}, ω_{c}, and ω_{b}, respectively, and the vacuum optomechanical coupling rates as g_{a}, and g_{c}. This is modelled by the Hamiltonian $\hat{H} = \hat{H}_0 + \hat{H}_{\mathrm{int}}$, where $\hat{H}_0$ describes the internal dynamics of each mode and $\hat{H}_{\mathrm{int}}$ is the interaction Hamiltonian

$$\begin{aligned}\hat{H}_0 &= \hbar\omega_{\mathrm{a}}\hat{a}^\dagger\hat{a} + \hbar\omega_{\mathrm{b}}\hat{b}^\dagger\hat{b} + \hbar\omega_{\mathrm{c}}\hat{c}^\dagger\hat{c},\\ \hat{H}_{\mathrm{int}} &= -\hbar g_{\mathrm{a}}\hat{a}^\dagger\hat{a}\left(\hat{b}+\hat{b}^\dagger\right) - \hbar g_{\mathrm{c}}\hat{c}^\dagger\hat{c}\left(\hat{b}+\hat{b}^\dagger\right).\end{aligned} \tag{5.11}$$

We describe the coupling between the optical modes and a waveguide using input-output theory

$$\begin{aligned}\dot{\hat{a}} &= \frac{\mathrm{i}}{\hbar}\left[\hat{H},\hat{a}\right] - \frac{\kappa_{\mathrm{a}}}{2}\hat{a} + \sqrt{\kappa_{\mathrm{a}}^{\mathrm{ex}}}\hat{a}_{\mathrm{in}},\\ \dot{\hat{c}} &= \frac{\mathrm{i}}{\hbar}\left[\hat{H},\hat{c}\right] - \frac{\kappa_{\mathrm{c}}}{2}\hat{c} + \sqrt{\kappa_{\mathrm{c}}^{\mathrm{ex}}}\hat{c}_{\mathrm{in}},\end{aligned} \tag{5.12}$$

where $\hat{a}_{\mathrm{in}}$ and $\hat{c}_{\mathrm{in}}$ are the input field operators for each optical mode, and κ_{a}, κ_{c} and $\kappa_{\mathrm{a}}^{\mathrm{ex}}$, $\kappa_{\mathrm{c}}^{\mathrm{ex}}$ are the total energy decay and waveguide–cavity coupling rates of mode a and c, respectively. Note that in this work the cavity is double-sided and consequently the cavity–waveguide coupling rate in each direction is $\kappa_{\mathrm{ex}}/2$.

For all scenarios described in this work control lasers were red-detuned from the cavity modes whereas probe lasers were tuned near resonance. Although the modulators create multiple sidebands, the spectral selectivity of the cavity is such that only one sideband will contribute to the physics of the problem. This allows us to linearize about the control fields using the substitutions $\hat{a} \to \alpha_{\mathrm{a}} + \hat{a}$, and $\hat{c} \to \alpha_{\mathrm{c}} + \hat{c}$, where $\alpha_{\mathrm{a}}, \alpha_{\mathrm{c}}$ are the classical control fields amplitudes, and $\hat{a}$, $\hat{c}$ now represent the cavity fluctuations near the probe frequencies. We also use similar substitutions for the input field amplitudes, such that $\hat{a}_{\mathrm{in}}$ and $\hat{c}_{\mathrm{in}}$ are the input

probe field operators. Neglecting small order terms, and accounting for a static mechanical shift induced by constant radiation pressure, our interaction Hamiltonian becomes

$$\hat{H}_{\rm int} = -\hbar g_{\rm a}\left(\alpha_{\rm a}\hat{a}^\dagger + \alpha_{\rm a}^*\hat{a}\right)\left(\hat{b}+\hat{b}^\dagger\right) - \hbar g_{\rm c}\left(\alpha_{\rm c}\hat{c}^\dagger + \alpha_{\rm c}^*\hat{c}\right)\left(\hat{b}+\hat{b}^\dagger\right). \tag{5.13}$$

We consider the case where the control lasers are red–detuned, with the probe fields on resonance such that $\Delta_{\rm i}^{\rm ctrl} = \omega_{\rm i}^{\rm ctrl} - \omega_{\rm i} = -\omega_{\rm b}$, and $\omega_{\rm i}^{\rm probe} - \omega_{\rm i}^{\rm ctrl} = \omega_{\rm b}$, where $i = \{\rm a,c\}$. In this case, selecting only the resonant terms under the rotating wave approximation, the above expression simplifies to

$$\hat{H}_{\rm int} = -\hbar\left(G_{\rm a}\hat{a}^\dagger\hat{b} + G_{\rm a}^*\hat{a}\hat{b}^\dagger + G_{\rm c}\hat{c}^\dagger\hat{b} + G_{\rm c}^*\hat{c}\hat{b}^\dagger\right), \tag{5.14}$$

where $G_{\rm a} = \alpha_{\rm a}g_{\rm a}$ and $G_{\rm c} = \alpha_{\rm c}g_{\rm c}$. Transforming into frequency space, in a frame rotating with the control lasers, and making use of Eqs. 5.12 and 5.14 we may solve for the mode operators using the set of coupled linear equations

$$\begin{bmatrix} \chi_{\rm a}^{-1}(\omega) & -{\rm i}\,G_{\rm a} & 0 \\ -{\rm i}\,G_{\rm a}^* & \chi_{\rm b}^{-1}(\omega) & -{\rm i}\,G_{\rm c}^* \\ 0 & -{\rm i}\,G_{\rm c} & \chi_{\rm c}^{-1}(\omega) \end{bmatrix} \begin{bmatrix} \hat{a} \\ \hat{b} \\ \hat{c} \end{bmatrix} = \begin{bmatrix} \sqrt{\kappa_{\rm a}^{\rm ex}}\hat{a}_{\rm in} \\ \sqrt{\gamma_{\rm b}}\hat{b}_{\rm in} \\ \sqrt{\kappa_{\rm c}^{\rm ex}}\hat{c}_{\rm in} \end{bmatrix}. \tag{5.15}$$

In the above we have written the cavity susceptibilities as $\chi_{\rm a}^{-1}(\omega) = \kappa_{\rm a}/2 - {\rm i}(\Delta_{\rm a}+\omega)$, and $\chi_{\rm c}^{-1}(\omega) = \kappa_{\rm c}/2 - {\rm i}(\Delta_{\rm c}+\omega)$, where, for notational cleanliness we have defined $\Delta_{\rm a} = \Delta_{\rm a}^{\rm ctrl}$, and $\Delta_{\rm c} = \Delta_{\rm c}^{\rm ctrl}$. We also define the mechanical susceptibility as $\chi_{\rm b}^{-1}(\omega) = \gamma_{\rm b}/2 - {\rm i}(-\omega_{\rm b}+\omega)$, including a mechanical input field, $\hat{b}_{\rm in}$, which can be used to model thermal contact with the environment.

From here the solutions become tractable if we make a change of basis to symmetric and antisymmetric combinations of the a and c modes which we refer to as the mechanically dark, $\zeta_{\rm dk}$, and bright, $\zeta_{\rm br}$, modes [151]

$$\hat{\zeta}_{\rm dk} = \frac{G_{\rm c}\hat{a} - G_{\rm a}\hat{c}}{\mathrm{i}\,\overline{G}}, \tag{5.16}$$

$$\hat{\zeta}_{\rm br} = \frac{G_{\rm a}^{*}\hat{a} + G_{\rm c}^{*}\hat{c}}{\overline{G}}, \tag{5.17}$$

where

$$\overline{G} = \sqrt{|G_{\rm a}|^2 + |G_{\rm c}|^2}. \tag{5.18}$$

Assuming $\kappa_1 = \kappa_2 = \kappa$, and $\Delta_{\rm a} = \Delta_{\rm c} = \Delta$, we arrive at de–coupled equations of motion, which have the solutions

$$\hat{\zeta}_{\rm dk} = \frac{1}{\kappa/2 - \mathrm{i}(\Delta+\omega)}\left(\frac{\sqrt{\kappa_{\rm a}^{\rm ex}}G_{\rm c}\hat{a}_{\rm in} - \sqrt{\kappa_{\rm c}^{\rm ex}}G_{\rm a}\hat{c}_{\rm in}}{\mathrm{i}\,\overline{G}}\right), \tag{5.19}$$

$$\hat{b} = \frac{1}{\gamma_{\rm b}/2 - \mathrm{i}(-\omega_{\rm b}+\omega)}\left(\sqrt{\gamma_{\rm b}}\hat{b}_{\rm in} + \mathrm{i}\,\overline{G}\hat{\zeta}_{\rm br}\right), \tag{5.20}$$

$$\hat{\zeta}_{\rm br} = \frac{1}{\kappa/2 - \mathrm{i}(\Delta+\omega) + \frac{\overline{G}^2}{\gamma_{\rm b}/2 - \mathrm{i}(-\omega_{\rm b}+\omega)}}\left(\frac{\sqrt{\kappa_{\rm a}^{\rm ex}}G_{\rm a}^{*}\hat{a}_{\rm in} + \sqrt{\kappa_{\rm c}^{\rm ex}}G_{\rm c}^{*}\hat{c}_{\rm in}}{\overline{G}} + \frac{\mathrm{i}\,\overline{G}\sqrt{\gamma_{\rm b}}\hat{b}_{\rm in}}{\gamma_{\rm b}/2 - \mathrm{i}(-\omega_{\rm b}+\omega)}\right). \tag{5.21}$$

To easily access the physics of the system we take $G_{\rm a} = G_{\rm c} = G$, and $\kappa_{\rm a}^{\rm ex} = \kappa_{\rm c}^{\rm ex} = \kappa_{\rm ex}$ to simplify these expressions. We also ignore any input mechanical drive by setting $\hat{b}_{\rm in} \rightarrow 0$. Finally, we assume classical probe fields of equal amplitude, $s_{\rm in}$, and drive each modulator at the same frequency with phase difference ϕ by making the substitutions $\hat{a}_{\rm in} \rightarrow s_{\rm in}e^{i\phi/2}$ and $\hat{c}_{\rm in} \rightarrow s_{\rm in}e^{-i\phi/2}$. This results in the expressions,

$$\zeta_{\rm dk} = \frac{\sqrt{2\kappa_{\rm ex}}\sin(\phi/2)s_{\rm in}}{\kappa/2 - \mathrm{i}(\Delta+\omega)}, \tag{5.22}$$

$$\zeta_{\rm br} = \frac{\sqrt{2\kappa_{\rm ex}}\cos(\phi/2)s_{\rm in}}{\kappa/2 - \mathrm{i}(\Delta+\omega) + \frac{2G^2}{\gamma_{\rm b}/2 - \mathrm{i}(-\omega_{\rm b}+\omega)}}. \tag{5.23}$$

5.3.5 Effect of Mismatched Parameters

In the above expressions, we developed a model assuming idealized parameters. This resulted in mechanically bright and mechanically dark states which were decoupled from each other, and which could be isolated by adjusting the phase of the probe lasers. However, in any physical implementation of DOMIT, there will be mismatch between various parameters. In the following sections we study the effect of these mismatched parameters one by one.

Mismatched Probe Amplitudes

Suppose that all parameters are matched according to the set of assumptions the led to Eqs. 5.22 and 5.23. We can include the effect of probe mismatch by instead making the substitutions $\hat{a}_{\rm in} \rightarrow (s_{\rm in} + \delta_{\rm s})\, e^{i\phi/2}$ and $\hat{c}_{\rm in} \rightarrow (s_{\rm in} - \delta_{\rm s})\, e^{-i\phi/2}$, where $s_{\rm in}$ is the average probe power, and $2\delta_{\rm s}$ is the difference in the probe powers. Proceeding as before, we find,

$$\zeta_{\rm dk} = \frac{\sqrt{2\kappa_{\rm ex}}\,(\sin(\phi/2)s_{\rm in} - i\cos(\phi/2)\delta_{\rm s})}{\kappa/2 - {\rm i}(\Delta+\omega)}, \tag{5.24}$$

$$\zeta_{\rm br} = \frac{\sqrt{2\kappa_{\rm ex}}\,(\cos(\phi/2)s_{\rm in} - i\sin(\phi/2)\delta_{\rm s})}{\kappa/2 - {\rm i}(\Delta+\omega) + \frac{2G^2}{\gamma_{\rm b}/2 - {\rm i}(-\omega_{\rm b}+\omega)}}.. \tag{5.25}$$

From the above expression, one can see that for $\delta_{\rm s} \neq 0$ no choice of ϕ will enable complete isolation of the dark or bright state. This is further elucidated by calculating the dependence of the mode energy on ϕ and $\delta_{\rm s}$ for constant input probe power,

$$|\zeta_{\rm dk}|^2 \propto \frac{(|s_{\rm in}|^2 - |\delta_{\rm s}|^2)\sin^2(\phi/2) + |\delta_{\rm s}|^2}{|s_{\rm in}|^2 + |\delta_{\rm s}|^2}, \tag{5.26}$$

$$|\zeta_{\rm br}|^2 \propto \frac{(|s_{\rm in}|^2 - |\delta_{\rm s}|^2)\cos^2(\phi/2) + |\delta_{\rm s}|^2}{|s_{\rm in}|^2 + |\delta_{\rm s}|^2}. \tag{5.27}$$

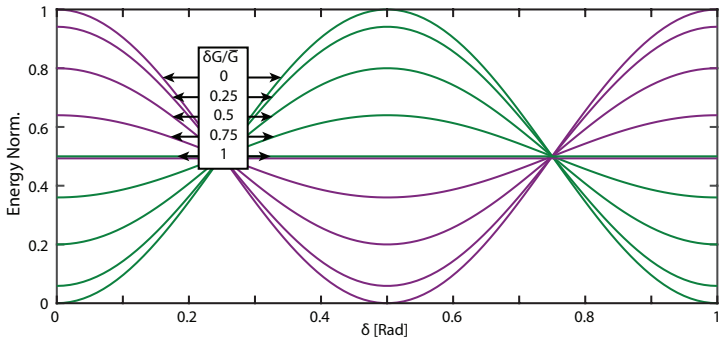

Figure 5.8: Effect of imbalance in the probe powers, or optomechanical coupling rates. As the mismatch is increased, the dark and bright state can no longer be isolated.

Mismatched Optomechanical Coupling

The effect of mismatch in the optomechanical coupling will have similar effects to mismatch in the probe amplitudes. This can be included by making the substitutions $G_{\rm a} \rightarrow G + \delta_{\rm G}$ and $G_{\rm c} \rightarrow G - \delta_{\rm G}$, where G is the average optomechanical coupling rate, and $2\delta_{\rm G}$ is the difference in optomechanical coupling rates. With these substitutions, the amplitudes of the mechanically bright and mechanically dark state are,

$$\zeta_{\rm dk} = \frac{\sqrt{2\kappa_{\rm ex}}s_{\rm in}}{\kappa/2 - {\rm i}(\Delta+\omega)}\left(\frac{G\sin(\phi/2) + i\delta_{\rm G}\cos(\phi/2)}{\overline{G}}\right), \tag{5.28}$$

$$\zeta_{\rm br} = \frac{\sqrt{2\kappa_{\rm ex}}s_{\rm in}}{\kappa/2 - {\rm i}(\Delta+\omega) + \frac{2G^2}{\gamma_{\rm b}/2 - {\rm i}(-\omega_{\rm b}+\omega)}}\left(\frac{G\cos(\phi/2)s_{\rm in} + i\delta_{\rm G}\sin(\phi/2)}{\overline{G}}\right), \tag{5.29}$$

where $\overline{G} = \sqrt{G^2+\delta_{\rm G}^2}$ in this case. Calculating the mode amplitudes, we find,

$$|\zeta_{\rm dk}|^2 \propto \frac{(|G|^2 - |\delta_{\rm G}|^2)\sin^2(\phi/2) + |\delta_{\rm G}|^2}{|\overline{G}|^2}, \tag{5.30}$$

$$|\zeta_{\rm br}|^2 \propto \frac{(|G|^2 - |\delta_{\rm G}|^2)\cos^2(\phi/2) + |\delta_{\rm G}|^2}{|\overline{G}|^2}. \tag{5.31}$$

Mismatched Frequency and Damping

Up until this point, we have found no direct coupling between the bright and dark mode. However, by detuning either our probe or pump lasers in equal and opposite directions, we can induce a coupling between these two modes. Furthermore, as we shall show, a mismatching the damping rates of the optical modes will also lead to a coupling. To see this, we make the substitutions $\Delta_{\rm a} \to \Delta + \delta_\Delta$, $\Delta_{\rm c} \to \Delta - \delta_\Delta$, $\kappa_{\rm a} \to \kappa + \delta_\kappa$, and $\kappa_{\rm c} \to \kappa - \delta_\kappa$. To clarify matters, we assume that the input mechanical is negligible ($\hat{b}_{\rm in} \to 0$), and set $G_{\rm a} = G_{\rm c} = G$, and $\kappa_1 = \kappa_2 = \kappa$ in Eqn. (4), which gives

$$\chi^{-1}(\omega)\hat{\zeta}_{\rm dk} = \frac{\sqrt{\kappa_{\rm a}^{\rm ex}}\hat{a}_{\rm in} - \sqrt{\kappa_{\rm c}^{\rm ex}}\hat{c}_{\rm in}}{\sqrt{2}\,{\rm i}} + \left(\delta_\Delta + i\frac{\delta_\kappa}{2}\right)\hat{\zeta}_{\rm br}, \tag{5.32}$$

$$\chi^{-1}(\omega)\hat{\zeta}_{\rm br} = \frac{\sqrt{\kappa_{\rm a}^{\rm ex}}\hat{a}_{\rm in} + \sqrt{\kappa_{\rm c}^{\rm ex}}\hat{c}_{\rm in}}{\sqrt{2}} + {\rm i}\,\overline{G}\hat{b} + \left(\delta_\Delta + i\frac{\delta_\kappa}{2}\right)\hat{\zeta}_{\rm dk}. \tag{5.33}$$

where $\chi^{-1}(\omega) = \kappa/2 - {\rm i}(\Delta+\omega)$. From these expressions we see that there is coupling between bright and dark mode. For differences in frequency we have dispersive coupling, at a rate δ_Δ, whereas for differences in damping, we have dissipative coupling at a rate $\delta_\kappa/2$.

5.3.6 Dark-Bright Mode Coupling

In this section, we consider dissipative coupling due to detuning either our probe or pump lasers in equal and opposite directions. To describe this coupling in the time domain we first consider the intermodal coupling for the case $\delta_\Delta = 0$, as illustrated in Fig. 5.9(a). Here, depending on the relative phase of the probe lasers, we arrive at a superposition of $\zeta_{\rm br}$ and $\zeta_{\rm dk}$ which is constant in time. In order for this process to remain stationary, we require interference to be between oscillations of the same frequency. From this, we can infer that by shifting the probe-cavity detuning by an amount δ_Δ, we cause interference to occur between differing frequencies, leading to beating between modes as illustrated in Fig. 5.9(b).

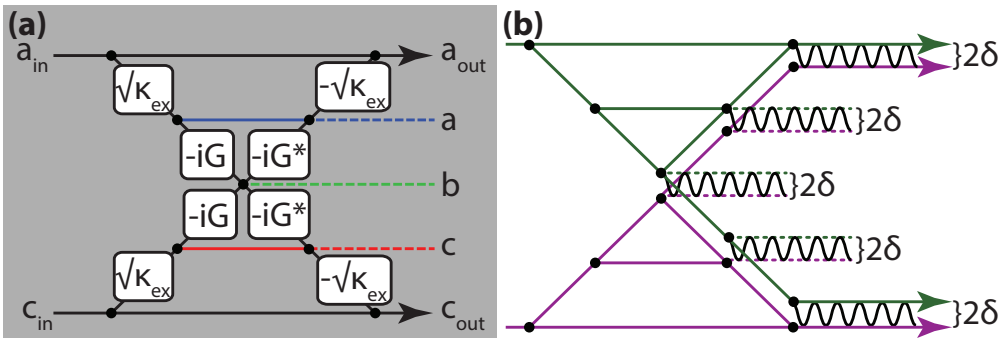

Figure 5.9: (a) Intermodal coupling for the case of stationary DOMIT. Direction of propagation is left to right. (b) Effect of frequency shifting the control-probe detunings in opposite directions. Unlike the stationary case, we will observe a beating between all modes of the system.

To solve this, we divide each of modes into two frequency components at $\pm\delta_\Delta$ of our original frequency terms as illustrated in Fig. 5.6(b). Considering first the dark state in the time domain, and choosing to set $\phi = 0$ for convenience, we find

$$\zeta_{\rm dk}(t) = \zeta_{\rm dk}^{(+)} + \zeta_{\rm dk}^{(-)} = \frac{e^{-\,{\rm i}(\omega_{\rm b}+\delta_\Delta)t}}{\kappa/2 - {\rm i}(\Delta+\omega_{\rm b}+\delta_\Delta)}\sqrt{\frac{\kappa^{\rm ex}}{2}}\frac{s_{\rm in}}{\rm i} + \frac{e^{-\,{\rm i}(\omega_{\rm b}-\delta_\Delta)t}}{\kappa/2 - {\rm i}(\Delta+\omega_{\rm b}-\delta_\Delta)}\sqrt{\frac{\kappa^{\rm ex}}{2}}\frac{s_{\rm in}}{\rm i}. \tag{5.34}$$

In a similar manner, we find that the bright state may be written as

$$\begin{aligned}\zeta_{\rm br}(t) &= \zeta_{\rm br}^{(+)} + \zeta_{\rm br}^{(-)} \\ &= \frac{e^{-\,{\rm i}(\omega_{\rm b}+\delta_\Delta)t}}{\kappa/2 - {\rm i}(\Delta+\omega_{\rm b}+\delta_\Delta) + \frac{|\overline{G}|^2}{\gamma_{\rm b}/2 - {\rm i}(-\omega_{\rm b}+\omega_{\rm b}+\delta_\Delta)}}\sqrt{\frac{\kappa^{\rm ex}}{2}}s_{\rm in} \\ &\quad - \frac{e^{-\,{\rm i}(\omega_{\rm b}-\delta_\Delta)t}}{\kappa/2 - {\rm i}(\Delta+\omega_{\rm b}-\delta_\Delta) + \frac{|\overline{G}|^2}{\gamma_{\rm b}/2 - {\rm i}(-\omega_{\rm b}+\omega_{\rm b}-\delta_\Delta)}}\sqrt{\frac{\kappa^{\rm ex}}{2}}s_{\rm in}.\end{aligned} \tag{5.35}$$

Setting $\Delta = -\omega_{\rm b}$, and assuming $\delta \ll \kappa$, we find

$$\zeta_{\rm dk}(t) = \frac{2\sqrt{\kappa_{\rm ex}}\sin(\delta_\Delta t)e^{-\,{\rm i}\,\omega_{\rm b}t}s_{\rm in}}{\kappa}, \tag{5.36}$$

$$\zeta_{\rm br}(t) = \frac{2\sqrt{\kappa_{\rm ex}}\cos(\delta_\Delta t)e^{-\,{\rm i}\,\omega_{\rm b}t}s_{\rm in}}{\kappa(1+\frac{\overline{C}}{1+4(\delta_\Delta/\gamma_{\rm b})^2})}. \tag{5.37}$$

This gives us the output fields as

$$a(t) = \frac{e^{-\,\mathrm{i}\,\omega_\mathrm{b} t}}{\sqrt{2}} \left(\mathrm{i}\sin(\delta_\Delta t)\zeta_\mathrm{dk}(0) + \cos(\delta_\Delta t)\zeta_\mathrm{br}(0)\right), \tag{5.38}$$

$$c(t) = \frac{e^{-\,\mathrm{i}\,\omega_\mathrm{b} t}}{\sqrt{2}} \left(-\,\mathrm{i}\sin(\delta_\Delta t)\zeta_\mathrm{dk}(0) + \cos(\delta_\Delta t)\zeta_\mathrm{br}(0)\right). \tag{5.39}$$

We note that near resonance, the amplitudes ζ_dk and ζ_br approach those calculated for steady state. For cases where we detuned away from the DOMIT transparency ($\delta \gg \gamma_\mathrm{b}$), or for small cooperativities, the amplitudes of the dark and light state approach each other, and the visibility of oscillations goes to zero. Explicitly, the resonance contrast of the oscillations is found to be

$$V(\delta) = 1 - \sqrt{\frac{\gamma_\mathrm{b}^2 + 4\delta_\Delta^2}{\gamma_\mathrm{b}^2(1+\overline{C})^2 + 4\delta_\Delta^2}}. \tag{5.40}$$

5.3.7 Switching

Although we previously found solutions in the frequency domain, it is instructive to reconsider the equations of motion in the time domain

$$\dot{\hat{a}} = (\mathrm{i}\,\Delta_\mathrm{a} - \kappa_\mathrm{a}/2)\,\hat{a} + \mathrm{i}\,G_\mathrm{a}\hat{b} + \sqrt{\kappa_\mathrm{a}^\mathrm{ex}}\hat{a}_\mathrm{in}, \tag{5.41}$$

$$\dot{\hat{b}} = (-\,\mathrm{i}\,\omega_\mathrm{b} - \gamma_\mathrm{b}/2)\,\hat{b} + \mathrm{i}\,G_\mathrm{a}^*\hat{a} + \mathrm{i}\,G_\mathrm{c}^*\hat{c} + \sqrt{\gamma_\mathrm{b}}\hat{b}_\mathrm{in}, \tag{5.42}$$

$$\dot{\hat{c}} = (\mathrm{i}\,\Delta_\mathrm{c} - \kappa_\mathrm{c}/2)\,\hat{c} + \mathrm{i}\,G_\mathrm{c}\hat{b} + \sqrt{\kappa_\mathrm{c}^\mathrm{ex}}\hat{c}_\mathrm{in}. \tag{5.43}$$

For the devices used in our experiment, the decay rate of our optics is much faster than our mechanics ($\kappa_\mathrm{a}, \kappa_\mathrm{c} \gg \gamma$). With this in mind we can use adiabatic elimination, and set $\dot{\hat{a}} = 0, \dot{\hat{c}} = 0$, and solve for the mechanics as

$$\dot{\hat{b}} = \left(-\,\mathrm{i}\,\omega_\mathrm{b} - \gamma_\mathrm{b}/2 + \frac{|G_\mathrm{a}|^2}{\mathrm{i}\,\Delta_\mathrm{a} - \kappa_\mathrm{a}/2} + \frac{|G_\mathrm{c}|^2}{\mathrm{i}\,\Delta_\mathrm{c} - \kappa_\mathrm{c}/2}\right)\hat{b} - \frac{\mathrm{i}\,G_\mathrm{a}^*\sqrt{\kappa_\mathrm{a}^\mathrm{ex}}\hat{a}_\mathrm{in}}{\mathrm{i}\,\Delta_\mathrm{a} - \kappa_\mathrm{a}/2} - \frac{\mathrm{i}\,G_\mathrm{c}^*\sqrt{\kappa_\mathrm{c}^\mathrm{ex}}\hat{c}_\mathrm{in}}{\mathrm{i}\,\Delta_\mathrm{c} - \kappa_\mathrm{c}/2} + \sqrt{\gamma_\mathrm{b}}\hat{b}_\mathrm{in}. \tag{5.44}$$

Using this expression we find that for $\Delta_{\rm a} = \Delta_{\rm c} = 0$, as in the experiment

$$\dot{\hat{b}} = -\left(\mathrm{i}\,\omega_{\rm b} + \tau^{-1}\right)\hat{b} + \frac{2\,\mathrm{i}\,G_{\rm a}\sqrt{\kappa_{\rm a}^{\rm ex}}\hat{a}_{\rm in}}{\kappa_{\rm a}} + \frac{2\,\mathrm{i}\,G_{\rm c}\sqrt{\kappa_{\rm c}^{\rm ex}}\hat{c}_{\rm in}}{\kappa_{\rm c}} + \sqrt{\gamma_{\rm b}}\hat{b}_{\rm in}. \tag{5.45}$$

This gives the switching speed as $\tau^{-1} = \frac{\gamma_{\rm b}}{2}\left(1 + C_{\rm a} + C_{\rm c}\right)$, where $C_{\rm j} = 4G_{\rm j}^2/\kappa_{\rm j}\gamma_{\rm b}$ is the optomechanical cooperativity and $j = \{\mathrm{a}, \mathrm{c}\}$.

Assuming travelling wave singlet modes, the transmission amplitudes through the switch are

$$t_{\rm br} = \frac{2\kappa_{\rm ex}}{\kappa}\frac{1}{1+\overline{C}} - 1, \tag{5.46}$$

$$t_{\rm dk} = \frac{2\kappa_{\rm ex}}{\kappa} - 1. \tag{5.47}$$

5.4 N-Mode Solution

5.4.1 Mechanically Bright and Dark States

The interference between probe fields in two optical modes can in principle be extended to any number of optical modes. Suppose we have a system where N optical modes are dissipatively coupled to a single mechanical mode. We label the creation and annihilation operators associated with these optical modes as $\hat{a}_n^\dagger, \hat{a}_n$ where our index runs from zero to $N-1$ and the mechanical mode creation and annihilation operators as is $\hat{b}^\dagger, \hat{b}$. We assume red detuned pumps, and that the system is sideband resolved. Our interaction Hamiltonian is:

$$\hat{H}_{\rm int} = -\hbar\sum_{n=0}^{N-1}\left(G_n\hat{a}_n^\dagger\hat{b} + G_n^*\hat{a}_n\hat{b}^\dagger\right). \tag{5.48}$$

Using the same set of assumptions as the DOMIT section above, we can use Eq. 5.48 and the input-output formalism to write a set of $N+1$ coupled equations,

$$\dot{\hat{a}}_n = \left(i\Delta_n - \frac{\kappa_n}{2}\right)\hat{a}_n + iG_n\hat{b} + \sqrt{\kappa_n^{\text{ex}}}\hat{a}_n^{\text{in}}, \tag{5.49}$$

$$\dot{\hat{b}} = \left(-i\omega_b - \frac{\Gamma_b}{2}\right)\hat{b} + i\sum_{n=0}^{N-1} G_n^*\hat{a}_n + \sqrt{\gamma_b}\hat{b}^{\text{in}}, \tag{5.50}$$

where we have indexed the decay rates for each mode to account for the possibility of mismatched decay rates.

This set of equations may be solved in a similar manner to DOMIT: we seek a new basis, where one mode is maximally coupled to the mechanics. To do so, we assume $\kappa_n = \kappa$, $\Delta_n = \Delta$, and $G_n = G$. Inspection of Eq. 5.48, reveals that the mechanics couples to the summation of all optical modes. Designating this as our mechanically bright mode, it then remains to construct a set of $N-1$ orthogonal modes. This may be achieved by applying a discrete Fourier transform to the optical modes,

$$\hat{\zeta}_m = \frac{1}{\sqrt{N}}\sum_{n=0}^{N-1}\hat{a}_n e^{-\frac{2\pi i}{N}nm}. \tag{5.51}$$

Here ζ_0 is the mechanically bright mode, and all others are mechanically dark modes. The optical input to the cavity is defined in the same manner,

$$\hat{\zeta}_m^{\text{in}} = \frac{1}{\sqrt{N}}\sum_{n=0}^{N-1}\hat{a}_n^{\text{in}} e^{-\frac{2\pi i}{N}nm}. \tag{5.52}$$

In this basis, our equations take on the simpler form,

$$\dot{\hat{\zeta}}_0 = \left(i\Delta - \frac{\kappa}{2}\right)\hat{\zeta}_0 + i\overline{G}\hat{b} + \sqrt{\kappa^{\text{ex}}}\hat{\zeta}_0^{\text{in}}, \tag{5.53}$$

$$\dot{\hat{b}} = \left(-i\omega_b - \frac{\gamma_b}{2}\right)\hat{b} + i\overline{G}\hat{\zeta}_0 + \sqrt{\gamma_b}\hat{b}^{\text{in}} \tag{5.54}$$

$$\dot{\hat{\zeta}}_m = \left(i\Delta - \frac{\kappa}{2}\right)\hat{\zeta}_m + \sqrt{\kappa^{\text{ex}}}\hat{\zeta}_m^{\text{in}}. \tag{5.55}$$

Where in the above the m index in the ζ_m equations runs from 1 to N, and $\overline{G} = \sqrt{N}G$.

These equations can be solved by transforming into frequency space,

$$\hat{\zeta}_0(\omega) = \frac{1}{\kappa/2 - i(\omega+\Delta) + \frac{N|G|^2}{\gamma_b/2 - i(\omega-\omega_b)}} \left(\sqrt{\kappa^{\mathrm{ex}}}\hat{\zeta}_0^{\mathrm{in}} + \frac{i\sqrt{\gamma_{\mathrm{b}}}\overline{G}\hat{b}^{\mathrm{in}}}{\gamma_b/2 - i(\omega-\omega_b)} \right), \tag{5.56}$$

$$\hat{b}(\omega) = \frac{1}{\gamma/2 - i(\omega-\omega_{\mathrm{b}}) + \frac{N|G|^2}{\kappa/2 - i(\omega+\Delta)}} \left(\sqrt{\gamma_{\mathrm{b}}}\hat{b}^{\mathrm{in}} + \frac{i\sqrt{\kappa^{\mathrm{ex}}}\,\overline{G}\hat{\zeta}_0^{\mathrm{in}}}{\kappa/2 - i(\omega+\Delta)} \right), \tag{5.57}$$

$$\zeta_m(\omega) = \frac{\sqrt{\kappa^{\mathrm{ex}}}\hat{\zeta}_m^{\mathrm{in}}}{\kappa/2 - i(\omega+\Delta)}. \tag{5.58}$$

To gain insight into these expressions, we consider the on resonance ($\Delta = -\omega_{\mathrm{b}}, \omega = \omega_{\mathrm{b}}$). This yields the expressions

$$\hat{\zeta}_0(\omega) = \frac{2/\kappa}{1+\overline{C}} \left(\sqrt{\kappa^{\mathrm{ex}}}\hat{\zeta}_0^{\mathrm{in}} + \frac{i2\overline{G}\hat{b}^{\mathrm{in}}}{\sqrt{\gamma_{\mathrm{b}}}} \right), \tag{5.59}$$

$$\hat{b}(\omega) = \frac{2/\gamma}{1+\overline{C}} \left(\sqrt{\gamma_{\mathrm{b}}}\hat{\hat{b}}^{\mathrm{in}} + \frac{i2\overline{G}\zeta_0^{\mathrm{in}}}{\kappa/\sqrt{\kappa^{\mathrm{ex}}}} \right), \tag{5.60}$$

$$\zeta_m(\omega) = 2\sqrt{\kappa^{\mathrm{ex}}}/\kappa\hat{\zeta}_m^{\mathrm{in}}. \tag{5.61}$$

From these expressions it can be seen that optomechanical coupling is only present between the mechanics and the mechanically bright mode. All other optical modes will see a bare cavity response. Initially, as the optomechanical coupling is increased, the degree of exchange between the bright mode and the mechanics will also increase. This situation has some resemblance to an add-drop filter. For very large cooperativities, both the mechanics and the bright mode will suppressed, and the system acts as notch filter for these modes.

Interestingly, this general case subsumes many well studied optomechanical effects. For example, in the case of a single optical mode, only the bright state can exist. In this case the filtering effect describes OMIT, where the occupation of the optical cavity is suppressed. In the case of two optical modes, as discussed previously in this paper, both a mechanically bright and a dark mode may exist. In this case, selection of the mechanically dark mode can

lead to coupling between different colours of input light, while avoiding decoherence due to the mechanics. The analysis here indicates that for larger dimensions, there will always exist $N-1$ such mechanically dark modes, which can avoid decoherence from the mechanics.

5.4.2 Outputs

Here we will calculate the output in the more physical basis of the individual optical modes. If we assume that b^{in} can be neglected, we can write out solutions in the simple form $\zeta_0 = \eta_0 \zeta_0^{\text{in}}$ for $m = 0$, and $\zeta_m = \eta_1 \zeta_m^{\text{in}}$ otherwise. Next we would like to return to our original basis in order to calculate the transmission at the physical ports. To do this, we use the inverse discrete Fourier transform, defined as

$$\hat{a}_n = \frac{1}{\sqrt{N}} \sum_{m=0}^{N-1} \hat{\zeta}_m e^{\frac{2\pi i}{N} nm}. \tag{5.62}$$

Placing our solutions into this expression we find

$$\begin{aligned}
a_n =& \frac{\eta_0}{\sqrt{N}} \zeta_0^{\text{in}} + \frac{\eta_1}{\sqrt{N}} \sum_{m=1}^{N-1} \zeta_m^{\text{in}} e^{\frac{2\pi i}{N} nm} \\
=& \frac{\eta_0}{N} \sum_{n'=0}^{N-1} a_{n'}^{in} + \frac{\eta_1}{N} \sum_{m=1}^{N-1} \sum_{n'=0}^{N-1} a_{n'}^{\text{in}} e^{\frac{-2\pi i}{N} m(n'-n)} \\
=& \frac{\eta_0 - \eta_1}{N} \sum_{n'=0}^{N-1} a_{n'}^{in} + \frac{\eta_1}{N} \sum_{n'=0}^{N-1} \left(\sum_{m=0}^{N-1} e^{\frac{-2\pi i}{N} m(n'-n)} \right) a_{n'}^{\text{in}} \\
=& \frac{\eta_0 - \eta_1}{N} \sum_{n'=0}^{N-1} a_{n'}^{in} + \frac{\eta_1}{N} \sum_{n'=0}^{N-1} N \delta_{n'n} a_{n'}^{\text{in}} \\
=& \frac{\eta_0 - \eta_1}{N} \sum_{n'=0}^{N-1} a_{n'}^{in} + \eta_1 a_n.
\end{aligned} \tag{5.63}$$

If we take the on-resonance case, $\eta_0 = \frac{2\sqrt{\kappa^{\rm ex}}}{\kappa}$ and $\eta_1 = \frac{2\sqrt{\kappa^{\rm ex}}}{\kappa}\frac{1}{1+\overline{C}}$ where $\overline{C} = NC = \frac{4N|G|^2}{\kappa\Gamma_b}$. This allows us to write,

$$a_n = \frac{2\sqrt{\kappa^{\rm ex}}}{\kappa}\left(a_n^{\rm in} - \frac{\overline{C}}{N(1+\overline{C})}\sum_{n'=0}^{N-1} a_{n'}^{\rm in}\right), \tag{5.64}$$

$$a_n^{\rm out} = \left(1 - \frac{2\kappa^{\rm ex}}{\kappa}a_n^{\rm in}\right) + \frac{2\kappa^{\rm ex}}{\kappa}\frac{\overline{C}}{N(1+\overline{C})}\sum_{n'=0}^{N-1} a_{n'}^{\rm in}. \tag{5.65}$$

For the case of critical coupling, and large cooperativity,

$$a_n^{\rm out} = -a_n^{\rm in} + \frac{2}{N}\sum_{n'=0}^{N-1} a_{n'}^{\rm in}. \tag{5.66}$$

This can be cast in matrix form as,

$$\begin{pmatrix} a_0^{\rm out} \\ a_1^{\rm out} \\ \vdots \\ a_{N-1}^{\rm out} \end{pmatrix} = \frac{1}{N}\begin{pmatrix} 2-N & 2 & \cdots & 2 \\ 2 & 2-N & \cdots & 2 \\ \vdots & \vdots & \ddots & \vdots \\ 2 & 2 & \cdots & 2-N \end{pmatrix}\begin{pmatrix} a_0^{\rm in} \\ a_1^{\rm in} \\ \vdots \\ a_{N-1}^{\rm in} \end{pmatrix}. \tag{5.67}$$

This indicates that complete conversion from one colour to another is only possible for the case $N = 2$.

Chapter 6

Multimode Optomechanics: II

6.1 Introduction: Processing Light stored in an Optomechanical Memory

The setting for this work is also a multimode optomechanical system. This system allows for novel and useful physical interactions. In this work we demonstrate that when this system is operated as an optomechanical memory, the storage time may be enhanced as compared to single-mode optomechanical systems. Furthermore, we demonstrate that the phase of the stored pulse may be controlled during pulse storage.

D.P. Lake and M.Mitchell fabricated the device, performed the experiments, and analyzed the data. D.P. Lake developed the theory and all authors contributed to writing the manuscript.

6.2 Processing Light Stored in an Optomechanical Memory

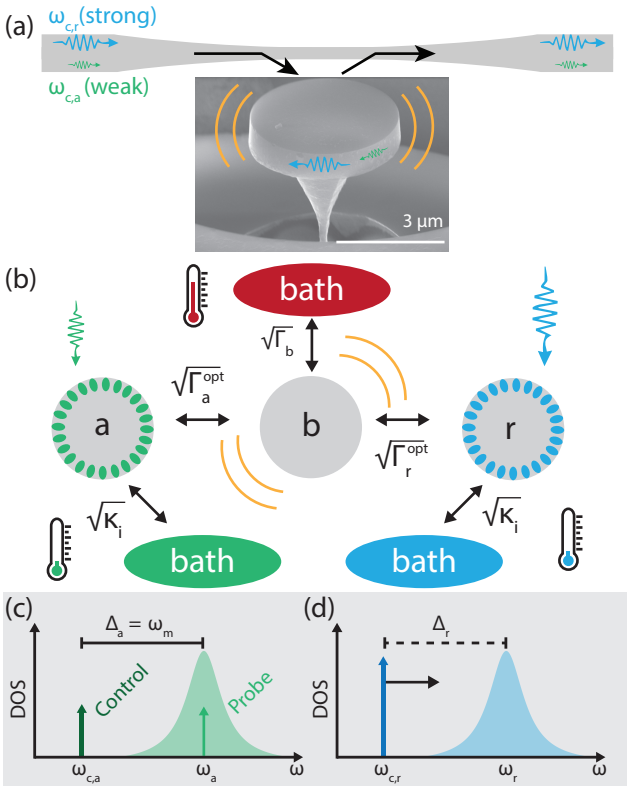

Figure 6.1: (a) Annotated scanning electron micrograph of the diamond microdisk optomechanical cavity. A tapered optical fiber is utilized to couple two colors of light to the microdisk which in turn is coupled to mechanical vibrations of the radial breathing mode of the microdisk. (b) Schematic of the system under study where the mechanical mode b is coupled to the environment (red bath), a reservoir, r, and optical mode a, at the indicated rates. While coupling of the mechanical mode to the surrounding environment is an intrinsic property of the device and environment, the coupling to r may be manipulated through the use of a control laser. (c) Density of states picture showing the detuning of the control and probe laser fields for mode a (green) and mode r (blue).

All real-world systems exhibit dissipation due to their coupling to external degrees of freedom. This permits energy to leave and fluctuations to enter the system [170], and is typically undesirable to the performance of information processing components such as memories. Reservoir engineering uses dissipation to enhance a system's properties [171]. For example, trapped ions with external coupling to carefully tailored reservoirs can be

prepared into desirable quantum states using this technique [172]. Here we show that when reservoir engineering is extended to incorporate dynamic control of external coupling, a system's steady state can be adiabatically manipulated. By applying this dynamic reservoir engineering to an optomechanical memory, we demonstrate that stored information can to be coherently modified. This is a crucial step towards full temporal control of quantum states of light stored in an optomechanical system.

In this letter, we use coherent multimode optomechanics to store information input to a single-crystal diamond microdisk's optical mode (a) in the device's mechanical mode (b), while simultaneously modifying the mechanical mode's dynamics through coupling to a second 'reservoir' optical mode (r), as illustrated in Fig. 6.1. Microdisks can operate as multimode cavity optomechanical systems whose optical whispering gallery modes are coupled by radiation pressure to motion of the device's mechanical radial breathing mode [35]. Coherent multimode optomechanical coupling is possible in these diamond microdisks even at room temperature and ambient conditions thanks to their low optical and mechanical loss and their ability to support intense intracavity fields. Multimode cavity optomechanical devices enable wavelength conversion [94, 103, 129, 151], entanglement between photons [152], and low-noise frequency conversion [97]. As we will show here, they are also excellent platforms for implementing reservoir engineering [173, 174]. Here, the reservoir is driven by a control laser whose detuning, Δ_{r}, sets the phase lag of its optomechanical coupling to the resonator, and whose power, P_{r}, sets the coupling strength. This tunable resonator–reservoir interaction induces mechanical dissipation $\Gamma_{\mathrm{r}}^{\mathrm{opt}}$ and shifts the mechanical resonator frequency by $\omega_{\mathrm{r}}^{\mathrm{opt}}$, two effects widely studied in single–mode optomechanical systems, for example in demonstration of mechanical ground state cooling [76, 77]. In our multimode system, we dynamically tune the reservoir coupling to process information stored in the mechanical

memory, whose dynamics we show to be governed by:

$$\dot{\hat{b}} = -\left(i\omega_{\mathrm{b}}^{\mathrm{eff}}(t) + \frac{\Gamma_{\mathrm{b}}^{\mathrm{eff}}(t)}{2}\right)\hat{b} + \sqrt{\Gamma_{\mathrm{b}}}\hat{e}_{\mathrm{in}} + g_{\mathrm{r}}\sqrt{\kappa_{\mathrm{r}}}\chi_{\mathrm{r}}(\omega_{\mathrm{b}})\hat{r}_{\mathrm{in}} + g_{\mathrm{r}}\sqrt{\kappa_{\mathrm{r}}}\chi_{\mathrm{r}\dagger}(\omega_{\mathrm{b}})\hat{r}_{\mathrm{in}}^{\dagger}, \tag{6.1}$$

where $\hat{b}$ is the phonon annihilation operator, $\hat{e}_{\mathrm{in}}$ is the thermal bath input field, and $\hat{r}_{\mathrm{in}}$ is the optical reservoir input field. The key feature that we test and exploit is the ability to dynamically control the memory's effective mechanical frequency, $\omega_{\mathrm{b}}^{\mathrm{eff}} = \omega_{\mathrm{b}} + \omega_{\mathrm{r}}^{\mathrm{opt}}(t)$, and effective damping, $\Gamma_{\mathrm{b}}^{\mathrm{eff}} = \Gamma_{\mathrm{b}} + \Gamma_{\mathrm{r}}^{\mathrm{opt}}(t)$ via the reservoir. We find that the memory operates *as if* it is a conventional optomechanical system composed of the renormalized mechanical resonator interacting with the 'signal' mode a. In this regime, which is valid if the mechanical dissipation rate $\Gamma_{\mathrm{b}} \ll \kappa_{\mathrm{r}}$ where κ_{r} is the reservoir's optical decay rate, the control laser becomes an input to b filtered by the reservoir mode's optical response χ_{r} (see Supplementary Material).

Below we test the validity of this description and demonstrate applications of dynamic reservoir coupling through three experiments. First we demonstrate a means to enhance the system's optomechanical cooperativity, and switch the dynamics of the system from overall loss to overall gain. We then demonstrate an enhancement in the optomechanical memory's storage time through control of $\Gamma_{\mathrm{b}}^{\mathrm{eff}}$. Finally we demonstrate that the phase of a stored mechanical pulse may be controlled through manipulation of $\omega_{\mathrm{b}}^{\mathrm{opt}}$.

6.2.1 Reservoir Engineering

As a first test of reservoir engineering, we probe how the dynamics of the mechanical resonator, and its resulting coupling to light, are affected by the resonator-reservoir interaction. This is accomplished using optomechanically induced transparency (OMIT) spectroscopy [88, 89]. OMIT creates a transparency window in the cavity lineshape whose properties depend on the dynamics of the optomechanical system [88,89]. By coherently coupling

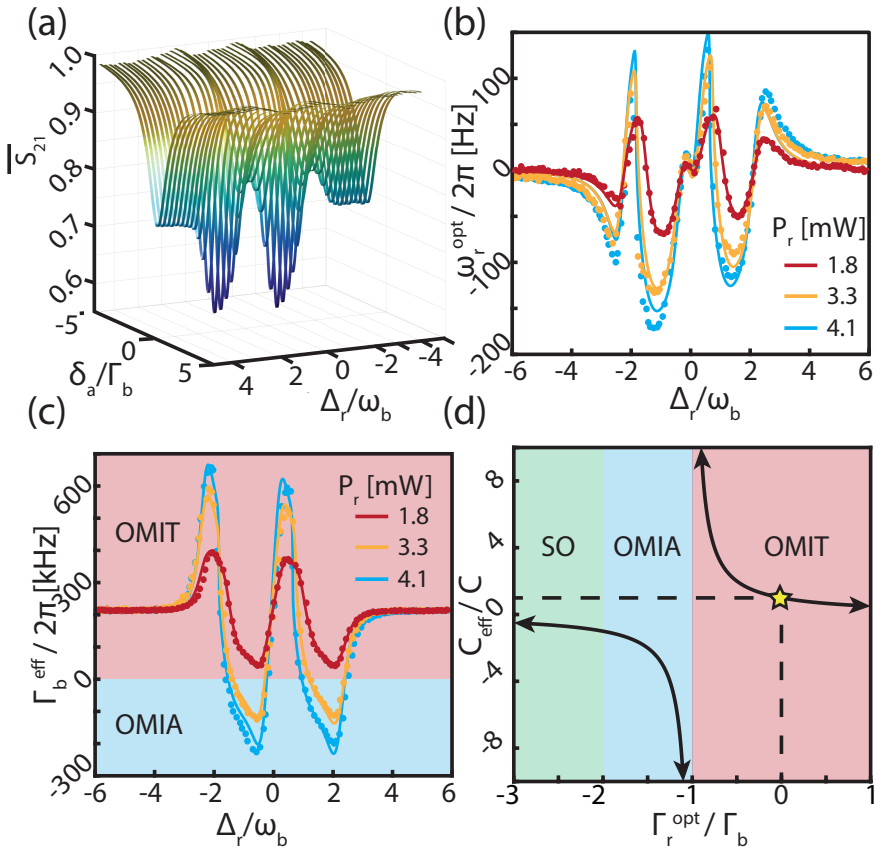

Figure 6.2: (a) Normalized OMIT scans as a function of mode a probe-cavity detuning, δ_a, and control-reservoir detuning, Δ_r, measured in transmission. The changes in the transparency window as a function of Δ_r is indicative of reservoir interactions. (b) Optomechanically manipulated effective mechanical frequency and damping (c) as a function of Δ_r and the input power at the device, P_i. (d) Effective cooperativity, C_{eff} for varying Γ_b^{eff} controlled by the reservoir mode, when $\Gamma_b^{eff} = \Gamma_b$ due to the presence of the mode a fields. Three different regimes of operation are shown: OMIT, OMIA, and self-oscillation (SO).

a probe field in a to the mechanical resonator for varying reservoir control laser settings, we can learn about the influence of the reservoir on the resonator. These measurements are shown in Fig. 6.2(c), which were obtained using a fiber taper waveguide to evanescently couple the reservoir control laser to mode r ($\omega_r/2\pi = 197$ THz) for varying Δ_r, while performing OMIT spectroscopy on mode a (frequency $\omega_a/2\pi = 192$ THz) using a weak resonant probe laser and a control laser red detuned by ω_b. This measurement was repeated for three different values of P_r. At each reservoir setting Γ_b^{eff} and ω_b^{eff} were extracted from the OMIT window shape (see Supplementary Material), and are plotted along with fits to the data

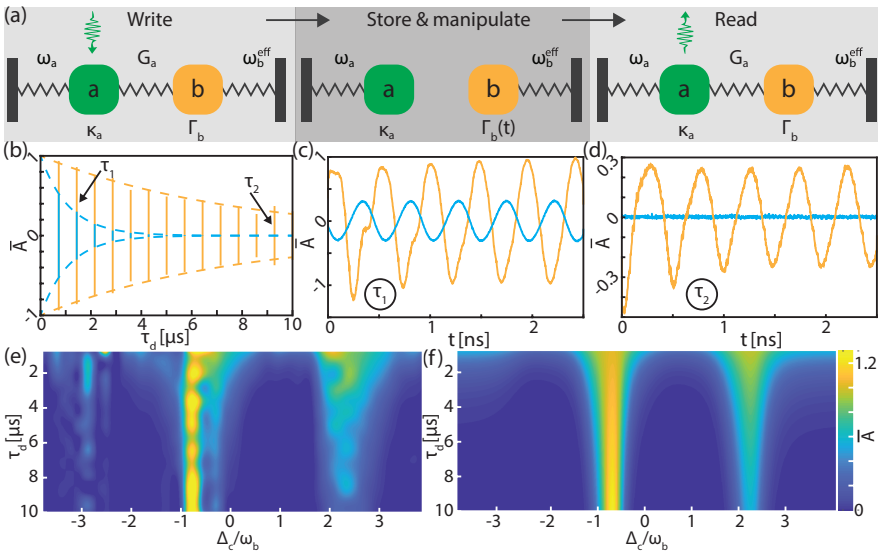

Figure 6.3: (a) Outline of pulse storage protocol where the optomechanical coupling between optical mode a and the mechanical mode facilitates storage of an optical pulse as a mechanical excitation. Mode r is used to manipulate the mechanical damping rate, $\Gamma_{\rm b}^{\rm eff}(t)$, and frequency, $\omega_{\rm b}^{\rm eff}(t)$ which can be carried out concurrently with the storage process. (b) Normalized read pulse amplitude, $\bar{A}$ for the off-resonant, $\Delta_{\rm r} \gg \omega_{\rm m}$, case (cyan) and for $\Delta_{\rm r} \sim \omega_{\rm m}$ (orange) as a function of $\tau_{\rm d}$. Here the control field for r was operated in continuous wave mode such there is no time dependence in $\Gamma_{\rm b}^{\rm eff}(t)$, and $\omega_{\rm b}^{\rm eff}(t)$. (c,d) Example measurements for points α and β illustrating the enhancement in $\bar{A}$ when $\Delta_{\rm r} \sim \omega_{\rm m}$.(e) Complete data set from which (b) was taken showing both an extension and reduction in storage time as a function of $\Delta_{\rm r}$, which is compared to the expected behavior (f) due to $\Gamma_{\rm r}^{\rm opt}$. Here we have taken $\Gamma_{\rm a}^{\rm opt} = \Gamma_{\rm b}$.

in Figs. 6.2(d) and (e). The fits, which show excellent agreement with measurements, were obtained with $g_{\rm r}$ as the only fitting parameter, confirming that optical spring effects from the reservoir field manifest in changes to resonator dynamics experienced by the spectrally isolated field in mode a. Note that the optical reservoir mode is a standing wave doublet (see Supplementary Material) formed from backscattering in the microdisk [12, 168], whose most apparent effect is the two sets of minima and maxima in Fig. 6.2(e), as well as related features in Figs. 6.2(c) and (d). In all measurements the mode a control field detuning was set relative to the lowest frequency doublet feature.

The system dynamics in the above measurements are most dramatically affected when $\Gamma_{\rm b}^{\rm eff}$ approaches zero. In a conventional OMIT system, the depth and width of the transparency window is parameterized by the optomechanical cooperativity, $C = \frac{4|g_{\rm a}|^2}{\kappa_{\rm a}\Gamma_{\rm b}}$, where $g_{\rm a}$ and

κ_a are the photon-assisted optomechanical coupling and optical cavity energy decay rates for a, respectively. However, in our multimode system OMIT is governed by an effective cooperativity $C_{\rm eff} = C \times \Gamma_b/\Gamma_b^{\rm eff}$. In the measurement presented here we achieve a maximum $C_{\rm eff} = 83$, which represents an enhancement of 158$\times$ the bare C in absence of the reservoir field. This allows our system to act as though it has large cooperativity, enabling large light delays and narrow transparency windows (see Supplementary Material). In principle this enhancement is limited only by drift in Δ_r, which dictates how close to zero $\Gamma_b^{\rm eff}$ can be, and is not limited by the optomechanical coupling rate.

As $\Gamma_b^{\rm eff}$ becomes negative, the mechanical resonator motion changes from experiencing an overall loss to an overall gain. Consequently, by adjusting our reservoir coupling, we are able to tune the system dynamics between OMIT and the regime of optomechanically induced amplification (OMIA). This gain would normally cause optomechanically induced self-oscillation to occur [167, 175]. However, this instability is repressed in our multimode measurements by the optomechanical damping $\Gamma_a^{\rm opt}$ induced by the a mode OMIT process, provided $\Gamma_a^{\rm opt} + \Gamma_b^{\rm eff} > 0$. The ability of the reservoir mode to tune the system dynamics between OMIT, OMIA and self-oscillation regimes is illustrated in Fig. 6.2(f) for the special case that $\Gamma_a^{\rm opt} = \Gamma_b$. In our measurements the OMIA regime was entered for the $P_r = 3.3$ mW and $P_r = 4.1$ mW settings when the control laser was blue detuned from the reservoir mode's optical doublets by approximately ω_b.

6.2.2 Pulse Storage Manipulation

Pioneering experiments in quantum optics utilizing Λ-type atomic systems have demonstrated that a strong control beam can dramatically alter the optical properties of a material, including rendering otherwise opaque materials transparent [176], enhancing nonlinear processes [177,178], and slowing the group velocity of a pulse of light [179,180]. Furthermore by dynamically altering the transparency of a material, a pulse of light may be trapped, and

deterministically released at a later time [181–184]. Such schemes have been used to store light pulses for over a minute [185], and have been proven to be a viable means to store single photons [186, 187].

Building on these experiments, cavity optomechanical systems have been shown to support an analogous process [88, 89]. A canonical cavity optomechanical system supports an optical mode with frequency ω_{a}, and a mechanical mode at frequency ω_{b}, where in the simplest case a mechanical displacement induces a linear shift in the frequency of the cavity. When a strong pump laser (ω_{p}) is incident on the cavity with detuning $\Delta_{\mathrm{a}} = \omega_{\mathrm{pa}} - \omega_{\mathrm{a}} = -\omega_{\mathrm{b}}$, where ω_{ca} is the frequency of the control laser, the system is governed by the beamsplitter Hamiltonian $\hat{H}_{\mathrm{bs}} = \hbar g_{\mathrm{a}} \left(\hat{a}^{\dagger}\hat{b} + \hat{a}\hat{b}^{\dagger} \right)$ [70], where $g_{\mathrm{a}} = \alpha_{\mathrm{a}} G_{\mathrm{a}} x_{\mathrm{o}}$. In the previous equation $\hat{a}^{\dagger}, \hat{a}$ and $\hat{b}^{\dagger}, \hat{b}$. In this way, by controlling the strength of the control beams, by adjusting the strength of the control beam, and hence n_{a}, energy can be coherently exchanged between optics and mechanics.

We now show that reservoir engineering can be harnessed to create a dynamically controlled optomechanical memory. Our memory protocol is illustrated using mass-on-spring systems in Fig. 6.3(a). During the write stage, a strong control laser red detuned from mode a by the mechanical frequency ($\Delta_{\mathrm{a}} = -\omega_{\mathrm{b}}$) is input to the microdisk. This couples a weak signal field input to resonant with mode $\hat{a}$ to mode $\hat{b}$ at rate, g_{a}, permitting the coherent conversion of signal photons to phonons [70]. Following the write stage, the control laser is removed, and modes a and b are decoupled. Our scheme then deviates from a conventional optomechanical memory [78, 79, 188], in that coupling to the reservoir is turned on with time varying amplitude, permitting control of the mechanical resonator's damping rate and frequency, which in effect modifies the stored information. Finally, during the read stage, the reservoir control laser is removed and the signal control laser is turned back on, converting the stored mechanical signal back to the optical domain.

Through continuous amplification of the stored mechanical pulse by the reservoir mode, we drastically extend the pulse storage lifetime. This is in a similar spirit to previous demonstrations of optomechanical amplification in waveguides [189], and has similarities to recent demonstrations of ORCA buffers [190]. To measure the storage time, we varied the delay between the write and read pulses by an amount τ_{d}. The measured amplitude output during the read pulse encodes the decay envelope of the mechanical signal, and decays exponentially at a rate $\Gamma_{\mathrm{b}}^{\mathrm{eff}}$. An example of this decay is plotted on Fig. 6.3(b) for the cases when the reservoir control is optimally detuned for storage ($\Delta_{\mathrm{r}} \approx -\omega_{\mathrm{b}}$), and for comparison, when it is far detuned ($\Delta_{\mathrm{r}} \gg \omega_{\mathrm{b}}$) and the effective damping rate is simply $\Gamma_{\mathrm{b}}^{\mathrm{eff}} = \Gamma_{\mathrm{b}}$. The ratio of the decay envelopes $\Gamma_{\mathrm{b}}^{\mathrm{eff}}/\Gamma_{\mathrm{b}}$ indicates a $7\times$ enhancement. This enhancement can also be compared to the achievable group delay via the OMIT window [89], which is $\sim 0.4\mu$s here, as described in the Supplementary Material. Examples of the signal extracted at two values of τ_{d} are shown on Fig. 6.3(c,d), demonstrating a dramatic difference in the amplitude of the enhanced versus the unenhanced signal at longer timescales. A full measurement of readout amplitude vs. Δ_{r} and τ_{d} was also acquired, the results of which are plotted in Fig. 6.3(e). This shows qualitative agreement to the theoretical amplitudes obtained from an analytic fit of $\Gamma_{\mathrm{b}}^{\mathrm{eff}}(\Delta_{\mathrm{r}})$ and plotted for the same delays as the experiment. Deviations between the two are understood to be a consequence of long-term thermal drifts in the resonance frequencies of the modes, as well as wavelength drifts in the readout laser used in the experiment. Note that this amplification process cannot be used indefinitely as the thermal phonons present due to the room temperature bath will eventually overwhelm the stored signal phonon, as described in the Supplementary Material.

Finally, we demonstrate that the phase of the stored pulse can also be controlled via the reservoir mode. By changing $\omega_{\mathrm{b}}^{\mathrm{eff}}$ adiabatically and hence the frequency of the stored pulse, we can complete a trajectory which moves away from and then returns to the original frequency. Over the course of this trajectory, the mechanical oscillator acquires a dynamical phase $\varphi(t_2) = \varphi(t_1) + \int_{t_1}^{t_2} \delta\omega(t)dt$, assuming that we return to the original mechanical

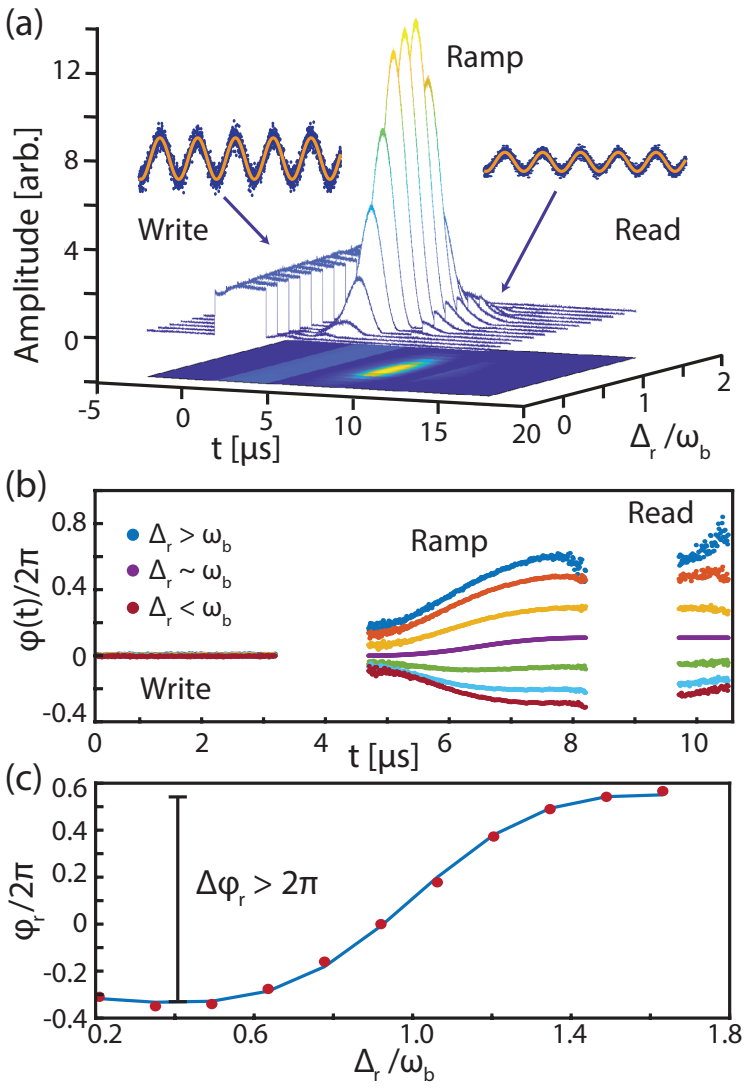

Figure 6.4: (a) Amplitude of the acquired signals vs. time and reservoir detuning for the phase manipulation experiment. In this experiment no optical filtering was used, so that the write, ramp, and read pulses may all be detected. (b) Phase of the mechanical oscillator vs. time as inferred from the optical output of the device. (c) Final phase as a function of Δ_r along with a fit to the data based on the optical spring effect associated with the ramp pulse.

frequency. This is analogous to a pendulum whose length is adjusted in time [191]. In our experiment, we varied the amplitude of the reservoir mode in time using an amplitude electro-optic modulator driven by a symmetric RF ramp pulse (see Supplementary Material) for various Δ_r as shown in Fig. 6.4(a). Here the ramp pulse was 3.5 μs long and was situated 1.5 μs after the write, and before the read pulse. By fitting the beat note detected at the fiber output for each of the write, ramp, and read pulse segments we can plot the phase as referenced to the well-defined write pulse, as shown in shown in Fig. 6.4(b). Here we have removed the phase shift associated with the spring effect induced by the write pulse, which added a linear slope to the ramp and read pulse segments. This allows us to isolate the shift due to the spring effect associated with the reservoir mode ramp pulse (see Supplementary Material). From the read pulse segments we extract the phase relative to the write pulse, demonstrating a reservoir controlled phase shift, $\Delta\varphi > 2\pi$ as shown in Fig. 6.4(c).

6.2.3 Summary

In this work we have demonstrated that the in-situ control offered by reservoir engineering is a powerful tool for enhancement of storage times, bypassing the usual limitations imposed by the intrinsic damping rate, and can be used to generate controllable phase shifts in the stored pulse. For optomechanical devices in the sideband resolved regime($\omega_b > \kappa$), Γ_b^{eff} and ω_b^{eff} are linearly independent in g_r and Δ_r [157]. The ability to control the damping rate dynamically would enable pulse compression by the realization of a time lens [192]. Furthermore, multiple pulses could be used in succession to realize very large phase shifts and pulse compression. As a mechanical mode is being used here, long storage times in excess of 90 μS [78, 79, 188] are possible, however, there is an associated inherent bandwidth limitation on the length of pulses that can be effectively stored, in contrast to Brillouin scattering devices [189, 193]. The long storage times enabled by this protocol will enable longer interaction times for interfacing the stored mechanical pulse with other systems, such as spins, or mechanical or

electric fields. The demonstrated phase manipulation techniques also highlights this systems potential for use as a logic gate, where the stored pulse is interfered with an incoming optical pulse.

6.3 Methods

6.3.1 Fabrication

The microdisks studied here (Fig. 6.5(a)) were fabricated from an optical grade, chemical vapor deposition (CVD) grown ⟨100⟩-oriented SCD substrate supplied by Element Six, according the process outlined in detail in Ref. [37]. The polished substrates were first cleaned in boiling piranha, and coated with $\sim$ 400 nm of PECVD Si_3N_4 as a hard mask. To avoid charging effects during electron beam lithography (EBL), $\sim$ 5 nm of Ti was deposited before the ZEP 520A EBL resist. The developed pattern was transferred to the hard mask via inductively coupled reactive ion etching (ICPRIE) with C_4F_8/SF_6 chemistry. The anisotropic ICPRIE diamond etch was performed using O_2, followed by deposition of $\sim$ 250 nm of conformal PECVD Si_3N_4 as a sidewall protection layer. The bottom of the etch windows were then cleared of Si_3N_4 using a short ICPRIE etch with C_4F_8/SF_6. This was followed by a zero RF power O_2 RIE diamond undercut etch to partially release the devices. The undercutting process was interrupted and an $\sim$ 100 nm layer of SiO_2 is deposited via electron beam evaporation to alter the microdisk pedestal profile before finishing the undercut. Lastly, the Si_3N_4 layer was removed using a wet-etch in 49% HF, and the devices were cleaned again in boiling piranha.

6.3.2 Mode Characterization

The power spectral density for the radial breathing mode was measured using a high speed photodetector (NewFocus 1554-B) and real time spectrum analyzer (Tektronix RSA5106A), and is shown in Fig. 6.5(b), which was carried out at low input power ($P_{\text{in}} \sim 50\mu$W) to avoid

optomechanical backaction. By fitting the power spectral density to a Lorentzian we extract a mechanical quality factor, $Q_{\rm m} \sim 1.1 \times 10^4$, at room temperature and pressure. Optical transmission scans are shown in Fig. 6.5(c,d), with intrinsic quality factors labelled for each of the doublet modes.

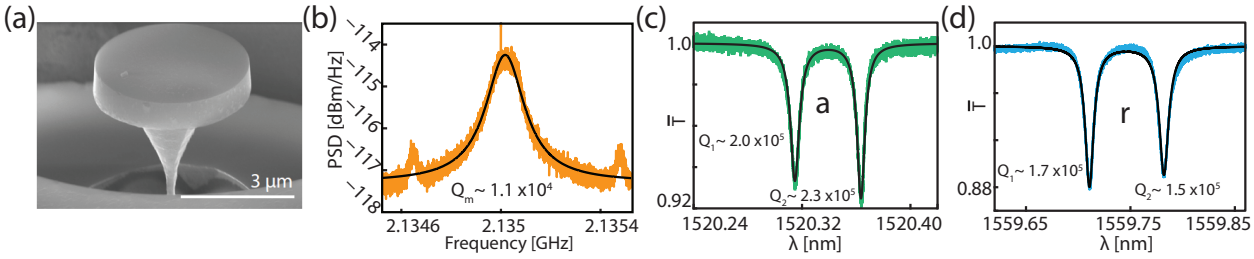

Figure 6.5: (a) Scanning electron micrograph of single-crystal diamond microdisk used in this work. (b) Measured power spectral density of radial breathing mode at room temperature and pressure (inset: COMSOL simulated displacement profile). (c,d) Fiber taper transmission scans for both optical modes used in this work. The doublet structure is a result of the lifting of degeneracy between the clockwise and counter clockwise propagating travelling wave modes of the disk.

In the limit that surface scattering effects are smaller than all other optical loss mechanisms ($g_{\rm ss} \ll \kappa$), microdisks will possess degenerate clockwise and anticlockwise propagating modes, with negligible coupling between them. However, once surface scattering begins to be comparable to, or exceeds the optical linewidth ($g_{\rm ss} \geq \kappa$), the clockwise and counter clockwise modes couple and will form pairs of modes known as optical doublets. These are simply symmetric and antisymmetric combinations of the travelling wave modes,

$$a_{\rm S} = \frac{a_{\circlearrowright} + a_{\circlearrowleft}}{\sqrt{2}};\ a_{\rm A} = \frac{a_{\circlearrowright} - a_{\circlearrowleft}}{\sqrt{2}i}; \tag{6.2}$$

$$r_{\rm S} = \frac{r_{\circlearrowright} + r_{\circlearrowleft}}{\sqrt{2}};\ r_{\rm A} = \frac{r_{\circlearrowright} - r_{\circlearrowleft}}{\sqrt{2}i}. \tag{6.3}$$

Due to the fact that $\int a_{\rm S}^{\star} a_{\rm A} dV = \int a_{\rm A}^{\star} a_{\rm S} dV = 0$, the overall mechanical frequency shift, or damping rate induced by a strong control laser is simply the sum of the contributions from the symmetric and antisymmetric mode.

6.3.3 Apparatus

The measurement apparatus for the results described in the main text is shown in Fig. 6.6, where the optical components added for each measurement described in the main text are outlined in the legend. Mode a was driven by a tunable diode laser at 1560 nm (Newport TLB-6700) while the reservoir mode or mode r was also driven by a tunable diode laser at 1520 nm (Newport TLB-6700) whose output was connected to a variable attenuator (VA: Exfo FVA-3100). For the verification of mutual coherence the mode a laser was passed through a phase electro-optic modulator ($\varphi(t)$: EOSpace PM-5S5-20-PFA-PFA-UV-UL) to generate a weak probe field from the control field, which was swept across the resonance using a vector network analyzer (VNA: Keysight E5063A) allowing the measurement of OMIT. The mode r laser was combined with the mode a laser on a fiber coupled 50/50 beamsplitter (BS: Newport F-CPL-L22355-A) where one output was sent to an erbium doped fiber amplifier (EDFA: Pritel LNHPFA-30-IO) and the other to an optical spectrum analyzer (OSA: Ando AQ6317B) such that the laser wavelengths could be tracked during the experiment. The output of the EDFA was sent to a fiber polarization unit followed by the fiber taper waveguide coupled to the diamond microdisk. The output of the fiber taper was then split on another 50/50 beam-splitter where one output is sent to a power meter (PM: Newport 1936-R) and one to a 1510/1550 nm wavelength division multiplexer (WDM: Montclair MFT-MC-51-30 AFC/AFC-1) to separate the light from modes a and c. The output of the WDM was then measured on a high speed photodetector (New Focus 1554-B) whose output is high-pass filtered and electronically amplified before being sent to the VNA for measuring OMIT or a digital serial analyzer (DSA:Tektronix DSA70804B) for the pulse storage measurements.

In the pulse storage enhancement measurement an amplitude modulator ($A(t)$: EOSpace AZ-0K5-10-PFA-SFA) was added to the mode a laser to generate the optical pulses, while the phase modulator was used to generate the signal to be written. The signal to be written was a sine wave at ω_{b} generated by an arbitrary waveform generator (AWG: Tektronix AWG70002A) which was superimposed on the optical pulses generated by a low pass filtered

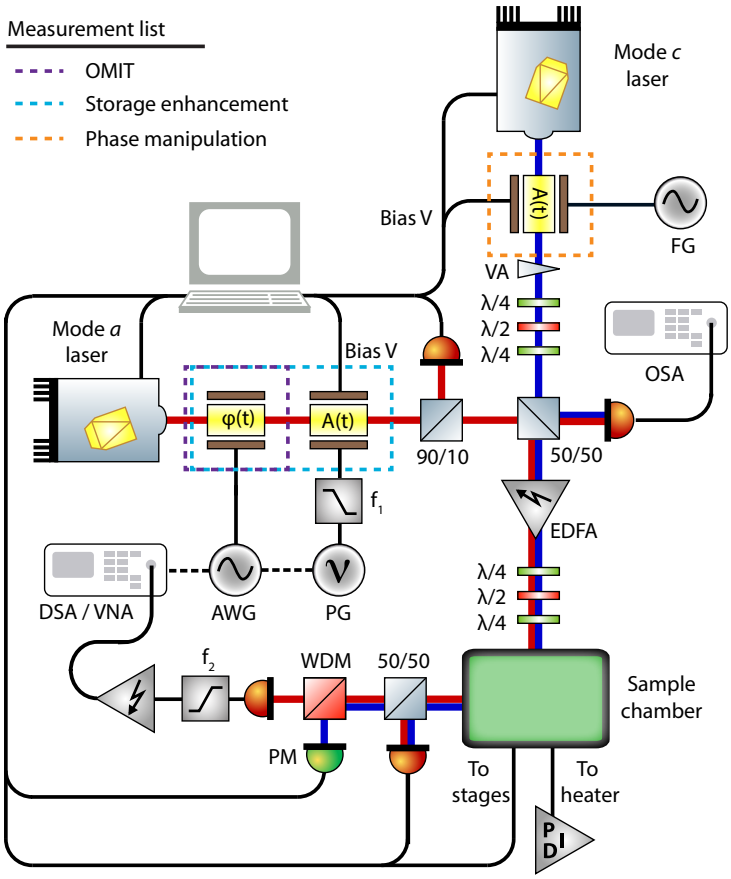

Figure 6.6: Measurement setup including the components necessary for all measurements described in the main text. The legend indicates the optical components necessary for each measurement presented and the components are discussed in detail in the text.

pulse generator (PG: Stanford Research Systems DG535), triggered by the AWG. Here the reservoir mode control laser was operated in c.w. mode, however, during the phase manipulation measurement an amplitude modulator ($A(t)$: Lucent Technologies 2623CS) is added to the output of the laser, which was driven by a separate function generator to generate the phase manipulation pulses. A thermoelectric heater/cooler was also placed under the sample and controlled with a PID for thermal stability during the measurement.

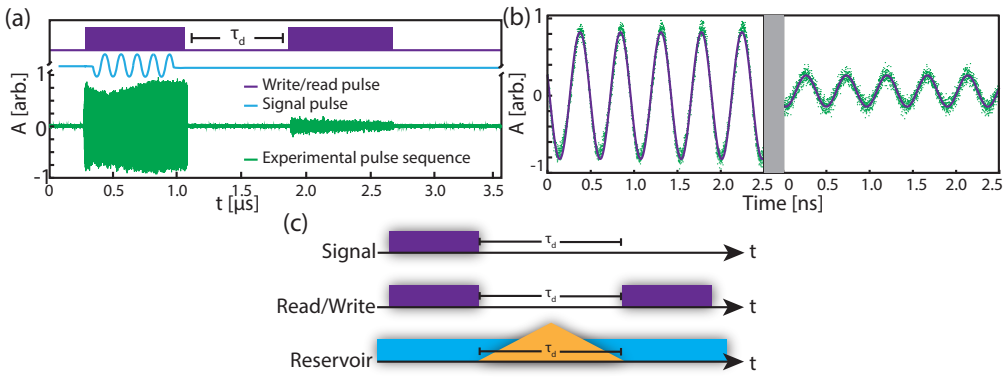

Figure 6.7: (a) Timing diagram for optomechanical pulse storage, along with an example of a typical measure signal (purple). (b) Detail of a short section of the write (left panel) and read pulse (right panel). (c) Timing diagram for the storage enhancement and phase manipulation experiments described in the main text.

6.3.4 Reservoir engineering

The results of this work are enabled by dynamic manipulation of a mechanical oscillator through engineering the degrees of freedom it is coupled to. The manifestation of this coupling is optomechanical damping, and the optomechanical spring shift, which have been extensively studied in the past [100, 101]. These previous approaches leveraged frequency domain calculations and a Kubo formula to calculate damping rates, and the minimum phonon occupation. The frequency shift was then calculated through the Kramers Kronig relations. In our approach, we directly solve expressions in the time domain in the form of retarded Green's functions, and then adiabatically eliminate the fast dynamics of the cavity.

In the absence of optomechanical coupling, the mechanical mode is modelled as a damped harmonic oscillator, with annihilation operator $\hat{b}$, intrinsic frequency ω_{b}, and intrinsic damping rate Γ_{b}. The damping is a consequence of coupling to the environment, and according to the fluctuation-dissipation theorem this damping will be accompanied by a dissipation term. In the input-output formalism, we write

$$\dot{\hat{b}} = -\left(i\omega_{\mathrm{b}} + \frac{\Gamma_{\mathrm{b}}}{2}\right)\hat{b} + \sqrt{\Gamma_{\mathrm{b}}}\hat{e}_{\mathrm{in}}, \tag{6.4}$$

where $\hat{e}_{\rm in}$ is the input from the environment. $\omega_{\rm b}$ and $\Gamma_{\rm b}$ are intrinsic properties of the device, however cavity optomechanics offers a way to manipulate the mechanical parameters of the cavity by optical means [70]. As we will show here, this can be viewed as coupling the mechanical mode to an optical reservoir mode, $\hat{r}$. Not only is this interaction easily controllable, but the reservoir can be arranged to have negligible thermal occupation through use of optical laser light.

We consider a reservoir mode with frequency $\omega_{\rm r}$ connected to an input port at a rate $\kappa_{\rm r}^{\rm ex}$ with a total decay rate $\kappa_{\rm r}$. This is dissipatively coupled to the mechanical mode with a strength $g_{\rm r}$. In the presence of a strong control laser with amplitude $\alpha_{\rm r}$, the optomechanical interaction can be linearized, and we can write expressions for the cavity fluctuation operator $\hat{r}$, which is coupled the mechanics at a rate $g_{\rm r} = G_{\rm r}\alpha_{\rm r}x_{\rm o}$, where $G_{\rm r} = \frac{d\omega}{dx}$ is the shift in cavity frequency due mechanical displacement, and $x_{\rm o}$ are the zero point fluctuations of the mechanics [70]. This leads to the coupled equations of motion

$$\begin{bmatrix} \left(\frac{d}{dt}+\frac{1}{\chi_{\rm b}}\right) & 0 & ig_{\rm r} & ig_{\rm r} \\ 0 & \left(\frac{d}{dt}+\frac{1}{\chi_{\rm b\dagger}}\right) & -ig_{\rm r} & -ig_{\rm r} \\ ig_{\rm r} & ig_{\rm r} & \left(\frac{d}{dt}+\frac{1}{\chi_{\rm r}}\right) & 0 \\ -ig_{\rm r} & -ig_{\rm r} & 0 & \left(\frac{d}{dt}+\frac{1}{\chi_{\rm r\dagger}}\right) \end{bmatrix} \begin{bmatrix} \hat{b} \\ \hat{b}^\dagger \\ \hat{r} \\ \hat{r}^\dagger \end{bmatrix} = \begin{bmatrix} \sqrt{\Gamma_{\rm b}}\hat{e}_{\rm in} \\ \sqrt{\Gamma_{\rm b}}\hat{e}_{\rm in}^\dagger \\ \sqrt{\kappa_{\rm r}^{\rm ex}}\hat{r}_{\rm in} \\ \sqrt{\kappa_{\rm r}^{\rm ex}}\hat{r}_{\rm in}^\dagger \end{bmatrix}, \tag{6.5}$$

where we define the relevant response functions as $\chi_{\rm b}^{-1}(\omega) = \Gamma_{\rm b}/2 - i(\omega - \omega_{\rm b})$, $\chi_{\rm b^\dagger}^{-1}(\omega) = \Gamma_{\rm b}/2 - i(\omega + \omega_{\rm b})$, $\chi_{\rm r}^{-1}(\omega) = \kappa_{\rm r}/2 - i(\omega + \Delta_{\rm r})$, and $\chi_{\rm r^\dagger}^{-1}(\omega) = \kappa_{\rm r}/2 - i(\omega - \Delta_{\rm r})$. The input modes at time t, are given in terms of the time t_0 in the far past as [20]

$$\hat{e}_{\rm in}(t) = \frac{1}{\sqrt{2\pi}}\int e^{-i\omega(t-t_0)}E_0(\omega)d\omega, \tag{6.6}$$

$$\hat{r}_{\rm in}(t) = \frac{1}{\sqrt{2\pi}}\int e^{-i\omega(t-t_0)}R_0(\omega)d\omega, \tag{6.7}$$

where E_0 and R_0 are the state of the input modes at time t_0. For the sake of simplicity, in what follows, we will assume $\kappa_{\rm r} = \kappa_{\rm r}^{\rm ex}$.

Using Eq. 6.5, we can solve for the reservoir dynamics as

$$\hat{r}(t) = \hat{r}_0 e^{-(t-t_0)/\chi_\mathrm{r}} + \int_{t_0}^{t} e^{-(t-t')/\chi_\mathrm{r}} \left(\sqrt{\kappa_\mathrm{r}}\hat{r}_\mathrm{in} + iG_\mathrm{r}\hat{b} + iG_\mathrm{r}\hat{b}^\dagger\right) dt', \tag{6.8}$$

$$\hat{r}^\dagger(t) = \hat{r}_0^\dagger e^{-(t-t_0)/\chi_{\mathrm{r}\dagger}} + \int_{t_0}^{t} e^{-(t-t')/\chi_{\mathrm{r}\dagger}} \left(\sqrt{\kappa_\mathrm{r}}\hat{r}_\mathrm{in}^\dagger - iG_\mathrm{r}\hat{b} - iG_\mathrm{r}\hat{b}^\dagger\right) dt'. \tag{6.9}$$

It is interesting to note the role of the optical cavity as a filter. The exponential terms are in the form of a retarded Green's function, and specify a sensitivity to frequencies near $\pm\Delta_\mathrm{r}$ to a history on the timescale $1/\kappa_\mathrm{r}$.

Inserting this into the expression for the mechanics given in Eq. 6.5, we find an equation of motion for the mechanics under the influence of both the environment and the reservoir

$$\begin{aligned}\left(\frac{d}{dt} + i\omega_b\right)\hat{b} = & -\frac{\Gamma_\mathrm{b}}{2}\hat{b} - |g_\mathrm{b}|^2 \int_{t_0}^{t} \left(e^{-(t-t')/\chi_\mathrm{r}}\hat{b}(t') - e^{-(t-t')/\chi_{\mathrm{r}\dagger}}\hat{b}(t')\right) dt' \\ & + \sqrt{\Gamma_\mathrm{b}}\hat{e}_\mathrm{in} + iG_\mathrm{b}\sqrt{\kappa_\mathrm{r}} \int_{t_0}^{t} \left(e^{-(t-t')/\chi_\mathrm{r}}\hat{r}_\mathrm{in}(t') + e^{-(t-t')/\chi_{\mathrm{c}\dagger}}\hat{r}_\mathrm{in}^\dagger(t')\right) dt', \end{aligned} \tag{6.10}$$

where in the above we used the fact the $t - t_0 \gg 1/\kappa_\mathrm{r}$ and applied the rotating wave approximation. The right side of the equation can be interpreted as the sum of damping and dissipation terms due to coupling to the environment, and damping and dissipation terms due to coupling to the reservoir. With the assumption that $\kappa_\mathrm{r} \gg \Gamma_\mathrm{b}$, we can make further simplifications. First we note that the integral associated with the dissipation term becomes

$$\begin{aligned}\int_{t_0}^{t} \left(e^{-(t-t')/\chi_\mathrm{r}} + e^{-(t-t')/\chi_{\mathrm{r}\dagger}}\right)\hat{b}(t')dt' \approx & \int_{t_0}^{t} \left(e^{-(t-t')/\chi_\mathrm{r}} - e^{-(t-t')/\chi_{\mathrm{r}\dagger}}\right) e^{i\omega_b(t-t')}\hat{b}(t)dt' \\ = & \left(\chi_\mathrm{r}(\omega_b) - \chi_{\mathrm{r}\dagger}(\omega_b)\right)\hat{b}(t). \end{aligned} \tag{6.11}$$

Next we simplify the fluctuation term as

$$
\begin{aligned}
&\int_{t_0}^{t} \left(e^{-(t-t')/\chi_{\rm r}} \hat{r}_{\rm in}(t') + e^{-(t-t')/\chi_{\rm r\dagger}} \hat{r}^{\dagger}_{\rm in}(t') \right) dt' \\
&= \frac{1}{\sqrt{2\pi}} \int \int_{t_0}^{t} \left(e^{\left(\chi_{\rm r}^{-1} - i\omega\right)t'} e^{-\chi_{\rm r}^{-1} t + i\omega t_0} \hat{R}_0(\omega) + e^{\left(\chi_{\rm r\dagger}^{-1} + i\omega\right)t'} e^{-\chi_{\rm r\dagger}^{-1} t - i\omega t_0} \hat{R}^{\dagger}_0(\omega) \right) dt' d\omega \\
&= \frac{1}{\sqrt{2\pi}} \int \left(\frac{e^{(\chi_{\rm r}^{-1} - i\omega)t} - e^{(\chi_{\rm r}^{-1} - i\omega)t_0}}{\chi_{\rm r}^{-1} - i\omega} e^{-\chi_{\rm r}^{-1} t + i\omega t_0} \hat{B}_0(\omega) + \frac{e^{(\chi_{\rm r\dagger}^{-1} + i\omega)t} - e^{(\chi_{\rm r\dagger}^{-1} + i\omega)t_0}}{\chi_{\rm r\dagger}^{-1} + i\omega} e^{-\chi_{\rm r\dagger}^{-1} t - i\omega t_0} \hat{R}^{\dagger}_0(\omega) \right) d\omega \\
&\approx \frac{1}{\sqrt{2\pi}} \int \left(e^{-i\omega(t-t_0)} \chi_{\rm r}(\omega) \hat{R}_0(\omega) + e^{i\omega(t-t_0)} \chi_{\rm r\dagger}(\omega) \hat{R}^{\dagger}_0(\omega) \right) d\omega \\
&\approx \frac{1}{\sqrt{2\pi}} \int \left(e^{-i\omega(t-t_0)} \chi_{\rm b}(\omega_{\rm b}) \hat{R}_0(\omega) + e^{i\omega(t-t_0)} \chi_{\rm r\dagger}(\omega_{\rm b}) \hat{R}^{\dagger}_0(\omega) \right) d\omega \\
&= \chi_{\rm r}(\omega_{\rm b}) \hat{r}_{\rm in} + \chi_{\rm r\dagger}(\omega_b) \hat{r}^{\dagger}_{\rm in}. \qquad (6.12)
\end{aligned}
$$

where once again we used the assumption that $\kappa_{\rm r} \gg \Gamma_{\rm b}$ to simplify. Combining Eqs. 6.10–6.12 we arrive at the solution

$$
\begin{aligned}
\left(\frac{d}{dt} + i\omega_{\rm b} \right) \hat{b} = &- \left(\frac{\Gamma_{\rm b}}{2} + |g_{\rm r}|^2 \chi_{\rm r}(\omega_{\rm b}) - |g_{\rm r}|^2 \chi_{\rm r\dagger}(\omega_{\rm b}) \right) \hat{b} \\
&+ \sqrt{\Gamma_{\rm b}} \hat{e}_{\rm in} + i G_{\rm r} \sqrt{\kappa_{\rm r}} \chi_{\rm r}(\omega_{\rm b}) \hat{r}_{\rm in} + i G_{\rm r} \sqrt{\kappa_{\rm r}} \chi_{\rm r\dagger}(\omega_{\rm b}) \hat{r}^{\dagger}_{\rm in}. \qquad (6.13)
\end{aligned}
$$

This can be rearranged to the simple expression reminiscent of Eq. 6.4

$$
\dot{\hat{b}} = - \left(i\omega_{\rm b}^{\rm eff} + \frac{\Gamma_{\rm b}^{\rm eff}}{2} \right) \hat{b} + \sqrt{\Gamma_{\rm b}} \hat{e}_{\rm in} + g_{\rm r} \sqrt{\kappa_{\rm r}} \chi_{\rm r}(\omega_{\rm b}) \hat{r}_{\rm in} + g_{\rm r} \sqrt{\kappa_{\rm r}} \chi_{\rm r\dagger}(\omega_{\rm b}) \hat{r}^{\dagger}_{\rm in}. \qquad (6.14)
$$

In the above we have absorbed a factor of i into the definition of R_0 and $R_0^{\dagger}$, and defined effective frequency and damping terms

$$
\omega_{\rm b}^{\rm eff} = \omega_{\rm b} + \omega_{\rm r}^{\rm opt} = \omega_{\rm b} + |g_{\rm r}|^2 \left(\frac{\omega_{\rm b} + \Delta}{\kappa_{\rm r}^2/4 + (\omega_{\rm b} + \Delta_{\rm r})^2} + \frac{\omega_{\rm b} - \Delta}{\kappa_{\rm r}^2/4 + (\omega_{\rm b} - \Delta_{\rm r})^2} \right), \qquad (6.15)
$$

$$
\Gamma_{\rm b}^{\rm eff} = \Gamma_{\rm b} + \Gamma_{\rm r}^{\rm opt} = \Gamma_{\rm b} + |g_{\rm r}|^2 \left(\frac{\kappa_{\rm r}}{\kappa_{\rm r}^2/4 + (\omega_{\rm b} + \Delta_{\rm r})^2} - \frac{\kappa_{\rm r}}{\kappa_{\rm r}^2/4 + (\omega_{\rm b} - \Delta_{\rm r})^2} \right). \qquad (6.16)
$$

Comparing Eq. 6.4 and Eq. 6.14, we see that coupling the reservoir mode induces both fluctuation and dissipation. By varying the strength or detuning of the control laser, the coupling to the reservoir is modified. In the sideband resolved regime ($\omega_{\rm b} \gg \kappa$) we note two special cases. For $\Delta_{\rm r} = -\omega_{\rm b}$ the effective interaction Hamiltonian is $H_{\rm eff} = -g_{\rm r}\left(\hat{b}^\dagger \hat{r} + \hat{b}\hat{r}^\dagger\right)$, and the mechanics has the equation of motion

$$\dot{\hat{b}} = -\left(i\omega_{\rm b} + \frac{\Gamma_{\rm b}}{2} + \frac{\Gamma_{\rm r}^{\rm opt}}{2}\right)\hat{b} + \sqrt{\Gamma_{\rm b}}\hat{e}_{\rm in} + \sqrt{\Gamma_{\rm r}^{\rm opt}}\hat{r}_{\rm in}^\dagger. \tag{6.17}$$

On the other hand, for $\Delta_{\rm r} = \omega_{\rm b}$ the interaction Hamiltonian takes the form $H_{\rm eff} = -g_{\rm r}\left(\hat{b}\hat{r} + \hat{b}^\dagger \hat{r}^\dagger\right)$, and the equation of motion is

$$\dot{\hat{b}} = -\left(i\omega_{\rm b} + \frac{\Gamma_{\rm b}}{2} - \frac{\Gamma_{\rm r}^{\rm opt}}{2}\right)\hat{b} + \sqrt{\Gamma_{\rm b}}\hat{e}_{\rm in} + \sqrt{\Gamma_{\rm b}}\hat{r}_{\rm in}. \tag{6.18}$$

6.3.5 Enhanced OMIT

The amplitude in cavity a, as a function of probe-control field detuning, $\delta_{\rm a}$, under the influence of the reservoir mode may be expressed as,

$$a(\delta_{\rm a}) = -\frac{\sqrt{\kappa_{\rm ex}}\hat{a}_{\rm in}(\omega)}{i(-\omega_{\rm b} + \delta_{\rm a}) - \kappa_{\rm a}/2 - \frac{|g_{\rm a}|^2}{i(\omega_{\rm b}+\omega_{\rm c}^{\rm opt}-\delta_{\rm a})+(\Gamma_{\rm b}+\Gamma_{\rm r}^{\rm opt})/2}}. \tag{6.19}$$

When our probe is on-resonance, such that $\delta_{\rm a} = \omega_{\rm b}$, we can write our effective cooperativity as:

$$C_{\rm a}^{\rm eff} = C_{\rm a}\frac{\Gamma_{\rm b}}{\Gamma_{\rm b}^{\rm eff}}, \tag{6.20}$$

where $C_{\rm a} = 4|g_{\rm a}|^2/\Gamma_{\rm b}\kappa_{\rm a}$ is our baseline cooperativity.

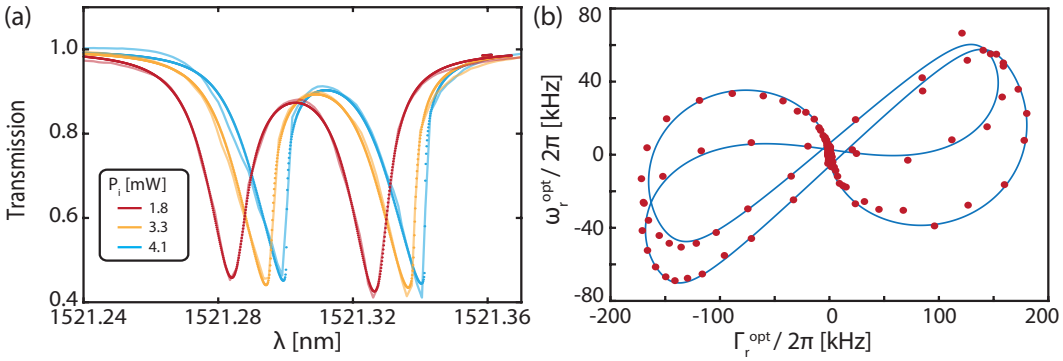

Figure 6.8: (a) Optical transmission as a function of laser wavelength for the reservoir mode for increasing input power illustrating the relatively small thermo-optic shift. The $P_{\mathrm{i}} = 1.8$ mW curve corresponds to the data presented in the main text. (b) Optomechanical damping and spring effect due to mode 'r' plotted as functions of each other, corresponding to the data shown in the main text. Here the separation of each trajectory is due to a difference in the resonance contrast of each doublet mode.

6.3.6 Group delay

The group delay imparted on the pulse in transmission and reflection can be calculated about a central signal frequency, ω_{s} with the spectrum confined to a small window ($< \Gamma_{\mathrm{b}}^{\mathrm{eff}}$) following Safavi-Naeini et al. [89] by computing

$$\tau^{(T)} = \mathcal{R}\left\{\frac{-i}{t(\omega_{\mathrm{s}})}\frac{dt}{d\omega}\right\}, \tag{6.21}$$

and

$$\tau^{(R)} = \mathcal{R}\left\{\frac{-i}{r(\omega_{\mathrm{s}})}\frac{dt}{d\omega}\right\}, \tag{6.22}$$

for the transmission and reflection group delay, respectively. These quantities are shown in Fig. 6.9 for both fixed and variable reservoir laser detuning.

6.3.7 Cooling and Heating

As a test of the reservoir engineering expressions, and as a step towards calculating the thermal occupations required for the memory calculations, we calculate full expressions for optomechanical heating and cooling here. Ignoring initial transients, the formal solution of

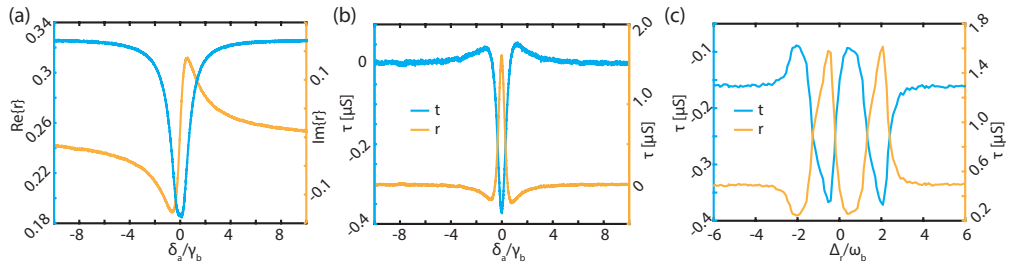

Figure 6.9: (a) Real and imaginary parts of the OMIT scan corresponding to the maximum $C_{\text{eff}} = 83$, where δ_{a} is the probe field detuning. (b) Extracted group delay as a function δ_{a}, for fixed control laser detuning, $\Delta_{\text{a}} = \omega_{\text{b}}$. (c) Extracted group delay as a function of the reservoir mode detuning, Δ_{r}, for fixed probe laser detuning, $\delta_{\text{a}} = \omega_{\text{b}}$.

Eq. 6.14 is

$$\hat{b}(t) = \int_{t_0}^{t} e^{-\left(i\omega_{\text{b}}^{\text{eff}} + \frac{\Gamma_{\text{b}}^{\text{eff}}}{2}\right)(t-\tau)} \left(\sqrt{\Gamma_{\text{b}}}\hat{e}_{\text{in}} + g_{\text{r}}\sqrt{\kappa_{\text{r}}}\chi_{\text{r}}(\omega_{\text{b}})\hat{r}_{\text{in}} + g_{\text{r}}\sqrt{\kappa_{\text{r}}}\chi_{\text{r}^\dagger}(\omega_{\text{b}})\right) d\tau. \tag{6.23}$$

We quantify the thermal statistics of the reservoir and environment with the correlators

$$\langle \hat{r}_{\text{in}}^\dagger(t)\hat{r}_{\text{in}}(t')\rangle = n_{\text{r}}^{\text{th}}\delta(t-t'), \tag{6.24}$$

$$\langle \hat{r}_{\text{in}}(t)\hat{r}_{\text{in}}^\dagger(t')\rangle = (n_{\text{r}}^{\text{th}}+1)\delta(t-t'), \tag{6.25}$$

$$\langle \hat{e}_{\text{in}}^\dagger(t)\hat{e}_{\text{in}}(t')\rangle = n_{\text{e}}^{\text{th}}\delta(t-t'), \tag{6.26}$$

$$\langle \hat{e}_{\text{in}}(t)\hat{e}_{\text{in}}^\dagger(t')\rangle = (n_{\text{e}}^{\text{th}}+1)\delta(t-t') \tag{6.27}$$

where $n_{\mathrm{r}}^{\mathrm{th}}$ is the number of thermal photons occupying the reservoir, and $n_{\mathrm{e}}^{\mathrm{th}}$ is the number of thermal phonons occupying the environment. Using these expressions, we can calculate the thermal occupancy of the cavity as

$$\begin{aligned}\langle \hat{b}^\dagger(t)\hat{b}(t)\rangle = & \int_{t_0}^{t}\int_{t_0}^{t} e^{-\left(-i\omega_{\mathrm{b}}^{\mathrm{eff}}+\frac{\Gamma_{\mathrm{b}}^{\mathrm{eff}}}{2}\right)(t-\tau)-\left(i\omega_{\mathrm{b}}^{\mathrm{eff}}+\frac{\Gamma_{\mathrm{b}}^{\mathrm{eff}}}{2}\right)(t-\tau')} \\ & \left(\sqrt{\Gamma_{\mathrm{b}}}\hat{e}_{\mathrm{in}}(\tau)+g_{\mathrm{r}}\sqrt{\kappa_{\mathrm{r}}}\chi_{\mathrm{r}}(\omega_{\mathrm{b}})\hat{r}_{\mathrm{in}}(\tau)+g_{\mathrm{r}}\sqrt{\kappa_{\mathrm{r}}}\chi_{\mathrm{r}^\dagger}\hat{r}_{\mathrm{in}}^\dagger(\tau)\right)\times \\ & \left(\sqrt{\Gamma_{\mathrm{b}}}\hat{e}_{\mathrm{in}}(\tau')+g_{\mathrm{r}}\sqrt{\kappa_{\mathrm{r}}}\chi_{\mathrm{r}}(\omega_{\mathrm{b}})\hat{r}_{\mathrm{in}}(\tau')+g_{\mathrm{r}}\sqrt{\kappa_{\mathrm{r}}}\chi_{\mathrm{r}^\dagger}\hat{r}_{\mathrm{in}}^\dagger(\tau')\right)d\tau d\tau' \\ = & \int_{t_0}^{t} e^{\Gamma_{\mathrm{b}}^{\mathrm{eff}}(t-\tau)}\left(\Gamma_{\mathrm{b}}n_{\mathrm{th,b}}+\kappa_{\mathrm{r}}|g_{\mathrm{r}}\chi_{\mathrm{r}}(\omega_{\mathrm{b}})|^2 n_{\mathrm{th,b}}+\kappa_{\mathrm{r}^\dagger}|g_{\mathrm{r}}\chi_{\mathrm{r}^\dagger}(\omega_{\mathrm{b}})|^2(n_{\mathrm{th,b}}+1)\right)d\tau \\ = & \frac{\Gamma_{\mathrm{b}}n_{\mathrm{th,b}}+\kappa_{\mathrm{r}}|g_{\mathrm{r}}\chi_{\mathrm{r}}(\omega_{\mathrm{b}})|^2 n_{\mathrm{th,b}}+\kappa_{\mathrm{r}^\dagger}|g_{\mathrm{r}}\chi_{\mathrm{r}^\dagger}(\omega_{\mathrm{b}})|^2(n_{\mathrm{th,b}}+1)}{\Gamma_{\mathrm{b}}^{\mathrm{eff}}}\end{aligned} \tag{6.28}$$

$$= \frac{\Gamma_{\mathrm{b}}n_{\mathrm{th,b}}+\kappa_{\mathrm{r}}|g_{\mathrm{r}}\chi_{\mathrm{r}}(\omega_{\mathrm{b}})|^2 n_{\mathrm{th,b}}+\kappa_{\mathrm{r}^\dagger}|g_{\mathrm{r}}\chi_{\mathrm{r}^\dagger}(\omega_{\mathrm{b}})|^2(n_{\mathrm{th,b}}+1)}{\Gamma_{\mathrm{b}}^{\mathrm{eff}}} \tag{6.29}$$

In the experiment considered in this work, our reservoir does not have thermal occupation. Setting $n_{\mathrm{r}}^{\mathrm{th}}=0$ we recover the usual limit of optomechanical cooling

$$\langle \hat{n}\rangle = \frac{\Gamma_{\mathrm{b}}n_{\mathrm{e}}^{\mathrm{th}}+\Gamma_{\mathrm{opt}}^{\mathrm{r}}n^{\mathrm{min}}}{\Gamma_{\mathrm{b}}+\Gamma_{\mathrm{opt}}^{\mathrm{r}}} \tag{6.30}$$

where, $n^{\mathrm{min}}=|g_{\mathrm{r}}|^2\kappa\chi_{\mathrm{r}^\dagger}(\omega_{\mathrm{b}})/\Gamma_{\mathrm{r}}^{\mathrm{opt}}$.

6.3.8 Storage Enhancement

Solving the equations of motion explicitly, we can divide the phonon population in the cavity during the storage time into signal phonons, which are proportional to $\hat{a}_{\mathrm{in}}$, and undesired thermal phonons, which are a consequence of $\hat{e}_{\mathrm{in}}$. These each evolve as,

$$\langle \hat{b}_{\mathrm{s}}^\dagger(t)\hat{b}_{\mathrm{s}}(t)\rangle = \langle \hat{b_{\mathrm{s}}}^\dagger(0)\hat{b_{\mathrm{s}}}(0)\rangle e^{-\Gamma_{\mathrm{b}}^{\mathrm{eff}}t} \tag{6.31}$$

$$\langle \hat{b}_{\mathrm{th}}^\dagger(t)\hat{b}_{\mathrm{th}}(t)\rangle = n_{\mathrm{e}}^{\mathrm{th}}\Gamma_{\mathrm{b}}\left(\frac{e^{-\Gamma_{\mathrm{b}}^{\mathrm{eff}}t}}{\Gamma_{\mathrm{b}}+\Gamma_{\mathrm{a}}^{\mathrm{opt}}}+\frac{1-e^{-\Gamma_{\mathrm{b}}^{\mathrm{eff}}t}}{\Gamma_{\mathrm{b}}+\Gamma_{\mathrm{c}}^{\mathrm{opt}}}\right). \tag{6.32}$$

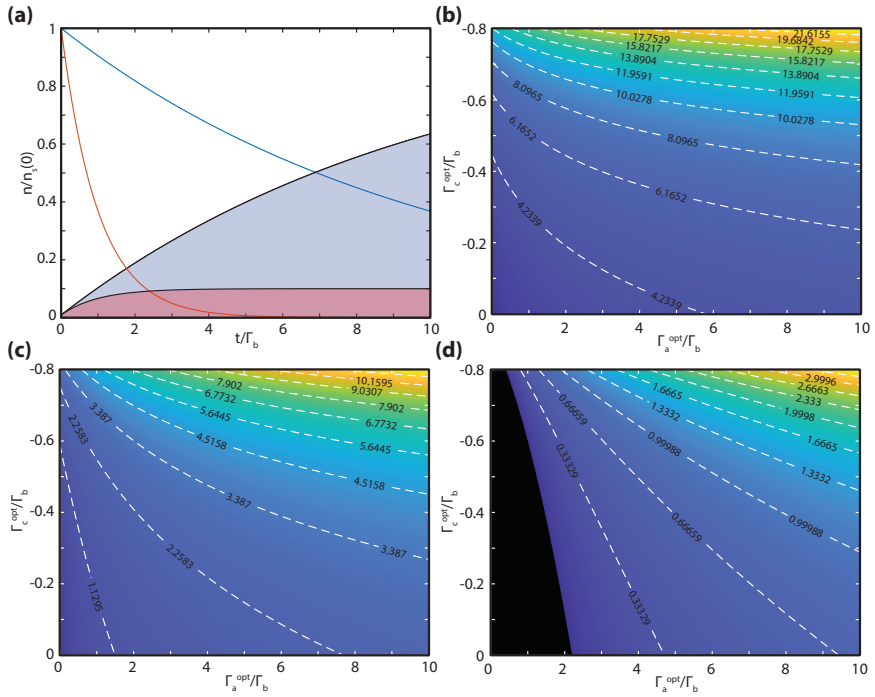

Figure 6.10: (a) Signal phonons (solid lines) and thermal phonons (shaded curves) plotted for $\Gamma_{\rm c}^{\rm opt}/\Gamma_{\rm b} = 0$ (red) and $\Gamma_{\rm c}^{\rm opt}/\Gamma_{\rm b} = -0.9$ (blue). The initial signal to noise ratio $n_{\rm s}(0)/n_{\rm th}(0) = 10$, and $\Gamma_{\rm a}^{\rm opt}/\Gamma_{\rm b} = 10$. (b-d) $t_s\Gamma_{\rm b}$ vs. optomechanical damping rates for initial signal to noise ratios $n_{\rm s}(0)/n_{\rm th}(0) = \{10, 1, 0.1\}$.

Defining the storage time as the moment the signal level decays to the level of the thermal phonons, we find,

$$t_s = \frac{1}{\Gamma_\mathrm{b} + \Gamma_\mathrm{c}^\mathrm{opt}} \ln\left(\frac{n_\mathrm{s}(0)}{n_\mathrm{th}(0)} + \frac{\Gamma_\mathrm{a}^\mathrm{opt} - \Gamma_\mathrm{c}^\mathrm{opt}}{\Gamma_\mathrm{b} + \Gamma_\mathrm{a}^\mathrm{opt}}\right). \tag{6.33}$$

6.3.9 Phase Shifting

Reservoir engineering also allows us to dynamically change the frequency of the mechanical mode. If the frequency is changed over a time interval δt, the change in phase may be expressed as,

$$\delta\phi = \int_0^{\delta t} \left(\omega_b(t) - \omega_b(0)\right) dt \tag{6.34}$$

For simplicity, we assume we change our mechanical frequency as a ramp function, with maximum frequency shift δ_b. Under the adibaticity requirement $1 \gg \frac{\delta\omega_\mathrm{b}}{\omega_\mathrm{b}}$. This yields the simple expression for the phase shift,

$$\delta\phi = \frac{\delta\omega_\mathrm{b}\delta t}{2}. \tag{6.35}$$

In the phase shifting experiment in the main text, we operate with the reservoir laser detuning $\Delta_\mathrm{r} \approx -\omega_\mathrm{b}$, so we may approximate the frequency shift as,

$$\delta\omega_\mathrm{b} \approx \frac{|g_r|^2(\Delta_\mathrm{r} - \omega_\mathrm{b})}{(\Delta_\mathrm{r} - \omega_\mathrm{b})^2 + \kappa_\mathrm{r}^2/4}. \tag{6.36}$$

6.3.10 Pulse Compression

The reservoir mode also permits the mechanical damping rate to be dynamically adjusted. For example, at $\Delta_\mathrm{r} \approx -\omega_\mathrm{b}$, the damping is approximately,

$$\Gamma_\mathrm{r}^\mathrm{opt} \approx \frac{-\kappa_\mathrm{r}|g_\mathrm{r}|^2/2}{(\Delta_\mathrm{r} - \omega_\mathrm{b})^2 + \kappa_\mathrm{r}^2/4}. \tag{6.37}$$

If we ramp the mechanical damping according the expression $\Gamma_{\mathrm{r}}^{\mathrm{opt}}(t) = \eta t$, we recover the expression for a time lens [192],

$$\langle \hat{b}_{\mathrm{s}}^{\dagger}(t)\hat{b}_{\mathrm{s}}(t)\rangle = \langle \hat{b_{\mathrm{s}}}^{\dagger}(0)\hat{b}_{\mathrm{s}}(0)\rangle e^{-(\Gamma_{\mathrm{b}}t+\eta t^2)}. \tag{6.38}$$

Chapter 7

Colour Centres

7.1 Introduction

Colour Centres are interstitial defects within a material, which in many ways act as a solid state analogue to trapped atoms. In this thesis we will primarily be concerned with Nitrogen-Vacancy (NV) colour centres, and secondarily with Silicon Vacancy (SIV) centres. An NV, as depicted on Fig 7.1(a), consists of a missing carbon in the diamond lattice (the vacancy), situated immediately adjacent to a nitrogen atom. NVs have been a topic of intense research interest in the last decade, due to amenable properties allowing it to be used for such applications as magnetometry [194], electric field sensing [195], quantum teleportation [24], and loophole free bell tests [25].

7.1.1 Characterization

The ground state manifold of the NV consists of a spin triplet and a singlet state. Remarkably, the ground state spin of NVs have been shown to posses up to mS coherence times at room temperature [196]. In such circumstances, the spin state of the NV may be read out by via a florescence measurement. First the NV is excited with laser pulse which is more energetic than the relevant optical transitions, as shown on Fig. 7.1(c). This operation is

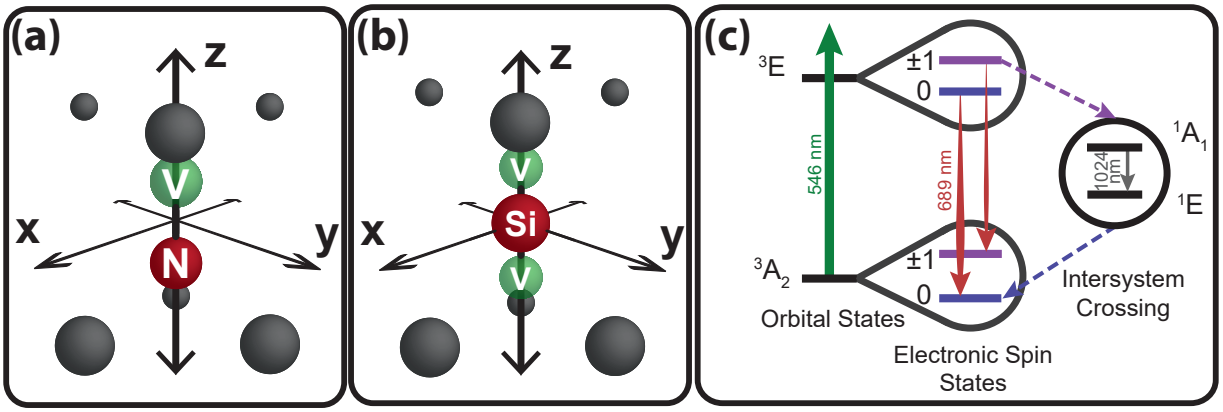

Figure 7.1: (a) Depiction of an NV colour centre. (b) Depiction of an SiV colour centre. (c) Ground state level structure for an NV.

spin preserving, so that if the NV was originally in the $|g,-1\rangle$ state, for example, it will decay into the $|e,-1\rangle$ state after this operation. Due to the existence of a slow decay path through the singlet state, the average florescence for decay from the ± 1 spin states will be lower than that of the 0 spin state on the order of a few percent. In this manner, one can infer the original ground state spin, by monitoring the florescence.

The ground state Hamiltonian for the NV may be written as,

$$\begin{aligned}\hat{H}_{\text{nv}} =& D_0\hat{S}_z^2 + P\hat{I}_z^2 + A_\parallel \hat{I}_z\hat{S}_z \\ &+ \gamma_{\text{nv}}\mathbf{B}\cdot\hat{\mathbf{S}} \\ &+ \epsilon_\parallel\sigma_x\left(\hat{S}_x^2 - \hat{S}_y^2\right) + \epsilon_\perp\sigma_y\left(\hat{S}_x\hat{S}_y + \hat{S}_y\hat{S}_x\right) + \epsilon_\parallel\sigma_z\hat{S}_z^2 \end{aligned} \tag{7.1}$$

In the first line above, $D_0 = 2.87$ GHz is the fine structure splitting, $A_\parallel/2\pi = -2.166$ MHz is the hyperfine coupling, and $P/2\pi = -4.945$ MHz is the nuclear electric quadrupole parameter. The second and third lines describe interaction with magnetic fields and strain, where $\gamma_{\text{NV}}/2\pi$ is the gyromagnetic ratio, $\epsilon_\parallel/2\pi = 0.012$ MHz, is the parallel stress coupling, and $\epsilon_\perp/2\pi = 0.015$ MHz is the perpendicular stress coupling [197, 198].

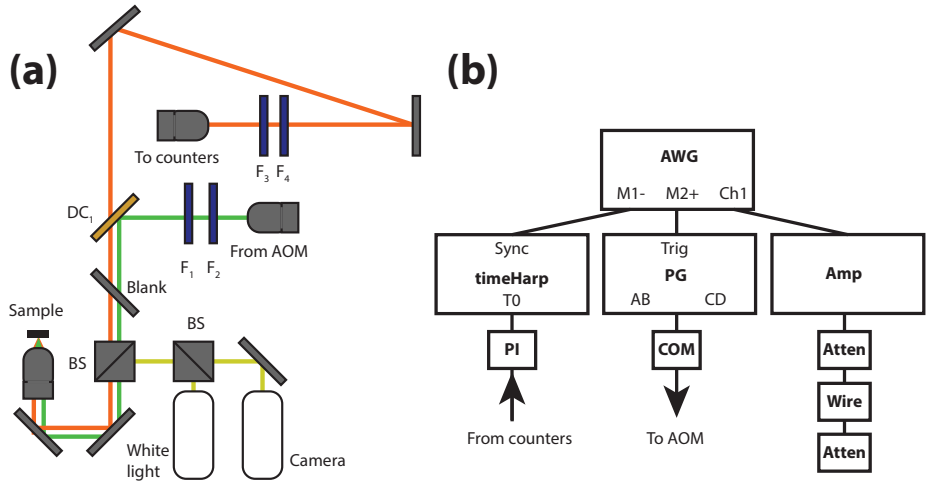

Figure 7.2: (a) Confocal microscope optical setup for NV characterization. Green light is first passed though an Acousto-Optic Modulator (AOM) and spurious light is removed through notch filters (F_1 and F_2). The signal is then sent reflected from a dichroic mirror and sent to a microscope objective and onto the sample. Light from the sample is then sent to the collection path, which the dichroic mirror and long-pass filters F_3 and F_4 are used to block green light reflected from the sample. The sample can optionally be observed with a camera by placing a beamsplitter and blank in the optical path. (b) Electrical setup for NV characterization. The arbitrary waveform generator (AWG) controls the timing of the histogramMER (timeHarp), pulse generator (PG) and send microwave pulses to an amplifier. These pulse are then sent to an antenna placed in close proximity to the sample.

Practically there are a number of calibration measurements one must do to be able to manipulate the ground state spin. Firstly, if one is working with samples with low concentrations of NVs, then the sample may be scanned on a confocal microscopy setup. Here the sample is sample is continuously excited by a 532 nm laser, and florescence from the phonon sideband is collected by optically filtering. The aperture of the confocal setup is provided by sending the light into a fiber optic cable. Isolated bright features in these scan could potentially be NVs. To verify this, one can measure the florescence spectrum on the spectrometer, and look for characteristic features of the NV such as a ZPL at 637 nm and a phonon sideband. There will also likely be Raman lines present at 573 and 738 nm generated from the green laser. Once one is confident that NVs are present, the optical filters

are placed back onto the path, and the fiber output is routed to a 50:50 fiber beamsplitter in a Hanbury-Brown-Twiss configuration to extract a $g_2(\tau)$ measurement. If the dip in the g_2 function is below 50%, then we can assume that we have found a single NV centre.

After applying a magnetic field to split the ± 1 spin states by the desired amount, one then performs an ODMR measurement to measure the frequency of the $0 \rightarrow -1$ transition, and the $0 \rightarrow +1$ transition. The setup we use for this measurement in our lab is shown on Fig. 7.2(a). Here once again the sample is pumped with a 532 green laser, and emission from the phonon sideband is collected in the confocal setup. A microwave signal is generated on a function generator and sent through a high power amplifier to a $\approx 20\mu m$ copper wire placed over the sample. The frequency of the microwave signal is then stepped, and the corresponding NV counts recorded. In the case that the microwave driving power is large, power broadening will wash out the hyperfine levels, and one will ideally see a single dip in florescence at each of the $0 \rightarrow -1$ and the $0 \rightarrow +1$ transition frequencies. If one then lowers the microwave rf power, then three hyperfine levels should emerge for N^{14}, or two hyperfine levels if N^{15} was implanted.

At this point the Rabi frequency of whichever transition we wish to control may be recorded. This is done using the setup shown on Fig. 7.2(b). Initialization of the NV into the 0-spin state, and readout of the final states are enacted through green laser pulses. One then measures the Rabi frequency by stepping the length of a microwave pulse situated between these two pulses, and recording the histogram of the counts received during the read pulse. The full dynamics of the read pulse is well modelled by the five level system given in [199]. However, one can also perform a much simpler analysis simply by binning the initial section of the read pulse. This can then be normalized the latter sections of the read pulse, where the system has reached steady state. This normalization helps to mitigate the effects of drift in the green laser power, for example.

Once the Rabi frequency has been measured, it is a good idea to do a pulsed ODMR measurement if one wants to ensure that the maximum possible population transfer is achieved. This is done by using a green laser initialization pulse, followed by a π rf pulse, and finally a green read pulse. One then steps the carrier frequency of the RF pulse, and measures the histogram of the read pulse. In this way a detailed OMDR scan can be acquired which does not suffer from power broadening due to the green laser. Note, however that the RF drive can still cause power broadening if set too high, so one must be cognizant of this if one wishes to measure the true linewidths. Once this scan is completed, a final Rabi measurement may be performed to calibrate the length of a π-pulse.

In order for the aforementioned measurements to work well, it is important to make sure that collection and excitation paths are co-aligned and collimated. To power of the green laser will also have an effect on the achievable resonance contrast, and can be optimized by performing a saturation measurement. Here the average phonon sideband counts are measured as a function of green laser power, and fit to a simple model $S(I) = S_0/(I/I_{\text{sat}}+1)$, where I is the green laser intensity, I_{sat} is the saturation power, and S_0 is the signal for low laser intensity. Optimal resonance contrast is achieved for powers just above the saturation power [200].

In addition to the above, it is essential to calibrate for delays in the electrical lines and equipment used, particularly whenever a new cable or instrument is introduced. This can then me compensated for in the various scripts in by introducing delays or advances in the timings as required. In the above experiments, the delay in the green laser pulses relative to the timeHarp histogrammer is measured by triggering the timeHarp from the AWG, and measuring a short green pulse. The delay in the microwave RF pulses is measured by placing an rf pulse inside of a longer green laser pulse. The reduction on florescence indicates the leading edge of the RF pulse. Alternatively, the digital series analyzer (DSA) can be used to measure the RF signal if the antenna output is sent through a high power attenuator.

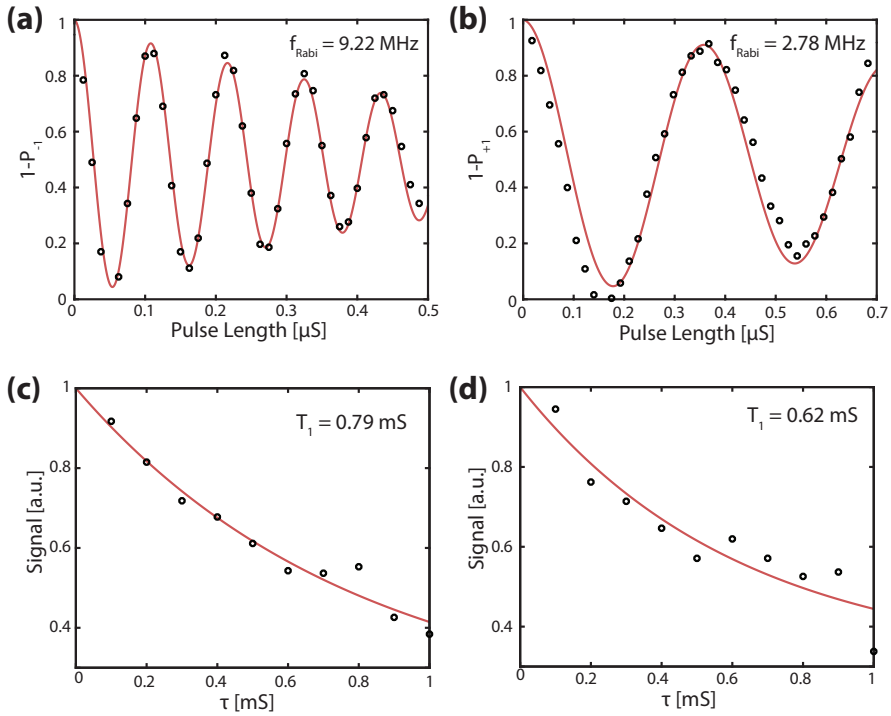

Figure 7.3: (a) Rabi oscillations in the $0 \rightarrow -1$ sublevel. (a) Rabi oscillations in the $0 \rightarrow +1$ sublevel. (c) T_1 on the $0 \rightarrow -1$ sublevel. (d) T_1 on the $0 \rightarrow +1$ sublevel.

7.2 Towards Optomechanical Spin-Strain Coupling

A number or experiments have probed the nature the ground state stress coupling in nitrogen vacancy centres. Work from the group of Marko Lončar used NVs embedded in the clamping point of a diamond cantilever, which was then actuated through electrostatic interactions [126]. These experiments induced shifts in the energy if the ± 1 spin states using the parallel strain components given in Eq. 7.1. These shifts could then be measured in an ODMR experiment.

In contrast to this, MacQuarrie et al. made use of the a perpendicular stress field, generated by piezoelectric actuation [197]. In this case, population could be coherently driven between the -1 and $+1$ spin states. Our longstanding goal then, is to use this scheme, but replace the piezoelectric actuation with an optomechanical drive. To do so, we drive a diamond microdisk into the self oscillation regime, by placing a laser blue detuned from the cavity by $\Delta = \omega_{\mathrm{m}}$, and increasing power until the mechanical damping is completely com-

pensated by the optomechanical anti-damping. In order to prevent drift in the mechanical phase and frequency, we utilize injection locking and amplitude feedback, according to the protocol of [201].

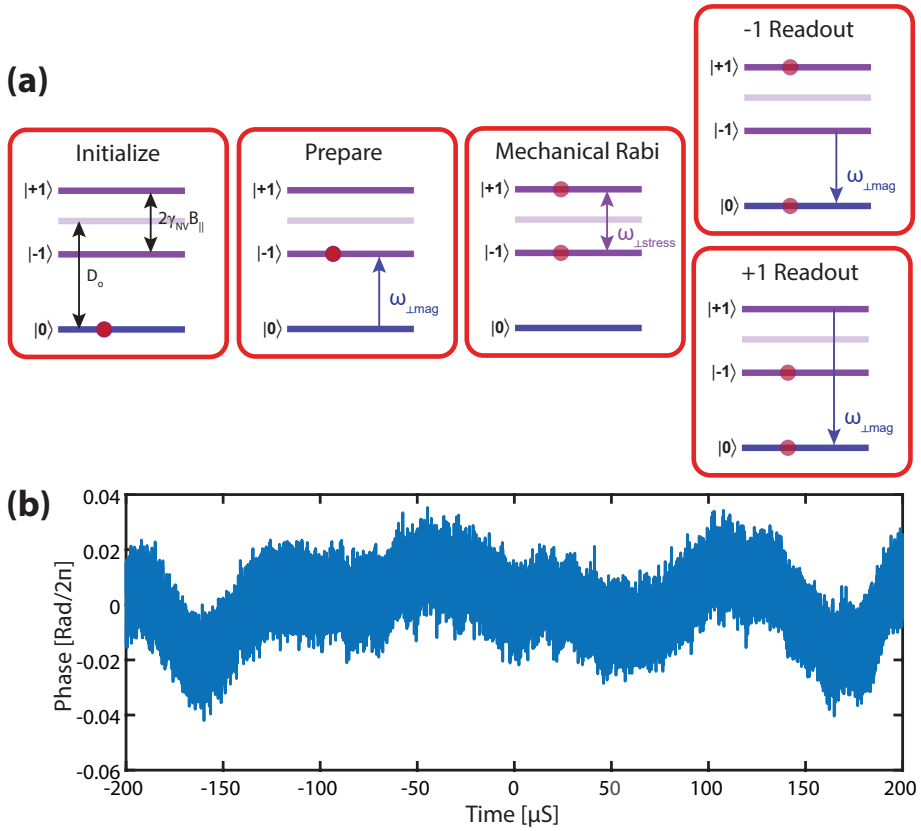

Figure 7.4: (a) Strain coupling protocol steps as explained in the main text. (b) Phase drift of unlocked mechanical oscillations.

Initially, we set the splitting of the ± 1 spin states to be equal to the mechanical frequency by tuning with a field as shown on Fig. 7.4(a). We then apply an ≈ 5 μS pulse to initialize in the 0-spin state. A microwave π-pulse from a wire adjacent to the sample then sends the population to the -1 spin state. We then allow the system to evolve for a period of time under perturbation by the mechanical stress field. Finally readout from either the -1 of the $+1$ state can be inferred by applying a π-pulse which will map the population back to the 0-spin state. This final step is required, as the florescence level of the ± 1 states are

identical. In order for the above scheme to work, we require that the Rabi frequencies of the microwave pulse are much greater than the Rabi frequencies of the mechanical pulse. Current experiments with this scheme are ongoing.

Chapter 8

Summary and Outlook

8.1 Summary

At the outset of this thesis, the stated goal was to present a series of experiments which were enhanced by interactions in a nanophotonic structure. We have shown that nonlinear interactions were enhanced by the small mode volumes achieved, which permitted the buildup of very large optical fields. Optomechanical coupling rates were also enhanced by the small dimensions of the devices involved, which enabled the study of a number of optomechanical effects. Finally, the presence of a localized stress field should allow for coupling to NV colour centres in diamond.

8.2 Outlook

The experiments detailed in this thesis have a number of potential future applications, some of which we summarize below. This list is by no means exhaustive.

8.2.1 Nonlinear Optics

The photonic structures which currently holds the record for SHG is a microring type resonator [202]. In this design, both the diameter of the ring, and the width of the waveguide may be independently adjusted. This allows for control of the resonance and phase matching conditions. These designs could be readily ported over to such a geometry. An obvious next step in our GaP research would be to create microring or racetrack type structures from GaP material.

Another interesting possibility would be to use a system of two adjacent microdisks. In this scheme, the fundamental mode resides in one microdisk, and the second harmonic mode resides in the other microdisk. The overlap between the modes would be used for SHG as in [203]. This has the advantage of maintaining the small mode volumes that the microdisk design offers.

8.2.2 Multimode Optomechanics

Due to the very large transparency window of diamond, optomechanical wavelength conversion and amplification could in principle be achieved using visible wavelengths. Initial steps in this direction are detail in [94], which were performed in the same devices as detailed in the multimode optomechanics section of this thesis. This range of wavelengths could be useful, for example to realize wavelength conversion from the zero phonon line of an NV to visible wavelengths.

The work on DOMIT in this thesis could also be further developed. In particular, one could envision a system where the output of the bright and dark states are filtered as a means to reduce the effects of thermal noise. There is also the possibility to initially 'seed' the system in the optomechanically dark state to reduce the noise in wavelength conversion. Another experiment could use the interference present in a DOMIT system to create a time

domain interferometer [164]. Finally, as alluded to in DOMIT chapter, these ideas can be extended to higher dimensions, to realize an N-channel add drop filter, and interesting interference effects.

8.2.3 Colour Centres

The ground state stress couplings detailed in this paper would greatly benefit from optomechanical crystal designs. An even more interesting regime is reached in situations where the mechanical frequency of the device exceeds the linewidth of embedded NVs or SiVs. In this case one could make use of the parallel stress component in the excited state, which has substantially higher coupling rates [204]. In such a situation, optomechanical interactions could be used to perform optical readout from a telecom frequency optical mode, mediated by a mechanical mode. One could also use colour centres to directly cool the mechanical mode [205].

Bibliography

[1] D.J. Griffiths. *Introduction to Electrodynamics*. Cambridge University Press, 2017.

[2] J.D. Jackson. *Classical Electrodynamics Third Edition*. Wiley, 1998.

[3] H.-T. Chen, A.J. Taylor, and N. Yu. A review of metasurfaces: physics and applications. *Reports on Progress in Physics*, 79(7):076401, 2016.

[4] R.W. Boyd. *Nonlinear Optics*. Academic Press, San Diego, CA, 2nd edition, 2003.

[5] J.D. Joannopoulos, S.G. Johnson, J.N. Winn, and R.D. Meade. *Photonic Crystals: Molding the Flow of Light*. Princeton University Press, 2nd edition, 2008.

[6] A.F. Oskooi, D. Roundy, M. Ibanescu, P. Bermel, J.D. Joannopoulos, and S.G. Johnson. Meep: A flexible free-software package for electromagnetic simulations by the FDTD method. *Comp. Phys. Comm.*, 181(3):687–702, 2010.

[7] Amno Yariv and Pochi Yeh. *Photonics: Optical Electronics in Modern Communications*. Oxford, 2006.

[8] A. Yariv and P. Yeh. *Photonics: Optical Electronics in Modern Communications*. Oxford, New York, 2006.

[9] C. Pollock and M. Lipson. *Integrated Photonics*. Kluwer Academic Publishers, 2003.

[10] E. A. J. Marcatili. Dielectric rectangular waveguide and directional coupler for integrated optics. *The Bell System Technical Journal*, 48(7):2071–2102, 1969.

[11] W.J. Westerveld and H.P. Urbach. Waveguides. In *Silicon Photonics*, 2053-2563, pages 2–1 to 2–36. IOP Publishing, 2017.

[12] M. Borselli. *High-Q microresonators as lasing elements for silicon photonics*. PhD thesis, California Institute of Technology, 2006.

[13] F. de Fornel. *Evanescent Waves From Newtonian Optics to Atomic Optics*. Springer, 2001.

[14] H. A. Haus and W. Huang. Coupled-mode theory. *Proc. IEEE*, 79(10):1505–1518, 1991.

[15] Wonjoo Suh, Zheng Wang, and Shanhui Fan. Temporal coupled-mode theory and the presence of non-orthogonal modes in lossless multimode cavities. *IEEE Journal of Quantum Electronics*, 40(10):1511–1518, 2004.

[16] D. F. Walls and Gerard J. Milburn. *Quantum Optics*. Springer-Verlag, Berlin, 2008.

[17] N. Quesada and J.E. Sipe. Why you should not use the electric field to quantize in nonlinear optics. *Opt. Lett.*, 42(17):3443–3446, 2017.

[18] J.E. Sipe, Navin A.R. Bhat, P. Chak, and S. Pereira. Effective field theory for the nonlinear optical properties of photonic crystals. *Phys. Rev. E*, 69:016604, 2004.

[19] C.W. Gardiner and M.J. Collett. Input and output in damped quantum systems: Quantum stochastic differential equations and the master equation. *Phys. Rev. A*, 31:3761–3774, 1985.

[20] C.W. Gardiner and P. Zoller. *Quantum Noise*. Springer, Berlin, 1991.

[21] M.D. Henry. *ICP etching of silicon for micro and nanoscale devices*. PhD thesis, Califonia Institute of Technology, 2010.

[22] M.H.P. Pfeiffer, A. Kordts, V. Brasch, M. Zervas, M. Geiselmann, J.D. Jost, and T.J. Kippenberg. Photonic damascene process for integrated high-q microresonator based nonlinear photonics. *Optica*, 3(1):20–25, 2016.

[23] H. Bernien, B. Hensen, W. Pfaff, G. Koolstra, M. S. Blok, L. Robledo, T. H. Taminiau, M. Markham, D. J. Twitchen, L. Childress, and R. Hanson. Heralded entanglement between solid-state qubits separated by three meters. *Nature*, 497:86–90, 2013.

[24] W. Pfaff, B.J. Hensen, H. Bernien, S.B. van Dam, M.S. Blok, T.H. Taminiau, M.J. Tiggelman, R.N. Schouten, M. Markham, D.J. Twitchen, and R. Hanson. Unconditional quantum teleportation between distant solid-state quantum bits. *Science*, 345(6196):532–535, 2014.

[25] B. Hensen, H. Bernien, A.E. Dréau, A. Reiserer, N. Kalb, M.S. Blok, J. Ruitenberg, R.F.L. Vermeulen, R.N. Schouten, C. Abellán, W. Amaya, V. Pruneri, M.W. Mitchell, M. Markham, D.J. Twitchen, D. Elkouss, S. Wehner, T.H. Taminiau, and R. Hanson. Loophole-free bell inequality violation using electron spins separated by 1.3 kilometres. *Nature*, 526:682–86, 2015.

[26] Y. Chu, N.P. de Leon, B.J. Shields, B. Hausmann, R. Evans, E. Togan, M. J. Burek, M. Markham, A. Stacey, A.S. Zibrov, A. Yacoby, D.J. Twitchen, M. Loncar, H. Park, P. Maletinsky, and M.D. Lukin. Coherent optical transitions in implanted nitrogen vacancy centers. *Nano Lett.*, 14(4):1982–1986, 2014.

[27] S. Sangtawesin, B.L. Dwyer, S. Srinivasan, J.J. Allred, L.V.H. Rodgers, K. De Greve, A. Stacey, N. Dontschuk, K.M. O'Donnell, D. Hu, D.A. Evans, C. Jaye, D.A. Fischer, M.L. Markham, D.J. Twitchen, H. Park, M.D. Lukin, and N. de Leon. Origins of diamond surface noise probed by correlating single-spin measurements with surface spectroscopy. *Phys. Rev. X*, 9:031052, 2019.

[28] B.C. Rose, D. Huang, Z.-H. Zhang, P. Stevenson, A.M. Tyryshkin, S. Sangtawesin, S. Srinivasan, L. Loudin, M.L. Markham, A.M. Edmonds, D.J. Twitchen, S.A. Lyon, and N.P. de Leon. Observation of an environmentally insensitive solid-state spin defect in diamond. *Science*, 361(6397):60–63, 2018.

[29] C.L. Lee, E. Gu, M.D. Dawson, I. Friel, and G.A. Scarsbrook. Etching and micro-optics fabrication in diamond using chlorine-based inductively-coupled plasma. *Diamond Relat. Mater.*, 17:1292–1296, 2008.

[30] JF Zeigler. The stopping range of ions in matter, srim-2008, 2008.

[31] B. Khanaliloo, H. Jayakumar, A.C. Hryciw, D.P. Lake, H. Kaviani, and P.E. Barclay. Single-crystal diamond nanobeam waveguide optomechanics. *Phys. Rev. X*, 5:041051, 2015.

[32] J. Riedrich-Möller, L. Kipfstuhl, C. Hepp, E. Neu, C. Pauly, F. Mücklich, A. Baur, M. Wandt, S. Wolff, M. Fischer, et al. One-and two-dimensional photonic crystal microcavities in single crystal diamond. *Nat. Nanotechnol.*, 7(1):69–74, 2012.

[33] M.J. Burek, D. Ramos, P. Patel, I.W. Frank, and M. Lončar. Nanomechanical resonant structures in single-crystal diamond. *Appl. Phys. Lett.*, 103(13), 2013.

[34] M.J. Burek, Y. Chu, M.S.Z. Liddy, P. Patel, J. Rochman, S. Meesala, W. Hong, Q. Quan, M.D. Lukin, and M. Lončar. High quality-factor optical nanocavities in bulk single-crystal diamond. *Nat. Commun.*, 5:5718, 2014.

[35] Matthew Mitchell, Behzad Khanaliloo, David P. Lake, Tamiko Masuda, J. P. Hadden, and Paul E. Barclay. Single-crystal diamond low-dissipation cavity optomechanics. *Optica*, 3(9):963–970, Sep 2016.

[36] S. Mouradian, N.H. Wan, T. Schröder, and D. Englund. Rectangular photonic crystal nanobeam cavities in bulk diamond. *Appl. Phys. Lett.*, 111:021103, 2017.

[37] M. Mitchell, D.P. Lake, and P.E. Barclay. Realizing $Q > 300\,000$ in diamond microdisks for optomechanics via etch optimization. *APL Photonics*, 4(1):016101, 2019.

[38] J. Hill. *Nonlinear optics and wavelength translation via cavity-optomechanics*. PhD thesis, California Institute of Technology, 2013.

[39] A.D. Logan, M. Gould, E.R. Schmidgall, K. Hestroffer, Z. Lin, W. Jin, A. Majumdar, F. Hatami, A.W. Rodriguez, and K.-M. Fu. 400%/w second harmonic conversion efficiency in 14 um-diameter gallium phosphide-on-oxide resonators. *Opt. Express*, 26(26):33687–33699, 2018.

[40] P. A. Franken, A. E. Hill, C. W. Peters, and G. Weinreich. Generation of optical harmonics. *Phys. Rev. Lett.*, 7:118–119, 1961.

[41] S. Nakagawa, N. Yamada, N. Mikoshiba, and D.E. Mars. Second-harmonic generation from gaas/alas vertical cavity. *Appl. Phys. Lett.*, 66(17):2159–2161, 1995.

[42] J.P. Mondia, H.M. Van Driel, W. Jiang, A.R. Cowan, and J.F. Young. Enhanced second-harmonic generation from planar photonic crystals. *Optics letters*, 28(24):2500–2502, 2003.

[43] V.S. Ilchenko, A.A. Savchenkov, A.B. Matsko, and L. Maleki. Nonlinear optics and crystalline whispering gallery mode cavities. *Phys. Rev. Lett.*, 92:043903, 2004.

[44] M.W. McCutcheon, J.F. Young, G.W. Rieger, D. Dalacu, S. Frédérick, P.J. Poole, and R.L. Williams. Experimental demonstration of second-order processes in photonic crystal microcavities at submilliwatt excitation powers. *Phys. Rev. B*, 76:245104, 2007.

[45] S. Yamada, B.-S. Song, S. Jeon, J. Upham, Y. Tanaka, T. Asano, and S. Noda. Second-harmonic generation in a silicon-carbide-based photonic crystal nanocavity. *Opt. Lett.*, 39(7):1768–1771, 2014.

[46] S. Mariani, A. Andronico, O. Mauguin, A. Lemaître, I. Favero, S. Ducci, and G. Leo. Algaas microdisk cavities for second-harmonic generation. *Opt. Lett.*, 38(19):3965–3968, 2013.

[47] S. Buckley, M. Radulaski, K. Biermann, and J. Vučković. Second harmonic generation in photonic crystal cavities in (111)-oriented gaas. *Appl. Phys. Lett.*, 103(21), 2013.

[48] S. Diziain, R. Geiss, M. Zilk, F. Schrempel, E.-B. Kley, A. Tünnermann, and T. Pertsch. Second harmonic generation in free-standing lithium niobate photonic crystal l3 cavity. *Appl. Phys. Lett.*, 103(5), 2013.

[49] P.S. Kuo and G.S. Solomon. On- and off-resonance second-harmonic generation in gaas microdisks. *Opt. Express*, 19(18):16898–16918, 2011.

[50] C. Wang, M.J. Burek, Z. Lin, H.A. Atikian, V. Venkataraman, I.-C. Huang, P. Stark, and M. Lončar. Integrated high quality factor lithium niobate microdisk resonators. *Opt. Express*, 22(25):30924–30933, 2014.

[51] P.S. Kuo, J. Bravo-Abad, and G.S. Solomon. Second-harmonic generation using quasi-phasematching in a gaas whispering-gallery-mode microcavity. *Nat. Commun.*, 5, 2014.

[52] S. Mariani, A. Andronico, A. Lemaître, I. Favero, S. Ducci, and G. Leo. Second-harmonic generation in algaas microdisks in the telecom range. *Opt. Lett.*, 39(10):3062–3065, 2014.

[53] W.H.P. Pernice, C. Xiong, C. Schuck, and H.X. Tang. Second harmonic generation in phase matched aluminum nitride waveguides and micro-ring resonators. *Appl. Phys. Lett.*, 100(22), 2012.

[54] J. L. Dominguez-Juarez, G. Kozyreff, and J. Martorell. Whispering gallery microresonators for second harmonic light generation from a low number of small molecules. *Nat. Commun.*, 2:254, 2011.

[55] K. Rivoire, S. Buckley, F. Hatami, and J. Vuković. Second harmonic generation in gap photonic crystal waveguides. *Appl. Phys. Lett.*, 98(26), 2011.

[56] K. Lenglé, L. Bramerie, M. Gay, J.-C. Simon, S. Combrié, G. Lehoucq, and A. De Rossi. Efficient second harmonic generation in nanophotonic waveguides for optical signal processing. *Appl. Phys. Lett.*, 102:151114, 2013.

[57] J. U. Fürst, D. V. Strekalov, D. Elser, M. Lassen, U. L. Andersen, C. Marquardt, and G. Leuchs. Naturally phase-matched second-harmonic generation in a whispering-gallery-mode resonator. *Phys. Rev. Lett.*, 104:153901, 2010.

[58] S. Buckley, M. Radulaski, J.L. Zhang, J. Petykiewicz, K. Biermann, and J. Vučković. Nonlinear frequency conversion using high-quality modes in gaas nanobeam cavities. *Opt. Lett.*, 39(19):5673–5676, 2014.

[59] T. Carmon and K.J. Vahala. Visible continuous emission from a silica microphotonic device by third-harmonic generation. *Nat. Phys.*, 3(6):430–435, Jun 2007.

[60] G. Shambat, K. Rivoire, J. Lu, F. Hatami, and J. Vučković. Tunable-wavelength second harmonic generation from gap photonic crystal cavities coupled to fiber tapers. *Opt. Express*, 18(12):12176–12184, 2010.

[61] Y. Dumeige and P. Feron. Whispering-gallery-mode analysis of phase-matched doubly resonant second-harmonic generation. *Phys. Rev. A*, 74(6):063804, 2006.

[62] T. Carmon, L. Yang, and K.J. Vahala. Dynamical thermal behavior and thermal self-stability of microcavities. *Opt. Express*, 12(20):4742–4750, 2004.

[63] D.A. Yaskov and A.N. Pikhtin. Optical properties of gallium phosphide grown by floating zone i. refractive index and reflection coefficient. *Mater. Res. Bull.*, 4(10):781–787, 1969.

[64] M. Mitchell, A.C. Hryciw, and P.E. Barclay. Cavity optomechanics in gallium phosphide microdisks. *Applied Physics Letters*, 104(14), 2014.

[65] C.W. Wong, P.T. Rakich, S.G. Johnson, M. Qi, H.I. Smith, E.P. Ippen, L.C. Kimerling, Y. Jeon, G. Barbastathis, and S.-G. Kim. Strain-tunable silicon photonic band gap microcavities in optical waveguides. *Appl Phys Lett*, 84(8):1242–1244, 2004.

[66] Qing Li, Marcelo I. Davanco, and Kartik Srinivasan. Chip-based frequency conversion by four-wave-mixing bragg scattering in si3n4 microrings. In *CLEO: 2015*, page JTu5A.43. Optical Society of America, 2015.

[67] W.C. Jiang, X. Lu, J. Zhang, O.J. Painter, and Q. Lin. Silicon-chip source of bright photon pairs. *Opt. Express*, 23(16):20884–20904, 2015.

[68] Z. Yang and J.E. Sipe. Generating entangled photons via enhanced spontaneous parametric downconversion in algaas microring resonators. *Opt. Lett.*, 32(22):3296–3298, 2007.

[69] L.G. Helt, Z. Yang, M. Liscidini, and J.E. Sipe. Spontaneous four-wave mixing in microring resonators. *Opt. Lett.*, 35(18):3006–3008, 2010.

[70] M. Aspelmeyer, T.J. Kippenberg, and F. Marquardt. Cavity optomechanics. *Rev. Mod. Phys.*, 86:1391–1452, 2014.

[71] M. Wu, N. Wu, T. Firdous, F. Fani Sani, J.E. Losby, M.R. Freeman, and P.E. Barclay. Nanocavity optomechanical torque magnetometry and radiofrequency susceptometry. *Nature Nanotechnology*, 12:127–131, 2016.

[72] A.G. Krause, M. Winger, T.D. Blasius, Q. Lin, and O.J. Painter. A high-resolution microchip optomechanical accelerometer. *Nature Photonics*, 6:768–772, 2012.

[73] M. Wu, A. C. Hryciw, C. Healey, D. P. Lake, M. R. Freeman, J. P. Davis, and P. E.. Barclay. Dissipative and dispersive optomechanics in a nanocavity torque sensor. *Phys. Rev. X*, 4:021052, 2014.

[74] T. Corbitt, Y. Chen, E. Innerhofer, H. Müller-Ebhardt, D. Ottaway, H. Rehbein, D. Sigg, S. Whitcomb, C. Wipf, and N. Mavalvala. An all-optical trap for a gram-scale mirror. *Phys. Rev. Lett.*, 98:150802, 2007.

[75] LIGO Scientific Collaboration. A gravitational wave observatory operating beyond the quantum shot-noise limit. *Nature Phys.*, 7(12):962–965, 2011.

[76] J. Chan, T.P. Alegre, A.H. Safavi-Naeini, J.T. Hill, A. Krause, S. Groblacher, M. Aspelmeyer, and O.J. Painter. Laser cooling of a nanomechanical oscillator into its quantum ground state. *Nature*, 478:89–92, 2011.

[77] J.D. Teufel, T. Donner, D. Li, J.W. Harlow, M.S. Allman, K. Cicak, A.J. Sirois, J.D. Whittaker, K.W. Lehnert, and R.W. Simmonds. Sideband cooling of micromechanical motion to the quantum ground state. *Nature*, 475(7356):359–363, 2011.

[78] V. Fiore, C. Dong, M.C. Kuzyk, and H. Wang. Optomechanical light storage in a silica microresonator. *Phys. Rev. A*, 87(2):023812, 2013.

[79] J.W. Palomaki, T.A .and Harlow, J.D. Teufel, R.W. Simmonds, and K.W. Lehnert. Coherent state transfer between itinerant microwave fields and a mechanical oscillator. *Nature*, 495(7440):210, 2013.

[80] K. Hammerer, A.S. Sørensen, and E.S. Polzik. Quantum interface between light and atomic ensembles. *Rev. Mod. Phys.*, 82:1041–1093, 2010.

[81] D. Wang, H. Kelkar, D. Martin-Cano, D. Rattenbacher, A. Shkarin, T. Utikal, S. Götzinger, and V. Sandoghdar. Turning a molecule into a coherent two-level quantum system. *Nat. Phys.*, 15(5):483–489, 2019.

[82] D. W. C. Brooks, T. Botter, S. Schreppler, T.P. Purdy, N. Brahms, and D.M. Stamper-Kurn. Non-classical light generated by quantum-noise-driven cavity optomechanics. *Nature*, 488(7412):476–480, 2012.

[83] A.H. Safavi-Naeini, S. Groblacher, J.T. Hill, J. Chan, M. Aspelmeyer, and O Painter. Squeezed light from a silicon micromechanical resonator. *Nature*, 500:185–189, 2013.

[84] T. P. Purdy, K. E. Grutter, K. Srinivasan, and J. M. Taylor. Quantum correlations from a room-temperature optomechanical cavity. *Science*, 356(6344):1265–1268, 2017.

[85] C.F. Ockeloen-Korppi, E. Damskägg, J.-M. Pirkkalainen, M. Asjad, A.A. Clerk, F. Massel, M.J. Woolley, and M.A. Sillanpää. Stabilized entanglement of massive mechanical oscillators. *Nature*, 556(7702):478, 2018.

[86] C.K. Law. Interaction between a moving mirror and radiation pressure: A hamiltonian formulation. *Phys. Rev. A*, 51:2537–2541, 1995.

[87] T.J. Kippenberg and K.J. Vahala. Cavity opto-mechanics. *Opt. Express*, 15(25):17172–17205, 2007.

[88] R. Weis, S.and Rivière, S. Deléglise, E. Gavartin, O. Arcizet, A. Schliesser, and T.J. Kippenberg. Optomechanically induced transparency. *Science*, 330(6010):1520–1523, 2010.

[89] A.H. Safavi-Naeini, T.P. Mayer Alegre, J. Chan, M. Eichenfield, M. Winger, Q. Lin, J.T. Hill, D.E. Chang, and O.J. Painter. Electromagnetically induced transparency and slow light with optomechanics. *Nature*, 472(7341):69–73, 2011.

[90] D.P. Lake, M. Mitchell, Y. Kamaliddin, and P.E. Barclay. Optomechanically induced transparency and cooling in thermally stable diamond microcavities. *ACS Photonics*, 5(3):782–787, 2018.

[91] A. Safavi-Naeini, J. Chan, J.T. Hill, S. Gr oblacher, H. Miao, Y. Chen, M. Aspelmeyer, and O.J. Painter. Laser noise in cavity-optomechanical cooling and thermometry. *New J. Phys.*, 15(3):035007, 2013.

[92] F.Y. Khalili, H. Miao, H. Yang, A.H. Safavi-Naeini, O.J. Painter, and Y. Chen. Quantum back-action in measurements of zero-point mechanical oscillations. *Phys. Rev. A*, 86:033840, 2012.

[93] R. W. Andrews, R. W. Peterson, T. P. Purdy, K. Cicak, R. W. Simmonds, C. A. Regal, and K. W. Lehnert. Bidirectional and efficient conversion between microwave and optical light. *Nat. Photonics*, 10:321–326, 2014.

[94] M. Mitchell, D.P. Lake, and P.E. Barclay. Optomechanically amplified wavelength conversion in diamond microcavities. *Optica*, 6(7):832–838, 2019.

[95] T.A. Palomaki, J.D. Teufel, R.W. Simmonds, and K.W. Lehnert. Entangling mechanical motion with microwave fields. *Science*, 342(6159):710–713, 2013.

[96] C. Galland, N. Sangouard, N. Piro, N. Gisin, and T.J. Kippenberg. Heralded single-phonon preparation, storage, and readout in cavity optomechanics. *Phys. Rev. Lett.*, 112:143602, 2014.

[97] CF Ockeloen-Korppi, Erno Damskägg, J-M Pirkkalainen, TT Heikkilä, Francesco Massel, and MA Sillanpää. Low-noise amplification and frequency conversion with a multiport microwave optomechanical device. *Phys. Rev. X*, 6(4):041024, 2016.

[98] A.A. Clerk, M.H. Devoret, S.M. Girvin, F. Marquardt, and R.J. Schoelkopf. Introduction to quantum noise, measurement, and amplification. *Rev. Mod. Phys.*, 82:1155–1208, 2010.

[99] R.J. Schoelkopf, A.A. Clerk, S.M. Girvin, K.W. Lehnert, and M.H. Devoret. *Qubits as Spectrometers of Quantum Noise*, pages 175–203. Springer Netherlands, Dordrecht, 2003.

[100] F. Marquardt, J.P. Chen, A.A. Clerk, and S.M. Girvin. Quantum theory of cavity-assisted sideband cooling of mechanical motion. *Phys. Rev. Lett.*, 99:093902, 2007.

[101] I. Wilson-Rae, N. Nooshi, W. Zwerger, and T.J. Kippenberg. Theory of ground state cooling of a mechanical oscillator using dynamical backaction. *Phys. Rev. Lett.*, 99:093901, 2007.

[102] P. Treutlein, C. Genes, K. Hammerer, M. Poggio, and P. Rabl. Hybrid mechanical systems. In *Cavity Optomechanics*, pages 327–351. Springer, 2014.

[103] Y. Liu, M. Davanço, V. Aksyuk, and K. Srinivasan. Electromagnetically induced transparency and wideband wavelength conversion in silicon nitride microdisk optomechanical resonators. *Phys. Rev. Lett.*, 110(22):223603, 2013.

[104] A.H. Safavi-Naeini, J. Chan, J.T. Hill, T. P. M. Alegre, A. Krause, and O. Painter. Observation of quantum motion of a nanomechanical resonator. *Phys. Rev. Lett.*, 108(3):033602, 2012.

[105] J.D. Cohen, S.M. Meenehan, G.S. MacCabe, S. Gröblacher, A.H. Safavi-Naeini, F. Marsili, M.D. Shaw, and O.J. Painter. Phonon counting and intensity interferometry of a nanomechanical resonator. *Nature*, 520(7548):522–525, 2015.

[106] R. Riedinger, S. Hong, R.A. Norte, J.A. Slater, J. Shang, A.G. Krause, V. Anant, M. Aspelmeyer, and S. Gröblacher. Non-classical correlations between single photons and phonons from a mechanical oscillator. *Nature*, 530(7590):313–316, 2016.

[107] V. Sudhir, R. Schilling, S.A. Fedorov, H. Schütz, D.J. Wilson, and T.J. Kippenberg. Quantum correlations of light from a room-temperature mechanical oscillator. *Phys. Rev. X*, 7:031055, 2017.

[108] W.H.P. Nielsen, Y. Tsaturyan, C.B. Moller, E.S. Polzik, and A. Schliesser. Multimode optomechanical system in the quantum regime. *Proceedings of the National Academy of Sciences*, 114(1):62–66, 2017.

[109] R. Riedinger, A. Wallucks, I. Marinkovic, C. Loschnauer, M. Aspelmeyer, S. Hong, and S. Groblacher. Remote quantum entanglement between two micromechanical oscillators. *arXiv:1710.11147*, 2017.

[110] C. A. Regal and K. W. Lehnert. From cavity electromechanics to cavity optomechanics. In *Journal of Physics: Conference Series*, volume 264, page 012025. IOP Publishing, 2011.

[111] D. Lee, K.W. Lee, J.V. Cady, P. Ovartchaiyapong, and A.C. Jayich. Topical review: spins and mechanics in diamond. *J. Opt.*, 19(3):033001, 2017.

[112] J. Bochmann, A. Vainsencher, D. D. Awschalom, and A. N. Cleland. Nanomechanical coupling between microwave and optical photons. *Nature Phys.*, 9:712–716, 2013.

[113] K.Y. Fong, L. Fan, L. Jiang, X. Han, and H.X. Tang. Microwave-assisted coherent and nonlinear control in cavity piezo-optomechanical systems. *Phys. Rev. A*, 90(5):051801, 2014.

[114] A. Pitanti, J.M. Fink, A.H. Safavi-Naeini, J.T. Hill, C.U. Lei, A. Tredicucci, and O.J. Painter. Strong opto-electro-mechanical coupling in a silicon photonic crystal cavity. *Opt Express*, 23(3):3196–3208, 2015.

[115] K. C. Balram, M. I. Davanço, J. D. Song, and K. Srinivasan. Coherent coupling between radiofrequency, optical and acoustic waves in piezo-optomechanical circuits. *Nat. Photonics*, 10(5):346–352, 2016.

[116] J.D. Burek, M.J.and Cohen, S.M. Meenehan, N. El-Sawah, C. Chia, T. Ruelle, S. Meesala, J. Rochman, H.A. Atikian, M. Markham, D.J. Twitchen, M.D. Lukin, O.J. Painter, and M Lončar. Diamond optomechanical crystals. *Optica*, 3(12):1404–1411, 2016.

[117] I. Aharonovich, A.D. Greentree, and S. Prawer. Diamond photonics. *Nat. Photonics*, 5:397–405, 2011.

[118] K. Stannigel, P. Komar, S. J. M. Habraken, S. D. Bennett, M. D. Lukin, P. Zoller, and P. Rabl. Optomechanical quantum information processing with photons and phonons. *Phys. Rev. Lett.*, 109:013603, Jul 2012.

[119] K. Stannigel, P. Rabl, A.S. Sørensen, P. Zoller, and M.D. Lukin. Optomechanical transducers for long-distance quantum communication. *Phys. Rev. Lett.*, 105(22):220501, 2010.

[120] N. Didier, S. Pugnetti, Y.M. Blanter, and R. Fazio. Quantum transducer in circuit optomechanics. *Solid State Commun.*, 198:61 – 65, 2014.

[121] S. D. Bennett, N. Y. Yao, J. Otterbach, P. Zoller, P. Rabl, and M. D. Lukin. Phonon-induced spin-spin interactions in diamond nanostructures: Application to spin squeezing. *Phys. Rev. Lett.*, 110:156402, 2013.

[122] A. Albrecht, A. Retzker, F. Jelezko, and M.B. Plenio. Coupling of nitrogen vacancy centres in nanodiamonds by means of phonons. *New J. Phys.*, 15(8):083014, 2013.

[123] E.R. MacQuarrie, T.A. Gosavi, N.R. Jungwirth, S.A. Bhave, and G.D. Fuchs. Mechanical spin control of nitrogen-vacancy centers in diamond. *Phys. Rev. Lett.*, 111:227602, 2013.

[124] P. Ovartchaiyapong, K. W. Lee, B. A. Myers, and A. C. Bleszynski Jayich. Dynamic strain-mediated coupling of a single diamond spin to a mechanical resonator. *Nat. Commun.*, 5:4429, 2014.

[125] J. Teissier, A. Barfuss, P. Appel, E. Neu, and P. Maletinsky. Strain coupling of a nitrogen-vacancy center spin to a diamond mechanical oscillator. *Phys. Rev. Lett.*, 113:020503, 2014.

[126] Srujan Meesala, Young-Ik Sohn, Haig A. Atikian, Samuel Kim, Michael J. Burek, Jennifer T. Choy, and Marko Lončar. Enhanced strain coupling of nitrogen-vacancy spins to nanoscale diamond cantilevers. *Phys. Rev. Applied*, 5:034010, Mar 2016.

[127] S.A. Momenzadeh, F.F. de Oliveira, P. Neumann, R.D.D. Bhaktavatsala, A. Denisenko, M. Amjadi, Z. Chu, S. Yang, N.B. Manson, M.W. Doherty, and J. Wrachtrup. Thin circular diamond membrane with embedded nitrogen-vacancy centers for hybrid spin-mechanical quantum systems. *Phys. Rev. Appl*, 6:024026, 2016.

[128] D. Andrew Golter, Thein Oo, Mayra Amezcua, Kevin A. Stewart, and Hailin Wang. Optomechanical quantum control of a nitrogen-vacancy center in diamond. *Phys. Rev. Lett.*, 116:143602, Apr 2016.

[129] J.T. Hill, A.H. Safavi-Naeini, J. Chan, and O.J. Painter. Coherent optical wavelength conversion via cavity optomechanics. *Nat. Commun.*, 3:1196, 2012.

[130] E. Verhagen, S. Deléglise, S. Weis, A. Schliesser, and T. J. Kippenberg. Quantum-coherent coupling of a mechanical oscillator to an optical cavity mode. *Nature*, 482(7383):63–67, 2012.

[131] P.E. Barclay, K. Srinivasan, and O.J. Painter. Nonlinear response of silicon photonic crystal microresonators excited via an integrated waveguide and a fiber taper. *Opt. Express*, 13:801–820, 2005.

[132] H.M. Gibbs. *Optical bistability: controlling light with light*. Academic Press, 1985.

[133] V.R. Almeida and M. Lipson. Optical bistability on a silicon chip. *Opt. Lett.*, 29(20):2387–2389, 2004.

[134] V.B. Braginsky and A.B. Manukin. Ponderomotive effects of electromagnetic radiation. *JETP*, 25:653, 1967.

[135] V.B. Braginsky, A.B. Manukin, and M.Yu. Tikhonov. Investigation of dissipative ponderomotive effects of electromagnetic radiation. *JETP*, 31:829, 1970.

[136] G. Anetsberger, R. Riviere, A. Schliesser, O. Arcizet, and T.J. Kippenberg. Ultra-low dissipation optomechanical resonators on a chip. *Nature Photon.*, 2:627–633, 2008.

[137] B. Khanaliloo, M. Mitchell, A.C. Hryciw, and P.E. Barclay. High-Q/V monolithic diamond microdisks fabricated with quasi-isotropic etching. *Nano Lett.*, 15(8):5131–5136, 2015.

[138] B.P. Abbott, R. Abbott, T.D. Abbott, F. Acernese, K. Ackley, C. Adams, T. Adams, P. Addesso, R.X. Adhikari, et al. Gw170104: observation of a 50-solar-mass binary black hole coalescence at redshift 0.2. *Phys. Rev. Lett.*, 118:221101, 2017.

[139] Ansheng Liu, Richard Jones, Ling Liao, Dean Samara-Rubio, Doron Rubin, Oded Cohen, Remus Nicolaescu, and Mario Paniccia. A high-speed silicon optical modulator based on a metal–oxide–semiconductor capacitor. *Nature*, 427:615–618, 2004.

[140] J.L. O'Brien, A. Furusawa, and J. Vuckovic. Photonic quantum technologies. *Nature Photon.*, 3:687–695, 2009.

[141] S. Clemmen, A. Farsi, S. Ramelow, and A.L. Gaeta. Ramsey interference with single photons. *Phys. Rev. Lett.*, 117:223601, 2016.

[142] H.-H. Lu, J.M. Lukens, N.A. Peters, B.P. Williams, A.M. Weiner, and P. Lougovski. Quantum interference and correlation control of frequency-bin qubits. *Optica*, 5(11):1455–1460, 2018.

[143] M. Kues, C. Reimer, P. Roztocki, L.R. Cortés, S. Sciara, B. Wetzel, Y. Zhang, A. Cino, S.T. Chu, B.E. Little, et al. On-chip generation of high-dimensional entangled quantum states and their coherent control. *Nature*, 546:622–626, 2017.

[144] G. Kurizki, P. Bertet, Y. Kubo, K. Mølmer, D. Petrosyan, P. Rabl, and J. Schmiedmayer. Quantum technologies with hybrid systems. *Proceedings of the National Academy of Sciences*, 112(13):3866–3873, 2015.

[145] S.E. Harris and Y. Yamamoto. Photon switching by quantum interference. *Phys. Rev. Lett.*, 81:3611–3614, 1998.

[146] D.E. Chang, V. Vuletić, and M.D. Lukin. Quantum nonlinear optics photon by photon. *Nat. Photonics*, 8:685–694, 2014.

[147] H.J. McGuinness, M.G. Raymer, C.J. McKinstrie, and S. Radic. Quantum frequency translation of single-photon states in a photonic crystal fiber. *Phys. Rev. Lett.*, 105:093604, 2010.

[148] T. Kobayashi, R. Ikuta, S. Yasui, S. Miki, T. Yamashita, H. Terai, T. Yamamoto, M. Koashi, and N. Imoto. Frequency-domain hong–ou–mandel interference. *Nat. Photon.*, 10(7):441, 2016.

[149] Q. Li, A. Singh, X. Lu, J. Lawall, V. Verma, R. Mirin, S.W. Nam, and K. Srinivasan. Tunable quantum beat of single photons enabled by nonlinear nanophotonics. *arXiv:1905.01698*, 2019.

[150] L.-Y. Qu, J. Cotler, F. Ma, J.-Y. Guan, M.-Y. Zheng, X. Xie, Y.-A. Chen, Q. Zhang, F. Wilczek, and J.-W. Pan. Color blind detectors enable chromatic interferometry. *arXiv:1905.01823*, 2019.

[151] C. Dong, V. Fiore, M.C. Kuzyk, and H. Wang. Optomechanical dark mode. *Science*, 338(6114):1609–1613, 2012.

[152] S. Barzanjeh, E.S. Redchenko, M. Peruzzo, M. Wulf, D.P. Lewis, and J.M. Fink. Stationary entangled radiation from micromechanical motion. *arXiv:1809.05865*, 2018.

[153] E.A. Korsunsky, N. Leinfellner, A. Huss, S. Baluschev, and L. Windholz. Phase-dependent electromagnetically induced transparency. *Phys. Rev. A*, 59:2302, 1999.

[154] H. Kang, G. Hernandez, J. Zhang, and Y. Zhu. Phase-controlled light switching at low light levels. *Phys. Rev. A*, 73:011802, 2006.

[155] H. Kang, B. Kim, Y.H. Park, C.-H. Oh, and I.W. Lee. Phase-controlled switching by interference between incoherent fields in a double-λ system. *Opt. Express*, 19(5):4113–4120, 2011.

[156] B. Kim, B.-U. Sohn, W. Shin, D.-K. Ko, and H. Kang. Anticorrelated light switching in an optical loop system. *J. Opt. Soc. Am. B*, 32(2):227–231, 2015.

[157] H. Xu, D. Mason, L. Jiang, and J.G.E. Harris. Topological energy transfer in an optomechanical system with exceptional points. *Nature*, 537(7618):80, 2016.

[158] M.C. Kuzyk and H. Wang. Controlling multimode optomechanical interactions via interference. *Phys. Rev. A*, 96:023860, 2017.

[159] M. Zhang, L. Wang, and P. Ye. All optical xor logic gates: technologies and experiment demonstrations. *IEEE Commun. Mag.*, 43(5):S19–S24, 2005.

[160] Y.-D. Wang and A.A. Clerk. Using interference for high fidelity quantum state transfer in optomechanics. *Phys. Rev. Lett.*, 108:153603, 2012.

[161] S. J. Buckle, S. M. Barnett, P. L. Knight, M. A. Lauder, and D. T. Pegg. Atomic interferometers. *Optica Acta: International Journal of Optics*, 33(9):1129–1140, 1986.

[162] D.V. Kosachiov, B.G. Matisov, and Y.V. Rozhdestvensky. Coherent phenomena in multilevel systems with closed interaction contour. *J. Phys. B.*, 25:2473–2488, 1992.

[163] L. Tian. Adiabatic state conversion and pulse transmission in optomechanical systems. *Phys. Rev. Lett.*, 108:153604, 2012.

[164] D.V. Reddy and M.G. Raymer. High-selectivity quantum pulse gating of photonic temporal modes using all-optical ramsey interferometry. *Optica*, 5(4):423–428, 2018.

[165] T.J. Kippenberg, H. Rokhsari, T. Carmon, A. Scherer, and K.J. Vahala. Analysis of radiation-pressure induced mechanical oscillation of an optical microcavity. *Phys. Rev. Lett.*, 95(3):033901, 2005.

[166] T. Carmon, H. Rokhsari, L. Yang, T.J. Kippenberg, and K.J. Vahala. Temporal behavior of radiation-pressure-induced vibrations of an optical microcavity phonon mode. *Phys. Rev. Lett.*, 94(22):223902, 2005.

[167] H. Rokhsari, T.J. Kippenberg, T. Carmon, and K.J. Vahala. Radiation-pressure-driven micro-mechanical oscillator. *Opt. Express*, 13(14):5293–5301, 2005.

[168] T. J. Kippenberg, S. M. Spillane, and K. J. Vahala. Modal coupling in traveling-wave resonators. *Opt. Lett.*, 27:1669–1671, 2002.

[169] L.-S. Yan, Q. Yu, A.E. Willner, and Y. Shi. Measurement of the chirp parameter of electro-optic modulators by comparison of the phase between two sidebands. *Opt. Lett.*, 28(13):1114–1116, 2003.

[170] H.B. Callen and T.A. Welton. Irreversibility and generalized noise. *Phys. Rev.*, 83:34–40, 1951.

[171] J. F. Poyatos, J. I. Cirac, and P. Zoller. Quantum reservoir engineering with laser cooled trapped ions. *Phys. Rev. Lett.*, 77:4728–4731, Dec 1996.

[172] D. Kienzler, H.-Y. Lo, B. Keitch, L. de Clercq, F. Leupold, F. Lindenfelser, M. Marinelli, V. Negnevitsky, and J.P. Home. Quantum harmonic oscillator state synthesis by reservoir engineering. *Science*, 347(6217):53–56, 2015.

[173] L. D. Tóth, N. R. Bernier, A. Nunnenkamp, A. K. Feofanov, and T. J. Kippenberg. A dissipative quantum reservoir for microwave light using a mechanical oscillator. *Nat. Phys.*, 13:787–793, 2017.

[174] K. Fang, J. Luo, A. Metelmann, M.H. Matheny, F. Marquardt, A.A. Clerk, and O.J. Painter. Generalized non-reciprocity in an optomechanical circuit via synthetic magnetism and reservoir engineering. *Nat. Phys.*, 13:465–471, 2017.

[175] M. Poot, K.Y. Fong, M. Bagheri, W.H.P. Pernice, and H.X. Tang. Backaction limits on self-sustained optomechanical oscillations. *Phys. Rev. A*, 86(5):053826, 2012.

[176] K.—J. Boller, A. Imamoğlu, and S. E. Harris. Observation of electromagnetically induced transparency. *Phys. Rev. Lett.*, 66:2593—-2596, 1991.

[177] M. Jain, A.J. Merriam, A. Kasapi, G.Y. Yin, and S.E. Harris. Elimination of optical self-focusing by population trapping. *Phys Rev Lett*, 75(24):4385, 1995.

[178] K. Hakuta, M. Suzuki, M. Katsuragawa, and J.Z. Li. Self-induced phase matching in parametric anti-stokes stimulated raman scattering. *Phys Rev Lett*, 79(2):209, 1997.

[179] A Kasapi, Maneesh Jain, GY Yin, and Stephen E Harris. Electromagnetically induced transparency: propagation dynamics. *Physical review letters*, 74(13):2447, 1995.

[180] L.V. Hau, S.E. Harris, Z. Dutton, and C.H. Behroozi. Light speed reduction to 17 metres per second in an ultracold atomic gas. *Nature*, 397:594–598, 1999.

[181] C. Liu, A. Dutton, C. H. Behroozi, and L. V. Hau. Oberservation of coherent optical information storage in an atomic medium using halted light pulses. *Nature*, 409:490, 2001.

[182] D.F. Phillips, A. Fleischhauer, A. Mair, R.L. Walsworth, and M.D. Lukin. Storage of light in atomic vapor. *Phys. Rev. Lett.*, 86:783–786, 2001.

[183] M.R. Sprague, P.S. Michelberger, T.F.M. Champion, D.G. England, J. Nunn, X.-M. Jin, W.S. Kolthammer, A. Abdolvand, P. St J. Russell, and I. A. Walmsley. Broadband single-photon-level memory in a hollow-core photonic crystal fibre. *Nat. Photonics*, 8(4):287–291, 2014.

[184] D.G. England, K.A.G. Fisher, J.-P.W. MacLean, P.J. Bustard, R. Lausten, K.J. Resch, and B.J. Sussman. Storage and retrieval of thz-bandwidth single photons using a room-temperature diamond quantum memory. *Phys. Rev. Lett.*, 114:053602, 2015.

[185] G. Heinze, C. Hubrich, and T. Halfmann. Stopped light and image storage by electromagnetically induced transparency up to the regime of one minute. *Phys Rev Lett*, 111(3):033601, 2013.

[186] T. Chaneliere, D.N. Matsukevich, S.D. Jenkins, S.-Y. Lan, T.A.B. Kennedy, and A. Kuzmich. Storage and retrieval of single photons transmitted between remote quantum memories. *Nature*, 438(7069):833, 2005.

[187] M. D. Eisaman, A. Andre, F. Massou, M. Fleischhauer, A. S. Zibrov, and M. D. Lukin. Electromagnetically induced transparency with tunable single-photon pulses. *Nature*, 438:837, 2005.

[188] A. Wallucks, I. Marinković, B. Hensen, R. Stockill, and S. Groblacher. A quantum memory at telecom wavelengths. *arXiv:1910.07409*, 2019.

[189] Birgit Stiller, Moritz Merklein, Christian Wolff, Khu Vu, Pan Ma, Stephen J. Madden, and Benjamin J. Eggleton. Coherently refreshed acoustic phonons for extended light storage. *arXiv:1904.13167*, 2019.

[190] S. Gao, O. Lazo-Arjona, B. Brecht, K. T. Kaczmarek, S. E. Thomas, J. Nunn, P. M. Ledingham, D. J. Saunders, and I. A. Walmsley. Optimal coherent filtering for single noisy photons. *arXiv:1902.07720*, 2019.

[191] H. Goldstein. *Classical Mechanics*. Addison Wesley, San Francisco, 2002.

[192] G Patera, J Shi, D B Horoshko, and M I Kolobov. Quantum temporal imaging: application of a time lens to quantum optics. *J. Opt.*, 19(5):054001, mar 2017.

[193] Moritz Merklein, Birgit Stiller, Khu Vu, Stephen J. Madden, and Benjamin J. Eggleton. A chip-integrated coherent photonic-phononic memory. *Nat. Commun.*, 8(1):574, 2017.

[194] J. M. Taylor, P. Cappellaro, L. Childress, L. Jiang, D. Budker, P. R. Hemmer, A. Yacoby, R. Walsworth, and M. D. Lukin. High-sensitivity diamond magnetometer with nanoscale resolution. *Nat. Phys.*, 4(10):810–816, October 2008.

[195] F. Dolde, H. Fedder, M. W. Doherty, T. Nöbauer, F. Rempp, G. Balasubramanian, T. Wolf, F. Reinhard, L. C. L. Hollenberg, F. Jelezko, and J. Wrachtrup. Electric-field sensing using single diamond spins. *Nature Physics*, 7(6):459–463, 2011.

[196] G. Balasubramanian, P. Neumann, D. Twitchen, M. Markham, R. Kolesov, N. Mizuochi, J. Isoya, J. Achard, J. Beck, J. Tissler, V Jacques, P.R. Hemmer, F Jelezko, and F Wrachtrup. Ultralong spin coherence time in isotopically engineered diamond. *Nat. Mater.*, 8(5):383–387, 2009.

[197] E.R. MacQuarrie, T.A. Gosavi, A.M. Moehle, N.R. Jungwirth, S.A. Bhave, and G.D. Fuchs. Coherent control of a nitrogen-vacancy center spin ensemble with a diamond mechanical resonator. *Optica*, 2(3):233–238, 2015.

[198] M.W. Doherty, F. Dolde, H. Fedder, F. Jelezko, J. Wrachtrup, N.B. Manson, and L.C.L. Hollenberg. Theory of the ground-state spin of the nv-center in diamond. *Phys. Rev. B*, 85(20):205203, 2012.

[199] L. Robledo, H. Bernien, T. van der Sar, and R. Hanson. Spin dynamics in the optical cycle of single nitrogen-vacancy centres in diamond. *New J. Phys.*, 13(2):025013, 2011.

[200] A. Gupta, L. Hacquebard, and L. Childress. Efficient signal processing for time-resolved fluorescence detection of nitrogen-vacancy spins in diamond. *J. Opt. Soc. Am. B*, 33(3):28–34, 2016.

[201] K. Huang and M. Hossein-Zadeh. Direct stabilization of optomechanical oscillators. *Opt. Lett.*, 42(10):1946–1949, 2017.

[202] J. Lu, J.B. Surya, X. Liu, A.W. Bruch, Z. Gong, Y. Xu, and H.X. Tang. Periodically poled thin film lithium niobate microring resonators with a second-harmonic generation efficiency of 250,000 *Optica*, 6(12):1455–1460, 2019.

[203] M. Menotti, B. Morrison, K. Tan, Z. Vernon, J.E. Sipe, and M. Liscidini. Nonlinear coupling of linearly uncoupled resonators. *Phys. Rev. Lett.*, 122:013904, 2019.

[204] E. R. Macquarrie, M. Otten, S. K. Gray, and G. D. Fuchs. Cooling a mechanical resonator with nitrogen-vacancy centres using a room temperature excited state spin-strain interaction. *Nat. Commun.*, 8:14358, February 2017.

[205] K.V. Kepesidis, S.D. Bennett, S. Portolan, M.D. Lukin, and P. Rabl. Phonon cooling and lasing with nitrogen-vacancy centers in diamond. *Phys. Rev. B*, 88(6):064105, 2013.

[206] A.D. Golter, T. Oo, M. Amezcua, I. Lekavicius, K.A. Stewart, and H. Wang. Coupling a surface acoustic wave to an electron spin in diamond via a dark state. *Phys. Rev. X*, 6:041060, 2016.

[207] J. Bardeen and W. Shockley. Deformation potentials and mobilities in non-polar crystals. *Phys. Rev.*, 80:72–80, 1950.

[208] J.R. Maze, A. Gali, E. Togan, Y. Chu, A. Trifonov, E. Kaxiras, and M.D. Lukin. Properties of nitrogen-vacancy centers in diamond: the group theoretic approach. *New J. Phys.*, 13(2):025025, 2011.

[209] M.W. Doherty, N.B. Manson, P. Delaney, F. Jelezko, J. Wrachtrup, and L.C.L. Hollenberg. The nitrogen-vacancy colour centre in diamond. *Phys. Rep.*, 528(1):1 – 45, 2013.

[210] S. Meesala, Y.-I. Sohn, B. Pingault, L. Shao, H.A. Atikian, J. Holzgrafe, M. Gündoğan, C. Stavrakas, A. Sipahigil, C. Chia, R. Evans, M.J. Burek, M. Zhang, L. Wu, J.L. Pacheco, J. Abraham, E. Bielejec, M.D. Lukin, M. Atatüre, and M. Lončar. Strain engineering of the silicon-vacancy center in diamond. *Phys. Rev. B*, 97:205444, 2018.

[211] F. Grazioso, B.R. Patton, P. Delaney, M.L. Markham, D.J. Twitchen, and J.M. Smith. Measurement of the full stress tensor in a crystal using photoluminescence from point defects: The example of nitrogen vacancy centers in diamond. *Appl. Phys. Lett.*, 103(10):101905, 2013.

[212] D. Leibfried, R. Blatt, C. Monroe, and D. Wineland. Quantum dynamics of single trapped ions. *Rev. Mod. Phys.*, 75:281–324, Mar 2003.

[213] B.M. Garraway. The dicke model in quantum optics: Dicke model revisited. *Philos. Trans. Royal Soc. A*, 369(1939):1137–1155, 2011.

[214] W. Miller. *Symmetry Groups and Their Applications*. Academic Press, 1972.

[215] B. Hall. *Lie Groups, Lie Algebras, and Representations*. Springer International Publishing, 2015.

Appendix A

Calculation Details

A.1 Input-Output Relations

In chapter 1, we found that for a cavity-waveguide system, the following relation will hold,

$$\dot{\hat{a}} = -\frac{i}{\hbar}\left[\hat{a}, \hat{H}_{\mathrm{a}}\right] - \frac{\kappa}{2}\hat{a} + \sqrt{\kappa}\hat{a}_{\mathrm{in}}. \tag{A.1}$$

In a more realistic system, a number of different loss channels may be present. In this case we can generalize this expression for any number of input ports,

$$\dot{\hat{a}} = -\frac{i}{\hbar}\left[\hat{a}, \hat{H}_{\mathrm{a}}\right] - \frac{\kappa}{2}\hat{a} - \sum_{n}\sqrt{\kappa_n}\hat{a}_{\mathrm{in},n}. \tag{A.2}$$

where the total loss is simply the sum of losses to each port, $\kappa = \sum_n \kappa_n$. It is conventional to group losses due to coupling to a waveguide into a single loss rate κ_{ex} (external loss rate), and to group all other losses into κ_{i} (intrinsic loss rate). While there are many possible combinations of waveguides and resonators, we will focus on four typical cases. They are, as detailed in Fig. A.1, (a) side-coupled, single-sided, (b) end-coupled, single-sided, (c) side-coupled, double-sided, (d) end-coupled, double-sided.

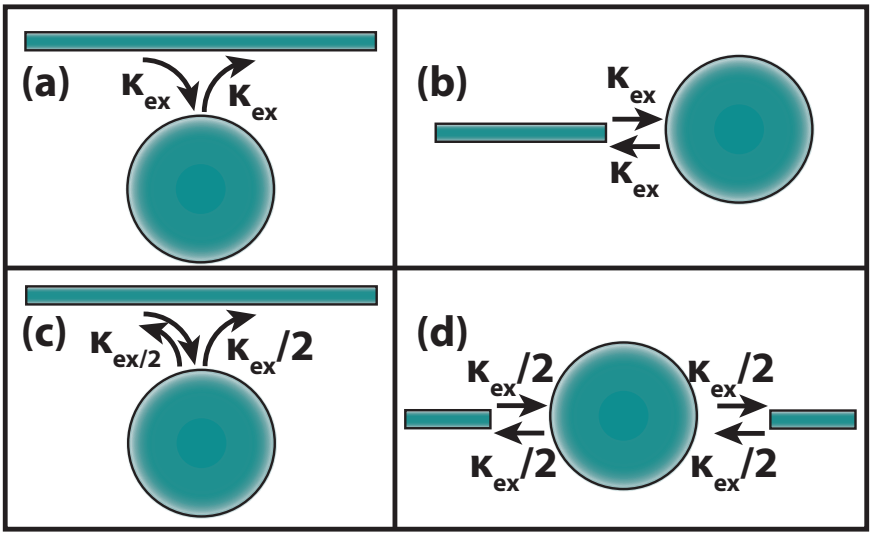

Figure A.1: (a) Side-coupled, single-sided, (b) End-coupled, single-sided, (c) Side-coupled, double-sided, (d) End-coupled, double-sided.

A.1.1 Side-Coupled, Single-Sided

Solving for the time evolution of $\hat{a}$ in terms of the inputs and then the outputs we find,

$$\dot{\hat{a}} = -\frac{i}{\hbar}\left[\hat{a}, \hat{H}_{\mathrm{a}}\right] - \frac{\kappa}{2}\hat{a} - \sqrt{\kappa_{\mathrm{ex}}}\hat{a}_{\mathrm{in}} - \sqrt{\kappa_{\mathrm{i}}}\hat{f}_{\mathrm{in}}, \tag{A.3}$$

$$\dot{\hat{a}} = -\frac{i}{\hbar}\left[\hat{a}, \hat{H}_{\mathrm{a}}\right] + \frac{\kappa}{2}\hat{a} - \sqrt{\kappa_{\mathrm{ex}}}\hat{a}_{\mathrm{out}} - \sqrt{\kappa_{\mathrm{i}}}\hat{f}_{\mathrm{out}}. \tag{A.4}$$

where we have defined $\kappa = \kappa_{\mathrm{i}} + \kappa_{\mathrm{ex}}$, $\hat{a}_{\mathrm{in}} = \frac{1}{\sqrt{2\pi}}\int_{-\infty}^{\infty} e^{-i\omega(t-t_0)}\hat{b}_0(\omega)d\omega$, and the output operator $\hat{a}_{\mathrm{out}} = \frac{1}{\sqrt{2\pi}}\int_{-\infty}^{\infty} e^{-i\omega(t-t_1)}\hat{b}_0(\omega)d\omega$. From Eq. A.3 and A.4, we find $0 = [\kappa_{\mathrm{ex}}\hat{a} - \sqrt{\kappa_{\mathrm{ex}}}(\hat{a}_{\mathrm{out}} - \hat{a}_{\mathrm{in}})] + [\kappa_{\mathrm{i}}\hat{a} - \sqrt{\kappa_{\mathrm{i}}}(\hat{f}_{\mathrm{out}} - \hat{f}_{\mathrm{in}})]$. This gives [19, 20],

$$\hat{a}_{\mathrm{out}} - \hat{a}_{\mathrm{in}} = \sqrt{\kappa_{\mathrm{ex}}}\hat{a}, \tag{A.5}$$

$$\hat{f}_{\mathrm{out}} - \hat{f}_{\mathrm{in}} = \sqrt{\kappa_{\mathrm{i}}}\hat{a}. \tag{A.6}$$

In the above we have explicitly enforced that in the absence of coupling of the cavity with the waveguide, $\hat{a}_{\mathrm{out}} = \hat{a}_{\mathrm{in}}$. The boundary conditions on the intrinsic loss has only been chosen for convenience here, as this port will not actually be measured.

A.1.2 End-Coupled, Single-Sided

In this case the output field will be left-going. In order to explicitly account for the phase shift on reflection, we will adopt the phase convention the right going waves receive a negative sign by defining $\hat{a}_{\text{out}} = -\frac{1}{\sqrt{2\pi}} \int_{-\infty}^{\infty} e^{-i\omega(t-t_1)} \hat{b}_0(\omega) d\omega$ [16]. This gives,

$$\dot{\hat{a}} = -\frac{i}{\hbar}\left[\hat{a}, \hat{H}_{\text{a}}\right] - \frac{\kappa}{2}\hat{a} - \sqrt{\kappa_{\text{ex}}}\hat{a}_{\text{in}} - \sqrt{\kappa_{\text{i}}}\hat{f}_{\text{in}}, \tag{A.7}$$

$$\dot{\hat{a}} = -\frac{i}{\hbar}\left[\hat{a}, \hat{H}_{\text{a}}\right] + \frac{\kappa}{2}\hat{a} + \sqrt{\kappa_{\text{ex}}}\hat{a}_{\text{out}} + \sqrt{\kappa_{\text{i}}}\hat{f}_{\text{out}}. \tag{A.8}$$

This gives the input-output relations,

$$\hat{a}_{\text{out}} + \hat{a}_{\text{in}} = \sqrt{\kappa_{\text{ex}}}\hat{a}, \tag{A.9}$$

$$\hat{f}_{\text{out}} + \hat{f}_{\text{in}} = \sqrt{\kappa_{\text{i}}}\hat{a}. \tag{A.10}$$

The difference in the end coupled case, as opposed to side coupled case is that in the absence of coupling to the waveguide all light will be reflected as opposed to transmitted. Because of the π-phase shift upon reflection, we have $\hat{a}_{\text{out}} = -\hat{a}_{\text{in}}$. Once again we have chosen the intrinsic loss boundary conditions out of convenience.

A.1.3 Side-Coupled, Double-Sided

Both left-going and right-going inputs and outputs are present in this case. We maintain our sign convention from the previous section, finding,

$$\dot{\hat{a}} = -\frac{i}{\hbar}\left[\hat{a}, \hat{H}_{\text{a}}\right] - \frac{\kappa}{2}\hat{a} - \sqrt{\frac{\kappa_{\text{ex}}}{2}}\hat{a}_{\text{in}}^{(\text{R})} + \sqrt{\frac{\kappa_{\text{ex}}}{2}}\hat{a}_{\text{in}}^{(\text{L})} - \sqrt{\kappa_{\text{i}}}\hat{f}_{\text{in}}, \tag{A.11}$$

$$\dot{\hat{a}} = -\frac{i}{\hbar}\left[\hat{a}, \hat{H}_{\text{a}}\right] + \frac{\kappa}{2}\hat{a} - \sqrt{\frac{\kappa_{\text{ex}}}{2}}\hat{a}_{\text{out}}^{(\text{R})} + \sqrt{\frac{\kappa_{\text{ex}}}{2}}\hat{a}_{\text{out}}^{(\text{L})} - \sqrt{\kappa_{\text{i}}}\hat{f}_{\text{out}}, \tag{A.12}$$

where the superscript 'R' and 'L' stand for right-going and left-going waves. Enforcing boundary conditions, we find,

$$\hat{a}_{\text{out}}^{(\text{R})} - \hat{a}_{\text{in}}^{(\text{R})} = \sqrt{\frac{\kappa_{\text{ex}}}{2}}\hat{a}, \tag{A.13}$$

$$-\hat{a}_{\text{out}}^{(\text{L})} + \hat{a}_{\text{in}}^{(\text{L})} = \sqrt{\frac{\kappa_{\text{ex}}}{2}}\hat{a}, \tag{A.14}$$

$$\hat{f}_{\text{out}} - \hat{f}_{\text{in}} = \sqrt{\kappa_{\text{i}}}\hat{a} \tag{A.15}$$

A.1.4 End-Coupled, Double-Sided

Starting with the same equations as the side-coupled/double-sided case, and enforcing boundary conditions we find,

$$\hat{a}_{\text{out}}^{(\text{R})} + \hat{a}_{\text{in}}^{(\text{L})} = \sqrt{\frac{\kappa_{\text{ex}}}{2}}\hat{a}, \tag{A.16}$$

$$\hat{a}_{\text{out}}^{(\text{L})} + \hat{a}_{\text{in}}^{(\text{R})} = \sqrt{\frac{\kappa_{\text{ex}}}{2}}\hat{a}, \tag{A.17}$$

$$\hat{f}_{\text{out}} - \hat{f}_{\text{in}} = \sqrt{\kappa_{\text{i}}}\hat{a}. \tag{A.18}$$

A.2 Boundary Conditions Perturbation

In Chapter 1, we have tried to understand the effects of various dielectric geometries on the flow of light. We found that placing boundary conditions, in the appropriate geometry results in the creation of optical modes. A natural question to ask at this point is what happens to the modes if we perturb the dielectric in some way? For example, we might expect that shifting the position of the boundary, or the strength of some part of the dielectric will alter the modes in some way. To make our statements more substantial, let's consider a seemingly simple problem. Suppose we have an interface between two dielectric materials, which are locally flat, with the interface normal to the x-axis, centred at the origin. In keeping with the notation of chapter 1, we will label the dielectric constants of each material as ϵ_{i}, and ϵ_{e},

respectively. Locally, this represents a small section of the boundary of a dielectric structure, such as the one we encountered in the previous sections. We assume that we have already solved the Helmholtz equation for this mode, which we denote as E_0, which has resonant frequency ω_0.

Now, we consider the effect of a perturbation of the dielectric, which we parametrize by the infinitesimal $\delta\alpha$. This allows us to write our solution and frequency as a polynomial series,

$$\mathbf{E} = \mathbf{E}_0 + \delta\alpha\mathbf{E}_1 + \delta\alpha^2\mathbf{E}_2 + ... \tag{A.19}$$

$$\omega = \omega_0 + \delta\alpha\omega_1 + \delta\alpha^2\omega_2 + ... \tag{A.20}$$

For our purposes, it will suffice to only find a first order correction. Placing our series solutions into the Helmholtz equation, we find,

$$\nabla^2 \left(\mathbf{E}_0 + \delta\alpha\mathbf{E}_1 + ...\right) = \left(\frac{\omega_0 + \delta\alpha\omega_1 + ...}{c}\right)^2 \left(\epsilon + \delta\alpha\frac{d\epsilon}{d\alpha} + ...\right)\left(\mathbf{E}_0 + \delta\alpha\mathbf{E}_1 + ...\right). \tag{A.21}$$

Equating terms proportional to $\delta\alpha$, we derive the expression,

$$\nabla^2\mathbf{E}_1 = \left(\left(\frac{\omega_0}{c}\right)^2 \frac{d\epsilon}{d\alpha} + \frac{2\omega_0\omega_1}{c^2}\epsilon\right)\mathbf{E}_0 + \left(\frac{\omega_0}{c}\right)^2 \epsilon\mathbf{E}_1. \tag{A.22}$$

Our original solution obeys the relation $\int \mathbf{E}_0^*\mathbf{E}_0 dv = \text{const}$, and our normalization conditions demand that the new mode solution equal the same constant. So we must have, $\int \mathbf{E}_0^*\mathbf{E}_0 dv = \int \left(\mathbf{E}_0^* + \delta\alpha\mathbf{E}_1^*\right)\left(\mathbf{E}_0 + \delta\alpha\mathbf{E}_1\right) dv$. This implies orthogonality, namely, $\int \mathbf{E}_0^*\mathbf{E}_1 dv = \int \mathbf{E}_1^*\mathbf{E}_0 dv = 0$. Using this in Eq. A.2, we arrive at the solution for first order perturbations,

$$\omega_1 = \frac{d\omega}{d\alpha} = -\frac{\omega_0}{2}\frac{\int \frac{d\epsilon}{d\alpha}|\mathbf{E}_0|^2 dv}{\int \epsilon|\mathbf{E}_0|^2 dv} \tag{A.23}$$

We note here, that there is no restriction that ω_1 is real. Perturbation theory only requires that ω_0 is real, such that the orginal problem is Hermitian. We could then, for example, use this expression to calculate the effect of adding loss to the dielectric constant.

While the above expression may be easily applied to changes of the strength of dielectrics, either by adding or subtracting a small real or imaginary part, we will encounter problems in the circumstance that the interface of the dielectrics shifts. To make this statement more substantial, consider the dielectric function $\epsilon(x) = \epsilon_\mathrm{i} + (\epsilon_\mathrm{e} - \epsilon_\mathrm{i})H(x-\alpha)$, where $H(x)$ is the Heaviside step function. Calculating the perturbation term involves evaluating an integral of the form,

$$\begin{aligned}\int_V \frac{d\epsilon}{d\alpha}|\mathbf{E}_0|^2 dV &= \int_V \left(\epsilon_\mathrm{i} + (\epsilon_\mathrm{e} - \epsilon_\mathrm{i})H(x-\alpha)|\mathbf{E}_0(x,y,z)|^2\right) dV \\ &= \int_V (\epsilon_\mathrm{e} - \epsilon_\mathrm{i})\delta(x-\alpha)|\mathbf{E}_0(x,y,z)|^2 dV \\ &= \int_A (\epsilon_\mathrm{e} - \epsilon_\mathrm{i}) \left(|\mathbf{E}_\perp(\alpha,y,z)|^2 + |\mathbf{E}_\parallel(\alpha,y,z)|^2\right) dA,\end{aligned} \tag{A.24}$$

where in the final step we have divided the electric field into components perpendicular and parallel to the interface. The problem in evaluating this integral is that according to the boundary conditions, stated in Eq. 1.9, we will have a discontinuity in $\mathbf{E}_\perp$ on either side of the interface. In the case where the perturbation was in the bulk dielectric, this was not a problem, as the interface had a negligible contribution. In the case of moving boundaries, the perturbation occurs precisely where electric field is undefined!

On the face of it, this situation is somewhat disconcerting, however on reflection, we can perhaps excuse this situation away. The material response, as given by the constitutive relations, are a macroscopic approximation, to what is in reality a response of a very large number of atoms, to an electromagnetic field. The approximation of a boundary defined by a step function cannot be expected to accurately convey the situation to all scales. In reality we would expect a smoother, or more blended response.

Accordingly, we make use of a smoothing function with the property, $\lim_{s\to 0} g_s(x) = \delta(x)$. This allows us to define different effective dielectric constants for the perpendicular and parallel components, $\epsilon_\parallel = \int g_s(x-x')\epsilon(x')dx$ and $\epsilon_\perp^{-1} = \int g_s(x-x')\epsilon(x')^{-1}dx$. As expected, these each return the physical dielectric constant in the limit $s \to 0$.

Calculating the derivative of the perpendicular component, we find,

$$\begin{aligned} \frac{d}{d\alpha}\frac{1}{\epsilon(x)_\perp} &= \int g_s(x-x')\frac{d}{d\alpha}\left(\frac{1}{\epsilon_\mathrm{i}} - \left(\frac{1}{\epsilon_\mathrm{e}} - \frac{1}{\epsilon_\mathrm{i}}\right)H(x'-\alpha)\right)dx', \\ \implies \frac{d\epsilon}{d\alpha} &= -\,g_s(x-h)\epsilon(x)_\perp^2\left(\frac{1}{\epsilon_\mathrm{e}} - \frac{1}{\epsilon_\mathrm{i}}\right). \end{aligned} \tag{A.25}$$

We will also require the derivative of the parallel component,

$$\begin{aligned} \frac{d\epsilon_\parallel(x)}{d\alpha} &= \int g_s(x-x')\frac{d}{d\alpha}\left(\epsilon_\mathrm{i} - (\epsilon_\mathrm{e}-\epsilon_\mathrm{i})\,H(x'-\alpha)\right)dx', \\ &= g_s(x-h)\left(\epsilon_\mathrm{e}-\epsilon_\mathrm{i}\right). \end{aligned} \tag{A.26}$$

Just as before, we calculate the numerator of our perturbation, to arrive at the following surface integral,

$$\begin{aligned} \int_V \frac{d\epsilon}{d\alpha}|\mathbf{E}_0|^2 dV &= \lim_{s\to 0}\int_V \left(\frac{\partial\epsilon_\perp}{d\alpha}|\mathbf{E}_\perp|^2 + \frac{\partial\epsilon_\parallel}{d\alpha}|\mathbf{E}_\parallel|^2\right)dV \\ &= \lim_{s\to 0}\int_V g_s(x-h)\left(\left(\epsilon_\mathrm{e}-\epsilon_\mathrm{i}\right)|\mathbf{E}_\parallel|^2 - \left(\frac{1}{\epsilon_\mathrm{e}} - \frac{1}{\epsilon_\mathrm{i}}\right)\epsilon(x)^2|\mathbf{E}_\perp|^2\right)dV \\ &= \int_A \left(\left(\epsilon_\mathrm{e}-\epsilon_\mathrm{i}\right)|\mathbf{E}_\parallel|^2 - \left(\frac{1}{\epsilon_\mathrm{e}} - \frac{1}{\epsilon_\mathrm{i}}\right)|\mathbf{D}_\perp|^2\right)dA. \end{aligned} \tag{A.27}$$

Comparison with the boundary conditions of Maxwell's equations show that all field components are now continuous across the boundary.

At this point I want to summarize what we have derived in this section. Starting with a mode solution for a particular dielectric geometry, we considered how slight perturbations to the dielectric environment would affect the mode. These perturbations could be broken down into two categories: (1) changes to the strength of the dielectric constant (2) changes

to the location of the dielectric. For the first case, we find the expression,

$$\boxed{\frac{d\omega}{d\alpha} = -\frac{\omega_0}{2}\frac{\int_V \frac{d\epsilon}{d\alpha}\left(|\mathbf{E}_\parallel|^2 + |\mathbf{E}_\perp|^2\right)dV}{\int_V \epsilon\left(|\mathbf{E}_\parallel|^2 + |\mathbf{E}_\perp|^2\right)dV},} \tag{A.28}$$

where α parameterizes changes in the strength of the dielectric. For the second case, we find the expression,

$$\boxed{\frac{d\omega}{d\alpha} = -\frac{\omega_0}{2}\frac{\int_V \left((\epsilon_\mathrm{e} - \epsilon_\mathrm{i})|\mathbf{E}_\parallel|^2 + (\epsilon_\mathrm{e}^{-1} - \epsilon_\mathrm{i}^{-1})|\mathbf{D}_\perp|^2\right)dV}{\int_V \epsilon\left(|\mathbf{E}_\parallel|^2 + |\mathbf{E}_\perp|^2\right)dV},} \tag{A.29}$$

where α parameterizes changes in the boundaries between different dielectrics.

A.3 Optomechanical Scattering Rates and Spectrums

In the main text, we used the fact that an external force acting on a harmonic oscillator can be described in terms of the spectrum of the force operator. To make this more clear, we adapt the arguments of Schoelkopf et al. [99]. We describe the harmonic oscillator with the usual Hamiltonian $\hat{H}_\mathrm{b} = \hbar\omega_\mathrm{b}\hat{b}^\dagger\hat{b}$, and describe the action of some time varying external force acting on the harmonic oscillator by $\hat{H}_\mathrm{int}(t) = -\hat{F}(t)\hat{x}$. We wish to find how the harmonic oscillator will evolve under these Hamiltonians.

We will assume that the coupling is weak, such that time dependent perturbation theory is valid. Furthermore, we assume that the system is separable into a subspace of the harmonic oscillator, and the external force. This gives,

$$|\psi(t)\rangle \otimes \mathbb{1} = \left(1 + \frac{i}{\hbar}\int_0^t A\hat{F}(\tau)\hat{x}d\tau\right)|\psi(0)\rangle \otimes \mathbb{1}. \tag{A.30}$$

From this, we can immediately calculate the amplitude for the harmonic oscillator initially in state n to be found in state $n+1$ after an interval t, provided that t is small,

$$\begin{aligned} p_{n\to n+1} &= \langle n+1| \left(1 + \frac{i}{\hbar}\int_0^t \hat{F}(\tau)\hat{x}d\tau\right)|n\rangle \\ &= \frac{ix_0}{\hbar}\int_0^t \hat{F}(\tau)\,\langle n+1|\left(\hat{b}e^{-i\omega_{\rm b}\tau} + \hat{b}^\dagger e^{i\omega_{\rm m}\tau}\right)|n\rangle\, d\tau \\ &= \frac{ix_0\sqrt{n+1}}{\hbar}\int_0^t \hat{F}(\tau)e^{i\omega_{\rm b}\tau}d\tau. \end{aligned} \tag{A.31}$$

where we have inserted the evolution of $\hat{b}(t)$ and $\hat{b}^\dagger(t)$ in the absence of force coupling. Squaring the above function to find the probability gives,

$$P_{n\to n+1} = \frac{x_0^2(n+1)}{\hbar^2}\int_0^t\int_0^t \hat{F}(\tau)\hat{F}(\tau')e^{i\omega_{\rm m}(\tau-\tau')}d\tau d\tau'. \tag{A.32}$$

At this point it would appear that we cannot make any headway without explicit information regarding the evolution of the force operator. We can sidestep this, however, by making use of the statistical information we have available about this force operator. Taking the average over the subspace of the force operator and assuming that it is not significantly affected by coupling to the harmonic oscillator, we find,

$$\overline{P}_{n\to n+1} = \frac{x_0^2(n+1)}{\hbar^2}\int_0^t\int_0^t \langle\hat{F}(\tau')\hat{F}(\tau)\rangle e^{i\omega_{\rm m}(\tau'-\tau)}d\tau' d\tau. \tag{A.33}$$

Assuming a stationary process we have that $\langle\hat{F}(\tau+\Delta\tau)\hat{F}(\tau)\rangle = \langle\hat{F}(\Delta\tau)\hat{F}(0)\rangle$. In this case the Wiener–Khinchin theorem will be valid, and we have the relations for the spectrum of the force operator,

$$S_{\hat{F}\hat{F}}(\omega) = \int_{-\infty}^{\infty} e^{i\omega t}\,\langle\hat{F}(t)\hat{F}(0)\rangle\, dt \tag{A.34}$$

$$\langle\hat{F}(t)\hat{F}(0)\rangle = \int_{-\infty}^{\infty} e^{-i\omega t}S_{\hat{F}\hat{F}}(\omega)d\omega \tag{A.35}$$

This can be inserted into Eq. A.33 with the substitution $\tau' \to \tau - \Delta\tau$, which gives,

$$\begin{aligned}
\overline{P}_{n\to n+1} &= \frac{x_0^2(n+1)}{\hbar^2}\int_0^t \int_{-\Delta\tau}^{t-\Delta\tau}\int_{-\infty}^{\infty} e^{i(\omega+\omega_{\rm m})\Delta\tau} S_{\hat{F}\hat{F}}(\omega) d\omega d\Delta\tau d\tau \\
&= \frac{x_0^2(n+1)}{\hbar^2}\int_0^t \int_{-\infty}^{\infty} \frac{\delta(\omega+\omega_{\rm m})}{2\pi} S_{\hat{F}\hat{F}}(\omega) d\omega d\tau \\
&= t\frac{x_0^2(n+1)}{\hbar^2} S_{\hat{F}\hat{F}}(-\omega_{\rm m}). \qquad \text{(A.36)}
\end{aligned}$$

This gives the rate of change $\Gamma_{n\to n+1} = \frac{x_0^2(n+1)}{\hbar^2} S_{\hat{F}\hat{F}}(-\omega_{\rm m})$. Proceeding with much the same arguments, one can also derive the rate $\Gamma_{n\to n-1} = \frac{x_0^2 n}{\hbar^2} S_{\hat{F}\hat{F}}(\omega_{\rm m})$.

A.3.1 Backaction–Shot Noise Uncertainty

As discussed in the main text of the thesis, shot noise and backaction noise are not decoupled. If one increases the strength of the control laser in order to reduce the shot noise, one will necessarily increase the backaction noise, and vice versa. While this argument is probably intuitive, a qualitative calculation is useful in order to precisely state the Standard Quantum Limit for this system. In what follows, we will attempt to convey and simplify the arguments of Clerk et. al [98].

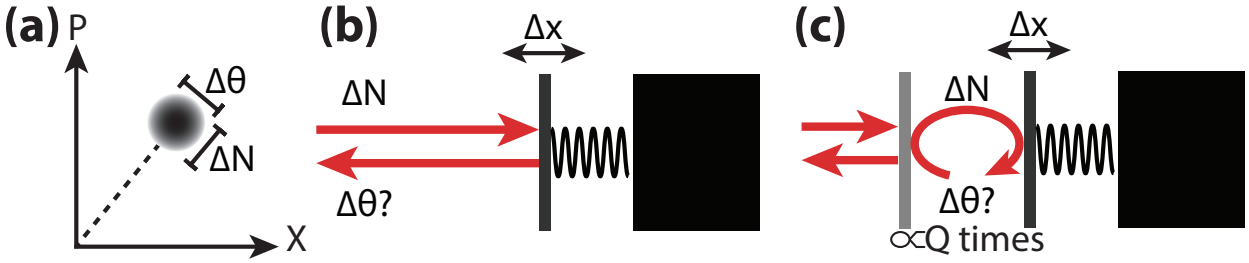

Figure A.2: (a) Illustration of the number-phase uncertainly relation for large coherent states. (b) Backaction of a mirror-spring system. (c) Backaction of a cavity optomechanical system.

It can be shown that a coherent state will in the limit of large photon number, N, obey a number–phase uncertainty principle [98]. Furthermore, coherent states obey Poissonian statistics. This sets the following relations,

$$\Delta N \Delta\phi = \frac{1}{2}, \qquad \text{Phase-Number Uncertainty} \tag{A.37}$$

$$(\Delta N)^2 = N, \qquad \text{Poissonian Statistics} \tag{A.38}$$

where in the above ΔN is the number uncertainty, $\Delta\phi$ is the phase uncertainty, and N is the average photon number.

Using the same language as the main text we can write the amplitude of the coherent state as a displaced vacuum state $\hat{\alpha}_{\rm in} = \alpha_{\rm in} + \hat{a}_{\rm in}$, where $\alpha_{\rm in}$ is the classical amplitude, and $\hat{a}_{\rm in}$ is a vacuum noise operator. All operators here are normalized to photon flux, so we have applied the "in" subscript as in the main text of the thesis to remind us of this fact. As in the main text we assume a stationary process, and the two-time correlators are $\langle \hat{\alpha}^\dagger_{\rm in}(t)\hat{\alpha}_{\rm in}(0)\rangle = 0$ and $\langle \hat{\alpha}_{\rm in}(t)\hat{\alpha}^\dagger_{\rm in}(0)\rangle = \delta(t)$. Finally, we note that the photon number flux operator may be written in terms of the above definitions as $\hat{\dot{N}} = \left(\alpha^*_{\rm in} + \hat{a}^\dagger_{\rm in}\right)(\alpha_{\rm in} + \hat{a}_{\rm in})$, and the average photon flux is simply $\dot{N} = |\alpha_{\rm in}|^2$.

We are now ready to define two spectrums that will be useful in our calculation. First we give the spectrum for the photon number flux,

$$\begin{aligned}
S_{\hat{\dot{N}}\hat{\dot{N}}}(\omega) &= \int e^{i\omega t}\left\langle \left(\hat{\dot{N}}(t) - \dot{N}\right)\left(\hat{\dot{N}}(0) - \dot{N}\right)\right\rangle dt \\
&= \int e^{i\omega t}\Big\langle \left(\left(\alpha^*_{\rm in} + \hat{a}^\dagger_{\rm in}(t)\right)(\alpha_{\rm in} + \hat{a}_{\rm in}(t)) - |\alpha_{\rm in}|^2\right)\times \\
&\quad \left(\left(\alpha^*_{\rm in} + \hat{a}^\dagger_{\rm in}(0)\right)(\alpha_{\rm in} + \hat{a}_{\rm in}(0)) - |\alpha_{\rm in}|^2\right)\Big\rangle dt \\
&= \int e^{i\omega t}\left\langle \alpha^*_{\rm in}\hat{a}_{\rm in}(t)\hat{a}^\dagger_{\rm in}(0)\alpha_{\rm in}\right\rangle dt \\
&= \int e^{i\omega t}\,|\alpha_{\rm in}|^2\,\delta(t)dt \\
&= \dot{N}.
\end{aligned} \tag{A.39}$$

This spectrum gives the shot noise of the incident light. Note that in the first step we have subtracted off the DC component of the photon flux as it does not contain the information we are interested in. One could measure this spectrum, for instance, with an AC-coupled photodetector connected to a spectrum analyzer.

The second useful spectrum is the phase fluctuation spectrum. To simplify matters, we take the phase on average zero. In this case we write the small angular fluctuations away from zero in terms of the quadrature operators $\hat{X} = 1/\sqrt{2}\left(\hat{\alpha}_{\text{in}}^{\dagger} + \hat{\alpha}_{\text{in}}\right)$ and $\hat{Y} = i/\sqrt{2}\left(\hat{\alpha}_{\text{in}}^{\dagger} - \hat{\alpha}_{\text{in}}\right)$. We can then write the approximate expression,

$$\hat{\theta} \approx \frac{\hat{y}}{\langle \hat{x} \rangle} = \frac{i/\sqrt{2}\left(\hat{\alpha}_{\text{in}}^{\dagger} - \hat{\alpha}_{\text{in}}\right)}{1/\sqrt{2}\left\langle \hat{\alpha}_{\text{in}}^{\dagger} + \hat{\alpha}_{\text{in}} \right\rangle} \approx \frac{i\left(\hat{a}_{\text{in}}^{\dagger} - \hat{a}_{\text{in}}\right)}{2\alpha_{\text{in}}^2} = \frac{i\left(\hat{a}_{\text{in}}^{\dagger} - \hat{a}_{\text{in}}\right)}{2\dot{N}}. \tag{A.40}$$

In the above we have explicitly taken the state to be aligned to the x-axis by taking α_{in} to be real. We can find the phase spectrum by using Eq. A.40 as,

$$\begin{aligned} S_{\hat{\theta}\hat{\theta}}(\omega) =& \int e^{i\omega t} \left\langle \hat{\theta}(t)\hat{\theta}(0) \right\rangle dt \\ =& -\frac{1}{4\dot{N}} \int e^{i\omega t} \left\langle \left(\hat{a}_{\text{in}}^{\dagger}(t) - \hat{a}_{\text{in}}(t)\right)\left(\hat{a}_{\text{in}}^{\dagger}(0) - \hat{a}_{\text{in}}(0)\right) \right\rangle dt \\ =& \frac{1}{4\dot{N}} \int e^{i\omega t} \left\langle \hat{a}_{\text{in}}(t)\hat{a}_{\text{in}}^{\dagger}(0) \right\rangle dt \\ =& \frac{1}{4\dot{N}} \int e^{i\omega t} \delta(t) dt \\ =& \frac{1}{4\dot{N}} \end{aligned} \tag{A.41}$$

Suppose that this coherent state models a laser beam which we measure using a homodyne measurement for some time interval $0 \rightarrow \text{T}$. Using Eqs. A.37 - A.39, and defining the average photon flux as $\dot{N}$ we find,

$$(\Delta N)^2 = N = \dot{N}T = S_{\hat{N}\hat{N}}T. \tag{A.42}$$

In the above we have defined the photon flux spectrum $S_{\hat{N}\hat{N}}$.

Similar manipulations of the phase uncertainty, and the use of Eq. A.41 lead to the relations,

$$(\Delta\theta)^2 = \frac{1}{4\left(\Delta N\right)^2} = \frac{1}{4N} = \frac{1}{4\dot{N}T} = \frac{S_{\hat{\theta}\hat{\theta}}}{T}, \tag{A.43}$$

where in the last inequality we have defined phase spectrum. On first impressions, the factor of T in the denominator may seem to be rather odd, especially when compared to Eq. A.42, where T is in the numerator. However, in the former case, consider that we wish to measure phase, which is accomplished by finding the average value of the phase readout over the interval. In the later case, we are interested in finding the *total* number of photons over an interval, so we multiply the average flux by the time interval.

Multiplying Eqs. A.42 and A.43 together, we find the flux–phase spectrum uncertainty relation,

$$S_{\hat{N}\hat{N}}S_{\hat{\theta}\hat{\theta}} = \frac{1}{4} \tag{A.44}$$

Suppose that we compare the phase difference between a photon striking the mirror in the equilibrium position, and striking the mirror when it has been displaced by an amount Δx. Because the photon reflects, it will travel and additional distance $2x$, which corresponds to $\Delta\phi = 2k\Delta x$, where k is the wavevector of the photon. This allows us to relate $S^{\mathrm{imp}}_{\hat{x}\hat{x}} = S_{\hat{\theta}\hat{\theta}}/4k^2$. In the same spirit, we note that a photon striking the mirror will impart a momentum $2\hbar k$, which gives the relation $S_{\hat{F}\hat{F}} = 4\hbar^2k^2S_{\hat{N}\hat{N}}$. Inserting these last two expressions into eq. A.44, we find,

$$\boxed{\overline{S}^{\mathrm{imp}}_{\hat{x}\hat{x}}(\omega)\overline{S}_{\hat{F}\hat{F}}(\omega) = \frac{\hbar^2}{4}.} \tag{A.45}$$

These results, although they have been calculated for the simple case of a beam striking a mirror, are still valid for the case of an optical cavity provided we drive the cavity on resonance. In this case changes in Δx will, to good approximation, result in changes in the phase of the intracavity light.

Appendix B

Orbital-strain Interactions

B.1 Coordinates, Stress, and Strain

Stress, which has units of force per area, describes the situation where a force is applied through a continuous media. Stress is written as a tensor with nine components, three for the normal components, and the remaining six corresponding to sheer components. This can be simplified even further by noting that the angular momentum of the infinitesimal piece must be zero, meaning that the sheer terms must cancel each other out, namely $\sigma_{ij} = \sigma_{ji}$, where σ_{ij} are the components of the stress vector.

Strain, like stress is a represented as a rank-2 tensor. Unlike strain, it is unitless, representing the deformation of a material normalized by its original length. In one dimension, for example, this could be written as $\epsilon = \frac{\Delta l}{l}$, where ϵ is the strain, Δl is the deformation, and l is the original length. Strain is related to stress through the elasticity tensor, which is

a continuum analogue to Hooke's law. For diamond, this is written as [197]:

$$\begin{bmatrix} \sigma_{xx} \\ \sigma_{yy} \\ \sigma_{zz} \\ \sigma_{yz} \\ \sigma_{zx} \\ \sigma_{xy} \end{bmatrix} = \begin{bmatrix} c_{11} & c_{12} & c_{12} & 0 & 0 & 0 \\ c_{12} & c_{11} & c_{12} & 0 & 0 & 0 \\ c_{12} & c_{12} & c_{11} & 0 & 0 & 0 \\ 0 & 0 & 0 & c_{44} & 0 & 0 \\ 0 & 0 & 0 & 0 & c_{44} & 0 \\ 0 & 0 & 0 & 0 & 0 & c_{44} \end{bmatrix} \begin{bmatrix} \epsilon_{xx} \\ \epsilon_{yy} \\ \epsilon_{zz} \\ \epsilon_{yz} \\ \epsilon_{zx} \\ \epsilon_{xy} \end{bmatrix}, \tag{B.1}$$

where $\{c_{11}, c_{12}, c_{44}\} = \{1075, 139, 567\}$ GPa [197]. This relation is particularly important in calculating the response of a colour center to an external drive, as often the drive is most easily related to stress, and the NV center to strain.

Colour centres can be oriented along one of four directions with respect to the unit crystal axes, namely $[111], [\bar{1}11], [1\bar{1}\bar{1}]$, and $[1\bar{1}1]$. The Element 6 diamond samples we buy are nearly all [100] cut diamond, so colour centres will never be precisely perpendicular to any face of the diamond chip. The Hamiltonian for colour centres is most intuitively written in a basis aligned to the colour centre, with the $\hat{z}$ direction pointing along the colour centre axis by convention. However stress and strain, unlike other perturbative fields such as magnetic and electric fields, reside within the diamond material itself, and are consequently most naturally described in a basis aligned with the unit crystal axes. As a consequence we will have to transform between the lattice and the NV basis. Using the fact that the rotation matrix, R, is both real and unitary, we can write this transformation as $\sigma' = R\sigma R^T$. Then one choice of rotation is $R = R_z(45°)R_x(54.7°)$, where the other three rotations are related to this by 45° rotations about the z-axis.

As an aside, it worth noting that the strain interaction of an NV and the environment will often (but not always) be written in terms of a deformation potential [205, 206]. A deformation potential describes a perturbation of a quantum state with respect to a particular

strain, which satisfies the expression [207],

$$H_{ij} = D_{ij}^{\alpha\beta}\epsilon_{\alpha\beta}. \tag{B.2}$$

In order to find the Hamiltonian describing strain coupling interactions in an NV, as well as other interactions, one can make use of group theory arguments [208]. To see this, consider some Hamiltonian $\hat{H}$ which is invariant under transformation by some unitary $\hat{U}$. This fulfills the expression,

$$U^{\dagger}HU\left|\psi\right\rangle = H\left|\psi\right\rangle = E\left|\psi\right\rangle. \tag{B.3}$$

From this, it immediately follows that, $H\left(U\left|\psi\right\rangle\right) = H\left|\psi'\right\rangle = E\left|\psi'\right\rangle$, which tells us that changing the basis under the action of U will leave the energy of the Hamiltonian unchanged. This is a powerful tool, as it allows us indirectly attain information about the unknown eigenstates of the system simply by knowing the symmetry operations which leave the Hamiltonian invariant. In the case of colour centre, for example, rotations of 120 degrees about the NV axis will leave the Hamilton unchanged in the absence of any externally applied fields. A detailed discussion of this may be found in ref [208, 209].

B.2 Orbital Strain

Using the above arguments, the interaction of colour centres with strain can be deduced. These can be grouped into spin-strain interactions, which affects the spin degree of freedom, and orbital-strain interactions, which directly affect the orbitals. These will not always be present, as shown in Table B.1. Note that for highly strained samples, these terms can become mixed. Written in terms of stress, for both the excited and the ground state, orbital strain may be written as,

$$H_{os} = \begin{bmatrix} \alpha - \beta & \gamma \\ \gamma & \alpha + \beta \end{bmatrix} \tag{B.4}$$

Table B.1: Strain interactions in NV and SiV centres, for excited and ground states.

Coupling Type	**NV**		**SiV**	
	GS	**ES**	**GS**	**ES**
Spin-strain	Yes	Yes	No	No
Orbital-strain	No	Yes	Yes	Yes

In the frame of the colour center, we have for stress,

$$\alpha = (A_1 - A_2)(\sigma_{xx} + \sigma_{yy}) + (A_1 + 2A_2)\sigma_{zz} \tag{B.5}$$

$$\beta = (B + C)(\sigma_{xx} - \sigma_{yy}) + \sqrt{2}(C - 2B)\sigma_{zx} \tag{B.6}$$

$$\gamma = -2(B + C)\sigma_{xy} + \sqrt{2}(C - 2B)\sigma_{yz} \tag{B.7}$$

Which can also be written in terms of strain as,

$$\alpha = t_{\perp}(\epsilon_{xx} + \epsilon_{yy}) + t_{\parallel}\epsilon zz \tag{B.8}$$

$$\beta = d(\epsilon_{xx} - \epsilon_{yy}) + f\epsilon_{zx} \tag{B.9}$$

$$\gamma = -2d\epsilon xy + f\epsilon yz, \tag{B.10}$$

where,

$$t_{\perp} = (c_{11} - c_{12})A_1 - c_{44}A_2 \tag{B.11}$$

$$t_{\parallel} = (c_{11} + 2c_{12})A_1 + c_{44}A_2 \tag{B.12}$$

$$d = (c_{11} - c_{12})B + c_{44}C \tag{B.13}$$

$$f = c_{44}C - (c_{12} + 2c_{11})B. \tag{B.14}$$

This allows us to make some comparison between the NV and SiV stress and strains on Table B.2 and Table B.3 [210, 211]

Table B.2: Stress comparison of NVs and SiVs.

Coupling term	**Units**	**NV**	**SiV**
$\mathbf{A}_{1,e}$	THz/GPa	2.23	?
$\mathbf{A}_{2,e}$	THz/GPa	-5.85	?
$\mathbf{B}_e$	THz/GPa	-1.58	0.484
$\mathbf{B}_g$	THz/GPa	N/A	0.630
$\mathbf{C}_e$	THz/GPa	-2.57	?

Table B.3: Strain comparison of NVs and SiVs.

Coupling term	**Units**	**NV**	**SiV**
$\mathbf{t}_{\parallel,e}$-$\mathbf{t}_{\parallel,g}$	PHz/strain	-3.6	1.7
$\mathbf{t}_{\perp,e}$ - $\mathbf{t}_{\perp,g}$	PHz/strain	5.39	0.078
$\mathbf{d}_e$	PHz/strain	-2.93	1.8
$\mathbf{d}_g$	PHz/strain	N/A	1.3
$\mathbf{f}_e$	PHz/strain	-4.63	-0.720
$\mathbf{f}_g$	PHz/strain	N/A	-0.250

B.3 Parallel Strain

B.3.1 Semi-Classical Treatment

Common to both the spin-strain and axial-strain Hamiltonians is the fact that a strain along the axis of a colour centre will induce a shift in the energy separating the energy levels. Under the assumption of a classical mechanical drive which is not significantly depleted by interaction with the colour centre, we can deduce from the Hamilton that we will have a shift in energy $\Delta\omega = d_{\parallel}\epsilon_{\parallel} \pm \sqrt{(\gamma B_z)^2 + (d_{\perp}\epsilon_{\perp})^2}$ [126]. Treating our mechanics classically, this allows us to rewrite the Hamiltonian governing our system as,

$$H = H_o + H_d \tag{B.15}$$

$$H_o = \hbar\omega_{cc}\left(1 + G\overline{x}\cos(\omega_m t)\right)\sigma^+\sigma^- \tag{B.16}$$

$$H_d = \frac{\hbar\Omega}{2}\left(\Omega^+ e^{-\mathrm{i}\omega_d t} + \Omega^- e^{\mathrm{i}\omega_d t}\right) \tag{B.17}$$

To account for dissipative effects, we can use the master equation approach, allowing the two level system to exchange energy with a bath. This yields the expression,

$$\begin{aligned}\dot{\rho} &= -\mathrm{i}\,[H,\rho] + \mathcal{L}\left(\sqrt{\kappa(\overline{n}+1)}\sigma^{-}\right)\rho + \mathcal{L}\left(\sqrt{\kappa\overline{n}}\sigma^{+}\right)\rho \\ &= -\mathrm{i}\,[H,\rho] + \mathcal{L}\left(\sqrt{\kappa\overline{n}}\sigma^{-}\right)\rho,\end{aligned} \tag{B.18}$$

where $\mathcal{L}$ is the Limblad operator, and in the second line we have enforced that the optical bath has zero thermal occupation. In order to find the emission and absorption spectrum we will need to solve for the raising and operator of the system,

$$\begin{aligned}\langle\dot{\sigma}^{+}\rangle &= \mathrm{Tr}\left\{\sigma^{+}\dot{\rho}\right\} \\ &= -\mathrm{i}\,\omega_{cc}\left[1+G\overline{x}\cos(\omega_m t)\right]\mathrm{Tr}\left\{\sigma^{+}\sigma^{+}\sigma^{-}-\sigma^{+}\rho\sigma^{+}\sigma^{-}\right\} \\ &\quad -\frac{\mathrm{i}\,\hbar\Omega}{2}\left(\mathrm{Tr}\left\{\sigma^{+}\sigma^{+}\rho-\sigma^{+}\rho\sigma^{+}\right\}e^{-\mathrm{i}\,\omega_d t}+\mathrm{Tr}\left\{\sigma^{+}\sigma^{-}\rho-\sigma^{+}\rho\sigma^{-}\right\}e^{\mathrm{i}\,\omega_d t}\right) \\ &\quad +\kappa\,\mathrm{Tr}\left\{\sigma^{+}\sigma^{-}\rho\sigma^{+}-\frac{1}{2}\sigma^{+}\sigma^{+}\sigma_{-}\rho-\frac{1}{2}\sigma^{+}\rho\sigma^{+}\sigma^{-}\right\}\end{aligned} \tag{B.19}$$

In the rotating frame this simplifies to,

$$\langle\dot{\sigma}^{+}\rangle = \mathrm{i}\,[\Delta+G\overline{x}\cos\omega_m t]\,\langle\sigma^{+}\rangle - \kappa\,\langle\sigma^{+}\rangle + \mathrm{i}\,\frac{\hbar\Omega}{2} \tag{B.20}$$

This can rearranged with an integrating factor,

$$\begin{aligned}&\frac{\mathrm{i}\,\hbar\Omega}{2}\exp\left[(-\mathrm{i}\,\Delta+\kappa)\,t-\frac{\mathrm{i}\,G\overline{x}}{\omega_m}\sin\omega_m t\right] \\ &= \frac{d}{dt}\left(\langle\sigma^{+}\rangle\exp\left[(-\mathrm{i}\,\Delta+\kappa)\,t-\frac{\mathrm{i}\,G\overline{x}}{\omega_m}\sin\omega_m t\right]\right).\end{aligned} \tag{B.21}$$

At this point we would like to Fourier transform our equation, however the sin in the exponent poses a difficulty. To solve this we use the Jacobi-Anger formula: $e^{\mathrm{i}\,z\sin\theta} = \sum_{n=-\infty}^{\infty} J_n(z)e^{\mathrm{i}\,n\theta}$. Beginning with the left side of Eq. B.23, we find,

$$\begin{aligned}&\mathcal{F}\left\{\frac{\mathrm{i}\,\hbar\Omega e^{(-\,\mathrm{i}\,\Delta+\kappa)t}}{2}\sum_{n=-\infty}^{\infty}J_n\left(\frac{G\overline{x}}{\omega_m}\right)e^{\mathrm{i}\,n\omega_m t}\right\} \\ &=\frac{\mathrm{i}\,\hbar\Omega}{2}\sum_{n=-\infty}^{\infty}J_n\left(\frac{G\overline{x}}{\omega_m}\right)2\pi\delta(\omega+\Delta-n\omega_m+\mathrm{i}\,\kappa),\end{aligned} \tag{B.22}$$

Next we simplify the right side of side of Eq. B.23,

$$\begin{aligned}&\mathcal{F}\left\{\frac{d}{dt}\left(\langle\sigma^+(t)\rangle\,e^{(-\,\mathrm{i}\,\Delta+\kappa)t}\sum_{n=-\infty}^{\infty}J_n\left(\frac{G\overline{x}}{\omega_m}\right)e^{\mathrm{i}\,n\omega_m t}\right)\right\} \\ &=\mathrm{i}\,\omega\sum_{n=-\infty}^{\infty}J_n\left(\frac{G\overline{x}}{\omega_m}\right)\int_{-\infty}^{\infty}\langle\sigma^+(t)\rangle\,e^{-\,\mathrm{i}(\omega+\Delta-n\omega_m+\mathrm{i}\,\kappa)t}dt \\ &=\mathrm{i}\,\omega\sum_{n=-\infty}^{\infty}J_n\left(\frac{G\overline{x}}{\omega_m}\right)\langle\sigma^+(\omega+\Delta-n\omega_m+\mathrm{i}\,\kappa)\rangle\,.\end{aligned} \tag{B.23}$$

Using these last two results, we arrive at the solution,

$$\langle\sigma^+(\omega)\rangle = \frac{\mathrm{i}\,\hbar\Omega}{2}\sum_{n=-\infty}^{\infty}J_n\left(\frac{G\overline{x}}{\omega_m}\right)\frac{2\pi\delta(\omega)}{-\,\mathrm{i}(\omega+\Delta+n\omega_m)+\kappa}. \tag{B.24}$$

From here we can calculate the florescence spectrum using, $s = \int_{-\infty}^{\infty}\langle\sigma^+(t)\sigma^-(t')\rangle\,e^{-\,\mathrm{i}\,\omega t}dt' = \frac{1}{2\pi}\int_{-\infty}^{\infty}\langle\sigma^+(\omega)\sigma^-(\omega')\rangle\,d\omega'$. For long time intervals, we can assume that we are dealing with a stationary process, and invoke the quantum regression theorem to find,

$$S = |s|^2 = \frac{\hbar^2\Omega^2}{4}\left|\mathrm{i}\sum_{n=-\infty}^{\infty}\frac{J_n\left(\frac{G\overline{x}}{\omega_m}\right)}{-\,\mathrm{i}(\omega+\Delta+n\omega_m)+\kappa/2}\right|^2 \tag{B.25}$$

While Eq. B.25 is exact assuming a stationary process, it is rather unwieldy. In most cases simpler expressions can be used. Here we identify three special cases,

1. Sideband resolved ($\omega_m \gg \kappa$)

$$S(\omega) = \frac{\hbar^2\Omega^2}{4} \sum_{n=-\infty}^{\infty} \frac{J_n^2\left(\frac{G\overline{x}}{\omega_m}\right)}{(\omega + \Delta + n\omega_m)^2 + \kappa^2/4}. \tag{B.26}$$

2. Sideband resolved, weak coupling ($\omega_m \gg \kappa, G\overline{x}$),

$$\begin{aligned} S(\omega) =& \frac{\hbar^2\Omega^2}{4}\Bigg[\frac{1}{(\omega+\Delta)^2+\kappa^2/4} \\ &+ \frac{G^2\overline{x}^2}{4\omega_m^2}\left(\frac{1}{(\omega+\Delta+\omega_m)^2+\kappa^2/4} + \frac{1}{(\omega+\Delta-\omega_m)^2+\kappa^2/4}\right)\Bigg]. \end{aligned} \tag{B.27}$$

3. Sideband unresolved, weak coupling ($\kappa \gg \omega_m \gg G\overline{x}$),

$$\begin{aligned} S(\omega) =& \frac{\hbar^2\Omega^2}{4}\Bigg[\frac{1}{(\omega+\Delta)^2+\kappa^2/4} + \frac{G\overline{x}}{4\omega_m}\left(\frac{1}{(\omega+\Delta)^2+\omega_m(\Delta+\omega)+\kappa^2/4}\right. \\ &\left. - \frac{1}{(\omega+\Delta)^2-\omega_m(\Delta+\omega)+\kappa^2/4}\right)\Bigg]. \end{aligned} \tag{B.28}$$

B.3.2 Quantum Treatment

Single Colour Centre

For the sake of simplicity, here we will work with a two-level system and parallel strain. This could represent, for instance, transitions between the ground state and one of the orbital excited states, or even as we shall see later on the transitions between certain spin states. In a frame rotating with the laser the Hamiltonian takes the form $\hat{H} = \hat{H}_o + \hat{H}_{\text{int}} + \hat{H}_d$, which is a summation of Hamiltonians governing the two level system, the interaction with

the strain, and external electromagnetic driving [206]. These terms are explicitly,

$$\hat{H}_o = \hbar\omega_{\rm cc}\hat{\sigma}^+\hat{\sigma}^- + \hbar\omega_m\hat{b}^\dagger\hat{b} \tag{B.29}$$

$$\hat{H}_{\rm int} = \hbar g_o\left(\hat{b}+\hat{b}^\dagger\right)\hat{\sigma}^+\hat{\sigma}^- \tag{B.30}$$

$$\hat{H}_{\rm drive} = \frac{\hbar\Omega}{2}\left(\hat{\sigma}^+e^{-{\rm i}\omega_d t} + \hat{\sigma}^-e^{{\rm i}\omega_d t}\right) \tag{B.31}$$

where σ_+, σ_- are the raising and lowering operators of the two level system, $\hat{b}^\dagger, \hat{b}$ are the raising and lowering operators of the harmonic oscillators representing the mechanics, $g_o = Gx_0$, is the strain coupling rate, and Ω is the Rabi frequency of the drive. As before, the zero point fluctuations of the mechanics are denoted by x_0.

In order to solve this we will look for an appropriate Schrieffer-Wolff transformation. This is a unitary transformation which will cancel the interaction part of the Hamiltonian, and allow us to uncover an effective Hamiltonian for low coupling strengths. In this case we find [206, 212],

$$\hat{U} = \exp\left[\frac{g_o}{\omega_m}\left(\hat{b}^\dagger - \hat{b}\right)\hat{\sigma}^+\hat{\sigma}^-\right]. \tag{B.32}$$

Using the exponential identity derived in Appendix C, we calculate,

$$\hat{U}\hat{H}_0\hat{U}^\dagger = \hbar\omega_{\rm cc}\hat{\sigma}^+\hat{\sigma}^- + \hbar\omega_m\hat{b}^\dagger\hat{b} - \frac{\hbar g_o^2}{\omega_{\rm m}}\hat{\sigma}^+\hat{\sigma}^- - \hat{H}_{\rm int}, \tag{B.33}$$

$$\hat{U}\hat{H}_{\rm int}\hat{U}^\dagger = \hat{H}_{\rm int} + \frac{2\hbar g_o^2}{\omega_{\rm m}}\hat{\sigma}^+\hat{\sigma}^-, \tag{B.34}$$

$$\hat{U}\hat{H}_{\rm drive}\hat{U}^\dagger = \frac{\hbar\Omega}{2}\left(\hat{\sigma}^+e^{-{\rm i}\omega_d t}e^{\frac{g_o}{\omega_m}\left(\hat{b}^\dagger-\hat{b}\right)} + \hat{\sigma}^-e^{{\rm i}\omega_d t}e^{-\frac{g_o}{\omega_m}\left(\hat{b}^\dagger-\hat{b}\right)}\right). \tag{B.35}$$

In the transformed frame the Hamiltonian now reads,

$$\hat{H} = \hbar\omega'_{\rm cc}\hat{\sigma}^+\hat{\sigma}^- + \hbar\omega_m\hat{b}^\dagger\hat{b} + \frac{\hbar\Omega}{2}\left(\hat{\sigma}^+e^{-{\rm i}\omega_d t+\frac{g_o}{\omega_m}\left(\hat{b}^\dagger-\hat{b}\right)} + \hat{\sigma}^-e^{{\rm i}\omega_d t-\frac{g_o}{\omega_m}\left(\hat{b}^\dagger-\hat{b}\right)}\right), \tag{B.36}$$

where $\omega'_{\rm cc} = \omega_{\rm cc} - g_o^2/\omega_{\rm m}$. As expected, Eq. B.36 does not have the linear interaction term present in our original Hamiltonian. The effect of coupling to the mechanics is now contained in the exponential terms. The slow dynamics of this coupling may be isolated by moving into an interaction picture which rotates about the mechanical frequency and the drive laser frequency. Note that this is quite similar to our treatment of the optomechanics Hamiltonian. We find,

$$\hat{H} = \frac{\hbar\Omega}{2}\hat{\sigma}_+\hat{\sigma}_- \exp\left(-\mathrm{i}\Delta t + \frac{g_o}{\omega_m}\left(\hat{b}^\dagger e^{\mathrm{i}\omega_m t} - \hat{b}e^{-\mathrm{i}\omega_m t}\right)\right) \tag{B.37}$$

$$+ \frac{\hbar\Omega}{2}\hat{\sigma}_+\hat{\sigma}_- \exp\left(\mathrm{i}\Delta t - \frac{g_o}{\omega_m}\left(\hat{b}^\dagger e^{\mathrm{i}\omega_m t} - \hat{b}e^{-\mathrm{i}\omega_m t}\right)\right), \tag{B.38}$$

where $\Delta = \omega_{\rm d} - \omega_{\rm cc}$ and g_o/ω_m plays a role analogous to the Lamb-Dicke parameter.

Expanding to lowest order in the exponential in order to isolate for the dynamics in weak coupling,

$$\hat{H} = \frac{\hbar\Omega}{2}\left(\hat{\sigma}_+ e^{-\mathrm{i}\Delta t} + \hat{\sigma}_- e^{\mathrm{i}\Delta t}\right)\left(1 + \frac{g_o}{\omega_m}\left(\hat{b}^\dagger e^{\mathrm{i}\omega_m t} - \hat{b}e^{-\mathrm{i}\omega_m t}\right)\right). \tag{B.39}$$

This can be decomposed into three frequencies by setting the detuning and pulling out the steady state terms, and then moving out of the interaction picture. Explicitly:

$$\hat{H}_{\rm int}(\Delta = -\omega_m) = \frac{\hbar g_o\Omega/2}{\omega_m}\left(\hat{\sigma}_+\hat{b} + \sigma_-\hat{b}^\dagger\right), \tag{B.40}$$

$$\hat{H}_{\rm int}(\Delta = 0) = \frac{\hbar g_o\Omega/2}{\omega_m}\left(\sigma_+ + \sigma_-\right)\left(\hat{b} + \hat{b}^\dagger\right), \tag{B.41}$$

$$\hat{H}_{\rm int}(\Delta = +\omega_m) = \frac{\hbar g_o\Omega/2}{2\omega_m}\left(\hat{\sigma}_+\hat{b}^\dagger + \hat{\sigma}_-\hat{b}\right). \tag{B.42}$$

Note that these three equations have optomechanical analoges in Eq. 4.33, Eq. 4.31, and Eq. 4.34 respectively.

Ensembles

By moving to a situation where one couples to multiple colour centres with the same mechanical mode, we can in priniple increase the interaction strength. To good approximation, we can assume that the colour centres are spaced far enough apart that they do not interact directly with each other. In this case Eq B.41 becomes,

$$\hat{H}_{\text{int}} = \frac{\hbar\Omega}{2\omega_m} \sum_{i=1}^{N} g_{o_i} \left(\sigma_i^+ + \sigma_i^-\right) \left(\hat{b} + \hat{b}^\dagger\right). \tag{B.43}$$

Note that we have indexed the strain coupling coefficient of each colour centre to account for spatial variations in the strain. Supposing that we are sampling an area where the strain is homogeneous (by, for example using a small laser spot size), we can simply us an average strain coupling coefficient. We can now describe the ensemble in terms of the collective spin operators $\hat{S}_\pm = \sum_{i=1}^{N} \hat{\sigma}_\pm$, $\hat{S}_z = \sum_{i=1}^{N} \hat{\sigma}_z$ [213]. From here we use the Holstein-Primakoff transformation, which states for our super operators:

$$\hat{S}_+ = \hat{a}^\dagger \sqrt{N - \hat{a}^\dagger \hat{a}}, \tag{B.44}$$

$$\hat{S}_- = \sqrt{N - \hat{a}^\dagger \hat{a}}\hat{a} \tag{B.45}$$

where N is the number of colour centres, and $\hat{a}^\dagger, \hat{a}$ are the creation and annihilation operators for a harmonic oscillator.

Supposing that we only pump the colour centres weakly with the control laser, we can assume that we are highly unlikely to saturate any individual centre, and can approximate $\hat{S}_- \approx \sqrt{N}\hat{a}$ and $\hat{S}_+ \approx \sqrt{N}\hat{a}^\dagger$. This allows us to write the interaction Hamiltonian as

$$\hat{H}_{\text{int}} = \frac{\hbar\Omega g}{2\omega_{\text{m}}} \left(\hat{a} + \hat{a}^\dagger\right) \left(\hat{b} + \hat{b}^\dagger\right), \tag{B.46}$$

where the effective coupling rate is $g = \sqrt{N} g_o$. This expression is analogous to Eq. 4.31, and will allow us access to many of the same physical effects, such as cooling of the mechanical mode, OMIT, and squeezing. Perhaps an even more interesting prospect would be to use this in conjunction with an additional optical mode to realize wavelength conversion or amplification of colour centre light to telecom frequency light.

Appendix C

Useful Identities

Here we collect some mathematical identities which are useful for the work in the main sections of the thesis. For some of the more uninutative of important identities we will sketch out 'proofs'.

C.1 Useful Transforms and Operators

Displacement Operator

$$\hat{D}(\alpha) = \exp\left(\alpha\hat{a}^\dagger - \alpha^*\hat{a}\right) \tag{C.1}$$

This unitary operator can be used in the linearization of the optomechanical Hamiltonian. It has the effect $\hat{D}^\dagger\hat{a}\hat{D} = \hat{a} + \alpha$.

Polaron Transform

$$\hat{U} = \exp\left(\frac{g_0}{\omega_\mathrm{m}}\hat{a}^\dagger\hat{a}(\hat{b} - \hat{b}^\dagger)\right) \tag{C.2}$$

This can be used to extract the Kerr nonlinearity in the canonical optomechanical Hamiltonian, where $\hat{U}^\dagger\hat{H}\hat{U} = \hbar\left(\omega_\mathrm{m} - \frac{g_0^2}{\omega_\mathrm{m}}\right)\hat{a}^\dagger\hat{a} + \hbar\omega_\mathrm{m}\hat{b}^\dagger\hat{b} - \hbar\frac{g_0^2}{\omega_\mathrm{m}}\left(\hat{a}^\dagger\hat{a}\right)^2$.

Schrieffer-Wolff Transform

$$\hat{U} = \exp\left(\frac{g_0}{\omega_{\mathrm{m}}} |e\rangle \langle e| (\hat{b} - \hat{b}^\dagger)\right) \tag{C.3}$$

Note that this is not a general Schrieffer-Wolff Transform, but one chosen to assist in solving the problem of an NV coupled to a mechanical oscillator [206].

Holstein-Primakoff Transform

$$\hat{S}_+ = \hat{a}^\dagger \sqrt{N - \hat{a}^\dagger \hat{a}}, \tag{C.4}$$

$$\hat{S}_- = \sqrt{N - \hat{a}^\dagger \hat{a}}\hat{a}, \tag{C.5}$$

$$\hat{S}_z = \hat{a}^\dagger \hat{a} - N/2. \tag{C.6}$$

In the above we are using the collective spin operators, which are sums of spin-1/2 operators according to $\hat{S}_\pm = \sum_{i=1}^N \hat{s}_\pm$, $\hat{S}_z = \sum_{i=1}^N \hat{s}_z$ [213].

C.2 Fourier Transforms

We use the Fourier transform definition $f(\omega) = \frac{1}{\sqrt{2\pi}} \int_{-\infty}^{\infty} f(t) e^{-i\omega t} dt$ and the reverse transform definition $f(t) = \frac{1}{\sqrt{2\pi}} \int_{\infty}^{\infty} f(\omega) e^{i\omega t} dt$. The following identities can be derived,

1. $\mathcal{F}[f'(t)] = i\omega f(\omega)$
2. $\mathcal{F}[f''(t)] = -\omega^2 f(\omega)$
3. $\mathcal{F}[f(t+a)] = e^{ia\omega} f(\omega)$
4. $\mathcal{F}[e^{at} f(t)] = f(\omega + ia)$

C.2.1 Useful Definitions

Dirac delta function

$\delta(t-u) = \frac{1}{2\pi}\int_{-\infty}^{\infty} e^{i\omega(t-u)d\omega}$

Jacobi-Anger expansion

$e^{iz\cos\theta} = \sum_{n_--\infty}^{\infty} i^n J_n(z)e^{in\theta}$, $e^{iz\sin\theta} = \sum_{n_--\infty}^{\infty} J_n(z)e^{in\theta}$, where n is an integer, and J_n are Bessel functions of the first kind.

Autocorrelation

$G(\tau) = \lim_{T\to\infty}\frac{1}{T}\int_0^T v(t)v(t+\tau)dt = \langle v(t)v(t+\tau)\rangle$.

Power Spectral Density

$S(\omega) = \lim_{T\to\infty}\frac{|v(\omega)|^2}{T} = \lim_{T\to\infty}\langle|v(\omega)|^2\rangle$

Wiener-Khinchin Theorem

$S(\omega) = \int_{-\infty}^{\infty} e^{-i\omega\tau}G(\tau)d\tau$, where $G(\tau)$ is the autocorrelation function. This is only valid for a stationary process.

Wiener-Khinchin Theorem 'proof'

Assuming that v is real, we can write this power spectral density as $S(\omega) = \lim_{T\to\infty}\langle v(\omega)v(-\omega)\rangle$. Using the one sided Fourier transform, signifying measurement from time 0 to T, we find that,

$$S(\omega) = \lim_{T\to\infty}\frac{1}{2\pi T}\left(\int_0^T e^{-i\omega t}v(t)dt\right)\left(\int_0^T e^{i\omega t'}v(t)dt'\right). \tag{C.7}$$

This integration is to be performed over a square area in the $t - t'$ plane. Using the change of variables $t \to t' + \tau$, we can convert the area of integration into a trapezoid as shown on Fig C.1. Writing the trapezoid as the sum of two triangles results in,

$$\begin{aligned} S(\omega) = &\lim_{T\to\infty} \frac{1}{2\pi T}\left(\int_0^T \int_0^{T-\tau} e^{-i\omega\tau} v(t'+\tau)v(t')dt'd\tau + \int_{-T}^0 \int_{-\tau}^T e^{-i\omega\tau} v(t'+\tau)v(t')dt'd\tau\right) \\ =&\frac{1}{2\pi}\left(\int_0^T e^{-i\omega\tau} G(\tau)d\tau + \int_{-T}^0 e^{-i\omega\tau} G(\tau)d\tau\right) \\ &- \lim_{T\to\infty} \frac{1}{2\pi T}\left(\int_0^T \int_{T-\tau}^T e^{-i\omega\tau} v(t'+\tau)v(t')dt'd\tau + \int_{-T}^0 \int_0^\tau e^{-i\omega\tau} v(t'+\tau)v(t')dt'd\tau\right) \end{aligned} \tag{C.8}$$

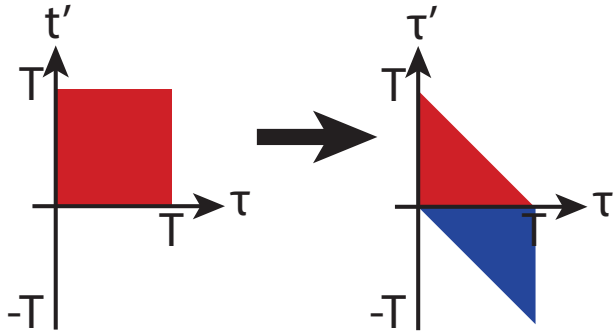

Figure C.1: Change of integration variables for the Wiener-Khinchin theorem.

Provided that we measure for a time much longer than the correlation timescales of v, we can discard the final line in the above expression. This gives the Wiener-Khinchin Theorem,

$$S(\omega) = \int_{-\infty}^{\infty} e^{-i\omega\tau} G(\tau)d\tau. \tag{C.9}$$

C.2.2 Operator Algebra

Quantum harmonic oscillator

$\left[\hat{a}, \hat{a}^\dagger\right] = 1, \left[\hat{n}, \hat{a}^\dagger\right] = \hat{a}^\dagger$, $[\hat{n}, \hat{a}] = -\hat{a}$.

Exponential identity

$e^{s\hat{X}}\hat{Y}e^{-s\hat{X}} = \hat{Y} + s\left[\hat{X},\hat{Y}\right] + \frac{s^2}{2!}\left[\hat{X},\left[\hat{X},\hat{Y}\right]\right] + \frac{s^3}{3!}\left[\hat{X},\left[\hat{X},\left[\hat{X},\hat{Y}\right]\right]\right] + ...$

Harmonic oscillator exponential identity

$e^{s\hat{a}^\dagger\hat{a}}\hat{a}^\dagger e^{-s\hat{a}^\dagger\hat{a}} = e^{-s}$, $e^{s\hat{a}^\dagger\hat{a}}\hat{a}e^{-s\hat{a}^\dagger\hat{a}} = e^{s}$.

Exponential identity 'proof'

Following the arguments of [214] [215], we define a super-operator, $\hat{O}_x$ which has the effect $\hat{O}_x\hat{Y} = \hat{X}\hat{Y} - \hat{Y}\hat{X}$ on some operator, $\hat{Y}$. Next we use this definition to simplify the following expression:

$$\frac{d}{ds}\left(e^{s\hat{X}}\hat{Y}e^{-s\hat{X}}\right) = s\hat{X}e^{s\hat{X}}\hat{Y}e^{-s\hat{X}} - e^{s\hat{X}}\hat{Y}s\hat{X}e^{-s\hat{X}} = s\left[e^{s\hat{X}}\hat{Y}e^{-s\hat{X}},\hat{X}\right] = s\hat{O}_x\left(e^{s\hat{X}}\hat{Y}e^{-s\hat{X}}\right). \tag{C.10}$$

Next we define yet another operator, $\hat{P}(s)$ which has the effect $\hat{P}(s)\hat{Y} = e^{s\hat{X}}\hat{Y}e^{-s\hat{X}}$. With this definition our previous expression now reads,

$$\frac{d}{ds}\hat{P}(s)\hat{Y} = s\hat{O}_x\hat{P}(s)\hat{Y} \rightarrow \frac{d}{ds}\hat{P}(s) = s\hat{O}_x\hat{P}(s). \tag{C.11}$$

This gives the solution $\hat{P}(s) = e^{s\hat{O}_x}$. Placing this solution into our original definition for the action of $\hat{P}$, we find:

$$e^{s\hat{X}}\hat{Y}e^{-s\hat{X}} = e^{s\hat{O}_x}\hat{Y} = \hat{Y} + s\left[\hat{X},\hat{Y}\right] + \frac{s^2}{2!}\left[\hat{X},\left[\hat{X},\hat{Y}\right]\right] + \frac{s^3}{3!}\left[\hat{X},\left[\hat{X},\left[\hat{X},\hat{Y}\right]\right]\right] + ... \tag{C.12}$$

Harmonic oscillator exponential identity 'proof'

With this identity, we would like to solve for the particular situation where $\hat{Y} = \hat{a}$ and $\hat{X} = \hat{a}^\dagger \hat{a}$.

$$\begin{aligned} e^{s\hat{a}^\dagger\hat{a}}\hat{a}e^{-s\hat{a}^\dagger\hat{a}} &= \hat{a} + s\left[\hat{a}^\dagger\hat{a}, \hat{a}\right] + \frac{s^2}{2!}\left[\hat{a}^\dagger\hat{a}, \left[\hat{a}^\dagger\hat{a}, \hat{a}\right]\right] + \frac{s^3}{3!}\left[\hat{a}^\dagger\hat{a}, \left[\hat{a}^\dagger\hat{a}, \left[\hat{a}^\dagger\hat{a}, \hat{a}\right]\right]\right] + ... \\ &= \hat{a} + (-s)^1\hat{a} + \frac{(-s)^2}{2!}\hat{a} + \frac{(-s)^3}{3!}\hat{a} + ... \\ &= \hat{a}e^{-s}. \end{aligned} \tag{C.13}$$

One can follow the same argument to derive $e^{s\hat{a}^\dagger\hat{a}}\hat{a}^\dagger e^{-s\hat{a}^\dagger\hat{a}} = \hat{a}^\dagger e^{s}$.

Appendix D

Copyright Forms

Permission to Reuse Content

REUSING AIP PUBLISHING CONTENT

Permission from AIP Publishing is required to:

- republish content (e.g., excerpts, figures, tables) if you are not the author
- modify, adapt, or redraw materials for another publication
- systematically reproduce content
- store or distribute content electronically
- copy content for promotional purposes

To request permission to reuse AIP Publishing content, use RightsLink® for the fastest response or contact AIP Publishing directly at rights@aip.org and we will respond within one week:

For RightsLink, use Scitation to access the article you wish to license, and click on the Reprints and Permissions link under the TOOLS tab. (For assistance click the "Help" button in the top right corner of the RightsLink page.)

To send a permission request to rights@aip.org, please include the following:

- Citation information for the article containing the material you wish to reuse
- A description of the material you wish to reuse, including figure and/or table numbers
- The title, authors, name of the publisher, and expected publication date of the new work
- The format(s) the new work will appear in (e.g., print, electronic, CD-ROM)
- How the new work will be distributed and whether it will be offered for sale

Authors do **not** need permission from AIP Publishing to:

- quote from a publication (please include the material in quotation marks and provide the customary acknowledgment of the source)
- reuse any materials that are licensed under a Creative Commons CC BY license (please format your credit line: "Author names, Journal Titles, Vol.#, Article ID#, Year of Publication; licensed under a Creative Commons Attribution (CC BY) license.")

Optomechanically Induced Transparency and Cooling in Thermally Stable Diamond Microcavities

Author: David P. Lake, Matthew Mitchell, Yasmeen Kamaliddin, et al

Publication: ACS Photonics

Publisher: American Chemical Society

Date: Mar 1, 2018